

Single Photon Transistor mediated by electrically tunable Rydberg-Rydberg Interactions

VON DER FAKULTÄT MATHEMATIK UND PHYSIK DER UNIVERSITÄT STUTTGART
ZUR ERLANGUNG DER WÜRDE EINES DOKTORS DER
NATURWISSENSCHAFTEN (DR. RER. NAT.) GENEHMIGTE ABHANDLUNG

VORGELEGT VON

HANNES M. GORNIACZYK

AUS SCHWÄBISCH GMÜND

HAUPTBERICHTER: DR. SEBASTIAN HOFFERBERTH

MITBERICHTER: PROF. DR. PETER MICHLER

PRÜFUNGSVORSITZENDER: PROF. DR. HANS PETER BÜCHLER

TAG DER MÜNDLICHEN PRÜFUNG: 02.12.2016

5. PHYSIKALISCHES INSTITUT, UNIVERSITÄT STUTTGART

2016

©2016 – HANNES M. GORNIACZYK

ALL RIGHTS RESERVED.

D 93

Single Photon Transistor mediated by electrically tunable Rydberg-Rydberg Interactions

ABSTRACT

Modern information technology is based on light as information carrier. Data is broadcast via optical fibers over long distances with huge bandwidths. It is a long-standing goal in nonlinear optics to develop materials and devices that allow optical data processing without interfacing it to electronic circuits which are subject to loss and time lag.

In this work, a versatile quantum optics experiment was built demonstrating an optical transistor which toggles its state by the input of the smallest energy unit possible: one *gate* photon. Mediated by interaction between Rydberg atoms, this single gate photon immediately affects the optical properties of the medium, a cloud of ultra-cold atoms, such that the transmission of a laser beam is reduced by hundreds of *source* photons through Rydberg blockade of electromagnetically induced transparency (EIT).

The effective interaction between a gate photon and the source photons can be tuned by applying constant electric fields. That way, a strong enhancement of the optical nonlinearity is obtained if the states are Stark-shifted to Förster resonances. Conversely, the interaction strength can be minimized at electric fields between resonances.

By reading out the stored gate excitation after scattering source photons, coherence properties of this quantum state are studied.

To sum up, our results are a distinct proof that huge optical nonlinearities can be generated with Rydberg-EIT. Our highly tunable optical transistor could advance classical information technology. The study of coherence properties is an important step towards the implementation of photonic quantum gates.

Author Publications

The following publications were written in the course of this thesis:

- [1] H. Gorniaczyk, C. Tresp, P. Bienias, A. Paris-Mandoki, W. Li, I. Mirgorodskiy, H. P. Buchler, I. Lesanovsky, and S. Hofferberth. “Enhancement of Rydberg-mediated single-photon nonlinearities by electrically tuned Förster resonances”. In: *Nat Commun* 7.12480 (Aug. 2016)
- [2] C. Tresp, C. Zimmer, I. Mirgorodskiy, H. Gorniaczyk, A. Paris-Mandoki, and S. Hofferberth. “Single-Photon Absorber Based on Strongly Interacting Rydberg Atoms”. In: *Physical Review Letters* 117.22 (Nov. 2016). Editors’ suggestion. ISSN: 1079-7114. DOI: 10.1103/physrevlett.117.223001
- [3] Asaf Paris-Mandoki, Hannes Gorniaczyk, Christoph Tresp, Ivan Mirgorodskiy, and Sebastian Hofferberth. “Tailoring Rydberg interactions via Förster resonances: state combinations, hopping and angular dependence”. In: *Journal of Physics B: Atomic, Molecular and Optical Physics* 49.16 (July 2016), page 164001. ISSN: 1361-6455. DOI: 10.1088/0953-4075/49/16/164001
- [4] C. Tresp, P. Bienias, S. Weber, H. Gorniaczyk, I. Mirgorodskiy, H. P. Büchler, and S. Hofferberth. “Dipolar Dephasing of Rydberg *D*-State Polaritons”. In: *Phys. Rev. Lett.* 115 (8 Aug. 2015), page 083602. DOI: 10.1103/PhysRevLett.115.083602
- [5] H. Gorniaczyk, C. Tresp, J. Schmidt, H. Fedder, and S. Hofferberth. “Single-Photon Transistor Mediated by Interstate Rydberg Interactions”. In: *Phys. Rev. Lett.* 113 (5 July 2014). Editors’ suggestion, APS Physics Viewpoint, page 053601. DOI: 10.1103/PhysRevLett.113.053601.

During my diploma thesis

- [6] Hannes Gorniaczyk. “A crossed optical dipole trap”. Master’s thesis. Universität Stuttgart, Dec. 2011

the following publication was written:

- [7] Markus Falkenau, Valentin V. Volchkov, Jahn Rührig, Hannes Gorniaczyk, and Axel Griesmaier. “Evaporation-limited loading of an atomic trap”. In: *Phys. Rev. A* 85 (2 Feb. 2012), page 023412. DOI: 10.1103/PhysRevA.85.023412.

Contents

0	ZUSAMMENFASSUNG	I
1	INTRODUCTION	7
2	CONCEPTUAL DESIGN AND IMPLEMENTATION OF AN ULTRACOLD QUANTUM OPTICS EXPERIMENT	13
2.1	Project outline, personnel and time schedule	13
2.2	Ultra-high vacuum chamber	14
2.3	Electric field control and ion detection setup	18
2.4	Rubidium level scheme and transitions	22
2.5	Laser setup and frequency stabilization	25
2.6	Laser intensity modulation	27
2.7	Preparation of an ultracold atomic cloud, magneto-optical trap	33
2.8	A crossed optical dipole trap with high power single mode Yb:YAG fiber lasers . .	36
2.9	Rydberg excitation setup and probing of the ground state density	43
2.10	Comprehensive experimental control with computer aided hardware programming, custom electronics and data acquisition	52
3	RYDBERG INTERACTION	65
3.1	Introduction to the physical mechanisms	65
3.2	Derivation of the interaction strength	68
3.3	Excitation exchange	71
3.4	Anisotropic interaction	72
3.5	Theoretical isolation of strong Förster Resonances	75
3.6	Interaction of two Rydberg atoms with the same state	84
4	GIANT OPTICAL NONLINEARITIES WITH RYDBERG-EIT	87
4.1	Simulating the optically driven three-level atom	87

4.2	Probing population and coherences	90
4.3	Electromagnetically induced transparency with Rydberg states using the D ₂ line of ⁸⁷ Rb	92
4.4	Slow light	95
4.5	Distortion mechanisms of EIT spectra	96
4.6	Nonlinear optics on the single photon level	101
4.7	Rydberg interactions affect the EIT spectrum	104
5	SINGLE PHOTON TRANSISTOR	109
5.1	Experimental scheme	109
5.2	Single photon switch	113
5.3	First demonstration of a free-space single photon transistor	114
5.4	High fidelity single Rydberg detection	115
5.5	Tuning parameters for the improvement of the optical transistor	117
6	ENHANCEMENT OF SINGLE-PHOTON NONLINEARITIES BY FÖRSTER RESONANCES	123
6.1	Theoretical analysis of the potentials and state mixing	124
6.2	Optical detection of electrically tuned Förster resonances	126
6.3	The dipole-enhanced single photon transistor on a Förster resonance	131
6.4	Towards photonic phase gates: readout of the gate excitation and susceptibility to source photon scattering	132
7	CONCLUSION AND THOUGHTS	137
7.1	Conclusion	137
7.2	Thoughts	138
	APPENDIX A RYDBERG ENERGY CALCULATION	141
	APPENDIX B ELECTROSTATIC POLARIZABILITIES	143
	ACRONYMS	151
	GLOSSARY	153
	REFERENCES	157

List of Figures

2.1	Vacuum chamber	15
2.2	Expected life time of a trapped atom	17
2.3	Photos of the electrodes and the multi channel plate (MCP)	19
2.4	In-vacuum electrical contacts for electric field control and ion detection	20
2.5	Level scheme of ^{87}Rb with most relevant transitions.	23
2.6	Overview of laser systems in experiment	26
2.7	Frequency stabilization of D_2 lasers	27
2.8	AOM driver operation scheme	28
2.9	AOM driver: front panel circuit	29
2.10	AOM driver calibration and perfect Gaussian light pulses.	30
2.11	Intensity stabilization scheme	32
2.12	Magneto-optical trap	34
2.13	Optical dipole trap setup	38
2.14	a.c. Stark shifts of the ground state, excited state and Rydberg state due to the trap laser	40
2.15	Rubidium ground state trapping at the YAG wavelength	42
2.16	Optical setup for Rydberg excitation and detection	44
2.17	Probe beam profile	45
2.18	From complex refractive index to transmission spectrum	48
2.19	Wavefront error caused by optical density performance	49
2.20	Optimization of optical depth by optical pumping	51
2.21	Graphical user interface of the computer control system	52
2.22	Computer control overview of peripheral devices	54
2.23	High-speed digital control with the Pulse Generator	55
2.24	Setting pulse patterns with the Pulse Generator GUI	56
2.25	High-speed data acquisition with the Time Tagger	57
2.26	GUI for the acquisition of photon and ion counts with the Time Tagger	58
2.27	Highly stable voltage source	59

2.28	Arbitrary waveform generator	61
2.29	Rydberg microwave transitions between 1 and 20 GHz	62
3.1	LeRoy radius: molecular distance, validity of our potential calculations	66
3.2	Rydberg interaction sketch.	67
3.3	Angular dependence of the dipole-dipole interaction	73
3.4	Interaction between S states	77
3.5	Interaction between S and D states	78
3.6	Interaction between D states	79
3.7	Using systematics between quantum numbers to find Förster resonances	80
3.8	Tuning Pair states to Förster resonances with magnetic fields	84
3.9	Interaction of two Rydberg atoms with the same S state	85
4.1	Level scheme and terminology for the three level atom	88
4.2	EIT scan and fitted model	90
4.3	Density matrix elements of the three-level system with off-resonant coupling	91
4.4	Offresonant EIT resonance shifts with control Rabi frequency	91
4.5	Transmission, ion counts and modeled population far detuned from the intermediate state	92
4.6	EIT level scheme of ^{87}Rb with dipole matrix elements	93
4.7	Slow light	95
4.8	Influence of detector saturation and background counts on EIT spectrum	97
4.9	EIT spectrum with variation of optical depth	100
4.10	Rydberg blockade: schematic explanation	102
4.11	Theoretical nonlinear transmission based on a hard rod model	104
4.12	Nonlinear probe transmission	105
4.13	Control Rabi frequency affects the nonlinearity of the probe transmission	105
4.14	Stored Rydberg excitations cause spectral red-shift of EIT.	106
4.15	Interaction effects in offresonant excitation	106
5.1	Transistor level scheme and pulse sequence	110
5.2	High contrast photon switch	113
5.3	Optical gain of the first transistor implementation	115
5.4	High fidelity Rydberg detection	116
5.5	Life time of Rydberg states. A temporal limit for the transistor.	118
5.6	Optical gain with different principal quantum numbers	119

5.7	Thermal atomic motion damps the transistor	119
5.8	Geometrical effects on source transmission: beam waists and blockade radius	121
6.1	Pair potentials and state mixing in an electric and magnetic field	124
6.2	Electric field cancellation with Stark maps	127
6.3	Electrical tuning of Rydberg pair states and the effect on the optical gain	130
6.4	Gain and single Rydberg detection enhanced by an electric field	131
6.5	Readout of gate photons after scattering source photons	132
6.6	Pulse shapes in the transistor experiment with gate photon read-out	134
B.1	Electrostatic polarizabilities of Rydberg S , P , D and F states	144

ΤΟ ΚΑΤJA.

Acknowledgments

I AM DEEPLY INDEPTED to many people contributing to this work and to my life in various ways. I would like to thank all colleagues, in particular

- Sebastian Hofferberth for the opportunity to work as the first PhD student on your first self-financed experiment. It must have either been trust in my experimental capabilities or insanity. Either way, I am extremely thankful for the vast amount of knowledge you have shared and the skills I have gained in the course of this work. No trace of smoke of deceit, we surely wore our gauntlets of strength firmly conceiving this experiment in a dust of appearance. May the helm of the dominator be symbol for your scientific future.
- Tilman Pfau for inspiring lectures on advanced atomic physics, for the employment as a lab assistant in the Cr-II team in 2008 and for the supervision of my diploma thesis in 2011. I enjoyed being part of this institute which not only pushes the frontiers of physics. Sports competitions, barbecues, institute hikes and Christmas parties including *kirikikiki* will always be remembered.
- Peter Michler and Hans-Peter Büchler for your efforts assessing my work, but also for excellent research cooperation within the SFB.
- Igor Lesanovsky and Weibin Li for your collaboration in the study of spin-wave coherence.
- Christoph Tresp for being a fantastic coworker. Your motivation despite your repetitive music playlists are admirable.
- Johannes Schmidt for your master's thesis which bought me chapter 4. Cheers!
- Ivan Mirgorodskiy for taking over the experiment – and for a ton of shared pine nuts!
- Asaf Paris-Mandoki for being a huge enrichment of our experiment. Impressive, how Asafito shaped the experiment in no time.
- Christian Zimmer for the next-generation dimple!

- Jahn Rührig for your motivation to jointly inflate our pecs. 87.5 kg or 120 % of my body mass on the bench press might be fine for a pale physicist. Hopefully no-one will ever see my legs.
- Markus Falkenau and Valentin Volchkov for great memories back in good old CR-II.
- Axel Griesmaier for your support ranging from joint electronics projects, the supervision of my diploma thesis and nowadays the development of high-class electronics for our labs.
- Ralf Ritter for piano jam sessions late at night. Very late.
- Matthias Schmitt for the *uke* sessions.

My special thanks are dedicated to my family and to my friends:

- my parents and my sister for your support in all life circumstances. Thanks for making this education even possible.
- my great-parents who are or would be very satisfied to know I made it.
- my aunts, uncles and cousins I grew up with.
- Katja for your ♥ and support in the past years. I am particularly grateful for the lasagna, the deer fillets with dumplings, the breakfasts with fruit smoothies, the walnut-crusted salmon fillets, [...] which have enlightened my PhD.
- my good 'ol friends from home, in particular Alex, Christian, Daniel, David, Dominik, Gerd, Michael, Michael, Moritz and Sebastian. I shall not miss out any more!
- the awesome Stuttgart connection, especially Alex, Alex, Hannes, Kai, Martina, Mesut, Nik and Roland.

I deeply acknowledge the Carl-Zeiss Foundation* for financial support and for networking events. I appreciate uncomplicated and friendly contact to Judith Schöffler who managed my scholarship. I congratulate Dr. Klaus Herberger for shaping this great foundation.

It is a major honor starting my professional career at Daimler. I would like to thank Dr. Helmut Keller and Joachim Missel for their trust.

Finally, I would like to acknowledge Alexander Franzen for the fancy optics template which I based my drawings on.

*<http://www.carl-zeiss-stiftung.de>

0

Zusammenfassung

Im Rahmen dieser Arbeit wurde der erste optische Transistor hergestellt, der seinen Schaltzustand schon durch ein einzelnes *Gate* Photon verändert um damit die Transmission von über 200 *Source* Photonen zu steuern.

Als erster Doktorand an einem neuen Forschungsprojekt um Dr. Sebastian Hofferberth, unterstützt durch das Emmy-Noether Programm HO 4787/1-1 und durch den SFB/TRR21, haben wir ein neues Quantenoptik-Experiment aufgebaut, dessen Ziel es ist, durch die mesoskopische Wechselwirkung zwischen Rydbergatomen Licht auf dem Niveau einzelner Photonen zu manipulieren. Die Demonstration des optischen Transistors ist dabei nur eine Anwendung. Tatsächlich gibt es verschiedenartige Ideen aus der Quantenoptik und der Atomphysik, die mit diesem Experiment umgesetzt werden könnten.

Basis für das Forschungsvorhaben waren technologische Entwicklungen und wissenschaftliche Erkenntnisse, die im Folgenden resümiert werden. Der technologische Wegbereiter für die vorliegende Arbeit ist ohne Zweifel der Laser. Die Grundlage der Quantenoptik und auch die Entwicklung des Lasers gehen auf das von Albert Einstein geschaffene Grundverständnis von Absorption und stimulierter oder spontaner Emission zurück [8].

Ein wichtiger Fortschritt war die theoretischen Entdeckung der Superradianz durch Robert H. Dicke [9], die eine erhöhte Emissionswahrscheinlichkeit und gerichtete Emission in kohärenten Medien.

Daraufhin konnte nach weiterer theoretischer Vorarbeit durch Charles H. Townes und Arthur

L. Schawlow [10] der erste Laser durch Theodore H. Maiman gebaut werden.

Durch die aufkommende Halbleiterindustrie und des Diodenlasers gab es einen technologischen Durchbruch, der sowohl für langanhaltenden Fortschritt in der Grundlagenforschung sorgte, der sich allerdings auch auf das Privatleben auswirkte durch disruptive Technologien wie zum Beispiel den CD-Player.

Die Lasertechnologie ermöglichte es, die Quantennatur der Materie zu erkunden [11]. Der mechanische Effekt von Laserstrahlung auf Atomgase [12] hat das Forschungsfeld der kalten Atomgase begründet. Ein Meilenstein dieses Feldes ist die Erfindung der magneto-optischen Falle (MOT) [13, 14]. Das war der Startschuss für das Wettrennen um das erste Bose-Einstein Kondensat (BEC) [15–17], das 1995 endete, etwa 70 Jahre nachdem dieser Aggregatzustand vorhergesagt worden war.

Trotz dessen, dass BECs verdünnte Atomgase sind, spielt die Zweikörper-Wechselwirkung eine wichtige Rolle für die statischen und dynamischen Eigenschaften. Die Kontaktwechselwirkung kann mit einem einzelnen Parameter quantifiziert werden: mit der s -Wellen-Streulänge [18, 19]. Falls das chemische Element ein höheres Magnetisches Moment aufweist, wie bei Chrom, Erbium oder Dysprosium, wird die Dipol-Dipol-Wechselwirkung relevant [20, 21] und kann sogar der dominante Wechselwirkungsbeitrag sein [22]. Mittels Feshbach Resonanzen kann die Kontaktwechselwirkung verändert werden [23, 24] und man kann ein rein dipolares Kondensat erzeugen [25], welches je nach Geometrie stabil ist oder eindrucksvoll anisotrop kollabiert [26]. Diese Geometrien können mit optischen Dipolfallen erstellt werden [27]. Diese nutzen die Dipolkraft der Lichtkraft aus um Atome um den Fokus eines weit rotverstimmten Laserstrahls zu fangen [28]. Mit blauer Verstimmung kann ein repulsives Potential hergestellt werden. Unterschiedliche Strahlgeometrien wie eine Doughnut Mode [29], Lichtblätter [30] oder ein Hohlstrahl [31] können dazu verwendet werden, Atome zu fangen. Obwohl das Herstellen diese Strahlformen schwieriger ist, gibt es bei blauverstimmten Fallen den Vorteil, dass die Atome an Orten niedriger Lichtintensität gefangen werden und dadurch der a.c. Stark Effect unterdrückt wird, wichtig für Spektroskopie. Die unterschiedlichsten Potentialgeometrien und die Abhängigkeit der Wechselwirkungseffekten von jenen machen Experimente mit kalten Atomen ideale Prüfstände für Grundlagenforschung.

Die makroskopische Erscheinung der Quantenmechanik in BECs weckt viele Möglichkeiten um neue Ideen umzusetzen, die die Eigenartigkeit der Quantenwelt ausnutzen. So können zum Beispiel neuartige exotische Materiezustände erstellt werden. Bosonische Atome können einen Übergang von der supraleitenden zur Mott Phase in einem optischen Gitter durchführen [32, 33]. Die Kontrolle einzelner Gitterplätze in optischen Gittern [34, 35] kann ausgenutzt werden um definierte Zustände zu erstellen und um die Dynamik zu detektieren, die durch das Zusammenspiel aus Gittereinschluss und quantenmechanischem Tunneln stattfindet [36]. Solche ordnungsverändernde Prozesse können auf andere physikalische Vielteilchensysteme übertragen werden, welche mit klassischen Ansätzen

schwierig oder überhaupt nicht berechenbar sind [37]. Beispielsweise können Probleme der Festkörperphysik wie der Antiferromagnetismus (Ising Hamiltonoperator) simuliert werden [38].

Vielversprechende Resultate auf dem Gebiet der Quanteninformationstechnik und -simulation kommen aus dem Forschung an Ionen [39]. Es ist möglich, magnetische Phasenübergänge zu simulieren [40], die Ising-Wechselwirkung in 2D [41], Quantendots [42] und sogar die Dirac-Gleichung [43]. Im Feld der Quanteninformationsverarbeitung sind Systeme gefangener Ionen womöglich die besten Kandidaten. Heutzutage können diese Systeme Quantenalgorithmen mit fünf Qubits rechnen mit Gatter Fidelity 98% [44]. Wenn nur zwei Qubits benötigt werden, können sogar 99.9(1)% und 99.9934(3)% erreicht werden [45]. Somit wird die 99%-Grenze für fehlertolerante Quanteninformationsverarbeitung überschritten.

Eine große Relevanz für diese Arbeit haben die Quantengatter, die für neutrale Atome vorgeschlagen sind [46–48]. Die Methoden beruhen auf der Dipolblockade, ein Effect, der eintritt wenn eine mesoskopische Atomwolke kollektiv zu Rydbergzuständen angeregt wird [49–51]. In diesem Fall erhält man typischerweise nur eine einzelne Anregung innerhalb eines *Blockadevolumens*, dessen Größe hauptsächlich von der Wechselwirkungsstärke der Rydbergzustände abhängt. Die Blockade führt zu einer räumlichen Anordnung der Anregung. Dies ist besonders gut erkennbar in zweidimensionalen Gasen [52]. Ähnlich wie bei der Blockade gibt es auch eine Art Antiblockade [53]. Diese kann die Ausbildung von Rydberg Aggregaten verursachen [54–56].

Mit der Rydbergblockade wurde ein CNOT-Gatter realisiert [57]. Dieses kann durch elementare Qubit Operationen ein universelle Quantenlogik implementieren [58]. Daher ist dieses System sehr interessant für die Quanten-IT [59]. Eine Hochskalierung der Anzahl an Qubits kann durch ein Microfallen-Array erreicht werden [60]. Um hohe Füllfaktoren auch bei großen Arrays zu erreichen, müssen Tricks angewandt werden, die teilweise deterministisches Laden ermöglichen [61–63]. Ein anderer Weg für die Skalierung der Qubits kann durch unterschiedliches Kodieren der Zustände erfolgen, zum Beispiel in Hyperfeinzuständen von Holmium [64].

Eine Methode, die die starke Wechselwirkung zwischen Rydbergzuständen ausnutzt aber gleichzeitig auch die lange Kohärenzzeit von Grundzuständen, ist Rydberg Dressing [65–68]. Dabei wird den Grundzuständen ein Anteil von Rydbergzuständen beigemischt durch das Koppeln an Laserlicht.

Die räumliche Skalierung der Rydberg Wechselwirkung ist abhängig von den Zuständen. Es kann eine langreichweitige r^{-3} Dipole-Dipole Wechselwirkung, aber auch eine kurzreichweitige r^{-6} van der Waals Wechselwirkung eintreten [59]. Bei bestimmten Zuständen kann die Wechselwirkung vergrößert werden durch das Koppeln an energetisch entartete Paarzustände. Dies ist als Förster-Resonanz bekannt [69]. Die Kopplung kann zu einem Austausch der Paarzustände führen und zu einem Energietransfer der Rydbergatome, was als Förster-Resonanzenergietransfer (FRET) bekannt ist. Falls die Atome anfangs in einem unterschiedlichen Rydbergzustand sind, können auch die einzelnen Zustände

ausgetauscht werden [70, 71], was auch als *Hopping* bezeichnet wird. Falls mehrere Rydbergatome beteiligt sind, kann eine Zustands-Diffusion stattfinden [72]. Bei zwei einzelnen Atomen können die kohärenten Rabioszillationen des Förster-Prozesses zeitaufgelöst detektiert werden [73]. Falls die Energie des Anfangspaares nicht mit dem gekoppelten Zustandspaars entartet ist, kann eine Försterresonanz mittels des d.c. Stark Effekts [51, 70, 74, 75] des a.c. Stark Effekts [76] herbeigeführt werden. Übrigens können durch die hohe elektrostatische Polarisierbarkeit [77] Rydbergatome verwendet werden, um sehr genau elektrische Felder zu bestimmen [78, 79].

Durch die extremen Eigenschaften von Rydbergatomen gibt es zahlreiche andere Effekte. Zum Beispiel kann ein Rydbergatom mit einem Grundzustandsatom eine heteronukleare Bindung eingehen, aber trotzdem ein starkes elektrisches Dipolmoment aufweisen [80, 81]. Ein anderes Beispiel für die Vielseitigkeit von Rydbergatomen ist die Tatsache, dass man mit ihnen Prozesse in Sternen simulieren kann [82].

Unsere Motivation ist die Generierung einer effektiven Wechselwirkung zwischen Photonen. In konventionellen nichtlinearen Medien ist dies zwar möglich [83], jedoch tritt dies erst bei riesigen Intensitäten auf. Daher wird an Systemen geforscht, die viel höhere Nichtlinearitäten aufweisen. Idealerweise sollte ein einzelnes Photon ausreichen um die optischen Eigenschaften für andere Photonen deutlich zu ändern.

Als Lösung dafür nutzen wir die Wechselwirkung zwischen Rydbergatomen aus, die oben eingeführt wurde. Um hohe Rydbergzustände zu erreichen, wendet man elektromagnetisch-induzierte Transparenz (EIT) [84, 85] in einer *Leiter-Konfiguration* mit zwei Lasern an, dem Probe- und Kontrollaser [86]. Dadurch wird eine kooperative optische Nichtlinearität für das Probelicht erzeugt [87]. Die Nichtlinearität ist stark genug um einen Effekt bei einem Photon zu erzeugen [88]. Mit der Technik der magischen Fallenwellenlänge [89] kann die Kohärenz der Zustände vergrößert werden, sodass Rydberg-EIT Rabi Oszillationen sogar bei größeren Atomwolken detektiert werden können [90], ein großer Schritt in Richtung der Quantensimulation mit Rydbergatomen. Die effektive Wechselwirkung zwischen Photonen kann die Lichtstatistik verändern. Durch die Rydberg blockade kann es zu einer starken Aufspaltung in einzelne Photonen kommen (anti-bunching) [91–93]. Wie von unserer Theoriekollaboration vorhergesagt [94], konnten wir experimentell zeigen, dass es möglich ist, deterministisch ein einziges Photon aus einem Lichtfeld zu entfernen [2, 95]. Desweiteren gibt es eine deutliche Änderung der Photonenstatistik in unserem optischen Transistor, von einer Poissonverteilung zu einer bimodalen Verteilung [5]. Dadurch kann mit hoher Wahrscheinlichkeit auf das Vorhandensein eines Rydbergatoms zurückgeschlossen werden, ähnlich der Vorschläge [96, 97] und Experimenten zur Abbildung von Rydbergatomen [72, 98].

Die Theorie wechselwirkender Rydbergpolaritonen ist sehr aktiv [88, 99–102]. Das Vielteilchensystem, das durch die Kollektivität binär wechselwirkender Anregungen zustande kommt, ist eine

große Herausforderung und findet seine Grenzen in mangelnder Rechenleistung. Daher sind neue Theorieansätze sehr gefragt. Erst kürzlich erschien eine effektive Feldtheorie zu diesem System [103]. Im Experiment wurden jedoch Effekte gemessen, die der Vierteilchen-Wechselwirkung zugeschrieben werden. In dieser Arbeit wurde der theoretischen Physik auch ein Beitrag geleistet, und zwar durch die Erweiterung der Lichtpropagation bei Rydberg-EIT mit Förster-Resonanzen [1].

Die Haupterrungenschaft dieser Doktorarbeit ist jedoch die Demonstration des optischen Schalters und Transistors [5]. Die grundlegende Idee ist, dass ein *Gate*-Photon das Medium der ultrakalten Rubidiumatome dahingehend verändert, dass die Transmission von *Source*-Photonen unterbunden wird. Dadurch, dass die Gate-Photonen als Rydberganregung gespeichert werden, bricht die EIT Transmission für die Source-Photonen ein. Mit dem d.c. Stark Effekt können wir Förster-Resonanzen durchstimmen um die Leistungsfähigkeit des Transistors zu erhöhen. Dadurch erreichen wir einen optischen Verstärkungsfaktor (Gain) von über 200 [1].

Es gibt andere Ansätze um einen optischen Schalter oder Transistor herzustellen. Man kann mit kalten Atomen in einer Hohlleiter und Grundzustands-EIT einen Switch herstellen, der allerdings erst ab einigen Hundert Photonen gut funktioniert [104]. Ähnliche Leistung hat eine Implementierung mit Farbstoffmolekülen [105]. Wenn Atome an einen optischen Resonator gekoppelt werden [106], kann man einen leistungsfähigen Transistor herstellen [107]. Allerdings ist die Skalierbarkeit dieses Systems fragwürdig. Außerdem existieren Transistor-Vorschläge: mit Nanooberflächenplasmonen [108] oder mit Supraleitern [109, 110].

Trotz Zweifel an der Realisierbarkeit von Nichtlinearitäten für Quanten-IT [111], gibt es Anstrengungen, diese zu demonstrieren. Ein Resultat ist die Realisierung eines Phasengatters, das einen Phasenhub von bis zu π erreicht [112]. Wir geben einen Ausblick über die Machbarkeit eines Quanten-Transistors durch die Untersuchung der atomaren Kohärenz der gespeicherten Gate-Rydberganregung. Wir können zwar einen großen Anteil an Gate-Anregungen auslesen – und das ist nur möglich bei endlicher Kohärenz – jedoch ist dies wahrscheinlich nur bei der Nullkomponente der Source-Photonenstatistik möglich. Es gibt jedoch Hoffnung, dass die Kohärenz in anderen Geometrien auch nach Streuung von Source-Photonen erhalten bleibt: wenn die Atomwolke kürzer ist als der Rydbergblockaderadius [113].

1

Introduction

This work, the first demonstration of a free-space single photon transistor, is a quantum optics project taking advantage of many techniques of modern atomic physics. These research fields shall be introduced in the following.

Basic understanding of fundamental light-matter interaction processes such as absorption, spontaneous or stimulated emission dates back 100 years to Einstein's theory work "Zur Quantentheorie der Strahlung" [8]. Of course, many following discoveries have contributed to the state-of-the-art of science and technology, such as the theoretical discovery of superradiance by Robert H. Dicke [9] (the increased probability for spontaneous emission due to coherence in an atomic sample) or optical pumping by Alfred Kastler [114].

But not many more ingredients were necessary for the inventions of the maser [115] and laser [10, 116]. The advent of the (GaAs) semiconductor diode laser [117] was the technological breakthrough enabling revolutionary applications which even found their way to every household (CD-players) and also pushed research significantly by providing cheap high-technology equipment.

That way, engineering atomic states with photons has enabled experimental access to the quantum nature of matter [11]. The mechanical effect of laser radiation on atomic vapour [12] has opened up the field of cold atom physics. A milestone in this field of research is the invention of the magneto-optical trap (MOT) [13, 14] which triggered the race towards the first realization of a Bose-Einstein condensate (BEC) in 1995 [15–17], around 70 years after Bose and Einstein initially predicted this state of matter.

Although BECs are still dilute atomic vapours, two-body interactions play an important role for static and dynamic properties. The contact interaction can be quantified with a single parameter: the s -wave scattering length [18, 19]. If the atomic species exhibits a high magnetic moment, such as chromium, erbium or dysprosium, long-range anisotropic dipole-dipole interactions take a significant part in the two-body interaction [20, 21] or can even be dominant [22]. Exploiting Feshbach resonances to tune the contact interaction [23, 24], a pure dipolar condensate can be obtained [25], which can be stabilized or can collapse depending on the geometry of the atomic sample [26]. These geometries can be tailored with optical dipole traps [27], which utilize the dipole force which confines atoms around the focus of a laser beam if it is far red-detuned to strong dipole transitions [28]. With blue detuning, a repulsive light potential is obtained. Thus, different geometries like a doughnut mode [29], light sheets [30] or a hollow beam [31] have been used to trap atoms. Although more sophisticated techniques need to be applied for blue detuned traps, a.c. Stark shifts can be minimized that way, making it interesting for precision spectroscopy. The ability to engineer almost arbitrary potentials and the dependence of interaction effects on the geometry are aspects that we employ in this work, and more generally, make cold atom experiments ideal test-beds for fundamental research.

The macroscopic manifestation of quantum mechanics in BECs is a huge potential providing a platform for novel ideas which make use of the *quantum weirdness*. For example, exotic states of matter can be created. Bosonic atoms can undergo a transition from the superfluid phase to the Mott phase in an optical lattice [32, 33]. Site-resolved control and detection in optical lattices [34, 35] can be used to define particular states and to investigate dynamics which occurs due to the interplay of confinement and tunneling between lattice sites [36]. Such ordering processes can be mapped to other physical many-body systems which are difficult or even impossible to simulate classically [37]. For example, problems in solid state physics such as antiferromagnetism (Ising Hamiltonian) can be simulated [38].

Very promising results for quantum information technology and quantum simulation are witnessed with cold trapped ions [39]. It is possible to simulate magnetic phase transitions [40], the Ising interaction in two dimensions [41], quantum dots [42] and even the Dirac equation [43]. In the field of quantum computing, trapped ion systems are probably the most prominent candidates. To date, systems are built which run quantum algorithms with five qubits with gate fidelities of 98% [44]. For two-qubit and single-qubit logic gates fidelities as high as 99.9(1)% and 99.9934(3)% are obtained [45], exceeding the 99% limit for fault-tolerant quantum computation.

Highly relevant to this thesis, fast quantum gates have been proposed for neutral atoms excited to Rydberg states [46–48]. The techniques rely on dipole blockade, an effect which occurs when a mesoscopic sample is collectively excited [49] to strongly interacting states such as Rydberg states [50, 51]. In this case, only a single excitation is observed in the *blockade volume* with the extent mainly given by the interaction strength. This blockade leads to a spatial ordering of the excitations, nicely visible

in a two-dimensional gas [52]. Similarly to the blockade mechanism, there is also a way to implement an antiblockade [53]. This can be exploited to create Rydberg aggregates [54–56].

With Rydberg blockade, a controlled NOT (C-NOT) gate has been realized experimentally [57], which, in combination with single qubit operations, forms a universal quantum logic gate [58] and makes this system very interesting for quantum information [59]. Scaling such a system to many qubits can be done in micro-trap arrays [60]. To achieve high fill factors, tricks for Rydberg trapping can be employed [61], which even allow deterministic loading [62, 63]. A different way to scale the system to many qubits is by using a different state encoding, such as in the rich hyperfine structure of Holmium [64].

An approach to make use of the strong interaction between Rydberg states while taking advantage of long coherence times of the ground states is by admixing a Rydberg state to the ground state. This is known as Rydberg dressing [65–68].

The spatial scaling of the interaction between Rydberg atoms depends on the involved state(s), it can vary from long-range r^{-3} dipole-dipole interaction to short-range r^{-6} van der Waals interaction [59]. For specific states, the interaction between the Rydberg atoms can be increased by dipole-coupling to energetically degenerate pair states, which is known as a Förster resonance [69]. The dipole-coupling to another pair state can cause a change in pair state population accompanied with an effective energy transfer between the interacting Rydberg atoms, known as Förster resonant Rydberg energy transfer (FRET). In case the atoms are in different Rydberg states initially, it is possible that they exchange their state [70, 71], which is also known as excitation *hopping*. If more Rydberg atoms are present, this hopping can diffuse throughout the atomic cloud [72]. On the level of two isolated atoms, the coherent oscillations back and forth between the pair states can even be tracked [73]. If the energy of the coupled pair states is not degenerate, it is possible to tune them to degeneracy (Förster resonance) by exploiting the d.c. Stark effect [51, 70, 74, 75] or the a.c. Stark effect [76]. Besides, the huge electrostatic polarizability of Rydberg states [77] makes these systems ideal for highly precise electrometry [78, 79].

There are many other effects which arise due to the extreme properties of Rydberg states. For example, Rydberg atoms can form homonuclear and yet dipolar molecules with ground state atoms [80, 81]. Another fact which shows the versatility of Rydberg atoms is the fact that Rydberg gases are even used to simulate stars [82].

Our motivation is to create an effective interaction between photons. This is possible in conventional nonlinear media [83], but huge intensities are needed. Systems need to be developed which mediate stronger optical nonlinearities. Ideally, one photon should suffice to considerably alter the optical properties for other photons.

Our solution is to employ the large dipole-dipole interaction between Rydberg atoms introduced

above. To address these high-lying electronic states, EIT [84, 85] is used in a *ladder configuration* with two lasers, probe and control [86].

That way, the strong dipolar interaction creates a cooperative optical nonlinearity for the probe light [87]. This cooperative nonlinearity offers good prospects for the advancement of nonlinear optics, since it works on the level of single photons [88]. By using magic wavelength trapping [89], Rydberg-EIT Rabi oscillations show that the atomic coherence can sustain even in a large atomic sample [90], which marks a big step in quantum simulation. The effective interaction between photons is used to alter the statistics of light fields. Rydberg blockade causes strong anti-bunching features [91–93]. As proposed by our theory collaborators [94], we have shown experimentally that the deterministic subtraction of single photons can be facilitated by Rydberg-Rydberg interaction [2, 95]. Also, our single photon transistor significantly changes the light statistics from Poissonian to bimodal [5], which can be used to detect single Rydberg excitations with a high fidelity, similarly to the proposals [96, 97] and realizations [72, 98] of Rydberg imaging schemes.

Theory on the propagation of interacting Rydberg polaritons is very active [88, 99–102]. Treating the multi-particle problem which arises from the collective nonlinearity is computationally intense already for binary interactions and thus, theoretical research in this field is sought-after. Only recently, an effective field theory was established [103]. However, experimentally, even four body interaction has been detected [118]. In our work, we extended existing theory on photon propagation to the case of Förster resonances [1].

The main achievement of this work was to demonstrate an all-optical switch and transistor [5]. The underlying idea is that a single *gate* photon alters a medium of ultra-cold Rubidium atoms such that the transmission of *source* photons is inhibited. By creating a Rydberg excitation with the gate photon, the Rydberg-EIT of the source photons breaks down due to Rydberg blockade, causing scattering of source photons. Employing Stark-tuned Förster resonances, we are able to increase the performance of this transistor, demonstrating an optical gain of over 200 [1].

There have been other realizations of optical switches and transistors. Cold atoms in a hollow core fiber can be utilized for all-optical switching in combination with ground-state (λ -) EIT [104]. Unfortunately, a few hundred photons are needed for efficient switching, but the use of fiber technology makes this approach still very interesting for technological applications.

Similarly, the transistor implementation with single dye molecules needs even more gate photons to flip its state [105].

The system of atoms coupled to an optical cavity [106] has been employed to demonstrate an optical switch and transistor [107]. However, these systems lack scalability.

Yet different systems have been proposed as single photon transistors, such as nanoscale surface plasmons [108] or superconductors [109, 110].

Despite doubts for the applicability of single-photon nonlinearities for quantum computation [111], cross-phase modulation with phase shifts up to π have been realized [112]. We give an outlook about the applicability of our single photon transistor by investigating the coherence of the stored gate spin-wave. Although we can read out a considerable fraction of gate photons (which proves coherence), this is most likely due to the zero component of the source photon distribution. However, there is hope that the atomic coherence is sustained in other experimental geometries even after a scattering event: if the cloud is shorter than the Rydberg blockade radius [113].

2

Conceptual design and implementation of an ultracold quantum optics experiment

BUILDING A STATE-OF-THE-ART QUANTUM OPTICS EXPERIMENT FROM SCRATCH requires clear plans due to the complexity and diversity of challenges spanning the disciplines vacuum technology, laser technology, optical and mechanical design, software development and others. This wide range of technology finally enables the central field of study of a research group only if subjects are well coordinated between participating PhD, bachelor and master students and lab assistants. For these reasons, this chapter will start with the general plans and schedules before the specific components and their implementations in the experiment are described in detail.

2.1 PROJECT OUTLINE, PERSONNEL AND TIME SCHEDULE

The time schedule of this project, as displayed in Table 2.1, is very similar to the one proposed for my research grant at the Carl Zeiss Foundation. There have been two setup phases: the initial buildup phase starting from ordering parts to fill an empty laboratory space and a second setup phase to rebuilt

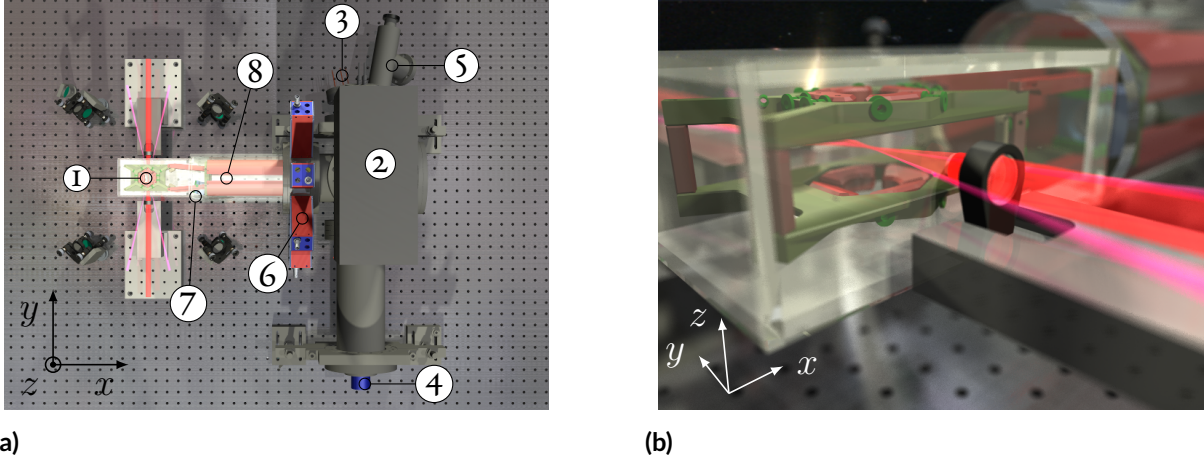


Figure 2.1: Setup of the vacuum chamber (many other parts are hidden in these rendered images for clarity). (a) Experiments are done in a custom made glass cell (1) providing good optical access. It is mounted on a larger stainless steel chamber to which vacuum peripheral devices are connected such as an ion pump (2), an ion gauge (3) and titanium sublimators (4). The chamber can be connected to a turbo-pump with a valve (5). Electrical feedthroughs (6) provide both control over electric fields around (1) and access to signals from a multi channel plate ion detector (7). Location of the Rubidium dispensers (8). (b) Close-up on the electric field plates and on the experiment region. Eight plates, here false-colored in red, are used to create homogeneous electric fields in their symmetry center, where atoms are prepared in a crossed optical dipole trap (purple beams) and manipulated with single probe photons (red beam).

ranges through the assembly, initial depumping, purification and permanent evacuation processes. To reach extremely low pressures for cold atomic physics experiments dealing with dilute gases, vacuum chambers are often split into two regions: a region with a high background pressure of the species that is dealt with and subject to laser cooling and trapping, and another region where these atoms are transported to. State-of-the-art techniques are to either transport atoms by means of an optical dipole trap that drags an atomic cloud behind [119, 120] or by a spatially moving magnetic trap potential [121, 122]. Other methods how atomic samples can be created in a dedicated low-pressure region are by loading atoms from a cold atomic beam created by a Zeeman slower [123], a 2D MOT [124], by a magnetic guide [125] or simply by pushing atoms out of another MOT with resonant light or by gravity.

Although these sophisticated approaches are well-established, they require substantial experimental effort and may also be a source for experimental instability. Therefore, the need of such methods is to be evaluated. Only if a very high number of atoms and extremely low temperatures are basic necessities, the experimental effort is justified. For the experiments described here, these are no major concerns, as shown by life time measurements, simulations in section 2.9 and finally and most promi-

nently by the successful transistor measurements in chapter 5.

Our vacuum chamber, as shown in Fig. 2.1 is largely made of stainless steel with DN100 conflat (CF) nipples and flanges. It consists of an elongated steel chamber with self-made stands and a glass cell which is attached to it in an L -shaped configuration via a 5-way vacuum cross. The glass cell is a custom design sold by Japan Cell. It is built of quartz glass, which has superior optical properties, in particular reduced thermal lensing for high-power lasers [126] such as our optical dipole trap laser, see section 2.8. A small disadvantage for the choice of this material is that light-induced atomic desorption (LIAD) [127, 128] is not as efficient as for borosilicate glasses (pyrex).

As can be seen in Figure 2.1b, the glass cell is attached to a cylindrical glass tube, which bonds vacuum-tightly to a steel flange with a glass-metal transition. The main cell has dimensions in the indicated frame of reference $(L_x, L_y, L_z) = (6, 8, 12)$ cm. An ion pump (Varian *VacIon Plus 40*) with a *StarCell*[®] pumping element is in constant operation. Its pumping speed is 15 L/s Argon at 1×10^{-10} mbar if the pump is saturated. In the long steel chamber, we employ three titanium-molybdenum sublimators (Varian Ti-Sublimation Cartridge) to further decrease the pressure by pumping chemically active gases. It is flashed every other month or during experiment down times. We apply currents of 45 A which are less than the maximum current of 50 A to increase the life time.

The atom sources for this quantum optics experiment which uses cold atoms are four Rubidium dispensers which are placed in the cylindrical glass part of the glass cell. Four electric feedthroughs are installed to independently drive currents through two serial pairs of dispensers. The dispensers contain Rubidium isotopes in their natural abundances: 72 % of ^{85}Rb and 28 % of ^{87}Rb . Judging from the abundance, one would use the dominant isotope ^{85}Rb . This, however, has a negative background scattering length and is therefore inconvenient for higher densities [129]. It can only be stabilized close to a Feshbach resonance, e.g. at 155 G, and only then Bose-Einstein-condensed [23]. Easier conditions are found in ^{87}Rb with a positive background scattering length [130] and rare/weak Feshbach resonances. Collisions between the two isotopes are in principle possible, impressively demonstrated by sympathetic cooling of ^{85}Rb with ^{87}Rb [131]. These collisions shall be suppressed as for the ^{87}Rb - ^{87}Rb collisions by working at a low Rubidium pressure.

Pressure measurement is done with an ion gauge (Varian UHV-24p). As with all ion gauges, the sensitivity is very different for different atomic and molecular species that contribute to the background pressure. The reason is that the pressure measurement relies on the ionization of the background gas with fast electrons. The electron impact ionization cross sections [132] for electron energies of 200 eV is for Rubidium $\sigma_{\text{Rb}} = 4.9\pi a_0^2 = 4.3 \text{ \AA}^2$ [133], in contrast to molecular nitrogen $\sigma_{\text{N}_2} = 2.6\pi a_0^2 = 2.3 \text{ \AA}^2$ [134]. As a result of this higher sensitivity to Rubidium, the interpretation of the measured pressures has to be done with care. The manufacturer specifies an empirical factor 4.3 [135] that corrects for the higher sensitivity to Rubidium as opposed to molecular nitrogen which

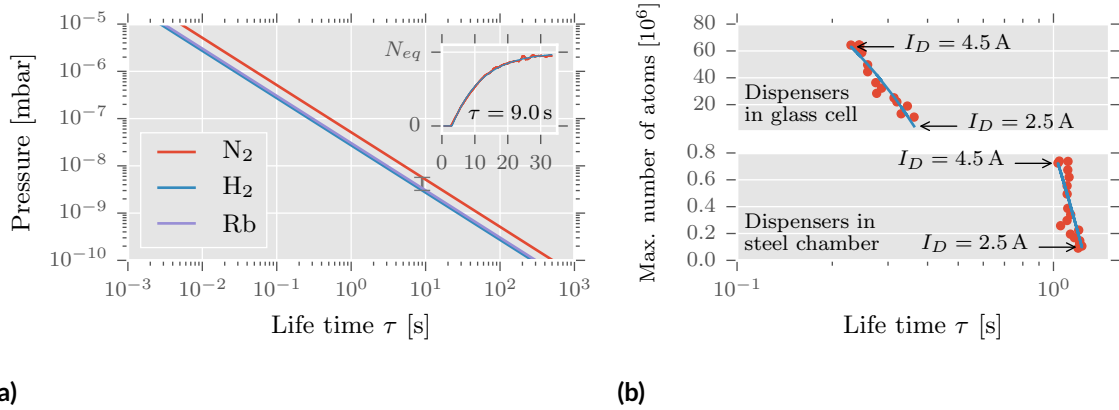


Figure 2.2: (a) Expected life time of ultra-cold ground state Rubidium atoms in a MOT (1 K deep) based on numbers from [136]. The life time is reduced due to collisions with the hot background gas with a small dependence on the composition. These curves have been used to correct for a bad dispenser position by discovering a low Rubidium pressure, as analyzed in (b). In the lower panel, even a high dispenser current does not create a necessary Rubidium pressure, so the life time is approximately unchanged and the number of atoms stays low. The upper panel shows the same measurement with the dispensers closer to the MOT. Much higher numbers of atoms are reached and a maximum Rubidium pressure of 5×10^{-8} mbar even though the life time is smaller here because vacuum baking has not been done yet. The inset in (a) shows a MOT loading curve with optimized vacuum conditions and with $I_D = 4.1$ A. With the loading time, we can directly read off an approximate background pressure in the big panel, depicted by the error bar.

the gauge is calibrated to. In this work, any specified pressure will not contain this correction factor because it is known that the background pressure does not solely consist of Rubidium. The position and orientation of the gauge is such that it does not directly face the experiment region in the glass cell. This is beneficial to reduce the black body radiation in the experiment region which limits the life time of Rydberg states as shown in Figure 5.5.

A better method to measure the partial pressures abundant in the vacuum chamber is to investigate the pressure dependent loss rates in a magneto-optical trap [136]. The influence of background gases with room temperature on the life time of an ultra-cold ground state Rubidium atom is shown in Figure 2.2a. By measuring the life time one can get a good estimate about the local total pressure. It is also possible to measure the partial pressure of Rubidium by measurements at different dispenser powers [137]. The measurements are done by analyzing the loading dynamics of the MOT.

The equilibration between the loading rate and the pressure dependent loss rate is characterized by an exponentially limited growth and the time constant corresponds to the life time τ [137]. Using this method, we could debug a low number of atoms in our MOT realizing that the position of the

dispensers was too far away from the position of the MOT. It was in the steel chamber previously. Due to the in-vacuum construction of the electric field control, atoms were likely to get stuck at the steel walls or the Kapton-insulated electrical wires thereby creating a low partial Rubidium pressure. After having placed the dispensers closer to the MOT, see position in Figure 2.1, the problem was solved. Figure 2.2 shows that in the first attempt with the dispensers in the steel chamber, the life time is essentially unchanged due to the dispensers and the background pressure is calculated to be 3×10^{-8} mbar. The calculation predicts a maximum Rubidium pressure of 5×10^{-9} mbar, but the uncertainty is high. A horizontal line could also fit the data fairly well, which would mean a negligible Rubidium pressure.

After this measurement, the dispensers were placed closer to the MOT, in the cylindrical part of the glass cell. On the next day already, the data in the upper panel of Figure 2.2 was taken, without heating the vacuum chamber. Even though the background pressure in this measurement is higher (7×10^{-8} mbar), we observe a strong change of the life time due to Rubidium from the dispensers. The Rubidium pressure is 5×10^{-8} mbar at the maximum dispenser current $I_D = 4.5$ A. With the number of atoms in the high 10^7 region, we can easily operate our experiments. Note that the number of atoms is even underestimated here because in these measurements the atoms are not fully spin-polarized in the stretched Zeeman state. The calculation of the number of atoms, however, assumes a spin-polarized sample.

2.3 ELECTRIC FIELD CONTROL AND ION DETECTION SETUP

As mentioned in section 2.2 and in Figure 2.1, our setup comprises in-vacuum electric field control and ion detection with an MCP. Since the electric field control is a central part of chapter 6, the construction shall be introduced here. The design, construction and assembly has been in the scope of Johannes Schmidt's master's thesis [138]. The characterization of the MCP was done by Thomas Dieterle [139]. Since ion detection does not play a central role in this work, details are not provided here. Please refer to the theses mentioned above.

CONSTRUCTION Figure 2.3 shows (a) the electrodes and (b) the MCP in the assembly. Our electrodes are set up in the established Löw configuration [140]. Schematically, four segments of a circle form the upper (1-4) and lower (5-8) electrodes respectively. The diameter of this circle and the separation of the circles are designed such that 1 inch MOT beams fit through. In general, the construction is designed to be as large as possible (limited by the glass cell) to create homogeneous fields in the center, and as closed as possible to shield surface charges on the glass. However, it is a trade-off with

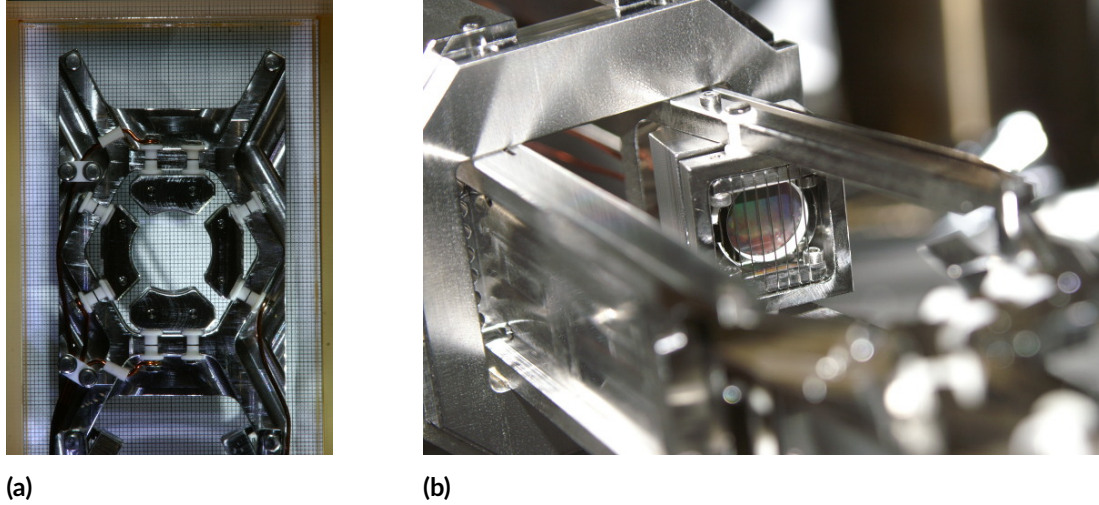


Figure 2.3: (a) The setup of the electric field control is aligned within the glass cell using the standard clearance of the mounting screw through holes (not visible here). The millimeter paper behind the glass cell serves as a reference for centering the construction. From this perspective, only the four upper electrodes are visible as they cover the lower four ones, which is a good sign for precise machining and assembly. (b) Small periodic structures on the MCP surface behave like a diffraction grating for incident light, causing rainbow colors. Wires in front of the MCP shield the electric field of the MCP to minimize field gradients at the position of the atomic cloud.

optical access. The construction is largely made of austenitic stainless steel^{*}, which, due to its superior vacuum-related and magnetic properties is the material of choice. To apply different voltages on each individual electrode, we mount the electrodes to the holder with brushes made of aluminum oxide (white pieces) that are attached with M2 screws. The screws act as electric contacts. In critical regions, we use aluminium oxide tubes around the wires to additionally assure electric insulation. The Kapton-insulated copper wires are connected to electrical feedthroughs, which, themselves, are mounted on an octagon[†]. The electric field construction is attached to the octagon via a pair of Grabber Grooves. The glass cell is attached to the 6CF sealing surface with 24 imperial 5/16-24 screws which provides the necessary stiffness. Fine-tuning of the alignment of the construction with respect to the glass cell is done with the clearance of some mounting screws in their through holes. This rather delicate task resulted in an off-center position of $\Delta x = 1$ mm measured with millimeter paper as shown in Figure 2.3a and $\Delta z = -2$ mm estimated by eye.

^{*}material: 316L (AISI/SAE), 1.4404 (DIN EN 10027-2), A4 (ISO 3506)

[†]Kimball Physics, *MCF600-SpbOct-F2A8*

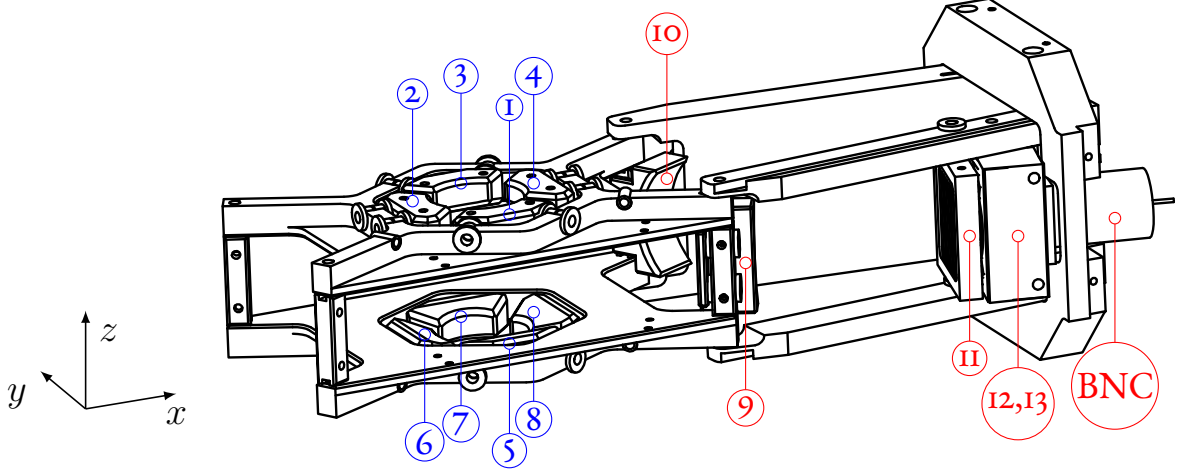


Figure 2.4: The in-vacuum construction has 14 electrical connections in total. Connections labeled in blue are used to apply defined electric fields in all directions to the atomic cloud. To apply voltages, we can toggle between an ultra-stable (-10 to 10) V voltage source and two (10 to 500) V sources for Rydberg ionization [141] (polarity: 2 and 6 pos., 4 and 8 neg.). The red colored contacts are used for ion detection. Electrodes 9 and 10 deflect ions towards the MCP. The grid voltage (11) shields the MCP front plate (13) voltage which is on -2 kV. An electron avalanche is realized by applying -500 V to the MCP back plate electrode 13. The resulting electron burst is detected as a negative voltage pulse (500 ps) at MCP anode which is grounded with a finite resistance.

ELECTRIC FIELDS The 3D electric field potentials arising from each individual electrode have been simulated using the software *SIMION 8.1* [138]. We use the following sets of electrodes and their simulated field conversion factors to apply fields in the three directions:

- $\epsilon_x > 0$: electrodes 4 and 8 negative ($-U_x$), 2 and 6 positive (U_x). $\frac{\epsilon_x}{U_x} = 0.350$ (Vcm $^{-1}$)/V
- $\epsilon_y > 0$: electrodes 3 and 7 negative ($-U_y$), 1 and 5 positive (U_y). $\frac{\epsilon_y}{U_y} = 0.410$ (Vcm $^{-1}$)/V
- $\epsilon_z > 0$: electrodes 1 and 3 negative ($-U_z$), 5 and 7 positive (U_z). $\frac{\epsilon_z}{U_z} = 0.398$ (Vcm $^{-1}$)/V

To create an arbitrary e-field $\vec{\epsilon} = (\epsilon_x, \epsilon_y, \epsilon_z)$, we simply enter these values and our computer-controlled voltage sources output the corresponding voltages according to the (inverted) conversion factors

$$U_1 = \frac{U_x}{\epsilon_x}(\epsilon_x - \epsilon_{x,0}) + \frac{U_z}{\epsilon_z}(\epsilon_z - \epsilon_{z,0}) \quad (2.1a)$$

$$U_2 = -\frac{U_x}{\epsilon_x}(\epsilon_x - \epsilon_{x,0}) \quad (2.1b)$$

$$U_3 = -\frac{U_y}{\epsilon_y}(\epsilon_y - \epsilon_{y,0}) + \frac{U_z}{\epsilon_z}(\epsilon_z - \epsilon_{z,0}) \quad (2.1c)$$

and similar for $U_4 \dots U_8$. We introduced here the variables $\epsilon_{x,0}$, $\epsilon_{y,0}$ and $\epsilon_{z,0}$ that are set to cancel constant or very slowly varying stray electric fields. With the precision voltage source from Section 2.10.5 covering ± 10 V, the field which can be generated, is in the range

$$\left(\begin{array}{l} -3.50 \text{ Vcm}^{-1} < \epsilon_x < 3.50 \text{ Vcm}^{-1} \\ -4.10 \text{ Vcm}^{-1} < \epsilon_y < 4.10 \text{ Vcm}^{-1} \\ -3.98 \text{ Vcm}^{-1} < \epsilon_z < 3.98 \text{ Vcm}^{-1} \end{array} \right). \quad (2.2)$$

To ionize the Rydberg atoms, we switch the connections of ϵ_x from the precision voltage source to two high voltage modules* which cover the voltage range of (10 to 500) V. Through polarity, we apply positive voltages at electrodes 2 and 6, and negative voltages to electrodes 4 and 8. That way, the same electric field conversion factor of $\frac{\epsilon_x}{U_x} = 0.350 \text{ (Vcm}^{-1})/\text{V}$ applies for ionization, but a much larger fields of $3.50 \text{ Vcm}^{-1} < \epsilon_x < 175.0 \text{ Vcm}^{-1}$ are reached. This is sufficient to ionize Rydberg states with $n > 37$ [142].

ORTHONORMALIZATION OF ELECTRIC FIELD DIRECTIONS. In Section 6.2.2, we will see that the high polarizability of Rydberg atoms provides a precise probe for the modulus of an electric field. We use this to investigate whether our electric field components as defined above, ϵ_x , ϵ_y , ϵ_z are independent variables. We study the dependence systematically for all combinations of directions by setting one component to a high value and reducing the modulus of the electric field with the other components. Specifically, we apply an offset field of $\epsilon_{\text{offset}} = 300 \text{ mV/cm}$ to one electric field component, say ϵ_x . Given the calculated electric polarizability $\alpha_{68S} = -2 \times 217 \text{ MHz}/(\text{V cm}^{-1})^2$, this Stark-shifts the $68S$ state by $\Delta E = \frac{1}{2} \alpha_{68S} \epsilon_{\text{offset}}^2 = -19.5 \text{ MHz}$. Next, we minimize the modulus of the electric field $\epsilon = \sqrt{\epsilon_x^2 + \epsilon_y^2 + \epsilon_z^2}$ by scanning another component, say ϵ_y . If ϵ is minimized at $\epsilon_y = \Delta\epsilon_{y,0}$, the angle between the two field directions is

$$\theta_{x,y} := \angle(\vec{\epsilon}_x, \vec{\epsilon}_y) = \arctan\left(\frac{\epsilon_{\text{offset}}}{\Delta\epsilon_{y,0}}\right). \quad (2.3)$$

The relatively high offset field in ϵ_x amplifies the resolution of the field dependence of the two directions, i.e., the angle. The emerging transverse field $\Delta\epsilon_{y,0}$ is proportional to the offset field, as can be seen in eqn. 2.3, because the angle is constant, given by the setup. The energy difference before and

* Applied KiloVolts, Exelis HP0 . 5xAA025

after the cancellation of the transverse field is

$$\Delta E_{x,y} = \frac{1}{2}\alpha_{68S}\epsilon_{\text{offset}}^2 - \frac{1}{2}\alpha_{68S} \left(\sqrt{\epsilon_{\text{offset}}^2 - \Delta\epsilon_{y,0}^2} \right)^2 = \frac{1}{2}\alpha_{68S}\Delta\epsilon_{y,0}^2 = \frac{\alpha_{68S}\epsilon_{\text{offset}}}{2 \tan \theta_{x,y}}. \quad (2.4)$$

With a spectral resolution of only 100 kHz after averaging over multiple runs, we can estimate an angular sensitivity of this procedure to 0.09° . The resultant angles between the electric field directions are measured to be as follows: $\theta_{x,y} = 89.82^\circ$, $\theta_{x,z} = 89.81^\circ$, $\theta_{y,z} = 92.7^\circ$. Now we could build a set of orthogonal e-field directions, since we can counteract all transverse fields. For the sake of simplicity, we only correct for the x, z tilt of the electrodes. This is easily done by the following map

$$\epsilon_y \mapsto \epsilon_y - \frac{13 \text{ mV cm}^{-1}}{300 \text{ mV cm}^{-1}}\epsilon_z \quad (2.5)$$

since we measured the transverse field of $\Delta\epsilon_{z,0} = 13 \text{ mV cm}^{-1}$ when applying the offset field to ϵ_z . This nice technique of orthogonalization has of course positive consequences. If a stray electric field needs to be canceled, this orthogonal set of variables allows the cancellation in three steps in contrast to the iterative cancellation if the variables are dependent. This method and the formulas were checked experimentally for consistency.

2.4 RUBIDIUM LEVEL SCHEME AND TRANSITIONS

This section shall give an overview of the level scheme of ^{87}Rb motivating the choice and setup of the laser systems which is described in the next section. Figure 2.5 shows all S , P and D states of ^{87}Rb with principal quantum numbers n from 5 to 200 with energies

$$E = \frac{-\mathcal{R}}{n^{*2}} \quad (2.6)$$

where \mathcal{R} is the Rydberg constant and n^* is the effective principal quantum number which differs from the principal quantum number n by small quantum defects which are described in Appendix A. Their exact values will become important for the prediction of Förster resonances in section 3.5.

The ground state of Rubidium is the $5^2S_{1/2}$ state. Since ^{87}Rb has a nuclear spin of $\mathcal{I} = 3/2$ and an electronic spin of $S = 1/2$, hyperfine splitting results in two states $F = 1$ and $F = 2$. The transition energy between the $m_F = m_{F'} = 0$ states has been measured with an incredible precision of 10^{-16} [143] and is therefore self-evidently called *the Rubidium clock transition*. There is no linear Zeeman shift of this transition, but the nonzero Zeeman states exhibit Landé factors of $g_F = -1/2$ for $F = 1$ and $g_F = 1/2$ for $F = 2$ [144]. Accordingly, the 6.835 GHz RF transition $F = 1, m_F = 1 \leftrightarrow F =$

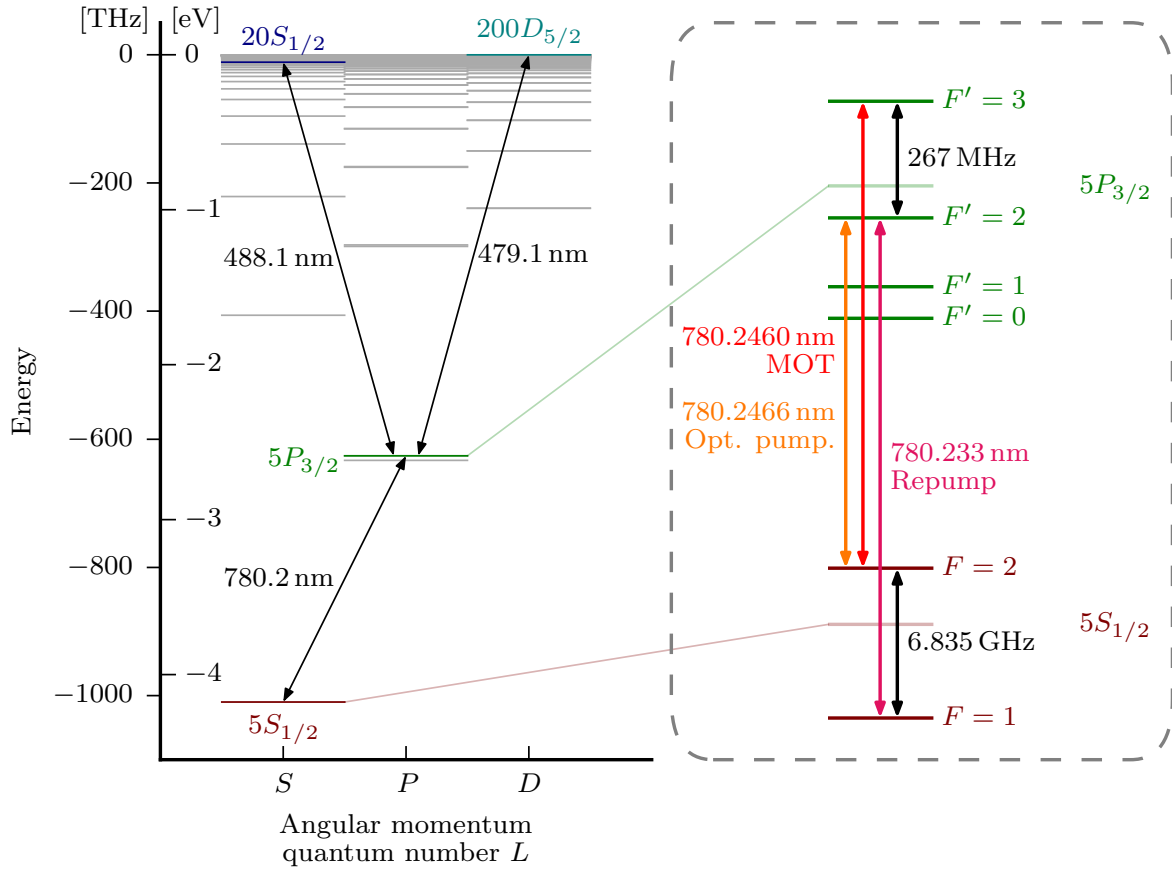


Figure 2.5: The most important transitions for our experiments with ^{87}Rb atoms are the transitions in the D_2 line near 780 nm. The strongest transition $F = 2 \rightarrow F' = 3$ is used for laser cooling and as Rydberg probe transition. Although it is a closed cycling transition, a small probability for off-resonant excitation to $F' = 0, 1, 2$ and subsequent decay leads to a considerable state transfer to the $F = 1$ hyperfine state, which needs to be repumped on the $F = 1 \rightarrow F' = 2$ transition. Optical pumping of the Zeeman states is done with σ^+ light on the $2 \rightarrow 2$ transition to the stretched dark state $m_F = 2$. Two Rydberg laser systems are installed with tunable wavelengths around 480 nm. Both S - and D -states can be excited with principal quantum numbers $n \gtrsim 20$. The $200D_{5/2}$ state is highlighted to visualize the energy scaling with the principal quantum number and is not of special importance for this work.

$2, m_F = 2$ is very sensitive to magnetic fields. In addition, since the linewidth of this magnetic dipole transition is very narrow, the spectrum is very well suited to measure magnetic fields. In particular, the currents through magnetic field coils can be calibrated and the magnetic field zero can be found very precisely, which was done within Christoph Braun's bachelor work [145].

Laser cooling is done on the $5S_{1/2}F = 2 \leftrightarrow 5P_{3/2}F' = 3$ transition which is common practice since the production of the first BEC [15]. The reason for this choice is that it is the strongest transition in Rubidium and it is a closed cycling transition, which means that the excited state can only decay back to $5S_{1/2}F = 2$ due to selection rules of electric dipole transitions. In practice, there is a small probability for off-resonant excitation of other F' levels, predominantly the energetically closest state $F' = 2$, which can decay to both $F = 1, 2$ ground states.

To counteract the loss from the MOT transition to the $F = 1$ state, we shine in light on the $5S_{1/2}F = 1 \leftrightarrow 5P_{3/2}F' = 2$ transition to repump the population back into the MOT cycle. This apparent loss mechanism can be advantageous when it comes to loading the optical dipole trap. Since the optical dipole trap is attractive for both hyperfine ground states, it can be used to decrease the radiation pressure similar to the concept of the *dark* MOT [146]. This is shown in sec. 2.8.

To prepare a spin-polarized atomic sample in the stretched state, $|5S_{1/2}, F = 2, m_F = 2\rangle$, we shine in σ^+ light on the $F = 2 \leftrightarrow F' = 2$ transition. Optical pumping could also be done on the MOT transition, but using the optical pumping transition reduces the amount of scattered photons since the stretched state is a dark state for the optical pumping light if the polarization is set perfectly. As a result, this method of optical pumping causes less heating.

We address Rydberg states with a two-photon process. To individually excite two different Rydberg states, we have two separate laser systems on the lower transition, called *Probe 1* and *Probe 2*, and two systems on the upper transitions, called *Control 1* and *Control 2*. The probe transition is equal to the MOT transition. This guarantees maximum absorption and consequently efficient Rydberg excitation. The upper transition is around 480 nm depending on the Rydberg state. The $20S_{1/2}$ state is highlighted in Figure 2.5 because our lasers are specified in the range (479 to 488) nm. However, there was no reason in this work to excite states with $n \lesssim 35$ because Rydberg interactions are too weak in that range. The upper limit in principal quantum number in this work is currently set to ~ 120 in Rydberg EIT experiments for two reasons:

1. The transition strength, quantified by the blue Rabi frequency Ω , scales with the effective principal quantum number as $(n^*)^{-3/2}$ [147]. Therefore, the Rabi frequency for high n is too low for experiments which are based on strong coupling (high EIT transmission).
2. The high sensitivity on electric fields. The static polarizability scales approximately as $(n^*)^7$ [148]. Thereby, small electric field fluctuations cause an effective line broadening for highly

excited states. Rydberg-EIT is damped which is a poor initial condition for an optical transistor.

None of these criteria are fundamental limits, but rather technical: limited laser intensity and limited electric field stability. In addition, the requirement on the experimental signals such as the EIT line shape or the efficiency of Rydberg excitation is specific to the experiments. So, the condition $n \lesssim 120$ applies for *this* setup in combination with the main experiments described in *this* work.

Another way for two-photon excitation is via the $6P_{3/2}$ transition, which requires light at 420 nm on the lower transition and 1020 nm on the upper transition. In this scheme, the upper transition has a higher Rabi frequency as compared to the previous scheme, but at the expense of the lower transition strength. We require a two-photon scheme to apply Rydberg EIT, although some experiments in this work, for example the incoherent excitation of gate Rydberg atoms would also be possible with other excitation schemes if they are efficient.

2.5 LASER SETUP AND FREQUENCY STABILIZATION

The preparation, manipulation and detection of ultra-cold quantum gases is largely made possible by the advent and advancements in the laser technology. The requirements on the light are monochromaticity and high power. Diode laser systems are available for many wavelengths nowadays, narrow line widths can be achieved and output powers of (20 to 200) mW are on the market. Tapered amplifiers can be installed to increase the laser power to the (0.5 to 3) W range while the spectral properties of the seed laser is approximately conserved due to stimulated emission. Despite the availability of commercial products, the systems still have to be tuned to satisfy the experimental conditions: specific wavelengths are to be set with high stability and arbitrary intensities shall be controlled with high bandwidth.

Figure 2.6 gives an overview of laser systems that were implemented in the course of this work. As elaborated in sec. 2.4, multiple laser systems are required at the D_2 transitions near 780 nm. Due to the superior stability and long experience, we employ five Toptica diode laser systems *DL Pro* numbered from 1 to 5.

In our frequency stabilization scheme for the 780 nm lasers, we use the *DL Pro 3* as a *Master* laser which provides an optical frequency reference for the other lasers by means of beat notes with respective envelope frequencies f_{beat} . The master laser is set to be between the $F = 3 \leftrightarrow F' = 3$ and the $F = 3 \leftrightarrow F' = 4$ transition of ^{85}Rb , which is monitored but not actively stabilized with a spectroscopy on a vapor cell, set up in dichroic atomic vapour laser lock (DAVLL) [149–151] configuration. Active stabilization of the master laser is done by locking a frequency sideband on a close-by fringe of

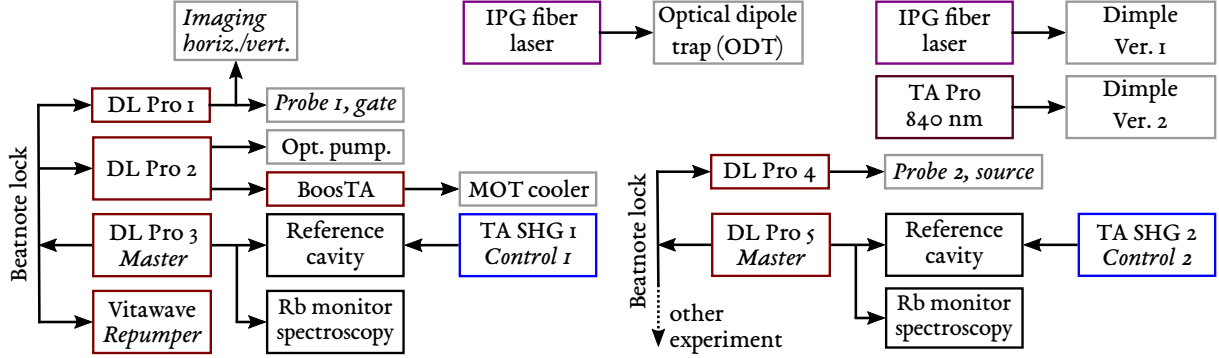


Figure 2.6: Overview of the installed laser systems, their purposes, and the way they are frequency stabilized. Our 780 nm lasers are frequency offset-locked to our master laser which in turn is locked to the reference cavity. The seed lasers of the blue laser systems are directly offset-locked to the cavity. Two lasers are borrowed from another experiment, so there is an additional master laser and a cavity, which is in principle redundant.

our ultra-stable *reference* cavity with the Pound-Drever-Hall technique [152], which is explained and characterized in detail in Christoph Tresp’s master’s thesis [142]. While most power of the master laser is free of modulations and available for the beat note offset-locks, the sidebands are solely created on a low-power (3 mW) branch with a fiber-based electro-optical modulator (EOM), introducing a shift of 496.3 MHz. This modulated light is coupled into the reference cavity, which has a finesse of 15000 and is extremely stable against thermal drifts because it is temperature-stabilized* to 30.500(5) °C, the temperature around which the bulky glass spacer for the mirrors exhibits a zero crossing in the thermal expansion coefficient. A special vacuum housing additionally provides thermal insulation, buffers mechanical shock and shields radiation.

As visualized in Figure 2.7b, the optical frequency of the master laser lies 5501 MHz below the $F = 1 \leftrightarrow F' = 2$ transition and 1333 MHz above the $F = 2 \leftrightarrow F' = 2$ transition, so all beat note frequencies are low enough to be detected with photo diodes and to be stabilized with an electronic feedback circuit. Since all lasers have AOMs for intensity control, the optical frequency is changed by the RF frequencies fed to the AOMs, which is 80 MHz for the D_2 lasers. By installing the optical beat between the lasers and the AOM, we have the flexibility to change the necessary beat frequency f_{beat} by $f_{\text{AOM}} = \pm 80$ MHz while still matching the correct optical frequency. Figure 2.7b shows the beat note frequencies and the resulting optical frequency due to the AOM shift.

To stabilize the beat note frequencies f_{beat} , we follow ref. [153] building some electronics to create a d.c. error signal around f_{beat} . The beat note is detected on a fast photo diode† and mixed with an

*Stanford Research Instruments, PTC10

†Hamamatsu, G4176-03

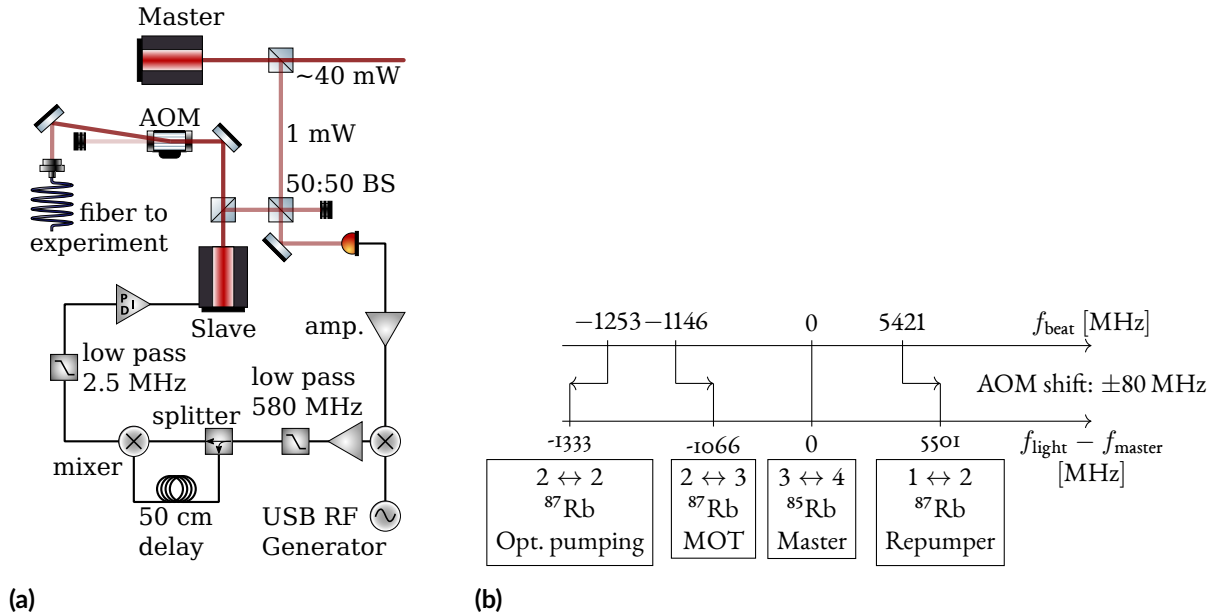


Figure 2.7: (a) All *slave* lasers around 780 nm are frequency-stabilized on a master laser, which runs at an optical frequency of 384 229 241.7 MHz and which itself is stabilized to a reference cavity. Beat notes with 0.5 mW laser power per beam are detected on photo diodes. An electronic circuit translates the beat frequency into an error signal which is fed back to the laser current and grating. (b) Our acousto-optical modulators (AOMs) additionally shift the light frequency in the experiment. The $\pm 1^{\text{st}}$ AOM diffraction order introduces a shift of ± 80 MHz. Since the sign of a frequency is physically meaningless, we use $\text{sign}(f_{\text{beat}})$ to denote red or blue detuning with respect to the master laser. In this scheme the axes are not to scale.

rf signal set to the desired frequency f_{beat} . Then, some power is branched off, electronically delayed by additional 50 cm of coaxial cable, and recombined with a mixer. With a 2.5 MHz low pass filter, a d.c. error signal is created which is fed back to the laser current and piezo voltage via a proportional–integral–derivative controller (PID).

2.6 LASER INTENSITY MODULATION

For a quantum optics experiment, it is self-evident that excellent control over laser intensities is required. To completely block our laser beams, we have included over 10 shutters into our experiment for the different laser beams. Both the electronic driver and the mechanical design are developed by Axel Griesmaier. This section describes our established way to perform high-bandwidth analog intensity modulation of laser beams using AOMs.

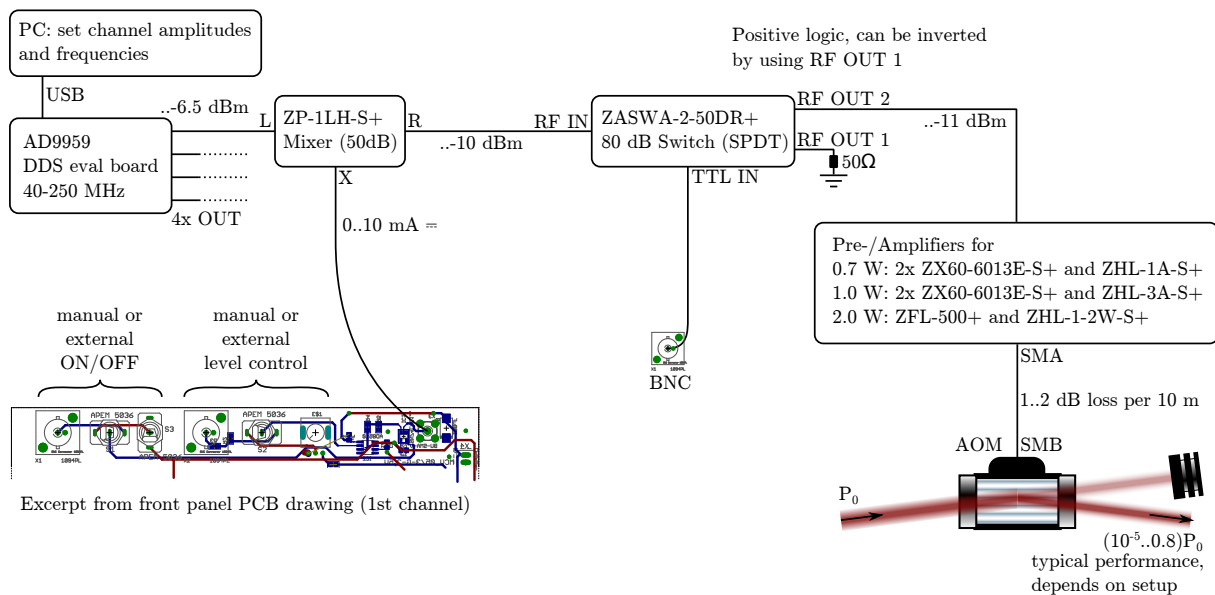


Figure 2.8: We have developed a custom RF driver for our AOMs. It is based on a direct digital synthesizer (DDS) RF frequency source. Arbitrary attenuation is set by admixing a DC signal which is produced by electronics in the front panel. An additional fast switch provides high additional attenuation. Depending on the AOM model (RF power and frequency requirements), different sets of amplifiers are used to optimize the performance while reducing the cost.

2.6.1 A VERSATILE RF SOURCE FOR ACOUSTO-OPTIC MODULATORS

While the reader is certainly familiar with the principle of operation of AOMs, our electronic drivers shall be introduced, since they constitute distinguished RF sources. This successful development is now spread out in several labs with more than 10 pieces built, each featuring 4 channels, which is a reason for documentation.

An overview of the scheme is shown in Figure 2.8. The DDS evaluation board AD9959 is used as a frequency synthesizer. It can run with external reference clocks such as Rubidium clocks. For our purpose, a quartz crystal is more than sufficient. This 25 MHz oscillator can be soldered on the evaluation board. The system clock of 500 MHz is realized by frequency multiplication with a factor of 20. This can be set in the software AD9959/59 Evaluation Software, provided by Analog Devices. The board features 4 channels which can each be configured in the software. Although there are more features like frequency sweeps, for this purpose, static frequency and amplitude settings are enough. Since in our setup the laser frequencies can be shifted, there is no need to perform a second shift by variation of the AOM frequencies. The amplitude is fixed at the DDS board such that the fixed gain amplifiers run in their specifications. Fast switching and analog adjustment of the RF power

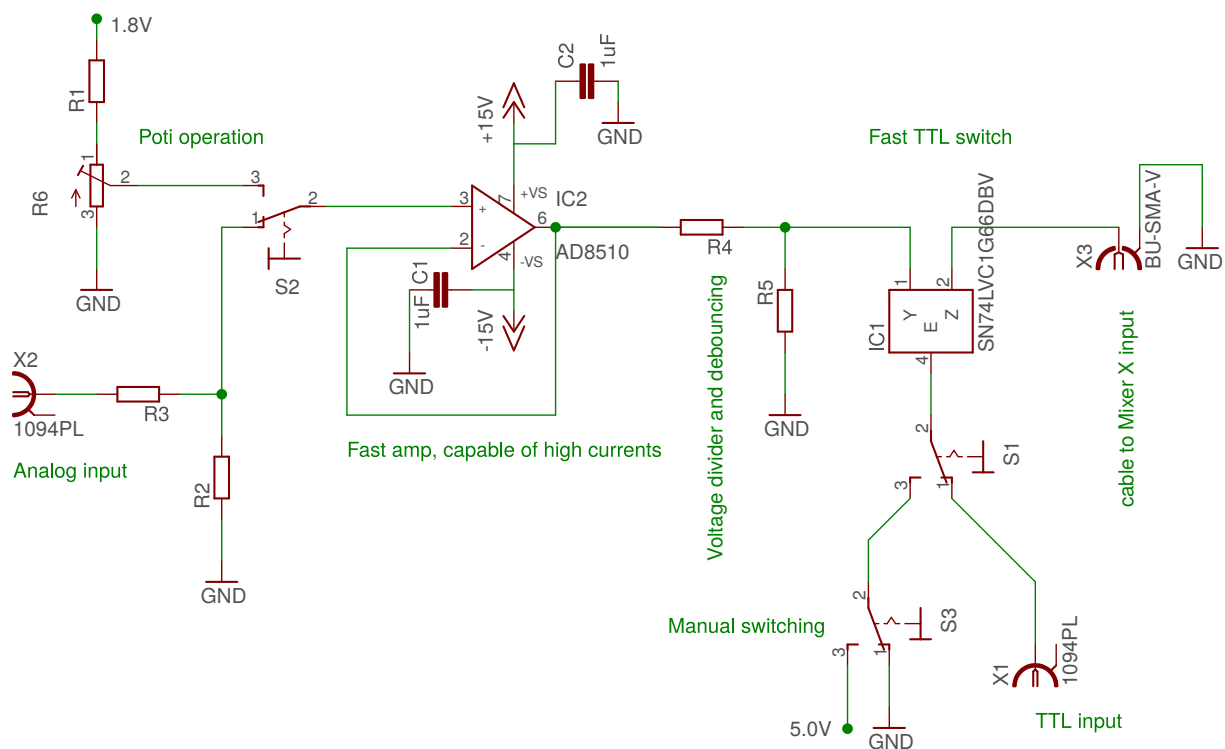


Figure 2.9: Front panel circuit for AOM driver. This circuit is used to control the attenuation of the RF by providing a current (0 to 10) mA in the mixer. The current can be controlled with digital and analog external and internal controls, i.e., by means of external digital and analog voltages or by flipping a switch and turning a potentiometer. Controlled externally, the circuit is fast: it switches within 10 ns using the analog input and within 0.5 ns using the digital input channel. Cable lengths cause additional delay which is on the same time scale.

is realized by a TTL signal on an RF switch* and by a frequency mixer† which operates as an RF attenuator. Transmission of the RF through the mixer is done by mixing a DC current of 10 mA. On the other hand, the RF is attenuated by 50 dB if no current is applied. To convert control voltages (0 to 10) V with high impedance to a current (0 to 10) mA at the mixer, an electronic circuit was developed. This circuit is contained in the front panel printed circuit board (PCB) and a schematic is shown in Figure 2.9. It is based on the operational amplifier AD8510, a fast and unity gain stable amplifier which is used as a buffer. The input impedance of the circuit $R2 + R3 = 0.68 \text{ k}\Omega + 3.3 \text{ k}\Omega = 3.98 \text{ k}\Omega$ is chosen low enough to inhibit noise pickup, and high enough to meet maximum current ratings of our analog voltage sources. As a result, 2.5 mA of current is drawn from the voltage sources at 10 V.

*Mini-Circuits ZASWA-2-50DR+

†Mini-Circuits ZP-1LH-S+

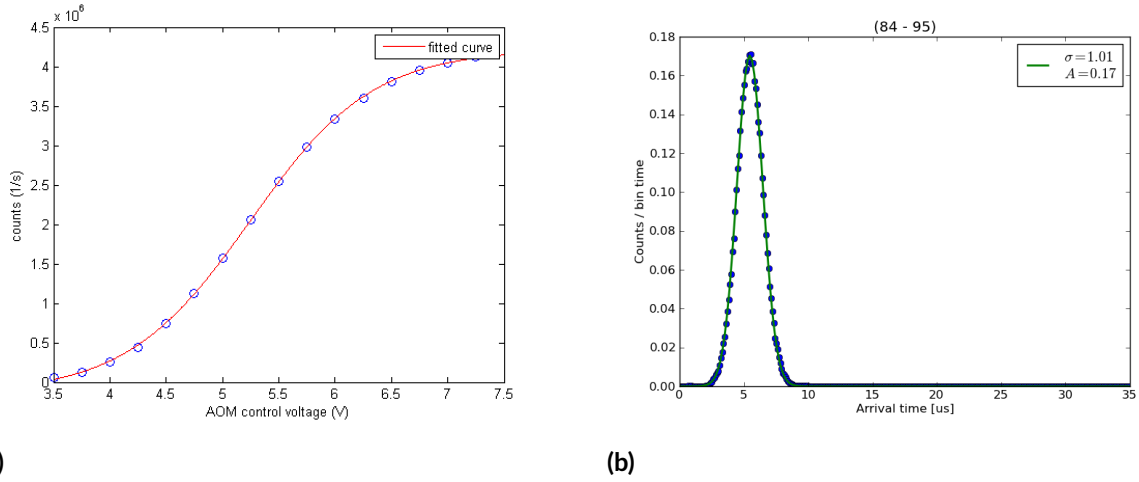


Figure 2.10: (a) AOM driver calibration curve and (b) demonstration of nearly perfect Gaussian light pulses. (a) Due to the nonlinear dependence of the attenuation of the laser light in the first diffraction order with the control voltage at the AOM driver, we determine the transfer function to construct a linear set parameter. An excellent fit is obtained with a sigmoid function. (b) To suppress Fourier broadening, Gaussian light pulses are desired in many experiments. With the linearization using the inverse function, excellent pulse shapes are produced, as can be seen by the perfect agreement between the detected pulse and the Gaussian fit.

The resistors $R4 = 180 \Omega$, $R5 = 100 \Omega$ are chosen such that the current through the mixer is limited to 10 mA. Better impedance matching is realized by using $R5 \neq \infty$. The reduction of reflections after contacting $R5$ was measured.

In addition to the operational amplifier, a fast analog switch SN74LVC1G66 with a switching time 0.5 ns is used to provide digital control. This high-impedance input is to be matched with a BNC T-connector externally. For all our digital output devices, 50 Ω terminations need to be plugged in.

Effectively, the driver allows to change the light intensity by typically around 5 orders of magnitude, depending on the setup. This dynamic range is limited by the overlap between the zeroth and first orders of the AOM diffraction pattern. The overlap reduces with distance to the AOM and may also decrease with beam waist if the diffraction efficiency does not decrease more. The bandwidth of light modulation is mostly limited by the beam size and position. Typically, for maximized diffraction efficiency, a laser beam with 1 mm diameter is used. Since the speed of sound in TeO_2 crystals is 4.2 mm/s, it takes 240 ns until the RF wave (un)covers the beam, which determines the rise and fall times of light switching. Additionally, there is a delay, which is usually dominated by the beam position in the crystal, but the cable length may also contribute significantly.

The attenuation of the mixer is not linear with the current, nor with the control voltage at the

analog input channel of the driver. As a result, as expected, the control voltage is not proportional to the light power in the first diffraction order. Figure 2.10a shows this nonlinear dependence. The measured intensities agree perfectly to a sigmoid function which we use for the fit

$$P = \frac{A}{1 + \exp((U - U_0)/w)} + P_{\text{off}}. \quad (2.7)$$

If the data is normalized to the maximum intensity, the fit result reads

$$U_0 = 5.2077 \quad (2.8)$$

$$w = -0.5628 \quad (2.9)$$

$$P_{\text{off}} = -0.0429 \quad (2.10)$$

$$A = 1.0445. \quad (2.11)$$

Still, it depends on the AOM model. Primarily U_0 changes if a different amplifier or AOM is used. But in general, this function is easy to invert

$$U(P) = U_0 + w \log(A/(P - P_{\text{off}}) - 1) \quad (2.12)$$

and shall be used in the experiment control to allow the user to specify powers P on a linear scale which are translated into control voltages $U(P)$ accordingly. A direct application is the realization of arbitrary pulse shapes as shown in Figure 2.10b. In this example, a perfect Gaussian light pulse is produced. This is necessary for many experiments, in particular to reduce higher Fourier components. For the transistor experiments in Chapter 5, any frequency components higher than the EIT linewidth both for source and for gate photons substantially limit the performance.

2.6.2 ACTIVE INTENSITY STABILIZATION IN A CLOSED-LOOP

In laser systems and optical setups, there are multiple sources of intensity noise. The output of a laser can deviate, in particular if the laser frequency is stabilized by feedback on the current as done in Section 2.5. Another source for intensity drifts is the coupling efficiency through a single-mode fiber, which can drift due to mechanical stress or local expansions of the setup if the temperature fluctuates. Yet another point, in particular if optical fibers are used, is the drift of the polarization, which translates to intensity drifts after polarization dependent optics, which comprises not only polarizing beam splitters, but also all optical elements with a nonzero angle to the incident beam, in particular if dielectric coatings are used.

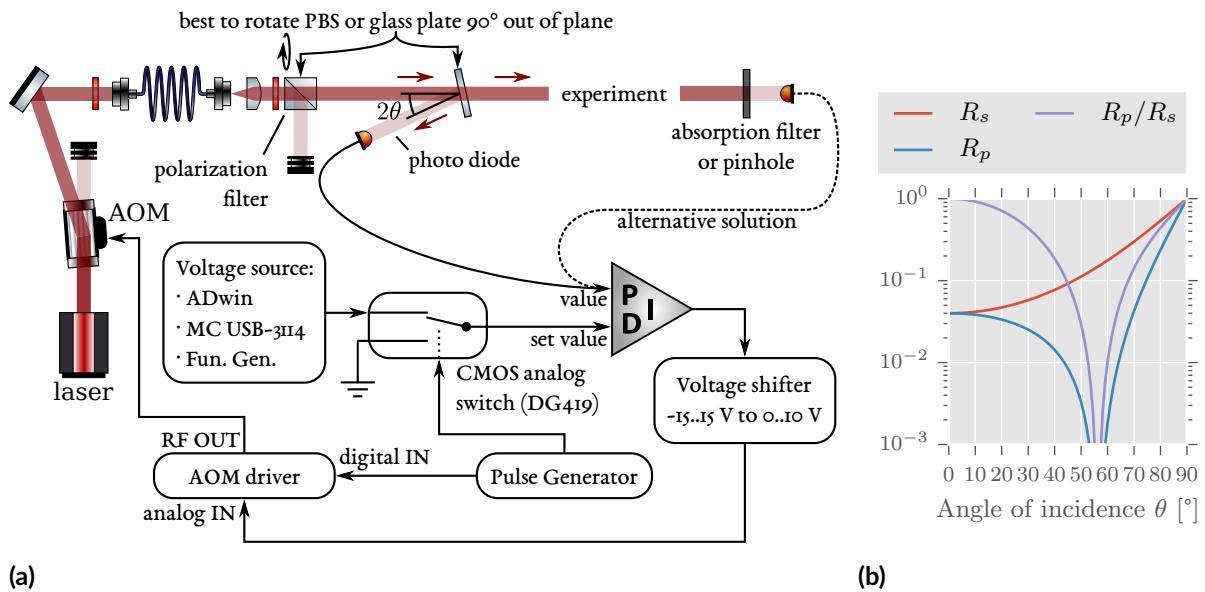


Figure 2.11: (a) To stabilize laser intensities in the experiment, photo diodes are placed on certain positions closely. Since polarization drifts affect the reflectivity, as the Fresnel equations show in (b) for uncoated glass with $n = 1.5$, it is important not to use the reflected p-polarization. The desired intensity can be controlled by a set voltage. Our digital pulse generator can additionally switch the light. To ensure that the PID integrator does not cause a divergence and high overshooting after re-enabling, a fast analog switch toggles the set value below the off value. That way, the scheme works also with constant voltage sources.

We can stabilize the laser intensity using a photo detector and an AOM in conjunction with the fast RF driver from Section 2.6.1, as shown in Figure 2.11. The best configuration depends on the requirement.

- If the intensity shall be stabilized regardless of small polarization drifts, it is advised to set up small angles of incidence, such that $R_s = R_p \Rightarrow R_p/R_s = 1$. If the time dependence of the light absorption in the experiment is negligible, the preferred situation is to work with the transmitted light and use absorption filters or a pinhole to adjust the optical power.
- If the intensity of a particular polarization needs to be stable, the best way is to work with a glass plate at Brewster's angle $\theta = \theta_B$ and detect the reflected s-component. Even at $\theta = 45$ deg, for $n = 1.5$, any p-polarized component is suppressed by a factor of 10 in reflection, and thus less detected.

The worst configuration is to use the p-polarization, because, for example at $\theta = 45$ deg, any s-component is reflected 10 times more than the p-component and will thereby strongly distort the stabilization.

Once the photo detector – we typically use photo diodes from Thorlabs DET10A/M with the power supply DET1B-EC – is placed according to these considerations, the PID needs to be configured. Our self-built PIDs [154] have two input channels from which the error signal is generated. The input impedance can easily be changed by replacing a resistor. For optimized bandwidth, the input impedance can be set to $R_{\text{load}} = 50 \text{ Ohm}$. The corresponding rise time of $t_r = 1 \text{ ns}$ is given by [155]

$$t_r = 0.35 \times 2\pi R_{\text{load}} C_J \quad (2.13)$$

with the junction capacitance $C_J = 6 \text{ pF}$ of the diode. At that load resistance, the voltage is very low, typically in the order of 10 mV which can lead to noise in the PID circuit. By using a higher resistance, it is possible to make a trade-off between bandwidth and voltage. A resistance on the order of 1 k Ω is suited for this application. That way, the rise time $t_r = 20 \text{ ns}$ is still fast enough, and the voltage on the load resistor reaches the order of 1 V. Very long cables should be avoided in this configuration because the imperfect impedance causes reflections. Since the PID is designed for $\pm 15 \text{ V}$, a voltage shifter is used to match the (0 to 10) V range of the AOM driver. The voltage shifter is a modification of Michael Schlagmüller’s isolation amplifier board [154].

The ability to switch the light using digital pulses such as from our Pulse Generator is desirable, in particular if voltage sources are used which do not exhibit high bandwidths. For that feature, a CMOS analog switch (DG419) is included in the scheme. It is used to prevent the divergence of the feedback loop and overshooting after re-enabling. If the AOM driver is switched off, the set value at the PID can be switched to ground. By fine-tuning the input offset at the PID, we can achieve that the output voltage drops to the lowest value. If both the AOM and the switch are turned on again, a smooth rise of the intensity is assured.

2.7 PREPARATION OF AN ULTRACOLD ATOMIC CLOUD, MAGNETO-OPTICAL TRAP

We implemented a MOT in our setup to produce a cloud of ultracold Rubidium atoms. Although the basic mechanism is easily understood and described in books [156, 157] and reviews [158] and the technique is widely used in cold atom experiments, there are many subtleties to the loading dynamics and the steady state. As the cooling performance is subject to many influences, precise theoretical predictions are difficult. The initial atom capture depends on the pressure and composition of the background gas, the exact laser alignment, the beam profiles, the power balance between counterpropagating beams and the magnetic fields. As the atomic density grows during the loading, two-body loss mechanisms [159] such as inelastic excited state collisions can cause heating and loss [158] eventually limiting the number of trapped atoms. Although these effects are interesting, they are not studied

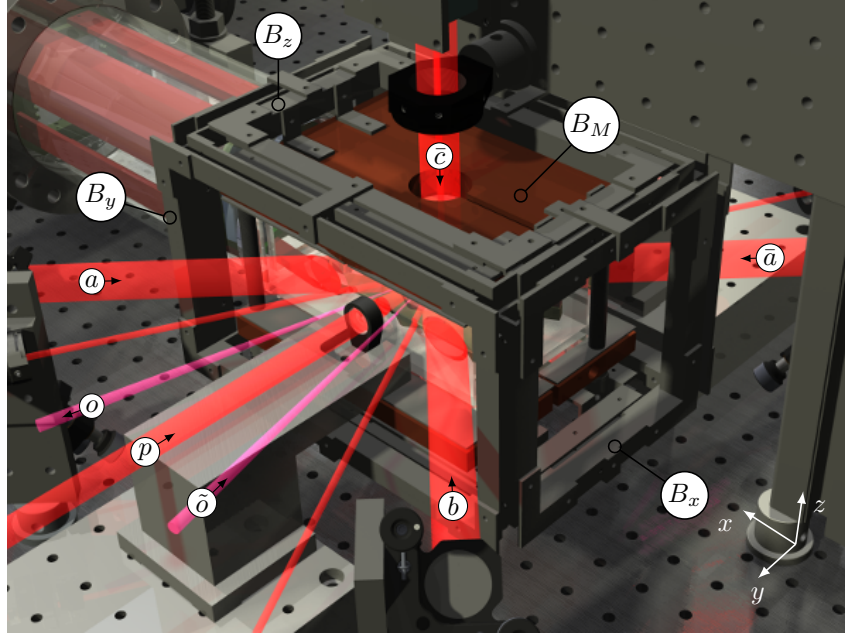


Figure 2.12: Setup of the magneto-optical trap. Six orthogonal beams, labeled (a) , (b) , (c) and counter-propagating (\bar{a}) , (\bar{b}) , (\bar{c}) cross inside the glass cell. Each beam is an overlap of 20 mW cooling and 0.5 mW repumping beams with beam waists limited by the 1 inch optics. The quadrupole magnetic field for the MOT is created by a coil (B_m) which is encapsulated in a water-cooled copper board. Nearly homogeneous additional magnetic fields can be applied with coils (B_x), (B_y), (B_z) wound in rectangularly arranged u-profiles. The picture additionally indicates the position of the Rydberg probe beam (p) which is on axis with the optical pumping beam. Also the incident (o) and reflected (\tilde{o}) optical dipole trap beams are shown.

here in detail since they are not limiting our experiments. Instead, a brief explanation of the setup and the performance shall suffice. The basic setup is shown in Figure 2.12. We begin by explaining the magnetic field setup, followed by the optical setup and finally provide measurements specifying the number of atoms and the temperature.

2.7.1 MAGNETIC FIELDS

Symmetrically above and below the glass cell with only 2 mm clearance, there are copper blocks with integrated magnetic field coils to produce a sufficiently large quadrupole magnetic field. The blocks are water-cooled to transport Ohmic heat away. As can be seen in Figure 2.12, the block is sliced. This reduces eddy currents and thus allows faster switching of magnetic fields. The MOT coil blocks are mounted on a cage of aluminum u-profiles. These profiles form six rectangles each containing one

Coil pair	windings	resistance	central field (gradient) at 1 A	Power supply	Control volt.
MOT coils	2×40		z : 2.1 G/cm, radial: 1 G/cm	EA-PS3016-40B, (0 to 40) A	4 A/V
x offset	2×30	0.57 Ω	0.95 G	EA-PS3016-10B, (0 to 10) A	1 A/V
y offset	2×30	0.72 Ω	2.15 G	EA-PS3016-20B, (0 to 20) A	2 A/V
z offset	2×30	0.66 Ω	2.30 G	EA-PS3016-10B, (0 to 10) A	1 A/V

Table 2.2: Specifications for magnetic field coils. From magnetic field simulations, we extract the field gradient along the vertical and the radial directions as well as the fields created by the offset coils. Since in most Rydberg experiments, our quantization axis is along y , we have the possibility to create large fields up to 43 G.

magnetic field coil, (*offset coils*). Each pair of coils facing each other, including the MOT coils, are contacted in series, such that the current through both coils of a pair is equivalent. However, to create the quadrupole magnetic field with the MOT coils and homogeneous fields with the other coils, the winding direction (or the polarity) is chosen to result in an opposite (MOT coils) or equal (offset coils) current direction respectively between two coils of a pair. We verified the polarities with a simple compass. For the offset coils, it points in the same direction on both sides of the cage when testing one pair of coils at a time. For the MOT coils, it points to opposite directions according to opposite currents. We choose thick copper wires for the coils to decrease Ohmic heating. For the offset coils, we use a $D = 1$ mm thick copper wire isolated with polyurethane. The wire for the MOT coils has a $2 \text{ mm} \times 1 \text{ mm}$ profile. We can estimate the resistance of the coils from the resistivity of copper, which is $\rho_{\text{Cu}} = 1.68 \times 10^{-8} \Omega \text{ m}$. For example, the x -coils with $N = 2 \times 30$ windings and $l = 0.4$ m per winding should have a resistance of

$$R = \frac{4\rho_{\text{Cu}}Nl}{\pi D^2} = 0.51 \Omega \quad (2.14)$$

which is in good agreement with measured 0.57 Ω . That way, it is possible to detect shorts due to possible scraping of the insulation. The specifications for the magnetic fields are summarized in table 2.2.

The power supplies provide electronic input channels to control the output current. The bandwidth is around 100 Hz, but we can switch the output on and off very quickly with an electronic circuit developed by Michael Schlagmüller [154]. Switching our MOT coils from the maximum current of 40 A to a 2 % level takes only 0.2 ms. Same switching with the power supply input would take 8.5 ms.

2.7.2 MOT: OPTICAL SETUP

As depicted in Figure 2.12, the horizontal MOT beams are incident into the glass cell with an angle of 45° . This is to reserve good optical access for the Rydberg excitation. Since the MOT beams are collimated, this nonzero angle of incidence should not lead to astigmatism. The eight MOT beams are created from one beam by polarization optics. $\lambda/2$ wave plates and polarizing beam splitters branch the initial beam into eight ones with equal power. The necessary circular polarization for the MOT is realized by a $\lambda/4$ wave plate just after the last mirror in each of the beams except for the beam pointing up, where the $\lambda/4$ wave plate is before the last mirror due to space constraints. The height of the horizontal MOT beams is 125 mm, tuned by a vertical arrangement of two mirrors per beam, our *beam elevators*. These beam elevators allow beam walking to some degree which we use to optimize the beam alignment and thus the number of trapped atoms. However, the large beam size limits this tunability, or, other mirrors in front of the beam elevators need to be adjusted for more tuning.

2.7.3 CHARACTERIZATION AND PERFORMANCE OF THE MAGNETO-OPTICAL TRAP

In the context of the measurement of the partial and total pressures in the vacuum chamber in section 2.2, we showed the atom loading dynamics.

The steady state number of atoms in our MOT is up to 10^8 . However, if we load the optical dipole trap, we barely load the MOT, since the number of atoms in the dipole trap saturates much earlier. After typically 40 ms compression and 5 ms optical molasses, the cloud is cooled to around $30 \mu\text{K}$, determined by time of flight measurements [160].

2.8 A CROSSED OPTICAL DIPOLE TRAP WITH HIGH POWER SINGLE MODE YB:YAG FIBER LASERS

2.8.1 INTRODUCTION

Optical dipole traps are versatile tools to shape and tightly confine clouds of ultra-cold atoms [27, 161]. Especially the use of far off-resonant optical dipole traps [162] has become a core utility in atomic physics. The large (usually red) detuning to the atomic transitions has two benefits. First, the excitation probability and thus heating is reduced which provides long trapping times. Second, the requirements on the light spectrum are usually not critical. If the detuning is hundreds of nanometers, a laser linewidth of a few nanometers is in principle irrelevant. In practice, other processes such as Raman transitions and excited state transitions might occur with frequency multi-mode laser light

limiting the life time [163–165]. Still, atoms can be trapped tens of seconds in such optical dipole traps made of cost-effective multi-mode fiber lasers [166] which have been and still are subject to industrial development for applications such as laser labeling, cutting and welding.

With modern optical techniques such as AOMs, piezo mirrors and spatial light modulators, almost arbitrary light patterns can be created thus resulting in interesting and precisely controlled potentials [167–169]. The combination of repulsive and attractive traps extends the possibilities further obtaining toroidal traps for instance [170]. Already the combination of two static laser beams can result in qualitatively different potential landscapes as compared to the single-beam situation. The most prominent example is the crossed optical dipole trap [6]. While often used to imprint drastic local density amplification by a tightly focused beam perpendicular to a larger beam (reservoir trap) to facilitate collisional thermalization [171], the motivation in our experiment is slightly different. Two optical tweezers with a small crossing angle of 31.4° results in a cigar-shaped potential. The long axis of this cigar is oriented in the symmetry plane of the two trap beams and thus enabling optical access for further manipulations such as optical pumping and Rydberg excitation. The benefit of this configuration aside from optical access is the large column density along this axis which causes a high optical density per Rydberg blockade volume, so, very efficient blockade.

2.8.2 SETUP

The setup for the dipole trap is depicted in Figure 2.13. The fiber laser* can be controlled through an analog and a digital input with bandwidths of 10 kHz and 50 kHz respectively. To increase the intensity modulation bandwidth to 5 MHz, we insert an AOM after the fiber outcoupler. Using this AOM according to Section 2.6.2, we stabilize the intensity with a photo diode† as shown in Figure 2.13 enabling a defined trap depth and minimizing heating due to intensity noise close to the trap frequencies [6, 172]. The best PID settings result in a total system bandwidth of 1 MHz. Still, fast digital switching is possible within 200 ns. To match the (1.75×1) mm aperture of the AOM‡, we insert a beam telescope with a 150 mm plano-convex lens and a -30 mm plano-concave lens. We use plano-concave lenses in the telescopes here to reduce the optical path and therefore reduce pointing instability which, due to the high power, is a serious issue for the high power single mode fiber§. This fiber is set up for two reasons: to filter the distortions (which are mainly from the AOM) to a single Laguerre-Gaussian mode and to improve the pointing stability at the position of the atoms. Since the laser power in front

*IPG Photonics YLR-100-LP-WC

†Thorlabs, DET10/M

‡Gooch & Housego, 3080-194

§OZ Optics, PMJ-A3HPC, A3HPC-1064-10/125-5AS-2-1-LMA

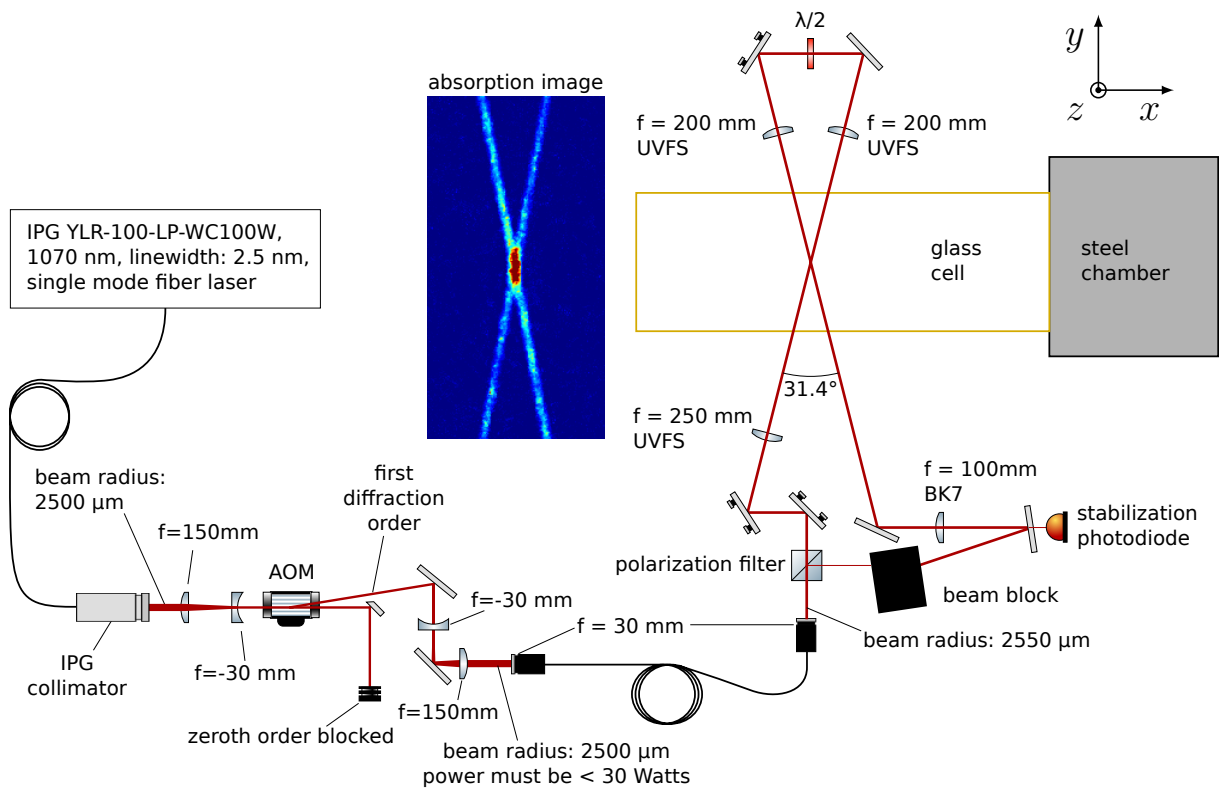


Figure 2.13: Setup of the optical dipole trap. A commercial fiber laser at 1070 nm is operated at 20 W of available 100 W. The intensity is set by the r.f. power in the AOM in conjunction with a feedback loop stabilizing a photo current in a photo diode. A high power fiber is used for mode cleaning and to increase the pointing stability. The laser beam is folded in an arrangement resembling a bow tie. Two foci overlap in the crossing point which is in the center of the glass cell. That way, atoms are confined in a cigar-shaped optical potential as visible in the center of the embedded absorption image (red).

of the high power fiber is up to 10 W at a coupling efficiency of around 70 %, thermal effects play a significant role. That is why the fiber is asymmetric, with special *power strippers* located on the incoupling side of the fiber. By absorption, they remove the light which is not in the single mode of the fiber core. The resultant heat is buffered with the bulky steel cladding and finally transported away to the environment. Complementary to the power strippers, we constructed a copper block with peltier elements to provide a heat sink with an ideally constant temperature. Although the fiber is polarization maintaining, we filter out the vertical polarization with a polarizing beam splitter (PBS) which is less than a few per mille of the total power, in accordance with the specified minimum polarization extinction ratio that ranges from 25 dB to 29 dB between three fibers that were in use. With this setup, the laser power after the fiber can be tuned by over six orders of magnitude with the AOM. On both

ends of the fiber, collimators* with the highest available power rating, 30 W, are used. The 30 mm focal length results in a collimated beam with a radius of $w = 2.5$ mm (intensity drops to $1/e^2$ at w).

The 15.7° angle of incidence on the glass cell causes an astigmatism in the beam, simulated with the optical design software *Zemax*. The foci in the different axes are separated by $100 \mu\text{m}$. However, since the Rayleigh range is 3 mm, this does not decrease the intensity in the focus significantly.

A more important effect is the loss at each glass-air surface of optics which causes a power imbalance between the first and the recycled beam. Even though optics with anti-reflection V-coatings are set up, the difference between the first beam and the recycled beam in the glass cell is 6 %. This loss can be compensated by walking both the 200 mm lenses such that the focal waist of the recycled beam is reduced by 3 %. So, the first lens is slightly closer to the glass cell such that the beam is still slightly diverging. In the end, if an absorption image shows symmetry such as in Figure 2.13, the alignment is satisfactory.

2.8.3 A.C. STARK SHIFTS AND GROUND STATE TRAPPING

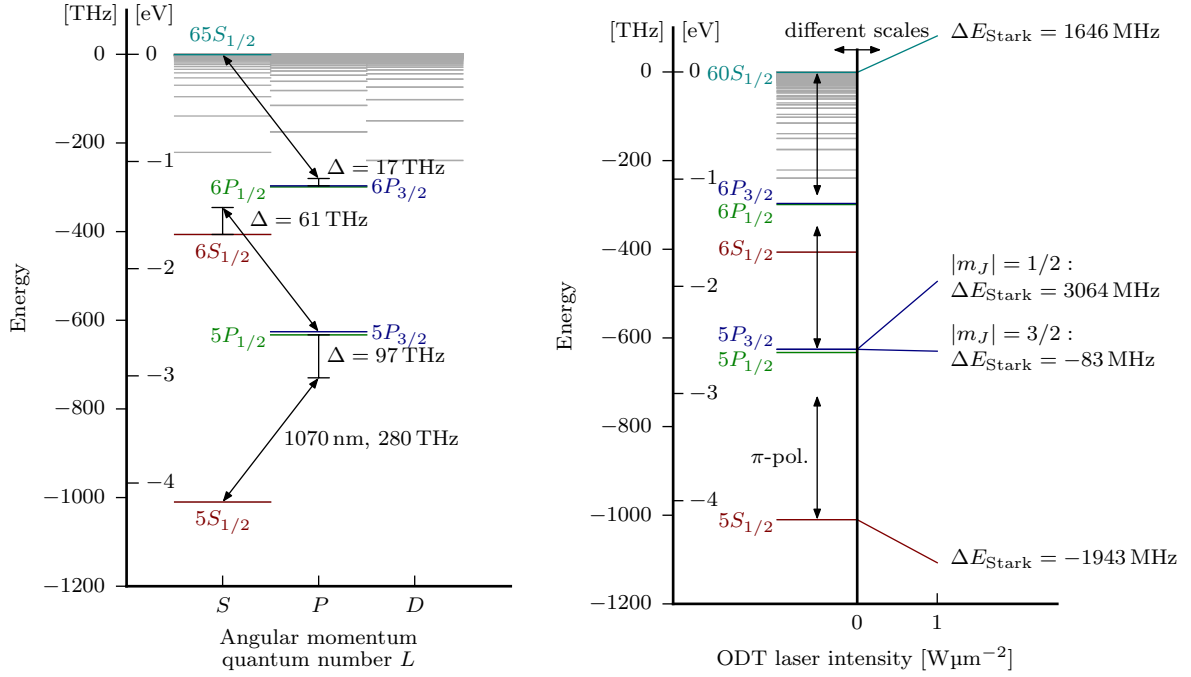
An important conceptual question was to determine what laser powers and beam waists are necessary to provide a sufficient optical potential for the ground state Rubidium atoms. From experience [6], as a rule of thumb, the trap needs to be a few times as deep as the thermal energy of the atoms. That way, a large fraction of the Maxwell-Boltzmann distributed atoms is trapped. The temperature in the MOT stage is around $100 \mu\text{K}$. So, the theoretical design goal is set to a trap depth of 1 mK.

If a collimated laser beam at wavelength λ with a beam radius w is incident on a lens with focal length f , the beam waist can be calculated with the simple formula

$$f \gg w \Rightarrow w_0 \approx \frac{\lambda f}{\pi w} \quad (2.15)$$

which is directly derived from the definition of the Gaussian beam and is valid for low numerical aperture, which, for us, is always a good experimental approximation since the minimum focal length is limited by the extent of the glass cell. The focal waist is plotted in Figure 2.15a for three realistic beam waists of our dipole trap laser at a wavelength of $\lambda = 1070$ nm. The trap depth for atoms in the $5S_{1/2}$ state is calculated in a perturbative approach based on the a.c. Stark shift, i.e., the offresonant dipole coupling of states due to the trap light. The energies are depicted in Figure 2.14a. Similar to considerations in chapter 3, the electrical polarizabilities need to be calculated. For the ground state, only red detunings to coupled excited states are possible, which results in an attractive potential. Accounting for principal quantum numbers from 5 to 11 with fine structure a compact expression can be derived

*OZ Optics, HPUCO-1, A3-1070-P-30AGR-HP



(a)

(b)

Figure 2.14: (a) Level scheme for the determination of a.c. Stark shifts of the ground state, excited state and Rydberg state due to the trap laser. The linearly polarized YAG laser creates far off-resonant coupling between the $5S$ and $5P$ states with red detuning resulting in an attractive trap potential as quantified by the shift in (b) taking multiple levels into account in a perturbative calculation. The excited state, $5P_{3/2}$ is coupled both to the ground state, but also to the $6S_{1/2}$ state. However, due to the polarization, this only occurs for the Zeeman states $|m_J| = 1/2$. For $|m_J| = 3/2$, the main contribution is from the $5D$ state. The Rydberg states are close to resonance with the $6P$ states, but due to the small dipole matrix element the contribution is still negligible at this detuning. The potential is dominated by neighboring states and obtained with a free electron model since perturbation cannot be applied.

for the trap depth in MHz and in Kelvin for our laser wavelength $\lambda = 1070$ nm

$$U_0 = -h \times 1943 \text{ MHz} \frac{P/[\text{W}]}{(w_0/[\mu\text{m}])^2} = -k_B \times 0.093 \text{ K} \frac{P/[\text{W}]}{(w_0/[\mu\text{m}])^2}. \quad (2.16)$$

This formula is evaluated in Figure 2.15b to quantify the dependence on the laser power P and beam waist w_0 . It is thought to be a reference for the design of YAG optical dipole traps with Rubidium. The very major contribution of the ground state shift is from coupling to the states $5P_{1/2}$ and $5P_{3/2}$, as can be seen in the level structure in Figure 2.14. There is only little dependence on the polarization:

The difference between π - and $\sigma^{+/-}$ -polarized light is less than 5 % (not shown in the figure). For a near-resonant trap, this effect is more important. In other words: fine structure as well as hyperfine structure of the $5P$ state are irrelevant for the ground state potential at $\lambda = 1070$ nm.

The polarization independence does not apply for the excited state. The stretched states $5P_{3/2}$, $|m_J| = 3/2$ only experience a very shallow potential with linear polarization since dipole coupling to S states is impossible. Only a small contribution from the $5D$ state results in a slightly attractive potential. Excited states with $|m_J| = 1/2$ are strongly coupled to the $5S$ and $6S$ states.

Similar evaluations can be done with Rydberg states. Here, the $60S_{1/2}$ is taken as an example. There is no qualitative difference to other Rydberg states. Apparently, the YAG wavelength causes a coupling from Rydberg states to the $6P$ states. A naive guess would be that this state contributes most to the a.c. Stark shift of the Rydberg state causing a repulsive light potential for the Rydberg state and an attractive potential for the $6P$ states due to the red detuning. However, the tiny overlap between the wave functions reduces the coupling strength a lot. In fact, neighboring Rydberg states are the dominant contributors to the a.c. Stark shift of $60S$. The coupling is so strong that the perturbation theory breaks down for typical laser intensities ($\Omega < \Delta$ not fulfilled). The $6S$ state is only dominant at much smaller detunings. At special detunings, the contribution from the $6S$ state can cancel all other contributions. The situation is called *magic wavelength trapping* if the detuning is set such that both the Rydberg state and the ground state experience the same shift [89, 173–175]. For Rubidium, this occurs at around 1012 nm depending on the Rydberg state. This situation is beneficial because the transition energy between the ground state and the Rydberg state is independent on the trap depth. Therefore, line shifts and broadening do not occur and as a result, the relative phase between the states is conserved, which allows the observation of coherent Rabi oscillations [90]. In our situation with far detuning, the light potential can be derived assuming a free electron subject to the ponderomotive force of the laser light [61, 176]. The potential is repulsive and amounts to [176]

$$V = \frac{e^2 E_0^2}{m_e \omega} = h \times 1646 \text{ MHz} \frac{P/[\text{W}]}{(w_0/[\mu\text{m}])^2} = k_B \times 0.079 \text{ K} \frac{P/[\text{W}]}{(w_0/[\mu\text{m}])^2} \quad (2.17)$$

where $-e$ is the electron charge, m_e is the electron mass, $\omega = 2\pi c/\lambda$ and E_0 is the electric field amplitude of the laser light.

In the future, the difference in polarization dependence, which, for example, occurs between the ground and excited states, could be utilized as a second parameter to tune magic traps (first parameter: detuning).

Finally, we apply the findings to our setup for the design of the ground state trap. With equations 2.15 and 2.16 and Figure 2.15, it is easy to find right parameters. Selecting the commercially available

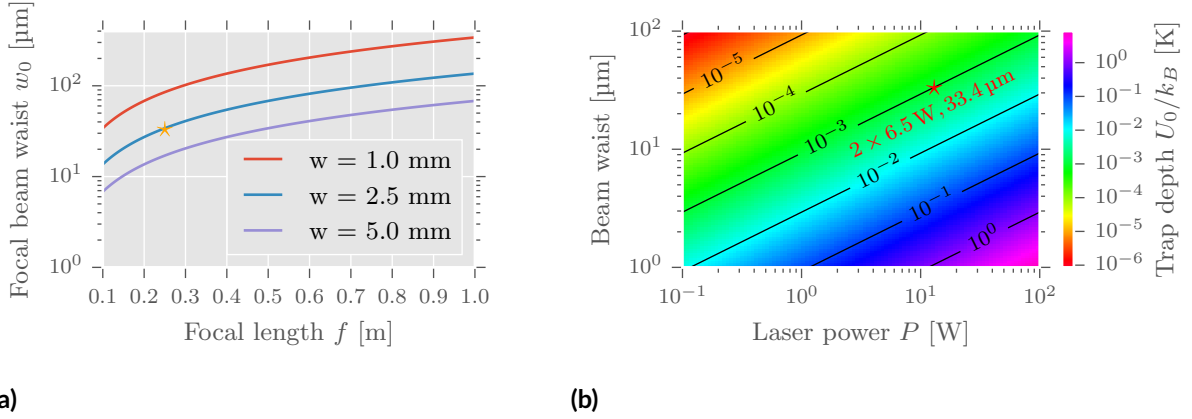


Figure 2.15: Rubidium ground state trapping with light at 1070 nm. Panels (a) and (b) can be used to design optical dipole traps for Rubidium experiments. Our parameters are denoted by stars. To meet the design goal, a trap depth of $U_0/k_B = 1$ mK, the laser beam from our high power fiber (waist $w = 2.5$ mm) is focussed with a lens with focal length $f = 250$ mm. No beam telescope to a waist other than 2.5 mm is necessary before the lens. At 6.5 W, the trap is deep enough to provide confinement. Note that the trapping performance (e.g. number of atoms) also depends on the trap size.

plano-convex lens ^{*} with $f = 250$ mm, a focal waist of $33.4 \mu\text{m}$ is achieved and we meet our design goal $U_0 = k_B \times 1$ mK at an optical power of $P = 2 \times 6.3$ W. Note that the laser power needs to be $P/2$ only, due to the beam arrangement (*recycling*).

2.8.4 CHARACTERIZATION AND PERFORMANCE OF THE OPTICAL DIPOLE TRAP

We can load around 2×10^5 atoms into our crossed optical dipole trap if the trap is operated at 6 W. For the measurements in this thesis, we have an evaporation sequence consisting of a short 10 ms plain evaporation time, followed by 2 evaporation ramps and a final hold time in the finally shallow trap. The total evaporation time is usually between 200 ms and 500 ms depending on the desired final optical depth and temperature and it is also a compromise between evaporation efficiency and data rate. A typically optimized evaporation ramp yields 2×10^4 atoms at $4 \mu\text{K}$ and results in an optical depth of 25(2) which is approximately constant on the scale of the measurement error over 23 pulses of atom recapture.

By the implementation of Raman sideband cooling within Christoph Braun's bachelor thesis [145], a substantial improvement of these numbers is achieved, which will be further documented in the PhD theses of Christoph Tresp and Ivan Mirgorodskiy.

^{*}Thorlabs, LA4158-YAG

2.9 RYDBERG EXCITATION SETUP AND PROBING OF THE GROUND STATE DENSITY

In this section, the optical setup of the Rydberg excitation beams is described, comprising two probe and two control lasers. The near infrared probe light, tuned to the MOT transition, is the lower transition of our ladder-type Rydberg EIT excitation scheme. The excitation scheme is designed such that the tightly confined probe beam defines the excitation volume transversally, while the cloud length defines the longitudinal extent of excitation. As a result, for large enough Rydberg blockade radii, the geometry can be considered one-dimensional, yielding efficient Rydberg blockade and thus high optical nonlinearity, as will be seen more quantitatively in Section 5.5.3. Since the Rydberg blockade and the performance of the optical transistor rely on the quality of this part of the optical setup, it is worth to describe both the design, discuss characterization measurements and to report experimental optimization methods.

2.9.1 SETUP

The optics for Rydberg excitation, as displayed in Figure 2.16, is set up symmetric to the focal point in the glass cell. That way, both probe laser beams – gate and source – and both control laser beams are mode-overlapped in the center. The only asymmetry in the setup is due to the overlap of the optical pumping beam with probe 2, via a 50:50 beam splitter. Dichromatic mirrors are used to overlap the blue and red light. To detect the transmitted probe light, it is separated from the respectively counterpropagating probe light with a PBS. To achieve overlapped foci in the center, two achromatic lenses with effective focal length $f = 50 \text{ mm}^*$ are placed before and behind the glass cell to focus and collimate the light. Even though the lenses are named *achromatic*, the manufacturer still specifies a difference in focal length of $150 \text{ }\mu\text{m}$ for our two wavelengths, which is a reduction of a factor 10 compared to a single lens. While the 3 mm thick walls of the glass cell shift the focus by 1 mm, the additional chromatic aberration is very small: $14 \text{ }\mu\text{m}$. The total focal offset is compensated by setting a small convergence angle of the incident blue beams. This is done by readjusting the collimators at the fibers.

For the probe beams, best overlap is achieved by coupling one probe laser into the single mode fiber of the counter-propagating probe laser by fine-tuning the collimation and the mirrors after the vacuum chamber. This can best be done by temporarily changing the polarization using the wave plates, to obtain sufficient transmitted intensity through the PBS. The 5-dimensional alignment of each of the achromatic lenses (on axis, no tilt) is very tedious but this is the crucial experimental step

*12.5mm diameter, VIS-NIR Coating (Edmund Optics #49-328)

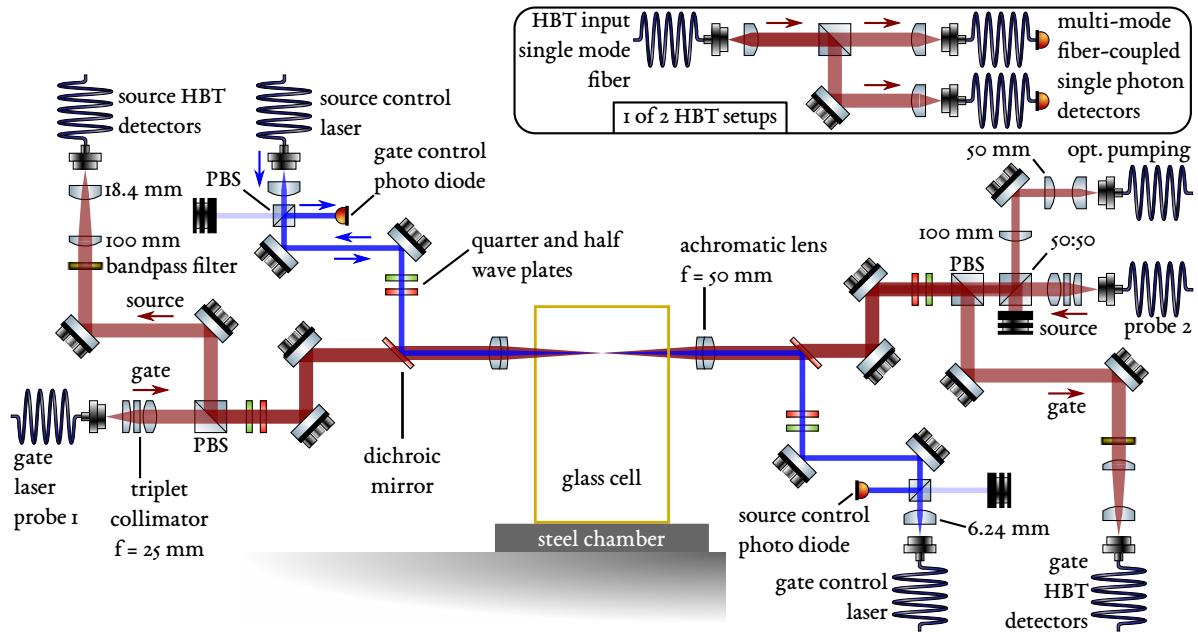
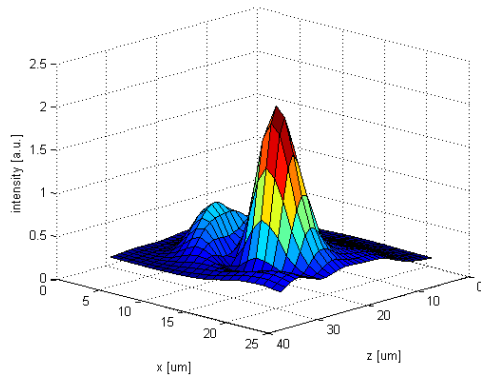


Figure 2.16: Optical setup for Rydberg excitation and detection. Two counterpropagating probe beams are overlapped and separated for detection by polarization optics. The control laser beams are superimposed with dichroic mirrors. On both sides, the PBSs serve both as polarization filters and as separators for active intensity stabilization or monitoring. Due to the combination of polarization filtering, a $\lambda/2$ - and a $\lambda/4$ -wave plate, arbitrary polarizations can be set in the glass cell for each of the four beams. The stretched ground state is prepared with optical pumping and repumping light using the same wave plates as for probe 2. That way, clean circular polarizations can be achieved for a pair of counterpropagating probe and control beams resulting in nice EIT. High blue intensities and a quasi 1D probe excitation geometry are realized with achromatic lenses, arranged symmetrically to the focus.

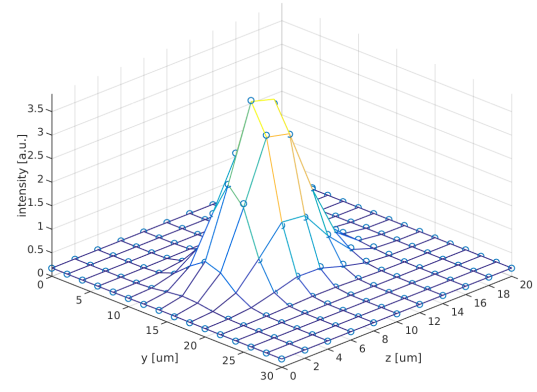
to avoid aberrations which lead to a larger focal waist. A coupling efficiencies over 90 % are achieved, value limited by the power measurement error. In a test setup, the intensity profile was analyzed with a 3D piezo translation stage which scanned the position of a 500 nm pinhole mounted on a photo diode. Clearly, the use of the triplet collimator* is a large improvement from the previously used aspheric lens†. The distortions in Figure 2.17a are most likely from a tiny tilt or offset of the aspheric lens. The triplet collimator is fixed directly to the fiber, so mechanical tolerances are reduced to a minimum. This fact and the design of the three lenses result in the superior Gaussian beam shape as seen in Figure 2.17b. Furthermore, the slightly larger focal length $f = 25.08$ mm as compared to previously $f = 18.4$ mm decreases the focal waist in the atomic cloud even more. From these measurements and from camera

*Thorlabs, TC25APC-780, triplet fiber optic collimator, $f = 25.08$ mm

†Thorlabs, A280TM-B, molded glass aspheric lens, $f = 18.4$ mm



(a)



(b)

Figure 2.17: To analyze the beam shape of the probe setup, a 3D map of the probe intensity was taken by scanning the position of a photodiode with a 500 nm pinhole across the beam with a 3D piezo translation stage. In (a) and (b), the intensity distribution in the focal plane is plotted for (a) the first setup where an aspheric lens collimates the light from the fiber and (b) the new setup using the triplet collimator (see text) which yields better results. In (b), the grid is a two-dimensional Gaussian fit of the data points (circles), whereas in (a), data points are connected to form a surface.

images with and without a microscope objective with a magnification of 40, the focal beam waist is measured to be $6.0 \mu\text{m}$. Taking axial lens alignment imperfection ($\sigma_z = 30 \mu\text{m}$) and for a given $1/e$ cloud length of $40 \mu\text{m}$, the most probable beam radius in the cloud can be specified as $\bar{w}_0 = 6.23^{+0.3}_{-0.1} \mu\text{m}$.

The control beams are pre-aligned to the probe beams by eye. For fine-tuning, the alignment of the focus is optimized by maximizing the probe EIT transmission, preferably at low principal quantum numbers and low probe power to suppress Rydberg interaction. The beam waist is $14 \mu\text{m}$.

2.9.2 DETECTION

The source and gate probe light is coupled through single mode fibers to separate Hanbury Brown and Twiss (HBT) setups [177]. These HBT detectors enable measurements of two- and multi-photon cross-correlations [93, 178]. If a high time resolution shall be obtained, it is important to experimentally achieve a high detection efficiency to gather enough events and produce significant data in a short time. For precise fiber mode matching, we use a combination of two lenses, a spherical $f_1 = 100 \text{ mm}$ lens and an aspheric lens with $f_2 = 18.4 \text{ mm}^*$. In the thin lens approximation, if the distance between

*Thorlabs, A28oTM-B

these lenses is $d = 45$ mm, the effective focal length of [179]

$$f_{\text{EFL}} = \left(\frac{1}{f_1} + \frac{1}{f_2} - \frac{d}{f_1 f_2} \right)^{-1} = 25 \text{ mm} \quad (2.18)$$

matches the focal length of the triplet outcoupler. The front focal length is

$$f_{\text{FFL}} = \frac{f_2(d - f_1)}{d - (f_1 + f_2)} = 13 \text{ mm} \quad (2.19)$$

which is the estimated separation of the $f_2 = 18.4$ mm lens from the fiber. We achieve 77 % fiber coupling efficiency including the finite transmission through this lens system and the bandpass filter.

Splitting the light into two branches in the HBT part, see Figure 2.16, is very efficient. Since the light is already filtered with the single mode fiber, we can use multi-mode fibers to guide the light to the two detectors. Each of the fibers has an ~ 95 % detection efficiency.

To infer the photon rates in the glass cell, we measure laser powers and the corresponding total coupling efficiencies at different parts of the setup. The laser power in the glass cell can be calculated after measuring the power before and behind the glass cell. In fact, due to space constraints, we need to measure it before the achromatic lens on the incident side of the glass cell (laser power P_{in}), and after the achromatic lens on the emission side (P_{out}). Assuming the same transmission on both sides, it is easy to calculate that the power in the glass cell is given by the geometric mean $P_{\text{gc}} = \sqrt{P_{\text{in}} P_{\text{out}}}$. We measure the laser power behind the multi-mode fibers, P_1 and P_2 . Of course, during this whole procedure, the counters need to be turned off to prevent damage. The detection efficiency of the photo detector is $\eta_{\text{pd}} = 0.65$ for the Excelitas counters and $\eta_{\text{pd}} = 0.60$ for the Laser Components counters.

Finally, the photon rate in the glass cell can be calculated. It can be inferred by each (i) of the HBT counters via the total detection efficiency

$$\eta_i = \frac{P_i}{P_{\text{gc}}} \eta_{\text{pd}}. \quad (2.20)$$

Given c_i counts in counter i , there must have been

$$N = c_i / \eta_i \quad (2.21)$$

photons in the glass cell. With two detectors in use, we can take the mean value^{*}, which reduces the

^{*}We shall not take the sum of both to infer the number of photons!

shot noise

$$N = \frac{c_1}{2\eta_1} + \frac{c_2}{2\eta_2}. \quad (2.22)$$

2.9.3 DISPERSION, TRANSMISSION SPECTRA AND OPTICAL DEPTH

The goal of this subsection is to investigate how the previously described tightly confined probe beam is transmitted through a dense ultracold atomic cloud. The detection of probe light can be used to measure the optical thickness of the atomic cloud on this transition which in turn can be used to infer the atomic density and the total number of atoms for a given cloud size. However, close to the resonance of the electronic transition, dispersion can have significant effects on the probe wave-front, as seen in the following. We restrict this discussion to the Lorentz oscillator model [180], which is still a good approximation for dilute gases below BEC densities [181, 182].

The interaction between laser light and a two-level atom is very well described and introduced from first principles in literature [156, 183, 184]. The complex notation of the refractive index for light close to resonance of a two-level atom is given by [160]

$$\tilde{n}_{\text{refr}} = n_{\text{refr}} + i\kappa = 1 + \frac{\sigma_0 n \lambda}{4\pi} \left(\frac{i}{1 + \delta^2} - \frac{\delta}{1 + \delta^2} \right) \quad (2.23)$$

where the detuning δ is defined in units of $\Gamma/2$ and $\sigma_0 = 6\pi\lambda^2$ is the resonant cross-section [160]. The real and imaginary parts are plotted in Fig. 2.18a and 2.18b respectively. The imaginary part of the refractive index, commonly denoted as *extinction coefficient*, is a convenient mathematical construction to account for absorption in the following way: the phase factor of the electric field component of light for plain waves

$$\begin{aligned} \exp(i\tilde{k}z) &= \exp(i(2\pi(n_{\text{refr}} + i\kappa))z/\lambda) \\ &= \exp(2\pi i n_{\text{refr}} z/\lambda) \exp(-2\pi\kappa z/\lambda) \\ &= \exp(ikz) \exp(-2\pi\kappa z/\lambda) \end{aligned} \quad (2.24)$$

is attenuated along z . Accordingly, the intensity is attenuated exponentially

$$I = I_0 \exp(-4\pi\kappa z/\lambda) \quad (2.25)$$

and thus the transmission reads

$$T = \exp(-4\pi\kappa z/\lambda). \quad (2.26)$$

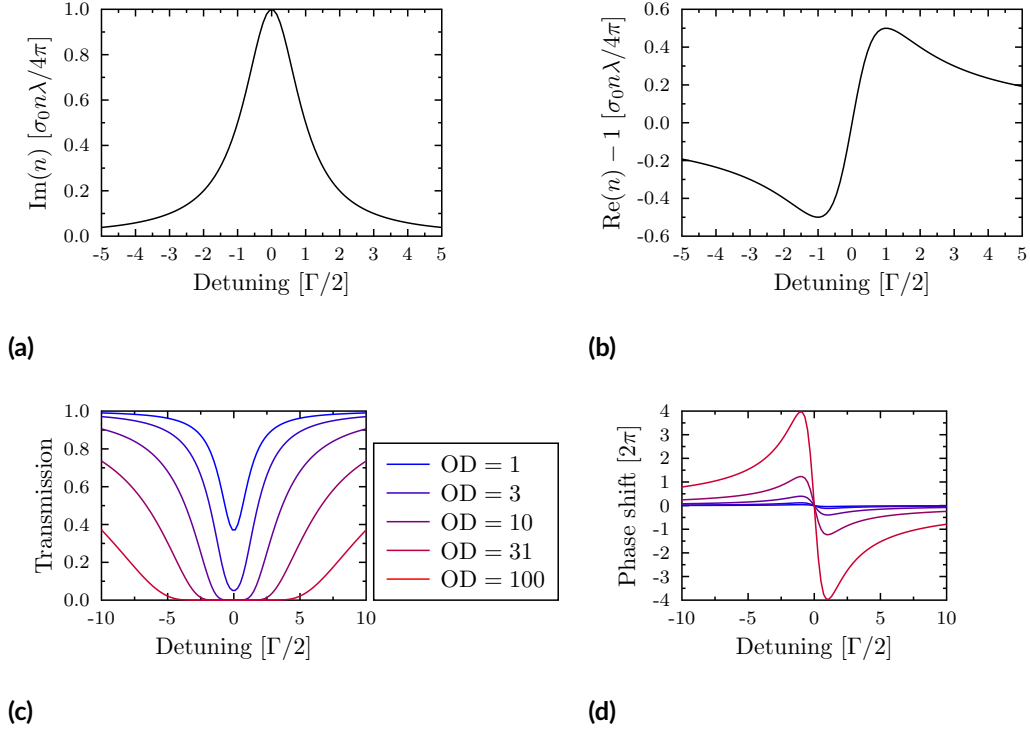


Figure 2.18: The complex notation of the refractive index contains (a) the extinction coefficient and (b) the refractive index which exhibits dispersion close to an atomic resonance. As a result, the atomic column density causes transmission spectra as shown in (c) exhibiting high optical thickness on resonance. In addition, the phase of the light field is altered as plotted in (d).

With κ from eqn. 2.23, the transmission of light that propagates through an atomic cloud with a density distribution $n = n(x, y, z)$ is

$$T = \exp\left(\frac{-\sigma_0 \int n(x, y, z) dz}{1 + \delta^2}\right). \quad (2.27)$$

The value $n_c = \int n(x, y, z) dz$ is called *column density*. As a result of this dependence, the transmission spectrum is invariant to stretch and compression of the atomic cloud. Most generally, the optical depth (OD)

$$\text{OD} = \frac{\sigma_0 n_c}{1 + \delta^2} \quad (2.28)$$

depends on the detuning. In this work, values for the optical depth correspond to $\delta = 0$. Theoretical transmission spectra are plotted in Figure 2.18c for different OD (or their corresponding column densities).

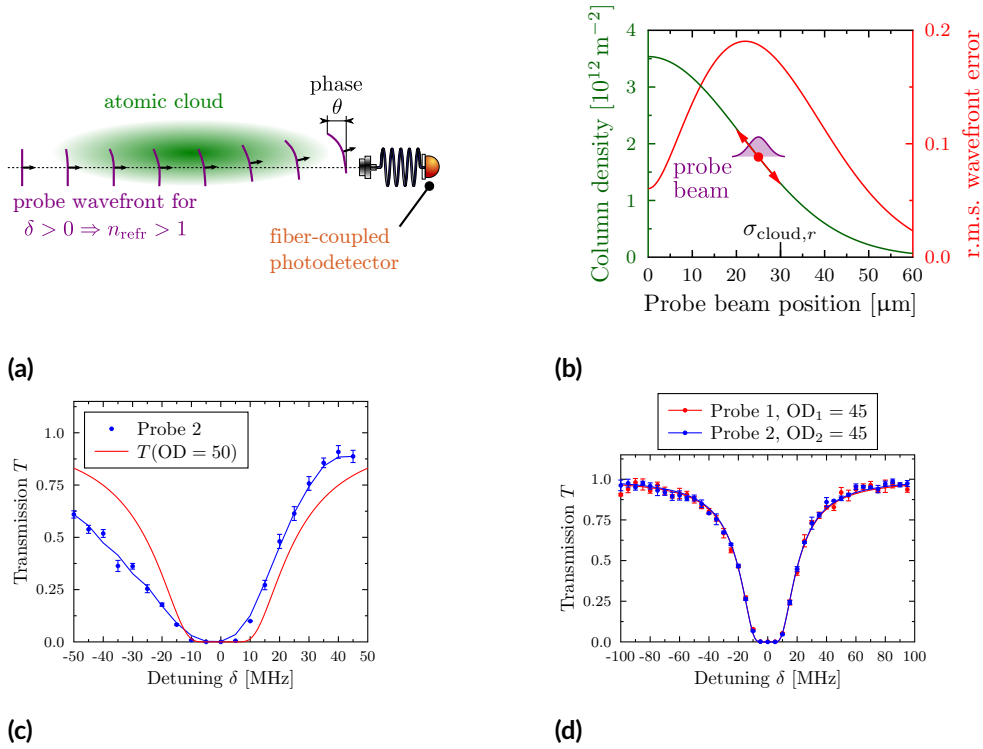


Figure 2.19: (a-d) Estimate of the wavefront distortions of near-resonant light transmitted through an atomic cloud with a Gaussian column density. As different densities are probed, the phase of the light is locally altered causing effectively a deflection and lensing effect which falsifies Lorentzian transmission spectra because the light detector is single mode fiber-coupled. (b) A $w_0 = 6 \mu\text{m}$ probe beam is incident on the cloud with an offset (misalignment) and at a detuning corresponding to half transmission. The 2×10^4 atoms trapped at $\sigma_r = 30 \mu\text{m}$ create a peak optical depth of 39. The slope in the column density over the probe beam profile causes distortions in the wavefront. The r.m.s. wavefront error quantifies the mean phase shift *differences* within the transmitted laser beam profile. It is zero for constant densities or for tiny probe beams. Instead, even for perfect overlap of the probe beam with the atomic cloud, considerable wavefront errors are present. The maximum error occurs on the position of highest density slope. Experimentally, in such a situation, transmission spectra such as the one in panel (c) are observed in contrast to the better alignment in panel (d).

The medium also imprints a phase shift on the transmitted light

$$\varphi = \frac{-n_c \sigma_0 \delta}{2(1 + \delta^2)}. \quad (2.29)$$

This shift is relative to a hypothetical beam propagating in the same mode in vacuum. The spectral dependence of the phase shift is plotted for various optical depths in Figure 2.18d. For typical exper-

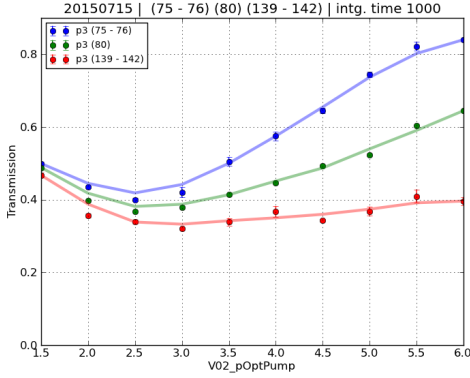
imental conditions such as $OD \sim 31$, the phase shift is on the order of π . If the probe beam waist is on the order of the cloud width, there will be a significant distortion of the wavefront due to the very inhomogeneous column density $n(x, y) \neq \text{const}$. This effect is illustrated in Figure 2.19a for a positive detuning. As a figure of merit, we calculate the r.m.s. wavefront error. The effect on the transmission spectrum (see example data in Figure 2.19c) depends on the experiment setup, for example on the distance to the (fiber-coupled) detector. The highest distortions are expected if the probe beam is centered on the highest slope of the column density, as shown in Figure 2.19b. But even if the beam has no transversal offset (position zero), there is a wavefront error due to the finite beam waist. To conclude, the transmission spectrum yields information about the column density. At high column densities $n_c \gtrsim 30$, the detected spectrum can be modified by lensing due to the atomic dispersion, thus falsifying predictions about the column density.

Note that similar lensing effects have been observed for EIT [185]. Due to stronger dispersion, it can play a big role. Even more alarming in this regard is any spatial inhomogeneity of the control field. The distortion of the EIT spectrum could be misinterpreted. For example, it could be erroneously identified as strong dephasing.

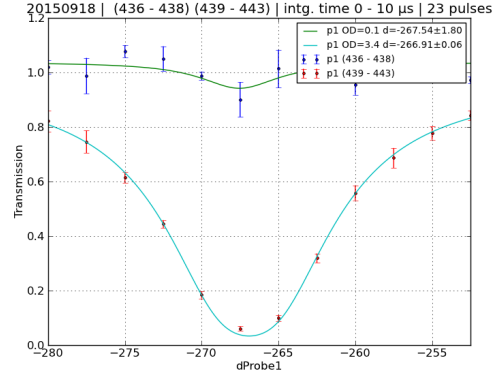
2.9.4 OPTIMIZATION OF OPTICAL DEPTH BY OPTICAL PUMPING

The previous considerations hold in case of two isolated levels driven by the probe light. The magnetic field, which we need to apply to define a quantization axis^{*}, lifts the Zeeman degeneracy of the ground state. After cooling, the atoms can be distributed randomly over these levels, due to the different polarizations and field directions during the cooling process. σ^+ polarized probe light couples these levels to the excited Zeeman states with a different strength cf. the dipole matrix elements in Figure 4.6. By optical pumping [114, 186] on the $F = 2 \leftrightarrow F' = 2 (D_2)$ transition we can transfer population to the stretched state. In addition to the optical pumping light, we have light on the $1 \leftrightarrow 2$ transition coupled through the fiber. If atoms spontaneously decay from the $F' = 2$ excited state to the $F = 1$ ground state, they are repumped, so the optical pumping cycle can continue. We use σ^+ light which is on axis and copropagating with probe 2, as can be seen in Figure 2.16. In contrast to the probe beams, the optical pumping light is collimated in the vacuum chamber, with a waist of around $250 \mu\text{m}$ amply covering the whole cloud and resulting in homogeneous pumping. This is achieved by a lens combination which create a focus 50 mm in front of the achromatic lens. We perform an optimization procedure on the $\lambda/2$ and $\lambda/4$ wave plates to create clean σ^+ polarization of the optical pumping, the repumping light and of probe 2. In this procedure, shown in Figure 2.20a, we try to increase the

^{*}Stray fields including the earth magnetic field and the field from the ion pump are canceled, and an additional field of typically 1 G is applied along \hat{y} .



(a)



(b)

Figure 2.20: Optimization of optical depth by optical pumping on the $2 \leftrightarrow 2$ transition. If the atoms are not spin-polarized in the stretched Zeeman ground state $|F = 3, m_F = 3\rangle$, the optical depth on the $2 \leftrightarrow 3$ probe transition is lower due to lower Clebsch-Gordan coefficients. The optical pumping is optimized by adjusting a set of $\lambda/2$ and $\lambda/4$ wave plates. (a) We detect the probe transmission at a detuning that results in transmissions of around 0.5 for sensitivity reasons. The plot shows a scan of the optical pumping power (AOM control voltage) at three different wave plate settings. If the polarization is correct, σ^+ (red), a dark state is prepared. Therefore, at high photon rates (numbers), the probe transmission is constantly low. Imperfect polarization causes an imperfect population distribution accompanied by additional cycling of the transitions causing heating. Both effects result in the unwanted transmission increase. (b) Another excellent indicator of good optical pumping is high transmission of probe light detuned to the optical pumping transition.

optical depth of the cloud. The probe 2 light is detuned such that the transmission is around 0.5 which offers high sensitivity. With increasing optical pumping intensity over a fixed optical pumping time of typically (200 to 500) μs , the transmission drops due to an increasing population of the stretched ground state. For imperfect polarizations, the transmission rises again at even higher intensities for several reasons. First, if π or σ^- light is present, a rate equation model predicts the steady state to be distributed also over states other than the stretched state. Second, if more photons are needed to polarize the atomic sample, higher heating is obtained, in particular if emitted photons are re-absorbed with undesired polarization in the optically thick medium.

Another way to determine the purity of the σ^+ polarization and the optical pumping performance is to detune the probe light to the optical pumping transition, as shown in the spectrum of Figure 2.20b. After successful optical pumping, the $2 \leftrightarrow 2$ transition should be transparent for the probe light.

The increase in OD due to the optical pumping of course depends on the initial population. While typical improvements in OD are in the range of (30 to 50) %, improvements by 75 % have been de-

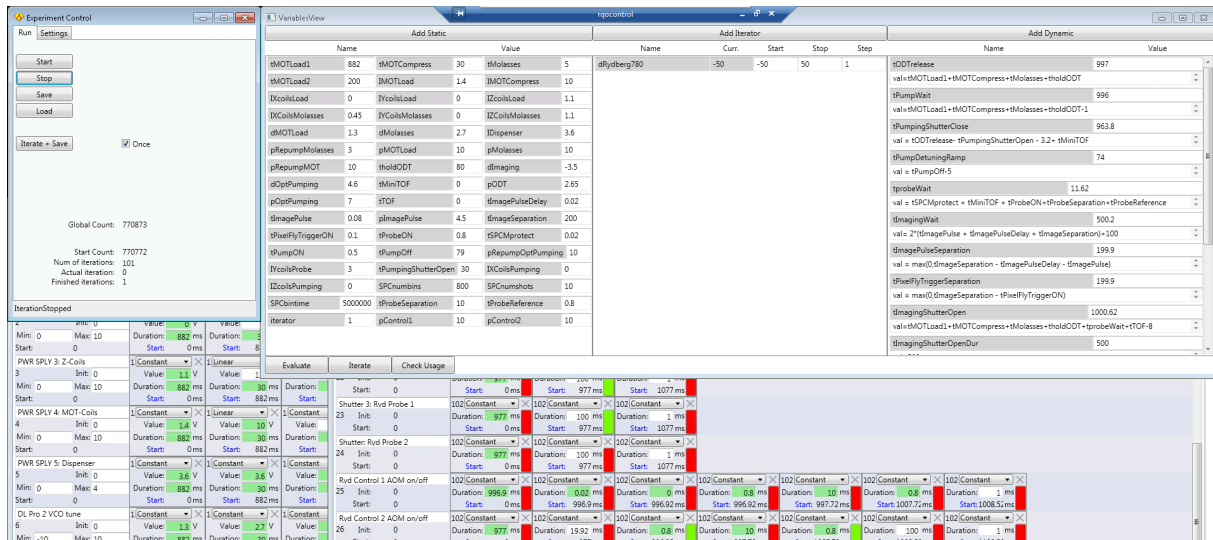


Figure 2.21: Graphical user interface of the computer control system. Time blocks for analog channels (lower left) and digital channels (lower right) define the sequence which is generated on the ADwin system. The sequence can depend on time or voltage variables, as defined in the large window. These variables can be static, iterative or dynamic, i.e., a function of other variables. The main window (top left) is used to start, stop or save the sequence. If an iteration is set, the iteration can be started using the *Iterate* button. Otherwise, the sequence is looped using the start value.

tected.

In the end of this section, please note that there was also a *Dimple* implemented in our setup in the course of Christian Zimmer's master thesis [187]. This dimple is a third optical dipole trap beam, incident from the side (from $-x$), with tight confinement along y .

2.10 COMPREHENSIVE EXPERIMENTAL CONTROL WITH COMPUTER AIDED HARDWARE PROGRAMMING, CUSTOM ELECTRONICS AND DATA ACQUISITION

The study of physical phenomena can best be done by systematic measurements. Such measurements require systematic control of experimental parameters. This section will introduce the way we control our experiments. First, the core experiment control is described. Next is a presentation of various laboratory devices and the way they are integrated into the computer-controlled sequence.

2.10.1 EXPERIMENTAL SEQUENCE WITH REAL-TIME HARDWARE

Based on previous work by Stephan Jennewein [188] and Michael Schlagmüller [154], computer software was developed that allows the user to define and run experimental sequences through a graphical user interface (GUI) which is displayed in Figure 2.21. These sequences contain digital and analog values that are uploaded to a real-time system which controls the digital and analog channels as desired. The software is programmed in a modular way to be extendable to various output devices. Current implementations support devices from *National Instruments* and *ADwin* systems by *Jäger Computergesteuerte Messtechnik GmbH*. In this experiment, an ADwin system is in use consisting of the Pro-CPU-T11 controller running a 300 MHz processor^{*}, a 32-channel digital (input/output) module[†] and two 8-channel analog modules[‡] with 16 bit resolution over the range from -10 V to 10 V . We manually limit the smallest time step of our ADwin sequence to $20\text{ }\mu\text{s}$. That way, the sequence processing is fast enough to reliably generate the next sequence during a 500 ms MOT loading time where all channels are constant. The sequences contain three different types of variables: static, iterative and dynamic variables. It is possible to run multi-dimensional parameter scans using iterator variables. In each cycle, the dynamic variables may change as a function of static, iterative or other dynamic variables which offers a huge flexibility. The dynamic variables are defined in their respective text areas as simple python methods

```
# any python code here
val = 3 # return value
```

which allocate the value of `val` to the dynamic variable. That way, many features do not need to be included in the main program, since they can already be solved by little python code. For example, if `N` is scanned from 0 to 10 in integer steps, a dynamic variable can be defined

```
triang = range(0,11,2)+range(9,0,-2) # stack two lists of numbers together
val = triang[N] # assign N-th value of triang to the dynamic variable
```

realizing a triangular scan with even values counting up and odd values counting down:

```
[0, 2, 4, 6, 8, 10, 9, 7, 5, 3, 1]
```

With such techniques, we can directly exclude some systematic measurement errors and enable smooth scans of critical parameters such as the ones responsible for laser lock frequencies.

^{*}Analog Devices, ADSP TS101

[†]Pro-II-AOut-8/16-B

[‡]Pro-II-DIO-32



Figure 2.23: Photo of the Pulse Generator. This FPGA-based device can output TTL pulses with a sample rate of 1 GHz on 24 channels.

2.10.2 INTERFACING SCIENTIFIC INSTRUMENTS WITH THE COMPUTER CONTROL

In the beginning of each experiment cycle, a python script `cycle.py` is executed. It broadcasts the message “*Cycle started.*” to the network. As displayed in Figure 2.22, clients on different machines can listen to this message and react accordingly. The clients can load current parameters from the database and configure connected hardware with these values appropriately. On the one hand, this approach causes time jitter for the hardware programming, but on the other hand, most of the hardware is externally triggered with digital pulses defined in the sequence. This method has a limitation: on one computer, only one script can listen to the network broadcast at a time. The opened socket connection blocks the used port for other programs. One solution would be to broadcast this message on multiple ports. Our solution is to create direct network socket connections if the port is already used. Both solutions have their own advantages. Broadcast messages enable high flexibility for adding devices. On the other hand, direct network socket connections enable more error handling. If a network socket is unavailable, the experiment control automatically produces a timeout error.

2.10.3 PULSE GENERATOR: DIGITAL PULSES WITH GIGAHERTZ BANDWIDTH

Our digital channels in the ADwin system are complemented both in number and in speed with a development by Helmut Fedder and Felix Engel, our Pulse Generator [189]. Commercial versions are available now at Swabian Instruments*. This device features 24 digital output channels with SMA jacks which drive TTL pulses into 50 Ω loads. With a sampling rate of 1 GHz, the Pulse Generator can easily fulfill our time scales $\gg 10$ ns in the experiment.

The device is based on an field-programmable gate array (FPGA) which is set up in python through a C++ application programming interface (API). The pulse sequence can be defined using the Pulse Editor, shown in Figure 2.24, a Python program with a GUI which creates or overwrites a file `pulsepattern.txt` containing all the information about the sequence. This file is saved in the Pulse Generator folder with a relative path. All code and the pulse patterns are stored in an SVN repository. The Pulse Editor expects the sequence to be definend in a special variable `pattern` which should be

*<http://swabianinstruments.com>

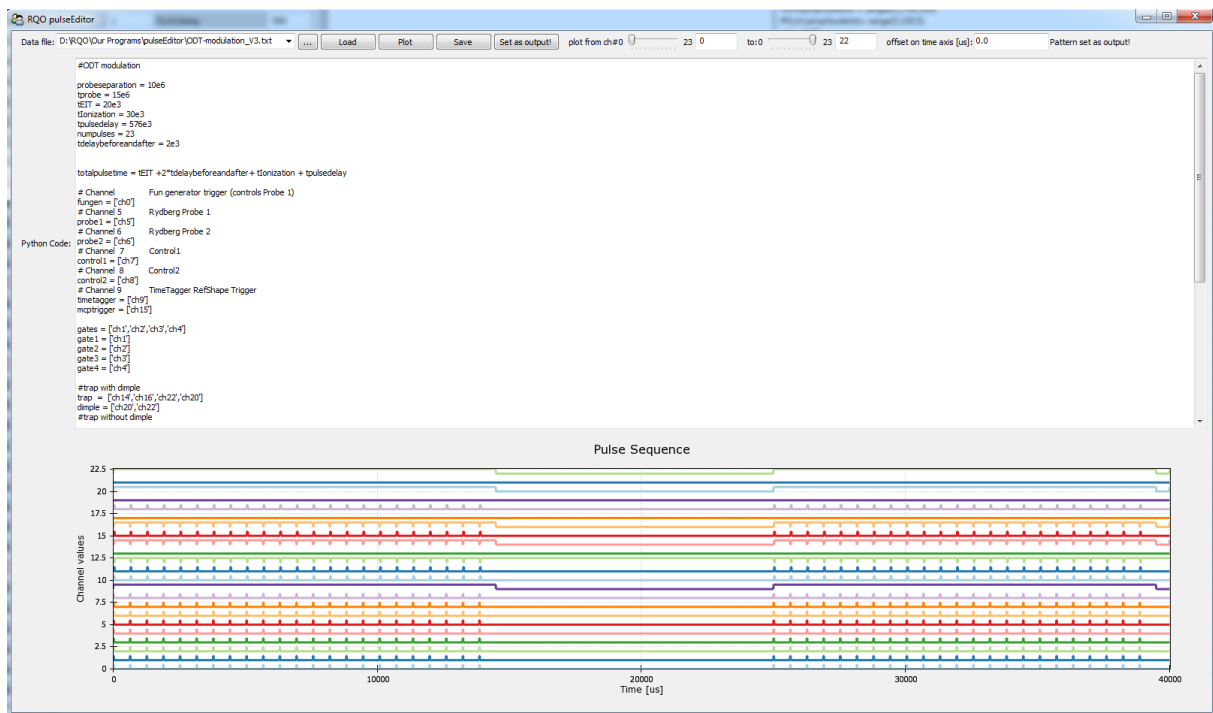


Figure 2.24: The output of the pulse sequence can be defined and cross-checked in a user interface. For highest flexibility, the sequences are set programmatically by the (dynamic) creation of Python lists.

a Python list of 2-tuples with the first entry containing a list of channels which should be set to TTL HIGH and the second channel specifying the duration of this state in nanoseconds. A rectangular pulse of $1\ \mu\text{s}$ can be created in the following way.

```
pattern=[([],1000),(['ch5'],1000),([],1000)]
```

It is advised to use variables. In the following example, two channels are pulsed 5 times.

```
probe1 = ['ch5']
control1 = ['ch7']
tpulseoff = 1e3
tpulseon = 1e3
npulses = 5
pattern=[([],tpulseoff),(probe1+control1,tpulseon)] * npulses + ([[],1000)]
```

Note the last time step with an arbitrarily chosen duration. It is used to set all channels low until the device is re-programmed. During programming, channels are set to TTL LOW by default. Channels specified in the variable



Figure 2.25: Photo of the Time Tagger, an FPGA-based device which allows the detection of TTL pulses with a resolution of 60 ps on 8 input channels. The detection can start with an external trigger and arrays of time-binned counts can be generated for convenient data analysis.

```
continuousChannels = ['ch0']+probe1 # example
```

are kept at TTL HIGH during programming. This is useful, for example, to control our dipole trap laser AOM. The logical variables

```
triggered = True # wait for trigger if not specified  
loop = False # no loop if not specified
```

specify if the sequence should start right after programming or after an external trigger command, and if the sequence should run once or keep repeating. To change the sequence dynamically, it is even possible to use variables that are defined in the computer control GUI. The Pulse Editor accesses these variables through the MySQL server before parsing the sequence. That way, pulse durations can be scanned using iterators in the computer control software and no manual changes need to be done by the user.

Note that the Pulse Editor is simply a helper application which allows to define pulse sequences. The actual programming of the Pulse Generator via USB is done in a separate Python script. This script also loads the computer control variables from the database before executing each line of Python code saved by the Pulse Editor.

2.10.4 TIME TAGGER: DETECTING DIGITAL PULSES WITH 60 PICOSECONDS RESOLUTION

Similarly to the Pulse Generator introduced in Section 2.10.3, we have a second FPGA based device which was developed by Helmut Fedder and our group, and was part of Fabian Böttcher's bachelor thesis [190]. The Time Tagger, showed in Figure 2.25 is a digital pulse detector featuring 8 input channels with SMA connectors and with an internal 50 Ω termination. While a 60 ps time resolution is possible, we configure the Time Tagger to create time bins with durations between 10 ns and 1 μ s,

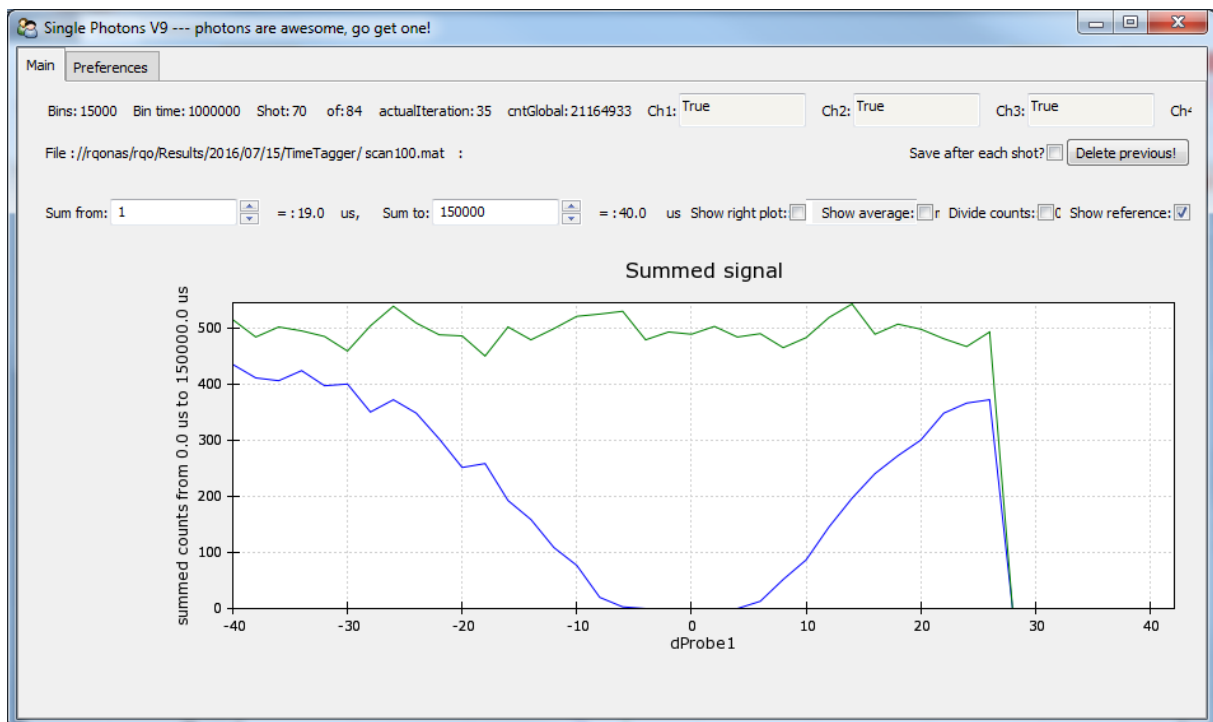


Figure 2.26: Our data sources are single photon counters and an ion detector. These devices send out pulses which are detected on our Time Tagger. A Python program is used to configure the Time Tagger and to read out and visualize the result in a graph. Once a scan is finished, the program saves the data to a new file on a network storage.

depending on the experiment. This is our main data acquisition device detecting data both from our single photon counters and from our MCP. For quick user response to an experimental outcome, the data is visualized in real-time on a GUI, shown in Figure 2.26. In addition to reading out the data, the program also configures the Time Tagger. Detection timing is realized by setting channel 0 as the trigger channel. In each experiment, a pulse from the Pulse Generator triggers the detection of one row of data stored in an array. The length of the row is given by the `SPCnumbins` variable in the computer control software while the bin time is `SPCbin time` in picoseconds. The next trigger causes counts to be stored in the next row of the array. The number of rows is determined automatically by the number of cycles in an experiment. Once the second last experiment is finished, the data is stored in a compressed MAT file, a file format which turned out to have the best compression and storage speed*. Not acquiring the last iteration does not limit the data rate dramatically but it assures enough time to read out the result from the time tagger, save it to the network disk and clear the array

*The compression is around a factor of 1000 compared to comma-separated values (CSV) saved as plain text.



Figure 2.27: Photo of a 16-channel highly stable voltage source. Each channel has 16 bit resolution over $(-10 \text{ to } 10) \text{ V}$. It is programmed automatically according to variables specifying the voltages in the computer control user interface. Image courtesy of Measurement Computing.

before the next scan starts. Starting from a hard-coded base folder, the software automatically creates a Folder in the format `YYYYMMDD` where it saves the data files with continuous numbering starting with the file `scan1.mat`. Scans that run over several days are saved in the first folder for easy evaluation. The program updates the date and folder only on restart, on purpose.

The Time Tagger is very versatile in its configuration. It is possible to create multiple measurement instances simultaneously. For example, one data channel can be used to trigger the acquisition of another channel and vice versa. That way, the device can automatically produce cross-correlations with the positive and negative sign. Another possibility, which we use actively, is to create instances with different external triggers and different time binning. This is particularly useful if precise time information is only needed for a specific time range. This can prevent a memory overflow, which can occur if the arrays are too large in size due to high time resolution *and* long detection time.

A future improvement of the acquisition of digital pulses is to run the Time Tagger in a mode in which it saves actual time tags. This is possible using the dump function provided by the Time Tagger class. It creates a binary file containing all events. This mode of operation can become beneficial for low data rates as compared to the bin time, which is generally the case in our experiment. Arbitrary and variable time binning depending on the amount of data could be postponed to the evaluation phase. The dump function does not offer triggering or gating. However, the trigger time tag is also saved. Our single photon counters can only cast output during the detection time, because we use the gate input. That means, no additional unnecessary data is stored. The MCP signal could be inhibited with a transistor-based power supply of the signal amplifier.

2.10.5 HIGH-PRECISION, HIGH-DRIVE VOLTAGE SOURCE: MEASUREMENT COMPUTING USB-3112 AND USB-3114

In addition to the 16 analog voltage channels provided by the ADwin system, we have included two special (-10 to 10) V sources: the high-drive (± 40 mA per channel) versions of Measurement Computing USB-3100 voltage output device series. While the USB-3112 provides 8 channels and the USB-3114 (shown in Figure 2.27) provides 16 channels, the core specifications are very similar. They feature 16-bit resolution which can be set over the full bipolar (-10 to 10) V or unipolar (0 to 10) V voltage range. Over the bipolar range, an absolute accuracy of ± 14 LSB is specified, where the least significant bit (LSB) equals a voltage difference of $300 \mu\text{V}$ in this case. Maybe even more important than the accuracy is the superior temperature stability $0.00055 \%/^{\circ}\text{C}$ which is essential for experimental reproducibility. The voltage ripple is specified to be $\pm 32 \mu\text{V}_{\text{rms}}$. We lower this by adding a low pass filter consisting of a 50Ω resistor and a $2.2 \mu\text{F}$ capacitor. This does not affect the temperature stability significantly. In the worst case, for a $1 \text{ k}\Omega$ load and for typically $100 \text{ ppm}/^{\circ}\text{C}$ stability of the 50Ω resistor, the voltage at the load deviates by only 90 ppb.

The voltages are set through a USB connection. To change voltages, it is possible to use a program provided by Measurement Computing. In this program, the channels must be configured for bipolar or unipolar voltages. Instead of setting the voltages by hand, we use the supplied programming API *Universal Library* to configure the channel voltages automatically according to voltage variables defined in our main experiment control. The API is available for some C-like programming languages and we actually use C#.

We use the 8-channel voltage source exclusively for defining the electric field with the in-vacuum electrodes as described in Section 2.2. The 16-channel voltage source provides control voltages for the high voltage drivers which are used for ionization and steering the ion trajectory, and one channel provides the MCP shielding voltage applied to the MCP mesh. While not all remaining channels are in use, many of them are used for application which are not time critical such as control voltages for some AOM channels which are used in conjunction with digital switching anyway.

2.10.6 ARBITRARY WAVEFORM GENERATORS

To generate arbitrary voltage patterns, we installed three Agilent two-channel 30 MHz Function / Arbitrary Waveform Generators 33522A in our experiment. They are connected to our lab network and programmed over network sockets with Python. We use them in combination with the AOMs, as discussed in Section 2.6.1. Figure 2.10b shows that nice Gaussian light pulses can be obtained. We also create more complex functions, as for the control light for storage and readout experiments. For

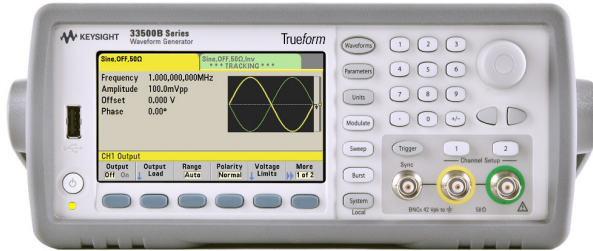


Figure 2.28: To generate arbitrary voltage waveforms, we included in our experiment three two-channel waveform generators Agilent 33522A, now sold by the spin-off company Keysight, model 33500B. The sampling rate of 30 MHz and the possibility to drive (-10 to 10) V into 50Ω or (-20 to 20) V into high impedance loads opens up wide application ranges. Our main application is optical pulse shaping with acousto-optical modulators. Reproduced with Permission, Courtesy of Keysight Technologies.

this purpose, two rectangular pulses are created with pulse heights, the separation of the pulses, and the fall time of the storage pulse specified as parameters. Precise control of the pulse start time is done by setting the device into a so-called burst mode. In this mode, the device is armed with the desired pulse shape and fires it upon external triggering by our Pulse Generator.

2.10.7 20 GHz MICROWAVE SYNTHESIZER

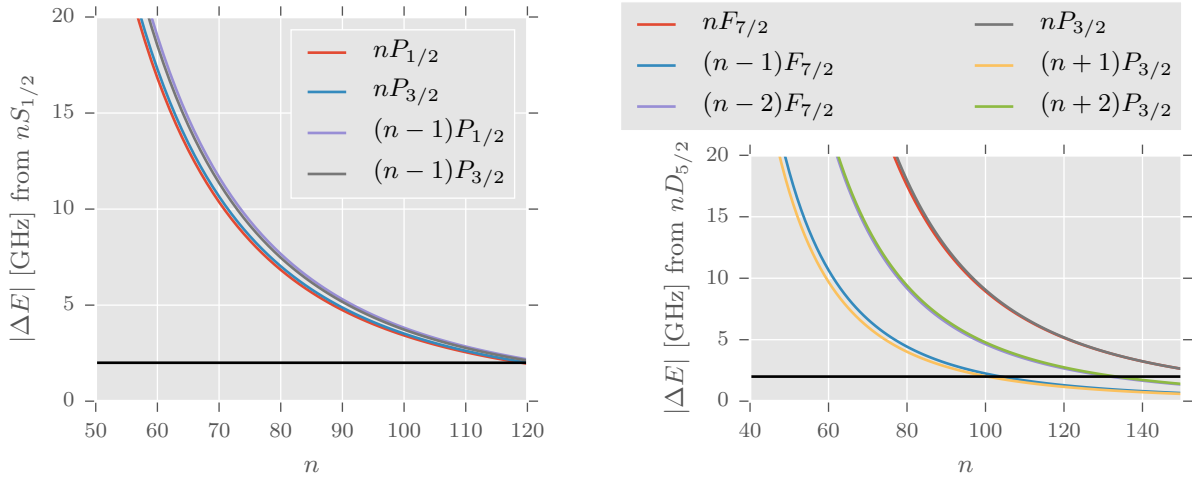
The experimental capabilities of a quantum optics experiment can largely be extended by the ability to produce microwave pulses. With our 20 GHz synthesizer from Anritsu, model MG3692C, two different types of transitions can be driven:

- Magnetic dipole transitions such as the clock transition $5^2S_{1/2}, F = 1 \leftrightarrow F' = 2$ of the Rubidium hyperfine ground states at 6.8 GHz as shown in Section 2.4 and as done in our experiment within Christoph Braun's bachelor thesis [145].
- Electric dipole transitions between Rydberg states, for example $nS_{1/2} \leftrightarrow (n+1)P_{3/2}$.

In general, these transitions can be used for shaping (ground) state potentials by state dressing [191]. That way, microwaves can be used to trap neutral atoms [192, 193] just like optical dipole traps but addressing other transitions. Similarly and just differing in the frequency, RF can be used to achieve the same thing, trapping of neutral atoms [194]. In that case, Zeeman states of one hyperfine state are coupled. However, the RF frequencies are typically in the MHz range and cannot be produced with this device.

Different ground state EIT schemes can be implemented [195] to create different blockade schemes in the future.

Highly interesting are microwaves applied to Rydberg states. RF or millimeter wave sources are excellent to spectroscopically resolve the level structure of Rydberg atoms [196, 197]. By coupling



(a)

(b)

Figure 2.29: Absolute energy difference of closest states to (a) S and (b) D Rydberg states. The S state is energetically higher than the $(n - 1)P$ states and lower than the nP states. Our microwave synthesizer is limited between 2 GHz (black line) and 20 GHz and can thus only drive transitions to states with neighboring principal quantum numbers in a certain range. For higher n , transitions are still possible, but with a higher difference in principal quantum number. In (b), $F_{5/2}$ and $P_{1/2}$ are not plotted for clarity since they almost coincide with their neighboring fine structure states.

the Rydberg states with weak microwave fields, new eigenstates can be tailored [198], even in hollow-core fibers [199]. The highly sensitive response of Rydberg atoms to this electromagnetic field can be exploited to do vector electrometry [200]. The field can lead to the controlled formation of exotic states such as Rydberg atom macrodimers [201]. Microwave-aided creation of states with high angular momenta, so-called circular states [202, 203], can serve as a sensitive electrometer [204]. Of very high relevance to this work is the possibility to tailor the effective probe photon-photon interaction by modifying the coupling of the Rydberg states via microwaves [205].

The frequency limits of the device set constraints on the states which can be coupled. Figure 2.29 gives an overview of principal quantum numbers which are within this technical limit. The plots are based on the optical excitation of Rydberg S and D states. With our frequency limit of 20 GHz we can drive Rydberg transitions of type $nS_{1/2} \leftrightarrow nP_{1/2}$ can be driven for $n \geq 57$. The transition to the other P state $nS_{1/2} \leftrightarrow nP_{3/2}$ is possible at $n \geq 58$. One can also drive transitions like $nS \leftrightarrow (n - 1)P$ with slightly higher transition frequencies: The $nS_{1/2} \leftrightarrow (n - 1)P_{1/2}$ can be reached for $n \geq 59$; the $nS_{1/2} \leftrightarrow (n - 1)P_{3/2}$ can be reached for $n \geq 60$. At $n > 120$, the energy difference becomes smaller than the lower frequency limit of the synthesizer: 2 GHz. In this situation, the microwave can only

couple states with $|n' - n| > 1$.

Slightly other ranges and more states are given for Rydberg D states as can be seen in Figure 2.29b. The first possible state is at $n = 48$.

The synthesizer is programmed with a Python script. It sets the frequency and output power on the device via TCP/IP in our lab network. The values are defined in the computer control GUI and the script loads them from the database each cycle. The synthesizer has different modes of operation. Currently, external pulse modulation is selected. As a result, microwave output is only active during TTL HIGH at the input channel.

3

Rydberg interaction

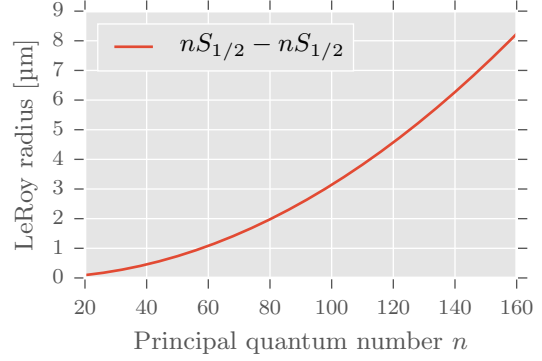
The goal of this chapter is to explain the most fundamental mechanism of this work: interaction between Rydberg atoms. Many core quantities that are in the scope of this thesis such as optical gain, switch contrast, Rydberg detection fidelity and the second order susceptibility of Rydberg EIT $\chi^{(2)}$ rely directly on the interaction between two excited Rydberg states. First, a qualitative description of the interacting system is given to provide an intuitive access to the processes. Then, a detailed theoretical study is carried out for a quantitative analysis, in particular to gain a controlled tunability of the interaction with parameters such as principal quantum numbers and electric fields. Finally, the angular dependence of the interaction is explained. The considerations and results of this chapter are published in reference [3]. Note that our treatment is based on static considerations. That means, for dynamic processes such as photon propagation, more sophisticated theory applies [1, 88, 100].

3.1 INTRODUCTION TO THE PHYSICAL MECHANISMS

The system under consideration contains two Rydberg atoms spatially separated by a distance R which is much larger than the LeRoy radius [206, 207],

$$R_{LR} = 2(\sqrt{\langle n_1 \ell_1 | r^2 | n_1 \ell_1 \rangle} + \sqrt{\langle n_2 \ell_2 | r^2 | n_2 \ell_2 \rangle}) \quad (3.1)$$

Figure 3.1: The LeRoy radius is plotted for two Rubidium atoms in the same S state. It specifies the interatomic distance below which molecular processes take place. Our Rydberg pair potential calculations are valid for larger radii since we neglect these processes. Due to the sum in Equation 3.1, the LeRoy radius of different states (n_1, n_2) can be read from this graph through the arithmetic mean of the radii of (n_1, n_1) and (n_2, n_2) .



a threshold distance related to the Kepler radii of the wave functions. It can be calculated with the formula for the expectation value of the hydrogen atom [208]

$$\langle r^2 \rangle = \frac{n^{*2}}{2} [5n^{*2} + 1 - 3\ell(\ell + 1)] a_0^2 \quad (3.2)$$

by using the effective principal quantum number for the desired Rubidium state. In case both states are the same ($n_1 = n_2 = n, \ell_1 = \ell_2 = \ell$), Equation 3.1 simplifies with Equation 3.2 to

$$R_{LR} = 4(\sqrt{0.5n^{*2}[5n^{*2} + 1 - 3\ell(\ell + 1)]})a_0 \quad (3.3)$$

which is plotted in Figure 3.1 versus n , calculating n^* with Appendix A.

For $\ell_1, \ell_2 > 0$, there is a more accurate definition [209] of the LeRoy radius (Equation 3.1), taking the anisotropy of the wave functions into account.

Below the LeRoy radius, molecular mechanisms have to be accounted for due to the overlap of the wave functions, such as the Fermi exclusion principle and (anti-) symmetrization of the total wave function. Therefore, the potential calculations in this work are only valid for larger distances. Fortunately, Rydberg-Rydberg interaction is strong enough such that the relevant interaction distance can be much larger than the LeRoy radius. For $n = 65$ ($n^* = 61.8688$), the LeRoy radius is $1.28 \mu\text{m}$, whereas the Rydberg blockade radius for our typical experimental parameters is $> 3 \mu\text{m}$. Moreover, the peak atomic density is typically less than $1 \mu\text{m}^{-3}$ which reduces the probability of probing these potentials near $r = 0$.

To calculate the interaction of two Rydberg atoms, we consider the situation depicted in Figure 3.2b. The interaction operator is given by all combinations of $1/r$ Coulomb interactions of the four particles. For large R , the leading term of the remaining operator terms is the interaction between the dipole moments of the atoms. Formally, a multipole expansion of the charge distributions in each

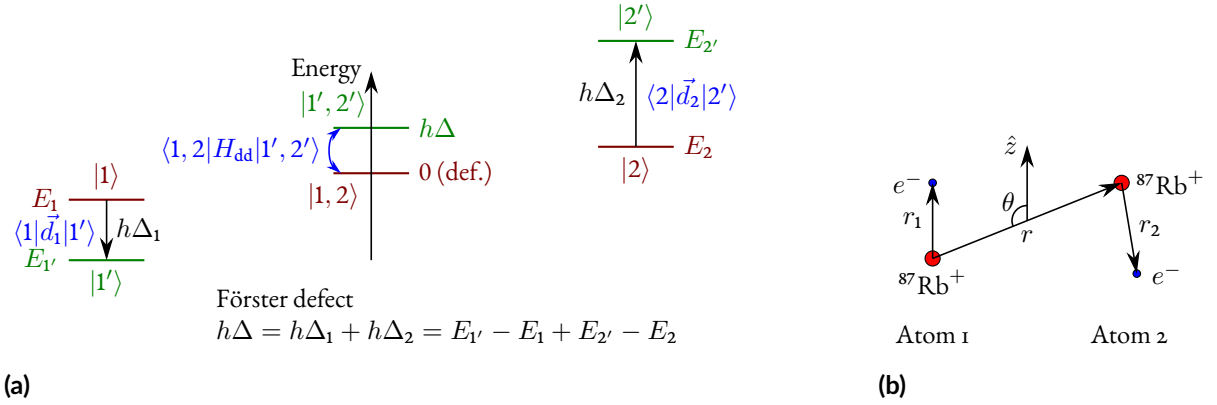


Figure 3.2: (a) The level structure of two Rydberg atoms, prepared in $|1\rangle$ (left) and $|2\rangle$ (right), affects the interaction strength between them by dipole-coupling to other states $|1'\rangle$ and $|2'\rangle$. For low energy differences (Förster defect) Δ of the pair states, the interaction is maximized. (b) Both the distance r between the Rydberg atoms and the angle θ between their inter-atomic axis and the quantization axis \hat{z} determine the interaction strength.

atom leads to several terms in the interaction Hamiltonian corresponding to the interaction of two charges, the interaction of a charge with a dipole, the interaction of two dipoles, and the interaction of combinations of higher modes [210]. In our case, the Rydberg atom is neutral, so the first nonzero and most prominent contribution is of type dipole-dipole. Higher orders are not of particular interest in this work due to the high suppression. However, higher interaction modes can modify interaction potentials. This fact has been treated theoretically [211] and observed experimentally [212]. It is not directly intuitive that an atom that is *initially* in an S state can interact with another atom in an S' state since S -states are isotropic and thus exhibit no permanent dipole moment. But, as the two atoms approach each other, dipole-coupling to close-by $|PP'\rangle$ pair states causes a state mixture as illustrated in Figure 3.2a. Mathematically, this is a consequence of the Hamiltonian matrix

$$H = \begin{pmatrix} 0 & H_{\text{dd}} & H_{\text{dd}} & 0 \\ H_{\text{dd}} & \Delta & 0 & H_{\text{dd}} \\ H_{\text{dd}} & 0 & \Delta & H_{\text{dd}} \\ 0 & H_{\text{dd}} & H_{\text{dd}} & 0 \end{pmatrix} = \begin{pmatrix} 0 & C_3/r^3 & C'_3/r^3 & 0 \\ C_3/r^3 & \Delta & 0 & C'_3/r^3 \\ C'_3/r^3 & 0 & \Delta & C_3/r^3 \\ 0 & C'_3/r^3 & C_3/r^3 & 0 \end{pmatrix} \quad (3.4)$$

in the basis

$$\mathcal{B} = \{|SS'\rangle, |PP'\rangle, |P'P\rangle, |S'S\rangle\}. \quad (3.5)$$

As a result of the dipolar coupling of the pair states, an atom in the initial state $|SS'\rangle$ evolves into a

superposition of new eigenstates and can in general be written as

$$\Psi = \alpha_1 |SS'\rangle + \alpha_2 |PP'\rangle + \alpha_3 |P'P\rangle + \alpha_4 |S'S\rangle \quad (3.6)$$

with $\alpha_1^2 + \alpha_2^2 + \alpha_3^2 + \alpha_4^2 = 1$ for normalization. Note again that the reversed states are not redundant due to the distinguishability of the two individual atoms. So there are four new eigenstates with different α_i . Often, there is one eigenstate with $\alpha_1^2 \approx 1$ and $\alpha_2^2, \alpha_3^2, \alpha_4^2 \approx 0$, so the state might be referred to as SS' state, but the better terminology is *asymptotic SS' state* meaning that the potential corresponds to the pure state SS' for $R \rightarrow \infty$. Following such a potential line to small distances, large positive or negative values are possible due to the R^{-3} dependence of the dipole coupling. Therefore, at very small distances other pair states contribute significantly even if they are far detuned and especially the hydrogenic manifold, a fan of many higher angular momentum states drastically affect the potential shape. The potentials can become so deep such that the strong admixture can lead to a significant redistribution of Rydbers states [70, 211, 213–215] and the attraction can cause Penning ionization [216].

3.2 DERIVATION OF THE INTERACTION STRENGTH

We follow considerations of [211] and aim to diagonalize the Hamiltonian. The dipol-dipole Hamiltonian including the full angular dependence is given by [217]

$$H_{\text{dd}} = \frac{\vec{d}_1 \cdot \vec{d}_2 - 3(\hat{r} \cdot \vec{d}_1)(\hat{r} \cdot \vec{d}_2)}{r^3} \quad (3.7)$$

which we rewrite with scalar operators to

$$H_{\text{dd}} = \frac{d_{1x}d_{2x}(1 - 3 \sin^2 \theta) + d_{1y}d_{2y} + d_{1z}d_{2z}(1 - 3 \cos^2 \theta)}{R^3} - \frac{3 \sin \theta \cos \theta (d_{1x}d_{2z} + d_{1z}d_{2x})}{R^3}. \quad (3.8)$$

We change the basis from cartesian to spherical. So we plug

$$d_{\pm} = \mp \frac{1}{\sqrt{2}}(d_x \pm d_y) \quad (3.9)$$

into the interaction operator and get the important general expression for the anisotropic dipole-dipole operator

$$H_{\text{dd}} = \frac{d_{1z}d_{2z}(1 - 3 \cos^2 \theta) - d_{1+}d_{2-} - d_{1-}d_{2+}}{R^3} - \frac{3 \sin^2 \theta(d_{1+}d_{2+} + d_{1-}d_{2-} - d_{1+}d_{2-} - d_{1-}d_{2+})}{2R^3} - \frac{3 \sin \theta \cos \theta(d_{1-}d_{2z} - d_{1+}d_{2z} + d_{1z}d_{2-} - d_{1z}d_{2+})}{\sqrt{2}R^3}. \quad (3.10)$$

In the following we consider Rydberg states including fine-structure splitting so that specific pair states are characterized by a total of eight quantum numbers

$$|1, 2\rangle = |n_1 \ell_1 j_1 m_1, n_2 \ell_2 j_2 m_2\rangle \quad (3.11)$$

$$|1', 2'\rangle = |n'_1 \ell'_1 j'_1 m'_1, n'_2 \ell'_2 j'_2 m'_2\rangle. \quad (3.12)$$

When evaluating the matrix elements $\langle 1, 2 | H_{\text{dd}} | 1', 2'\rangle$ it becomes clear that it is composed of a sum of terms of the form

$$\langle 1, 2 | d_{1q_1} d_{2q_2} | 1', 2'\rangle = \langle 1 | d_{1q_1} | 1'\rangle \langle 2 | d_{2q_2} | 2'\rangle. \quad (3.13)$$

Each single-atom dipole matrix element $\langle k | d_{iq} | p\rangle$ can be expressed as a product of two factors: a radial part $\tilde{\mu}_{k,p}$ that depends on all quantum numbers except the magnetic quantum numbers m_k , m_p , and an angular factor $\mathcal{C}_{k,p}^q$ which only depends on j_k , m_k , j_p , m_p , and the component index q of the dipole operator. The single-atom matrix element is then written as

$$\langle k | d_q | p\rangle = \tilde{\mu}_{k,p}(n_k, \ell_k, j_k, n_p, \ell_p, j_p) \mathcal{C}_{k,p}^q(j_k, m_k, j_p, m_p), \quad (3.14)$$

where $\mathcal{C}_{k,p}^q$ is a coefficient given by

$$\mathcal{C}_{k,p}^q = (-1)^{j_p - 1 + m_k} \begin{pmatrix} j_p & 1 & j_k \\ m_p & q & -m_k \end{pmatrix} \quad (3.15)$$

with $(:::)$ denoting the Wigner 3- j symbol. The radial factor is given by

$$\begin{aligned} \tilde{\mu}_{k,p} &= (-1)^{j_p + s + 1} \sqrt{(2j_k + 1)(2j_p + 1)(2\ell_k + 1)(2\ell_p + 1)} \\ &\times \begin{Bmatrix} j_k & 1 & j_p \\ \ell_p & s & \ell_k \end{Bmatrix} \begin{pmatrix} \ell_k & 1 & \ell_p \\ 0 & 0 & 0 \end{pmatrix} \int_0^\infty R_k(r) e r R_p(r) r^2 dr \end{aligned} \quad (3.16)$$

where $\{\dots\}$ is a Wigner 6- j symbol and $R_i(r)$ is the radial wave function of state i .

Since the radial factor does not depend on q , it is the same for all terms in a matrix element of the operator defined in Equation 3.10 and therefore can be factored out:

$$\langle 1, 2 | H_{\text{dd}} | 1', 2' \rangle = \frac{\tilde{\mu}_{1,1'} \tilde{\mu}_{2,2'}}{r^3} \left[\left(C_{1,1'}^{\pi} C_{2,2'}^{\pi} (1 - 3 \cos^2 \theta) - C_{1,1'}^{\sigma^+} C_{2,2'}^{\sigma^-} - C_{1,1'}^{\sigma^-} C_{2,2'}^{\sigma^+} \right) \right. \quad (3.17)$$

$$\begin{aligned} & - \frac{3}{2} \sin^2 \theta \left(C_{1,1'}^{\sigma^+} C_{2,2'}^{\sigma^+} + C_{1,1'}^{\sigma^-} C_{2,2'}^{\sigma^-} - C_{1,1'}^{\sigma^+} C_{2,2'}^{\sigma^-} - C_{1,1'}^{\sigma^-} C_{2,2'}^{\sigma^+} \right) \\ & \left. - \frac{3}{\sqrt{2}} \sin \theta \cos \theta \left(C_{1,1'}^{\sigma^-} C_{2,2'}^{\pi} - C_{1,1'}^{\sigma^+} C_{2,2'}^{\pi} + C_{1,1'}^{\pi} C_{2,2'}^{\sigma^-} - C_{1,1'}^{\pi} C_{2,2'}^{\sigma^+} \right) \right] \\ =: & \frac{\tilde{\mu}_{1,1'} \tilde{\mu}_{2,2'}}{r^3} A_{j_1 m_1, j_2 m_2, j_1' m_1', j_2' m_2'}(\theta) =: \frac{C_3(\theta)}{r^3}. \end{aligned} \quad (3.18)$$

The factor $\tilde{\mu}_{1,1'} \tilde{\mu}_{2,2'}$ may vary several orders of magnitude depending on the states used and it is this factor that determines the overall interaction strength given that the angular one is of order unity. The independence of the geometry makes this factor a good measure for the interaction strength. Therefore it is used as a parameter classifying state combinations in Section 3.5.

The angular dependence is contained in the factor $A_{j_1 m_1, j_2 m_2, j_1' m_1', j_2' m_2'}(\theta)$ which depends only on the angular momentum quantum numbers and, for example, its structure will be common to describe the interaction between all pair states with the same numbers. In particular, this part of the Hamiltonian contains all information about the anisotropic character of the interaction. A more detailed discussion of this factor is carried out in section 3.4.

While the dipole-dipole Hamiltonian H_{dd} provides the coupling between different pair states, the atomic part of the Hamiltonian $H_1 + H_2$ determines the initial energy difference $h\Delta$ between the specific pair states as shown in Figure 3.2a. Although the separate energy levels for each of the atoms can be quite different, these levels can result in a small Förster defect in the pair state basis. If such a near-resonance exists, the involved levels can make up the dominant contribution to the dipole-dipole interaction. Therefore, the Hamiltonian which, in principle, is an infinite-dimensional matrix can be approximated by a much smaller matrix, as done in Equation 3.4, where only near-resonant states are involved. A so-called Förster resonance occurs when the energy of two coupled pair states is degenerate, $\Delta = 0$ in Figure 3.2a. This degeneracy results in a resonant coupling between the states leading to a $\sim 1/r^3$ dependence of the interaction.

For a large Förster defect ($|h\Delta| \gg |C_3(\theta)/r^3|$), the dipole-dipole coupling can be understood as a second-order perturbation to the atomic Hamiltonian and the resulting interaction has an $\sim 1/r^6$ dependence [207, 210, 218].

3.3 EXCITATION EXCHANGE

If $\tilde{C}_3, \tilde{C}'_3 > 0$, the flip-flop (*hopping*) process might be possible on resonance ($\hbar\Delta = 0$) as:

$$\begin{array}{ccccc}
 & & |1', 2'\rangle & & \\
 & \tilde{C}_3 \rightarrow & & \tilde{C}'_3 \leftarrow & \\
 |1, 2\rangle & \leftarrow & & \rightarrow & |2, 1\rangle \\
 & \tilde{C}'_3 \leftarrow & & \tilde{C}_3 \rightarrow & \\
 & & |2', 1'\rangle & &
 \end{array}$$

where the result is that the two atoms exchange their internal state as a consequence of dipole-dipole interaction [219]. It is worth noting that, if the two initial single atom states are not fully spin-polarized in the stretched states of equal signs, this process may not swap the Zeeman states. For example, two S -states that undergo this process

$$|n_1 S_{1/2} \downarrow, n_2 S_{1/2} \uparrow\rangle \xleftrightarrow{\tilde{C}_3} |n'_1 P_{1/2} \downarrow, n'_2 P_{1/2} \uparrow\rangle \xleftrightarrow{\tilde{C}'_3} |n_2 S_{1/2} \downarrow, n_1 S_{1/2} \uparrow\rangle \quad (3.19)$$

do not end up in the fully flipped state because the π coupling is the only non-zero term in eqn. (3.17). This simple example shows that while some quantum numbers are exchanged, not the full quantum state is exchanged. In the case where both atoms are in $m = \uparrow$ or both are in $m = \downarrow$, an exchange of the full quantum state is only guaranteed at $\theta = 0$. For non-zero angles, $m_1 + m_2$ is not conserved, as can be nicely seen in eqn. (3.17), so there is a nonzero probability to undergo again a state transition as in eqn. (3.19). If we consider the interaction in the full Zeeman Basis, i.e., we calculate C_3, C'_3 instead of $\tilde{C}_3, \tilde{C}'_3$, then, $C_3, C'_3 \neq 0$ is a sufficient condition for the hopping. However, as described above, because of the different interaction channels for the magnetic quantum numbers, the quantum state may not flip completely. To sum up, the experimental geometry and level structure has to be carefully examined to judge if a *true* state exchange is possible.

In order to quantify the tendency of a pair state to flip into another state we consider a Hamiltonian with a form as in Equation 3.4 on resonance ($\Delta = 0$). The flipping probability after a short time t is given by

$$\begin{aligned}
 \langle 2, 1 | e^{-iHt/\hbar} | 1, 2 \rangle &\approx \langle 2, 1 | 1 - iHt/\hbar - H^2 t^2 / 2\hbar^2 | 1, 2 \rangle \\
 &= -t^2 / 2\hbar^2 \langle 2, 1 | H^2 | 1, 2 \rangle \\
 &= C_3 C'_3 (-t^2 / \hbar^2 r^6).
 \end{aligned}$$

This motivates the definition of a *hopping coefficient* given by $C_3 C'_3$. Again, this term includes the angular and radial factors and we can define a *radial hopping coefficient* by $\tilde{C}_3 \tilde{C}'_3$. We plot this coefficient for SS , SD and DD combinations in figures 3.4d, 3.5d and 3.6d respectively. It is striking that this

quantity may vary over ten orders of magnitude depending on the choice of states.

When choosing a Rydberg pair state for performing a specific experiment, both the coupling strength and the radial hopping coefficient should be taken into account. For example, for an energy transfer experiment, it is desirable to have strong coupling together with strong hopping. However, for an experiment involving interaction-enhanced imaging where hopping is not desirable, a strongly coupled pair state with reduced hopping can be chosen.

3.4 ANISOTROPIC INTERACTION

The angular dependence of the interaction between Rydberg atoms is certainly an enriching property, which has been exploited experimentally [4, 220]. Here, we analyze the highly anisotropic character close to a Förster resonance [77].

In order to understand the angular behavior of the interaction, we consider the case where $\tilde{C}'_3 \approx 0$ while $\tilde{C}_3 \neq 0$ in which the hopping dynamics described in subsection Section 3.3 are not present. Furthermore, the magnetic sub-levels do not couple to each other under this condition and the Hamiltonian matrix has the general form

$$H = \begin{pmatrix} 0 & \vec{C}_3^T \\ \vec{C}_3 & \text{diag}(h\vec{\Delta}) \end{pmatrix}$$

where the first element of the basis is the initial state $|1, 2\rangle$ with fixed values of j_1, m_1, j_2 and m_2 and the following ones are all the magnetic substates of energetically close pair state $|1', 2', p\rangle$. Here, p indexes all the possible values of m'_1 and m'_2 . Also, the components of \vec{C}_3 are $C_3^p = \langle 1, 2 | H_{\text{dd}} | 1', 2', p \rangle$ which are calculated using eq. 3.18. Furthermore, $\text{diag}(h\vec{\Delta})$ is a diagonal matrix with entries given by $h\Delta_p$ which is the energy of the level $|1', 2', p\rangle$ with the energy origin set to that of the $|1, 2\rangle$ state. It is worth noting that the θ -dependence is completely contained in \vec{C}_3 .

For the sake of concreteness we consider an initial state $|S_{1/2}^1, \uparrow, S_{1/2}^2, \uparrow\rangle$ and a neighboring $|P_{1/2}^1, m_P^1, P_{1/2}^2, m_P^2\rangle$ pair state as shown in Fig. 3.3. For this case, the Hamiltonian matrix takes the form

$$H = \begin{pmatrix} 0 & C_3^{\downarrow\downarrow}/r^3 & C_3^{\downarrow\uparrow}/r^3 & C_3^{\uparrow\downarrow}/r^3 & C_3^{\uparrow\uparrow}/r^3 \\ C_3^{\downarrow\downarrow}/r^3 & h\Delta_{\downarrow\downarrow} & 0 & 0 & 0 \\ C_3^{\downarrow\uparrow}/r^3 & 0 & h\Delta_{\downarrow\uparrow} & 0 & 0 \\ C_3^{\uparrow\downarrow}/r^3 & 0 & 0 & h\Delta_{\uparrow\downarrow} & 0 \\ C_3^{\uparrow\uparrow}/r^3 & 0 & 0 & 0 & h\Delta_{\uparrow\uparrow} \end{pmatrix},$$

where the C_3 coefficients depend on θ and the energy defects depend on the magnitude of the elec-

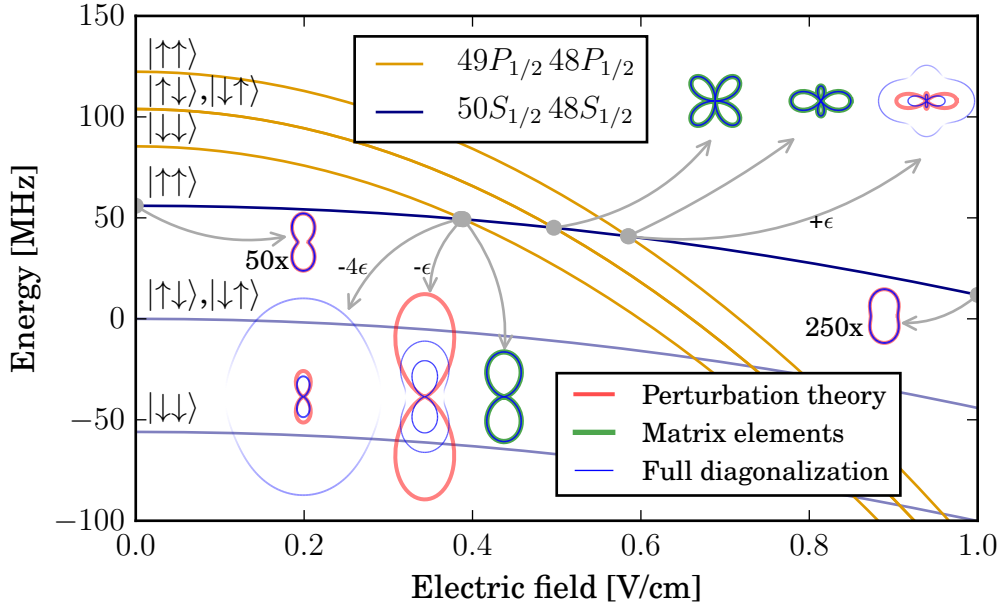


Figure 3.3: Angular dependence of the dipole-dipole interaction. The pair state energies of the $|50S_{1/2} \uparrow, 48S_{1/2} \uparrow\rangle$ and $|49P_{1/2} m_1, 48P_{1/2} m_2\rangle$ states are shown as a function of electric field subject to a magnetic field of 20 G parallel to the electric field. Strong θ -dependent dipole coupling between the pair states leads to a set of new eigenstates with θ -dependent eigenenergies. The green polar plots (horizontal axis is $\theta = 0$) show the respective coupling matrix elements. The eigenenergies are shown in the blue polar plots and the projection of new eigenstates onto the initial state is encoded in the line opacity. The exact diagonalization coincides with the matrix elements on the resonances and with the perturbative calculation far from resonance. As the Förster defect increases (leftmost and rightmost polar plots), the interaction energy is reduced, so we enlarge the plots by a factor of 50 and 250 as indicated. The plots next to the matrix element plots are slightly off resonance by an amount indicated in the arrow, where $\epsilon = 1 \text{ mV/cm}$. The dipole coupling was calculated at a distance of $r = 1.5 \mu\text{m}$.

tric field and magnetic field. Here we consider only the case where the state mixing caused by the electric field is negligible.

Applying an external magnetic field causes the Förster defects $h\Delta_p$ of each of the magnetic sub-states to be different. As a result, several closely-spaced Förster resonances appear. The resulting eigenvalues of the Hamiltonian, which give the interaction potential, will have contributions of varying importance that arise from the various angular factors and therefore, the shape of the interaction will depend on the external electric field.

On resonance with a specific state p_0 , the angular dependence will be predominantly determined by the $C_3^{p_0}(\theta)$ factor. By changing the electric field, the angular dependence of the interaction will also change because the weight of the different angular contributions is also modified.

However, as is the case with the radial dependence of the interaction, exactly on resonance there is no single eigenvalue that can be identified as the interaction potential for atoms in the initial pair state. In fact, there are two such eigenvalues $\pm C_3^{p_0}(\theta)/r^3$ whose corresponding eigenvectors

$$\frac{1}{\sqrt{2}} (|1, 2\rangle \pm |1', 2', p_0\rangle),$$

have a significant overlap with the initial pair state as illustrated in Fig. 3.3. Here, both eigenvalues are shown (blue). They overlap with each other, as well as with the matrix elements (green). On the other hand, in the vicinity of the resonance, these two eigenvalues become different as seen in the plots indicated with -4ϵ , $-\epsilon$, and $+\epsilon$. While exactly on resonance the two eigenstates corresponding to these eigenvalues have a 50% overlap with the initial pair state, away from resonance the overlap of one of the eigenstates increases while the other decreases. The result of this is that away from resonance one eigenvector can be well identified with the initial pair state as the case shown in the polar plots corresponding to 0 V/cm and 1 V/cm.

Far from resonance (when $|C_3^p(\theta)/r^3| \ll |h\Delta_p|$), second order perturbation theory can be used and the interaction potential is given by

$$V(r, \theta) = - \sum_p \frac{(C_3^p(\theta))^2}{r^6 h\Delta_p}, \quad (3.20)$$

where it is evident how the different defects Δ_p give different weighting to the various angular factors resulting in an E-field dependent anisotropy of the interaction. The perturbation theory results are shown in Fig. 3.3. While far from resonance they have a very good agreement with the eigenvalues, close to resonance this approximation breaks down. The shape of the interaction changes the most in the vicinity of the Förster resonance where the perturbative treatment is not valid.

It is clear from Fig. 3.3 that by adjusting the electric field, the anisotropy of the interaction can be tuned from a side-by-side interaction (resonance at lowest E-field) to a head-to-tail interaction (resonance at highest E-field). These multi state resonances thus greatly increase the tunability of the angular shape of the Rydberg interaction additionally to the significant boost of the interaction strength.

3.5 THEORETICAL ISOLATION OF STRONG FÖRSTER RESONANCES

The quest of Förster resonances shall be done in three steps: finding pair states with similar energies, determining the magnitude of their interaction, check if excitation hopping is possible and tuning the pair state to resonance. In the following, these steps are described in an instructive, hands-on way.

3.5.1 RESONANCES WITH LOW ZERO-FIELD FÖRSTER DEFECTS.

Let $|n_1\ell_1j_1, n_2\ell_2j_2\rangle$ be our initially prepared pair state and $|n'_1\ell'_1j'_1, n'_2\ell'_2j'_2\rangle$ a nearby pair state with energies E, E' respectively calculated according to Appendix A. The vastness of states is to be reduced by limiting the range of the 12 quantum numbers. From a practical viewpoint, we reduce our initial state combinations to the ones that are experimentally possible such as combinations of S -, P - and D -states. We will create calculated sets of resonances between (different) S -states, between different D -states and between SD -state combinations. Once the initial state is chosen according to the experiment, the selection rules for the dipole operator drastically reduce the set of primed quantum numbers, for instance

- $|n_1S_{1/2}, n_2S_{1/2}\rangle$ couples to $\ell'_1, \ell'_2 = P$ with $J'_1, J'_2 = 1/2, 3/2$ only.
- $|n_1S_{1/2}, n_2D_{5/2}\rangle$ couples to $\ell'_1 = P$ with $J'_1 = 1/2, 3/2$, and $\ell'_2 = P, J'_2 = 3/2$ or $\ell'_2 = F, J'_2 = 5/2, 7/2$ only.
- ...

With such constraints, we can already collect all pair state combinations with a zero-field Förster energy defect of less than $\Delta E_{cut} = 10$ GHz and for principal quantum numbers between 30 and 100 on a regular computer, although the most interesting or experimentally feasible resonances will be at smaller energy defects. The large set is still very useful, in particular to calculate far off-resonant coupling strengths such as C_6 coefficients and blockade radii for SS interaction. For initial states of type $|\ell_1 = S, \ell_2 = S\rangle$, we find 5305 such resonances, for resonances of type $|\ell_1 = S, \ell_2 = D\rangle \leftrightarrow |\ell'_1 = P, \ell'_2 = P\rangle$, we find 21590 resonances, and 43972 if we include $\ell'_2 = F$ target states. More reductions apply if the initial state is in a well-known Zeeman state. For example, due to total angular momentum conservation $\Delta M = m_1 + m_2 - (m'_1 + m'_2) = 0$, the initial state

$|n_1 S_{1/2} m_1 = 1/2, n_2 D_{5/2} m_2 = 5/2\rangle$ is not coupled to $|n'_1 P_{1/2}, n'_2 P_{3/2}\rangle$ with any m'_1, m'_2 , whereas the initial state $|n_1 S_{1/2} m_1 = 1/2, n_2 D_{5/2} m_2 = -5/2\rangle$ couples to that state. Similarly, a $D_{5/2} m = \pm 5/2$ state is not dipole coupled to a $P_{1/2}$ state. Since we would like to make a most general analysis here, we do not restrict to specific magnetic quantum numbers.

3.5.2 DETERMINATION OF THE INTERACTION STRENGTH.

Due to the anisotropic character of the interaction potentials, our aim is to provide the strength of the interaction of the atoms in $|1, 2\rangle$ in terms of a *radial coupling factor*

$$\begin{aligned}\tilde{C}_3 &= \tilde{\mu}_{1,1'} \tilde{\mu}_{2,2'} \\ \tilde{C}'_3 &= \tilde{\mu}_{1,2'} \tilde{\mu}_{2,1'}.\end{aligned}$$

As shown in Section 3.3, there are two possible interaction paths which may differ significantly in strength. Note that for specific magnetic quantum numbers and a certain experimental geometry (angle θ), this quantity is to be multiplied with the angular part to obtain the full interaction energy, see Equation 3.17. Without this angular part, we can classify state combinations according to their interaction properties.

The values for $\tilde{\mu}_{k,p}$ are calculated using Equation 3.16 with radial wave functions derived with a model potential experienced by the Rydberg electron arising from the (shielded) ionic core, according to references [221, 222].

For high precision and reduction of memory usage, it is worth doing these calculations in atomic units. The conversion factor from atomic units to SI units is

$$\frac{C_3[\text{GHz um}^3]}{C_3[\text{au}]} = \frac{(ea_0)^2}{4\pi\epsilon_0 h} \times 10^{3 \times 6 - 9} = \frac{(ea_0)^2}{4\pi\epsilon_0 h} \times 10^9. \quad (3.21)$$

We calculate the coefficients $\tilde{C}_3, \tilde{C}'_3$ for each of the previously found near-resonant pairs. If both coefficients are almost zero, the pair combination is not of particular interest and we remove it from our data set. That way, we obtain the results. In Figure 3.4, Förster resonances between two S states are displayed. Figure 3.5 shows the results for a combination of S and D states, and Figure 3.6 shows the case for two D states. There is a lot of information, so we take advantage of color, opacity and marker type for a better interpretation of the data. In panel a) of the figures, the Förster defect Δ is plotted versus one of the principal quantum numbers (n_1). We need another dimension to give information about the other principal quantum number, so we use the color to encode the difference $\Delta_n = n_2 - n_1$. Additionally, plot c) gives this principal quantum number information on the figure

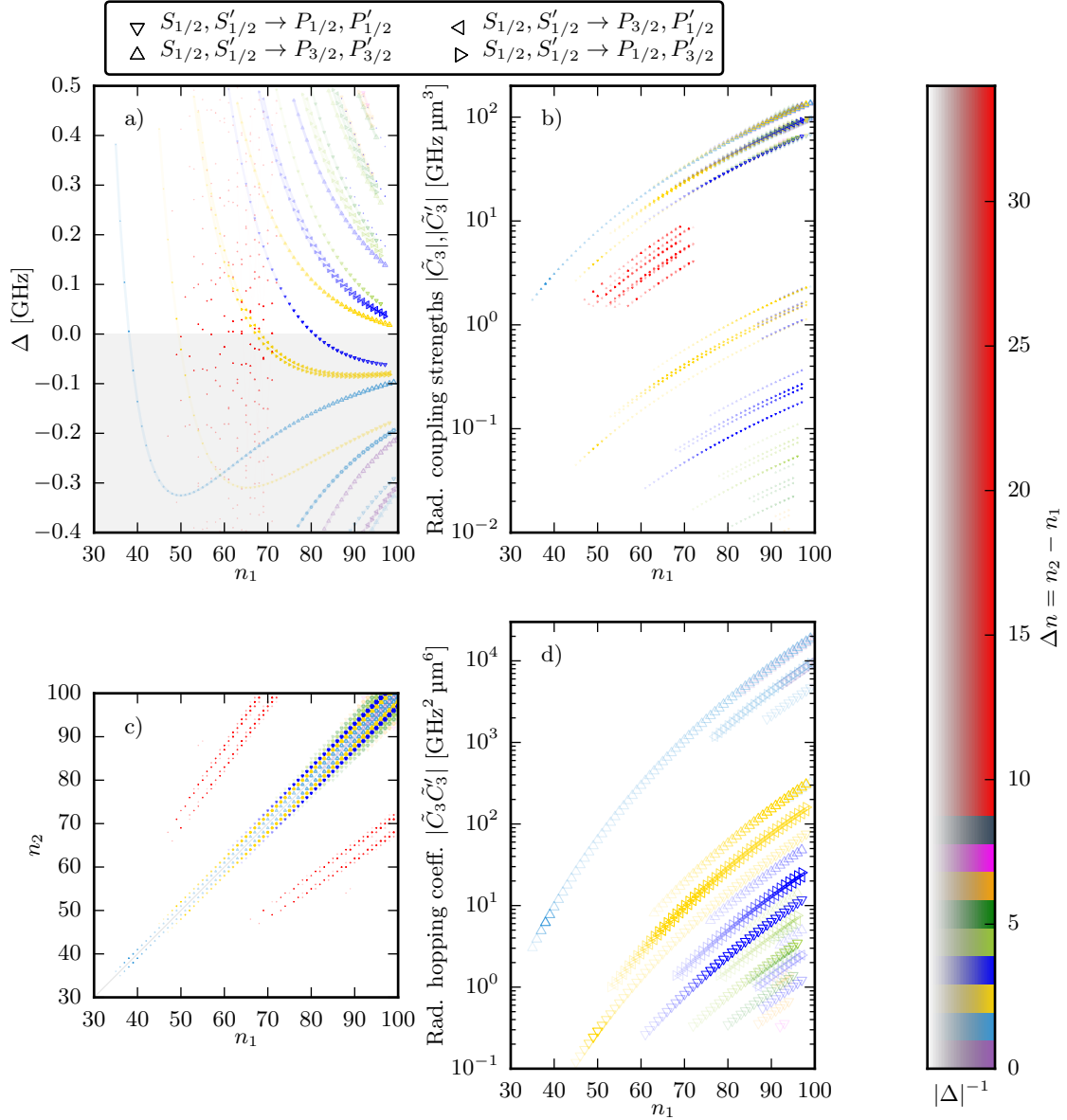


Figure 3.4: Interaction properties between two Rydberg atoms initially in an SS' -state. Each state combination results in two data points in these figures, one corresponding to \tilde{C}_3 and one for \tilde{C}'_3 . Plots are shown as a function of principal quantum number of the first atom n_1 while n_2 is encoded in the color of each data point. The opacity of the points represents the Förster defect, where a higher opacity is used for a smaller defect. In plots a), b), and c), the area of each point is proportional to \tilde{C}_3 or \tilde{C}'_3 accordingly. a) Förster defect as a function of n_1 . Lines are a guide to the eye and relate similar states which only differ in n_1 . The $\Delta < 0$ region is grayed out because it is not accessible using a static electric field. b) Radial coupling constants as a function of n_1 . c) Overview of all SS' -states. The visibility of the points depends on both having a small defect and a significant radial coupling constant. d) Hopping coefficient as a function of n_1 .

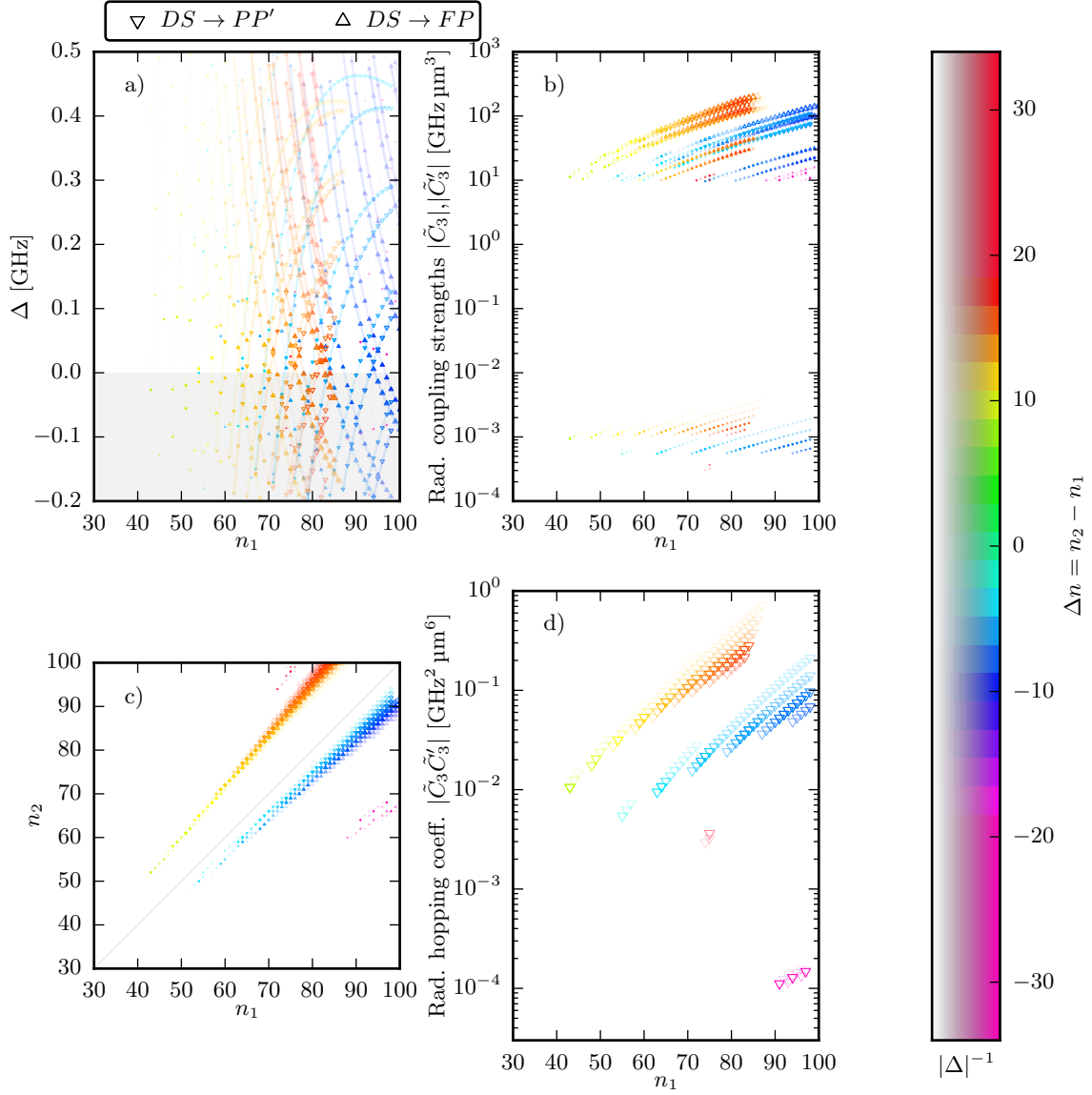


Figure 3.5: Interaction properties between two Rydberg atoms initially in an SD -state. Each state combination results in two data points in these figures, one corresponding to \tilde{C}_3 and one for \tilde{C}'_3 . Plots are shown as a function of principal quantum number of the first atom n_1 while n_2 is encoded in the color of each data point. The opacity of the points represents the Förster defect, where a higher opacity is used for a smaller defect. In plots a), b), and c), the area of each point is proportional to \tilde{C}_3 or \tilde{C}'_3 accordingly. a) Förster defect as a function of n_1 . Lines are a guide to the eye and relate similar states which only differ in n_1 . The $\Delta < 0$ region is grayed out because it is not accessible using a static electric field. b) Radial coupling constants as a function of n_1 . c) Overview of all SD -states. The visibility of the points depends on both having a small defect and a significant radial coupling constant. d) Hopping coefficient as a function of n_1 .

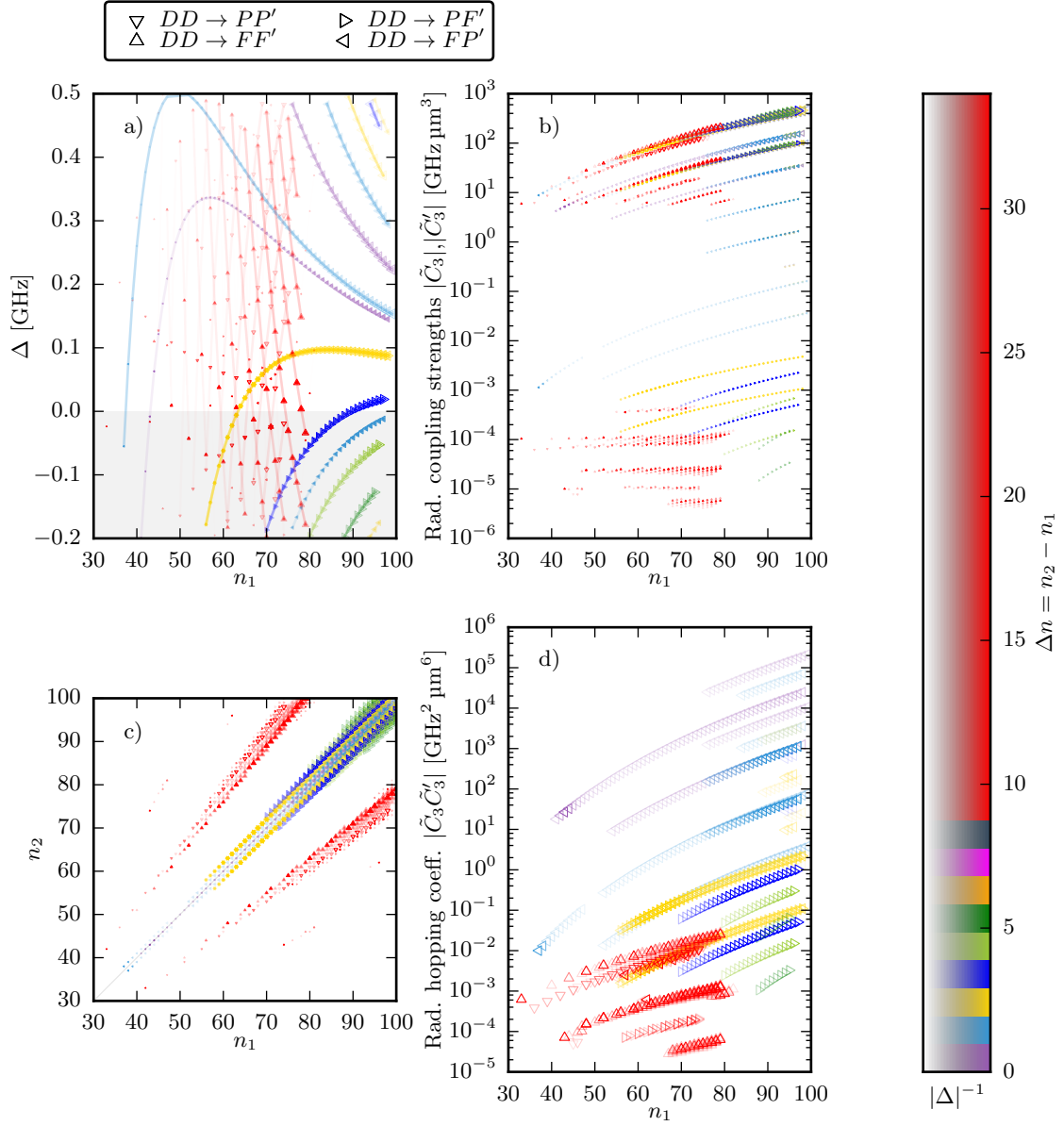


Figure 3.6: Interaction properties between two Rydberg atoms initially in an DD' -state. Each state combination results in two data points in these figures, one corresponding to \tilde{C}_3 and one for \tilde{C}'_3 . Plots are shown as a function of principal quantum number of the first atom n_1 while n_2 is encoded in the color of each data point. The opacity of the points represents the Förster defect, where a higher opacity is used for a smaller defect. In plots a), b), and c), the area of each point is proportional to \tilde{C}_3 or \tilde{C}'_3 accordingly. a) Förster defect as a function of n_1 . Lines are a guide to the eye and relate similar states which only differ in n_1 . The $\Delta < 0$ region is grayed out because it is not accessible using a static electric field. b) Radial coupling constants as a function of n_1 . c) Overview of all DD' -states. The visibility of the points depends on both having a small defect and a significant radial coupling constant. d) Hopping coefficient as a function of n_1 .

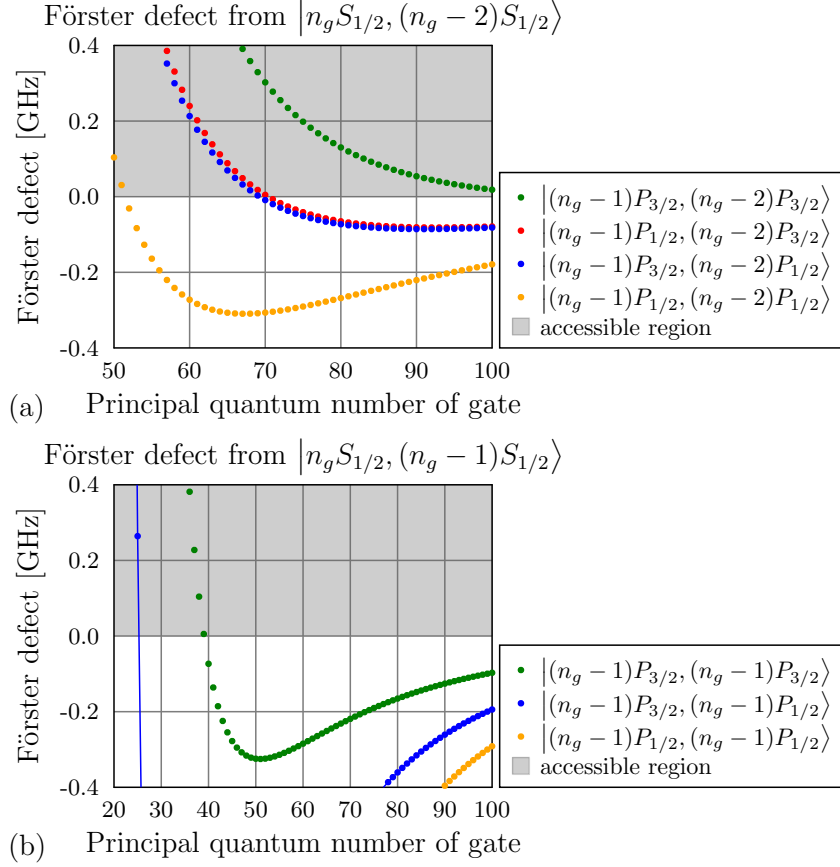


Figure 3.7: The panels show that certain combinations of quantum numbers lead to low Förster defects over wide ranges of the principal quantum number. This is an alternative technique to find Förster resonances. States in the gray shaded region can be tuned to resonance with an electric field.

axes. Coming back to panel a), there is a huge amount of pair state combinations which are close to resonance at zero field. To suppress weak resonances in the plot, the marker size is chosen proportional to \tilde{C}_3 or \tilde{C}'_3 . The marker type gives further information about the coupled states. In Figure 3.4a), where only P states are possible, it depicts the angular quantum numbers, whereas in Figure 3.5a) and Figure 3.6a) the marker type is to discriminate between coupled P and F state combinations. The lines between the points depict systematics of the relations between the quantum numbers. For example, in Figure 3.4, $n_2 = n_1 + 1$ (cyan) couples to $|n'_1 = n_1, P_{3/2}; n'_2 = n_1, P_{3/2}\rangle$ with a resonance close to zero Förster defect at $n_1 = 38$. This is actually a *famous* resonance, used in [72]. For clarity, there are two separate plots in Figure 3.7 which show some of these kinds of resonances. Only the Förster defect is visible there. Investigating such resonances, which have a constant relation between the principal quantum numbers, and a small Förster defect over a wide range of n_1 , is a reasonable approach which

has been followed earlier [218, 223]. In our approach, we can find all resonances, especially the ones with a high Δn .

Panel b) of the three figures quantifies the interaction with our radial coupling strength parameters. To distinguish between the Förster defect, the marker opacity is chosen such that pronounced points are close to resonance at zero field.

Finally, panel d) gives information about the probability of state exchange (hopping).

Our brute force method adds value: there are surprisingly strong resonances in $n_1 D_{5/2}, n_2 D_{5/2}$ state combinations with $n_2 - n_1 \gg 1$ which have not been reported before, to our best knowledge. For instance, a strong zero field resonance occurs at

$$|78D_{5/2}, 99D_{5/2}\rangle \longleftrightarrow |77F_{7/2}97F_{7/2}\rangle, \quad (3.22)$$

where $\tilde{C}_3 = 206 \text{ GHz } \mu\text{m}^3$, $\tilde{C}'_3 \approx 0 \text{ GHz } \mu\text{m}^3$ and $\Delta = 3 \text{ MHz}$, which is approximately as strong as the strongest resonance with small Δn

$$|78D_{5/2}, 80D_{5/2}\rangle \longleftrightarrow |79P_{3/2}79F_{7/2}\rangle, \quad (3.23)$$

for which $\tilde{C}_3 = 184 \text{ GHz } \mu\text{m}^3$, $\tilde{C}'_3 \approx 0 \text{ GHz } \mu\text{m}^3$ and $\Delta = 92 \text{ MHz}$. The latter is not resonant at zero field, so the choice of a large difference in principal quantum numbers greatly increase the available options for accessing a Förster resonance and is even the only possibility if no electric field control is available. Additionally, even if an experiment can control electric fields, zero-field resonances can be preferred because the Stark admixture of other states which originates in finite electric fields can be an undesired disturbance. Second, tuning to high electric fields requires increased precision due to the quadratic order of the Stark shift. Third, these combinations are particularly interesting for Rydberg transistors [3, 5, 224] and interaction-enhanced imaging [96, 97], where the desired situation is a maximized interaction between two different states (source: $78D$, gate: $99D$), and minimized interaction between atoms in the low state ($78D, 78D$). Strong interaction between two gate photons can be advantageous if explicitly one excitation shall be present in the medium. A second excitation would be subject to Rydberg blockade.

3.5.3 TUNING STATES TO RESONANCE.

The atomic energy spectrum is an intrinsic property which cannot be changed. What can be changed, is the eigenstate of an atom. It is affected by external perturbations such as d.c. and a.c. electric and magnetic fields, the Stark and Zeeman effect respectively.

ELECTRIC FIELD TUNING

The high polarizability of Rydberg states offers large energy shifts at fields which can be produced in the laboratory conveniently for a certain range in principal quantum numbers. Electrically tuning these states to resonance has been observed [51, 70, 74]. Due to the n^7 scaling of the d.c. Stark shift [59], the magnitude of the energy shift is very sensitive to the principal quantum number. While our precise voltage source can shift the $40S$ state by -90 MHz at 10 V which produces a field of $\epsilon_y = 4.1 \text{ Vcm}^{-1}$, the $100S$ state is shifted by the same energy already at an electrode voltage of 0.37 V which corresponds to 0.15 Vcm^{-1} . The absolute limit for practical use of Stark shifts is given by the ionization threshold. For $100S$, this already occurs at 3 Vcm^{-1} [142] which is achieved at 7.3 V. A second and more restrictive limit is given by the electric fields that evoke state crossings and mixing with the hydrogenic manifold. It is possible to apply larger electric fields, but the cleanliness and controllability of the system suffers if the state is significantly admixed.

The question if a pair state combination can be tuned to resonance, depends on the sign of the Förster defect Δ at zero field and on the values of the single atom electrostatic polarizabilities α_1 of $|1\rangle$, α_2 of $|2\rangle$, α'_1 of $|1'\rangle$ and α'_2 of $|2'\rangle$. Since the Stark shifts of the atomic states in an electric field ϵ are, at least for S and P states, given by $E_i^{\text{Stark}} = -\alpha_i \epsilon^2$, the Förster defect can be changed as

$$\Delta = \sum_{i \in \{1', 2'\}} (E_i - \alpha_i \epsilon^2) - \sum_{i \in \{1, 2\}} (E_i - \alpha_i \epsilon^2) = E_{1'} + E_{2'} - (E_1 + E_2) - (\alpha_{1'} + \alpha_{2'} - \alpha_1 - \alpha_2) \epsilon^2. \quad (3.24)$$

So, if $\Delta > 0$ at $\epsilon = 0$, the state combination can only be tuned to resonance if

$$\alpha_{1'} + \alpha_{2'} > \alpha_1 + \alpha_2 \quad (3.25)$$

which is the case in Chapter 6. Likewise, if $\Delta < 0$ at $\epsilon = 0$, the state combination can only be tuned to resonance if

$$\alpha_{1'} + \alpha_{2'} < \alpha_1 + \alpha_2. \quad (3.26)$$

Simply speaking, the lower pair state should have lower polarizabilities than the upper state, otherwise, there is no energy degeneracy.

For D states and for higher angular momentum, the Stark shift needs to be calculated by diagonalizing the Stark Hamiltonian.

A practical description of electric tuning of Förster resonances is given in Chapter 6.

In Table 3.1, some electric field values are listed for a series of resonances to give a quick reference.

initial SS' state	coupled PP' state	e-field of resonance
$ 66S_{1/2}, 64S_{1/2}\rangle$	$ 65P_{3/2}, 64P_{3/2}\rangle$	480(10) mVcm ⁻¹
$ 70S_{1/2}, 68S_{1/2}\rangle$	$ 69P_{3/2}, 68P_{3/2}\rangle$	330(10) mVcm ⁻¹
$ 80S_{1/2}, 78S_{1/2}\rangle$	$ 79P_{3/2}, 78P_{3/2}\rangle$	130(10) mVcm ⁻¹
$ 90S_{1/2}, 88S_{1/2}\rangle$	$ 89P_{3/2}, 88P_{3/2}\rangle$	55(1) mVcm ⁻¹
$ 100S_{1/2}, 98S_{1/2}\rangle$	$ 99P_{3/2}, 98P_{3/2}\rangle$	22(1) mVcm ⁻¹
$ 110S_{1/2}, 108S_{1/2}\rangle$	$ 109P_{3/2}, 108P_{3/2}\rangle$	2.5(1) mVcm ⁻¹
$ 111S_{1/2}, 109S_{1/2}\rangle$	$ 110P_{3/2}, 109P_{3/2}\rangle$	no crossing

Table 3.1: Electric fields for a series of Förster resonances. The corresponding Förster defects are depicted in green in Figure 3.7(a). The Zeeman shift due to a magnetic field of 1 G is taken into account. All three resulting different Zeeman state combinations, which are coupled to the SS' state in a head to tail configuration with $m_1 = m_2 = \frac{1}{2}$, lie within the precision of the given values.

MAGNETIC FIELD TUNING

The Zeeman effect can be used to tune the pair state energies, as shown in Figure 3.8. This is a good method for low principal quantum numbers, where the electrostatic polarizability is low, or also for high n if no electric field control is available.

Most effective tuning occurs if the magnetic quantum numbers differ. As can be seen in Figure 3.8, the dashed line has the first crossing with the prepared state (red). However, coupling between $|m_1 = \frac{1}{2}, m_2 = \frac{1}{2}\rangle$ and $|m'_1 = -\frac{1}{2}, m'_2 = -\frac{1}{2}\rangle$ is only nonzero for nonzero angles θ between the interatomic axis and the quantization axis, for example in a side-by-side configuration.

Although the experiment was designed to be quasi-1D, there are measurements in Chapter 6 where the blockade radius is on the order of the beam waist (low n). In such a situation, these kind of resonances can help to increase the radial blockade radius beyond the beam waist.

RADIOFREQUENCY OR MICROWAVE TUNING

It is possible to tune pair states into Förster resonances by microwave dressing [191, 205, 225]. In that case, the sign of the Förster defect is unimportant. Although deep explanations are beyond the scope of this thesis, this is a powerful technique which can be taken into account for future experiments.

Since many states around $|90S, 90S\rangle$ are dominated by a Förster resonance with slightly lower energy,

$$|nS_{1/2}, nS_{1/2}\rangle \leftrightarrow |nP_{3/2}, (n-1)P_{3/2}\rangle \quad (3.27)$$

with $\Delta = -296$ MHz for $90S, 90S$, an easy experiment could be to tune to this resonance in a single EIT experiment. One would expect an increased optical nonlinearity. For the microwave dressing of the single atoms, the neighboring $P_{1/2}$ and $P_{3/2}$ states are (4.7 to 5.3) GHz away, which is easily

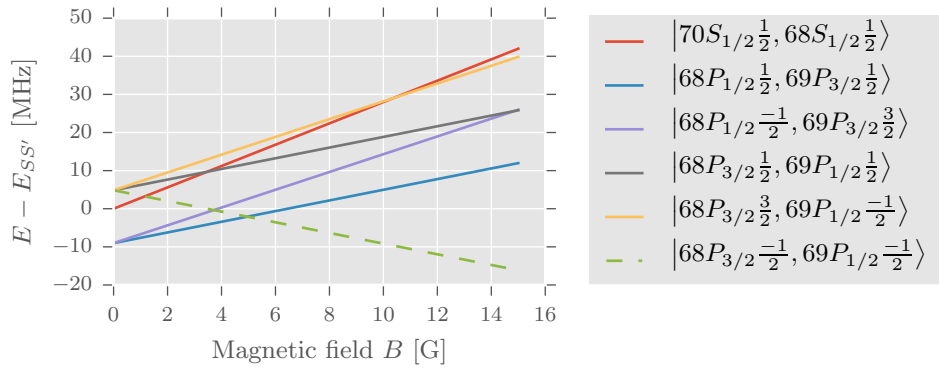


Figure 3.8: Pair states can be tuned to Förster resonances with magnetic fields. In this example, Förster resonances occur at 3.5 G and 10 G. Here, the solid lines depict P states which are coupled in a head to tail configuration ($\theta = 0$). The dashed line corresponds to one of many pair states which only interact with the SS' state for finite inter-atomic angles $\theta > 0$. This anisotropy can be exploited to customize the interaction geometry. Also, note that the resonance with the dashed line occurs much earlier than the others due to the different sign of the shift. Especially at low principal quantum numbers, magnetic pair state tuning can be advantageous.

achievable with our microwave synthesizer in Section 2.10.7.

For comparison, $|50S, 50S\rangle \leftrightarrow |50P_{3/2}, 49P_{3/2}\rangle$ is off by $\Delta = -2.37$ GHz. The neighboring $P_{1/2}$ and $P_{3/2}$ states are 30 GHz away.

3.6 INTERACTION OF TWO RYDBERG ATOMS WITH THE SAME STATE

A very interesting special case which is actually contained in the previous data, is to consider the interaction between two atoms in the same state: $|nS, nS\rangle$. This case is the most relevant one occurring in all Rydberg experiments. The Förster defects and interaction strengths are plotted in Figure 3.9. While there are only tiny zero-field Förster resonances, it is evident that the interaction is dominated by a group of P states with respective angular momentum combinations of $J = 1/2$ and $J = 3/2$ which has a negative Förster defect. With increasing n , these resonances approach $\Delta = 0$, which is the reason that high Rydberg states interact very strongly.

An interesting experiment would be to tune these resonances away by applying an electric field.

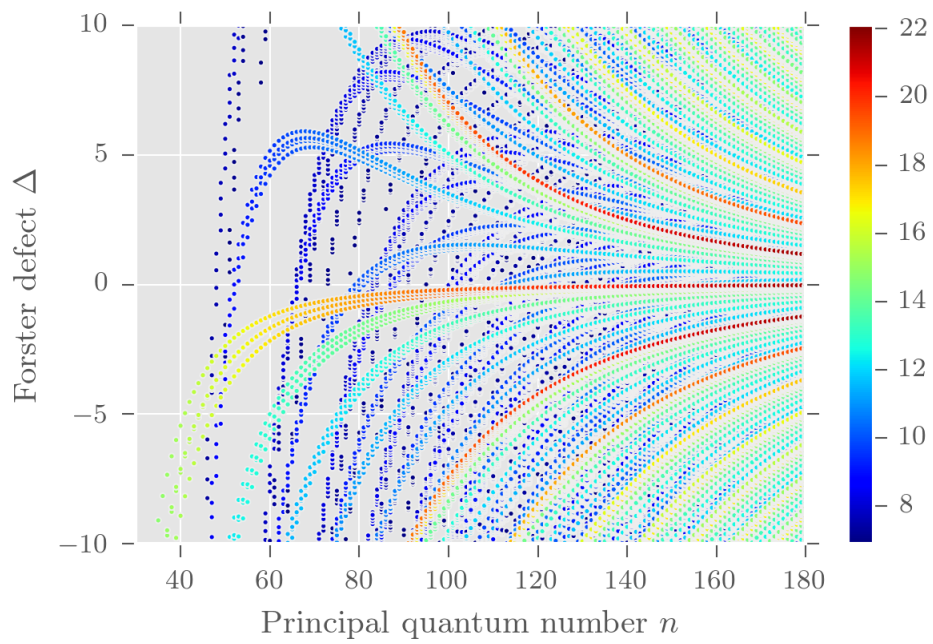


Figure 3.9: Interaction between Rydberg atoms with the same nS state. The logarithms of the radial coupling constants (in $\text{Hz}\mu\text{m}^3$) are encoded in the color. The interaction is dominated by P state contributions which approach $\Delta = 0$ for large n causing the interaction strength to increase with n .

4

Giant optical nonlinearities with Rydberg-EIT

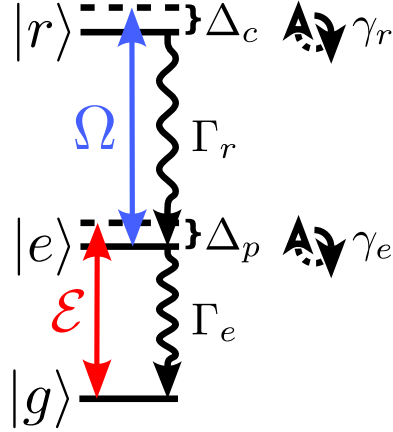
This chapter treats the way interaction between Rydberg states is mapped on the excitation light field. We start by understanding the three-level atom with a concise theory part, which is followed by different EIT measurements that show the properties of the system. Finally, measurements are presented that show how Rydberg blockade evidently mediates interaction between probe photons. This ultimately leads to a huge nonlinearity in the transmission.

4.1 SIMULATING THE OPTICALLY DRIVEN THREE-LEVEL ATOM

This section sketches the theoretical treatment of the three-level atom driven by two light fields (probe and control). The results presented are based on the review [226], which elaborates on the physical foundations of this model. The main purpose of this section is to provide information about the model used to describe EIT. It is important to note that interaction between Rydberg states is not treated in this theory. As a consequence, the theory only applies in cases where Rydberg blockade is suppressed: at low probe photon rates and/or low Rydberg states and/or high control Rabi frequencies.

The coupled three-level system, as sketched in Figure 4.1, is governed by the Hamiltonian (in fre-

Figure 4.1: Level scheme and terminology for the three level atom. The ground state $|g\rangle$ is coupled to the excited state $|e\rangle$ by the probe laser with Rabi frequency \mathcal{E} . The control laser with Rabi frequency Ω couples $|e\rangle$ to $|r\rangle$. The decay rates are denoted by capital Gammas, and the dephasing rates by lowercase Gammas.



quency units, $\hbar \equiv 1$)

$$H = \begin{pmatrix} 0 & \frac{\mathcal{E}}{2} & 0 \\ \frac{\mathcal{E}}{2} & -\Delta_p & \frac{\Omega}{2} \\ 0 & \frac{\Omega}{2} & \Delta_c - \Delta_p \end{pmatrix} \quad (4.1)$$

in the basis $\mathcal{B} = \{|g\rangle, |e\rangle, |r\rangle\}$. The time evolution is given by the von Neumann equation

$$\frac{d}{dt}\rho = -i[H, \rho]. \quad (4.2)$$

A more general form, the Lindblad equation*

$$\frac{d}{dt}\rho = -i[H, \rho] + \mathcal{L}(\rho) \quad (4.3)$$

allows to treat non-unitary evolution due to interaction with the environment. That way, we can include spontaneous decay terms

$$\mathcal{L}_{\text{decay}} = \begin{pmatrix} 0 & \frac{-\Gamma_e}{2}\rho_{1,2} & 0 \\ \frac{-\Gamma_e}{2}\rho_{2,1} & 0 & \frac{-\Gamma_e}{2}\rho_{2,3} \\ 0 & \frac{-\Gamma_e}{2}\rho_{3,2} & 0 \end{pmatrix} + \begin{pmatrix} 0 & 0 & \frac{-\Gamma_r}{2}\rho_{1,3} \\ 0 & 0 & \frac{-\Gamma_r}{2}\rho_{2,3} \\ \frac{-\Gamma_r}{2}\rho_{3,1} & \frac{-\Gamma_r}{2}\rho_{3,2} & 0 \end{pmatrix} \quad (4.4)$$

*also known as master equation

and dephasing terms

$$\mathcal{L}_{\text{dephasing}} = \begin{pmatrix} \gamma_e \rho_{2,2} & \frac{-\gamma_e}{2} \rho_{1,2} & 0 \\ \frac{-\gamma_e}{2} \rho_{2,1} & -\gamma_e \rho_{2,2} & \frac{-\gamma_e}{2} \rho_{2,3} \\ 0 & \frac{-\gamma_e}{2} \rho_{3,2} & 0 \end{pmatrix} + \begin{pmatrix} 0 & 0 & -\gamma_r \rho_{1,3} \\ 0 & \gamma_r \rho_{3,3} & \frac{-\gamma_r}{2} \rho_{2,3} \\ \frac{-\gamma_r}{2} \rho_{3,1} & \frac{-\gamma_r}{2} \rho_{3,2} & -\gamma_r \rho_{3,3} \end{pmatrix} \quad (4.5)$$

with rates as depicted in Figure 4.1. In-depth explanation about such terms and about the master equation in general can be found in [183]. With $\mathcal{L}(\rho) = \mathcal{L}_{\text{decay}} + \mathcal{L}_{\text{dephasing}}$, we can solve Equation 4.3 using Lindblad solvers [227] such as from the QuTiP* Python package. To find a stationary solution

$$0 = [H, \rho] + i\mathcal{L}(\rho) \quad (4.6)$$

we can also solve this set of coupled equations using other mathematics software such as Mathematica. Note that the solutions shall preserve unity population. Mathematically, the trace of the density matrix $\text{Tr}[\rho] = \rho_{1,1} + \rho_{2,2} + \rho_{3,3} = 1$ shall be preserved. The solution yields the density matrix with the population on the diagonal and the coherences on the off-diagonal. The transmission for the different light fields are obtained from the imaginary parts of the coherences. For the probe transmission, we get

$$T = \exp \left[\frac{\Gamma_e}{\mathcal{E}} \text{OD} \Im(\rho_{2,1}) \right] \quad (4.7)$$

where $\Im(\cdot)$ denotes the imaginary part.

In the weak probe limit ($\mathcal{E} \ll \Omega$), there is an analytical solution to Equation 4.6 [99]. The susceptibility for the lower transition is given by

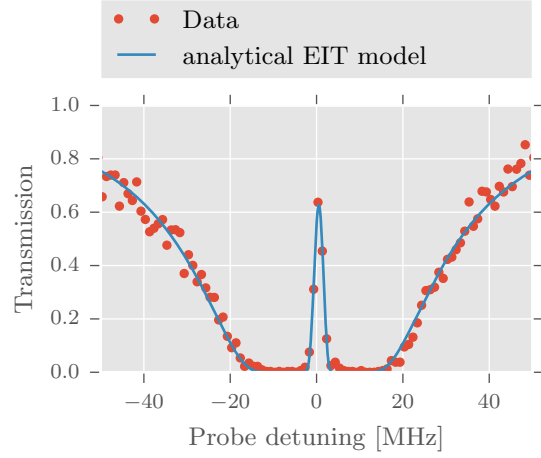
$$\chi_{2,1} = \frac{4(\Delta_p - \Delta_c)(\Omega^2 - 4(\Delta_p - \Delta_c)\Delta_p - \gamma_c^2) + i(8(\Delta_p - \Delta_c)^2\gamma_p + 2\gamma_c(\Omega^2 + \gamma_p\gamma_c))}{|\Omega^2 + (\gamma_p + 2i\Delta_p)(\gamma_c + 2i(\Delta_p - \Delta_c))|^2} \quad (4.8)$$

with coherence decay rates defined by $\gamma_p = \Gamma_e + \gamma_e \approx \Gamma_e$ and $\Gamma_c = \Gamma_r + \gamma_r$ with $\Gamma_c \approx \gamma_r$ in this work, which means that the coherence decay rates are dominated by spontaneous decay for the excited state $|e\rangle$ and by dephasing for Rydberg states $|r\rangle$. From the susceptibility, the transmission is derived to be

$$T = \exp \left[\frac{-\text{OD} \gamma_p (\gamma_c^2 \gamma_p + 4\gamma_p (\Delta_p - \Delta_c)^2 + \gamma_c \Omega^2)}{4\gamma_p^2 (\Delta_p - \Delta_c)^2 + \gamma_c^2 (\gamma_p^2 + 4\Delta_p^2) + 2\gamma_c \gamma_p \Omega^2 + (\Omega^2 - 4(\Delta_p - \Delta_c)\Delta_p)^2} \right] \quad (4.9)$$

*<http://qutip.org>

Figure 4.2: The analytical EIT model from Equation 4.9 fits our transmission spectrum nicely. This spectrum was measured at high optical depth $OD = 79$. The blue Rabi frequency from the fit result yields $\Omega = 2\pi \times 13$ MHz. The coherence decay rate here is $\gamma_c = 2\pi \times 0.17$ MHz, a common value found in many of our EIT measurements.



which we use as regression model to our EIT spectra, as shown in Figure 4.2. For EIT condition: $\Delta_p = \Delta_c = 0$, Equation 4.9 simplifies to

$$T = \exp \left[\frac{-OD}{1 + \frac{\Omega^2}{\gamma_p \gamma_c}} \right] \quad (4.10)$$

which means that significant EIT can be observed in the situation where

$$\Omega^2 \gtrsim \gamma_p \gamma_c OD. \quad (4.11)$$

4.2 PROBING POPULATION AND COHERENCES

By detecting the transmission, we can probe the off-diagonal elements of the density matrix, as described in Section 4.1. With our ion detector, we can also measure the population in the Rydberg state. That way, the full density matrix can be reconstructed, even with spatial resolution if a camera is used to detect the transmission [228]. Figure 4.3 shows the spectral distribution of the excited state and Rydberg state populations. State dressing due to laser light detuned by $\Delta_c = 40$ MHz to the upper transition causes a slight red shift of the state which is dominated by $|e\rangle$, visible by the horizontal offset of the blue and orange lines. Close to $\Delta_p = 40$ MHz, it is very likely to excite a Rydberg atom because it has the dominant density matrix element. The resonance for the Rydberg excitation has a blue-shift ($\Delta_p > \Delta_c$). Mixing of the states causes a finite probability (local maximum) of Rydberg excitation at $\Delta_p = 0$ and increased excited state population at $\Delta_p = \Delta_c$. The occurrence of these smaller maxima are strong indicators for quantum interference which governs EIT.

density elements matrix

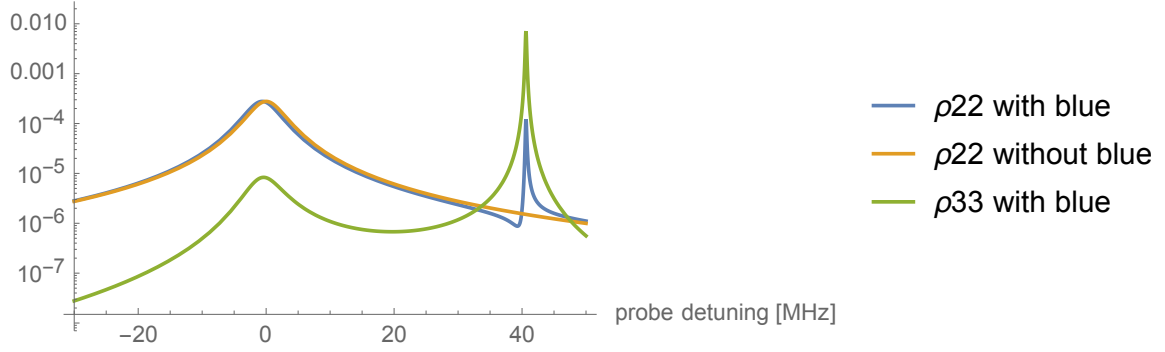


Figure 4.3: Density matrix elements of the three-level system with off-resonant coupling (detuning $\Delta_c = 40$ MHz). The blue light, which couples the excited state to the Rydberg state enables Rydberg excitation at $\Delta_p \approx \Delta_c$. But interestingly, the state dressing also increases the excited state probability off-resonantly (blue spike) and there is also Rydberg character at $\Delta_p = 0$. Note the small red shift of the excited state population close to zero and the Rydberg peak which is blue-shifted: $\Delta_p > \Delta_c$. Both shifts increase with Ω .

Of particular practical interest is the question: what probe detuning Δ_p is necessary to excite a Rydberg atom at a given blue detuning $\Delta_c = 40$ MHz? And how does this resonant detuning depend on Ω ? These questions are answered in Figure 4.4. Maximum Rydberg population (ρ_{33}) is obtained at

$$\Delta_p = 40 \text{ MHz} + 0.0059\Omega^2 \approx \Delta_c + \frac{\Omega^2}{4\Delta_c} = 40 \text{ MHz} + 0.00625\Omega^2. \quad (4.12)$$

The left part of the approximation is obtained for typical probe powers, the right one is valid for $\mathcal{E} \ll \Omega$. This translates to control powers P_c for the state $66S$ and for our control waist of $14 \mu\text{m}$ in

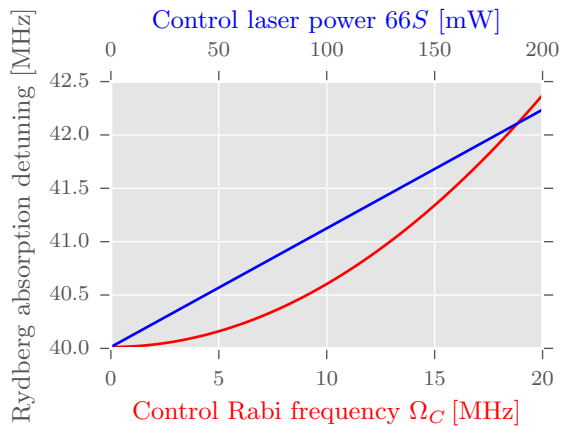


Figure 4.4: This figure shows the probe detuning which results in maximum Rydberg population if the upper transition is detuned to $\Delta_c = 40$ MHz. There is a linear dependence on the control laser power. The slope, however, depends on the principal quantum number and the control waist, which is $14 \mu\text{m}$ here. The dependence on the Rabi frequency is universal for all Rydberg states.

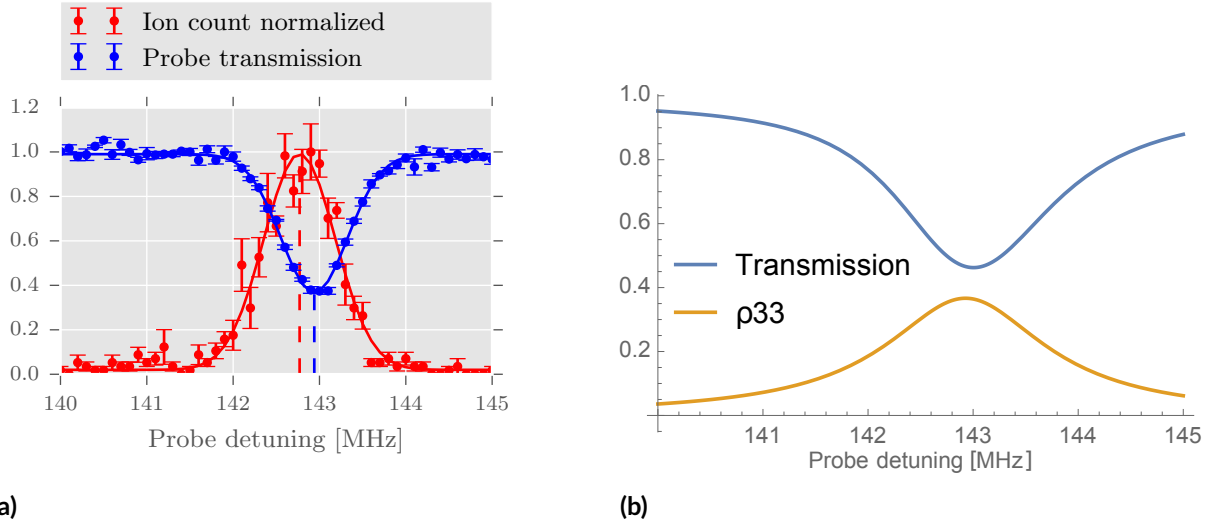


Figure 4.5: (a) In this experimental data, the control laser was detuned by around 140 MHz. There is a two photon resonance for probe detuning of 143 MHz (blue). The absorbed probe photon is stored as a Rydberg excitation. This is made visible after ionization. Our MCP detects the Rydberg atoms (red). (b) We can model both the transmission and the population with our theory.

the following way

$$\Delta_p = 40 \text{ MHz} + \frac{2 \text{ MHz}}{170 \text{ mW}} P_c = 40 \text{ MHz} + 0.12 \text{ MHz/mW} P_c. \quad (4.13)$$

Note the linear dependence because $\Omega \propto \sqrt{P_c}$.

When comparing minimum transmission and maximum Rydberg population experimentally in Figure 4.5, a slight difference in probe detuning is detected, as indicated by the vertical dashed lines.

4.3 ELECTROMAGNETICALLY INDUCED TRANSPARENCY WITH RYDBERG STATES USING THE D₂ LINE OF ⁸⁷Rb

In practice, the three-level atom as treated in Section 4.1 is an idealized case which can be a good approximation but in reality, atomic level structures are rich, and (their eigenstates) even depend on the environment such as electric and magnetic fields causing Zeeman and Stark splittings.

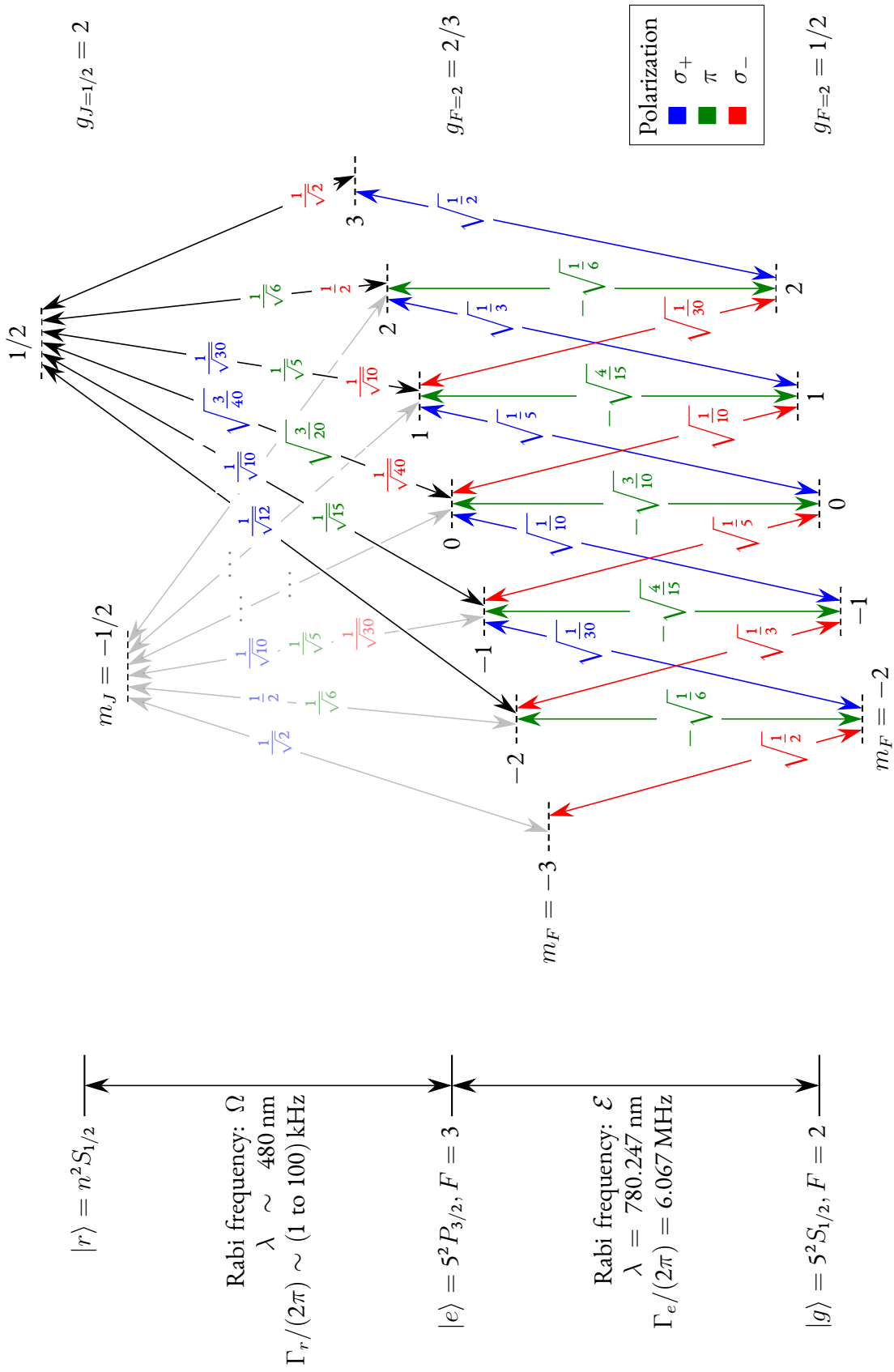


Figure 4.6: The transition matrix elements are expressed as multiples of the reduced dipole matrix elements, which is $4.23ea_0 = 3.58 \times 10^{-29}$ Cm for the lower transition [144]. For the upper transition it depends on the principal quantum number. Due to the transition between a hyperfine structure state in $|r\rangle$ and a fine structure state in $|e\rangle$, different light polarizations can couple the same transition.

For that reason, it is worth studying the neighboring states of the three-level system in a magnetic field as displayed in Figure 4.6. Instead of three levels in total, there are five ground states, seven excited states and two Rydberg states. If the atomic cloud is not perfectly prepared in one of the stretched ground states, different excitation paths become possible and the EIT spectrum shows multiple transmission peaks with a damped main peak. This damping is critical for the performance of the transistor, since fewer source photons can be transmitted (or attenuated).

Similarly as for imperfect population, imperfect polarization enables multiple paths on the level scheme resulting in multiple transmission resonances and a damped main peak.

The different optical dipole transitions have different transition dipole matrix elements. In Figure 4.6, they are expressed in terms of the reduced dipole matrix elements. For the lower transition, the reduced transition dipole matrix element is a fixed value of $4.23ea_0 = 3.58 \times 10^{-29}$ Cm [144]. The values for the D_1 and D_2 lines are obtained by the very precise measurement of the excited state life time [229], whereas the matrix elements to other transitions can be measured by investigating the light shift cancellation [230] which occurs if the laser is detuned between states. For the upper transition, on the other hand, it depends on the principal quantum number of the Rydberg state. The dipole matrix elements can be measured, for example with the control laser power scaling of the Autler-Townes splitting of Rydberg EIT [231]. We can also calculate the transition dipole matrix elements based on theoretical models similar to the ones used in Chapter 3. From these calculations, the dipole matrix element from $|e\rangle$ to Rydberg S states can be approximated by explicit expressions. The radial transition dipole matrix element to the Rydberg S state with an effective principal quantum number n^* is

$$\mu_r = 4.4025(n^*)^{-3/2}ea_0. \quad (4.14)$$

The reduced transition dipole matrix element is given by

$$\mu_r \langle J = 3/2 || er || J' = 1/2 \rangle = 7.1893(n^*)^{-3/2}ea_0 \quad (4.15)$$

and most applicable for this experiment, the transition dipole matrix element between stretched states reads

$$d_{2,3} = 5.0836(n^*)^{-3/2}ea_0. \quad (4.16)$$

Note that these approximative formulae are only valid at low electric and magnetic fields.

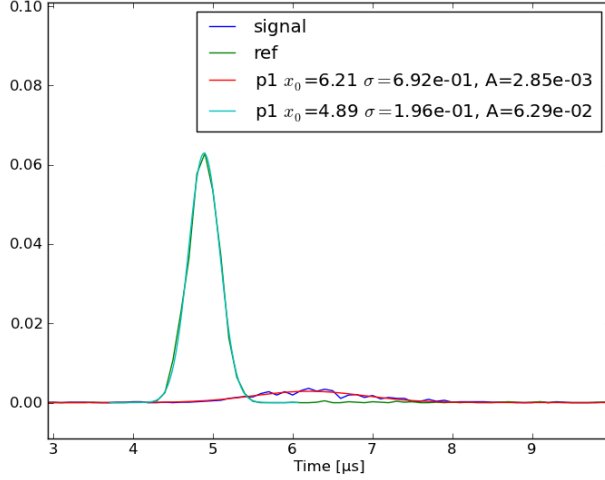


Figure 4.7: Slow light. The pulse retardation of $t_{\text{ret.}} = 1.3 \mu\text{s}$ due to the $100 \mu\text{m}$ medium results in a mean group velocity of 80 m/s . The optical depth was measured to be $\text{OD} = 27$. To obtain a retardation of $1.3 \mu\text{s}$, the control laser must yield a Rabi frequency $\Omega = 2\pi \times 2.5 \text{ MHz}$ according to Equation 4.17. This is consistent with the pulse transmission of 4.5% if compared to the EIT formula, Equation 4.9.

4.4 SLOW LIGHT

The strong dispersion features on EIT result in a reduced group velocity of probe light [232, 233]. Light can be slowed down to a few meters per second [234, 235] and, if the control light is ramped down, a light pulse can even be stored [236].

If we keep the control light at a constant level and send a probe photon pulse through the medium, we can study the retardation $t_{\text{ret.}}$, which depends on the optical depth and the blue Rabi frequency in the following way [226, 237]

$$t_{\text{ret.}} = \frac{2\Gamma_{\epsilon}\text{OD}}{\Omega^2}. \quad (4.17)$$

Large retardations can be realized by applying a low control Rabi frequency, as done in Figure 4.7. However, there is an evident tradeoff between retardation and transmission, cf. Equation 4.10.

In case we model the atomic cloud as a homogeneous cylinder with length $L = 100 \mu\text{m}$ in this measurement, we can easily calculate the group velocity of the slowed light from the measured retardation of $t_{\text{ret.}} = 1.3 \mu\text{s}$

$$v = \frac{L}{t_{\text{ret.}}} = 80 \text{ m/s}. \quad (4.18)$$

Regardless of the length of the cloud, but with previously measured $\text{OD} = 27$, we can infer the blue Rabi frequency Ω from the retardation. Since, from Equation 4.17, $\Omega \propto \sqrt{t_{\text{ret.}}}$, this method should give a precise result. On the other hand, the approximation of a homogeneous medium is rough. If we do so, we obtain $\Omega = 2\pi \times 2.5 \text{ MHz}$. We can cross-check this value by comparing the transmission of the pulse with the transmission expected from the analytical EIT formula, Equation 4.9. The detected

transmission, as derived from the Gaussian fits, is $0.00285/0.0629 = 4.5\%$. This value is obtained with the EIT model for the realistic choice $\gamma_c = 2\pi \times 0.13$ MHz which suggests that this method works approximately.

Another interesting observation is in the pulse width. The incident pulse has a Gaussian width of $\sigma_{\text{in}} = 2\ \mu\text{s}$, whereas the transmitted pulse is as long as $\sigma_{\text{in}} = 7\ \mu\text{s}$. The underlying reason for this broadening is that the incident pulse width causes a Fourier-broadening. Frequency components of the pulse correspond to different velocity classes due to the dispersion relation and as a result, the pulse expands. This effect can be reduced by applying longer pulses. In that case, however, the determination of the pulse position becomes more uncertain and due to the larger overlap, the effect seems less obvious.

4.5 DISTORTION MECHANISMS OF EIT SPECTRA

The deviation of a measured EIT spectrum from the ideal model, Equation 4.9, may be due to various mechanisms. To help troubleshooting, this section describes common spectral features which have come up during this work.

4.5.1 LASER STABILITY

One obvious source for broadened spectral lines is due to the frequency instability of the laser systems used to measure the spectrum. For EIT, both lasers contribute to the width of the EIT signal [238]. The laser linewidth is often blamed for the width of the EIT feature [87][239].

In early experiments [240], the laser linewidth indeed had a significant impact on the spectrum. With new laser frequency stabilization techniques, see Section 2.5, this effect is drastically reduced up to the point that we can neglect it in this work.

4.5.2 BACKGROUND PHOTON COUNTS

A common problem is a spectrum which exhibits a transmission offset such that zero transmission is never detected despite high optical depth. This can occur for absorption scans of the lower transition, but can be more pronounced for EIT scans as shown in Figure 4.8b. Typically, this phenomenon arises whenever an increased dark count rate is present in the single photon detectors. In EIT measurements, the blue light can cause background counts due to the co-linear alignment. Note that one blue laser can cause high count rates in all HBT detectors because reflections from the glass cell, for instance, are

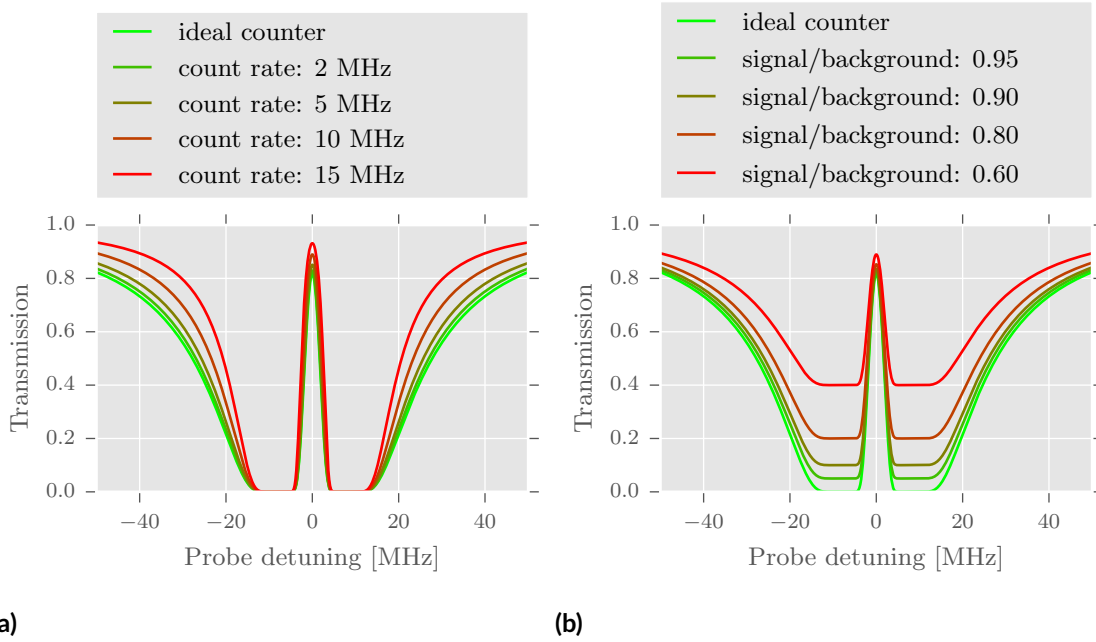


Figure 4.8: Technical error sources which distort the signal. In (a), a saturation effect of the single photon detectors is shown. The dead time of 45 ns causes a nonlinear response at high count rates. We keep the count rates below 2 MHz to suppress this effect. (b) It occurred to us several times that there is an offset in minimum transmission. This can be due to increased background counts coming from the control light, from room light or from the dipole trap. It is worth measuring a spectrum at very low light power to make sure that the dark counts do not depend on the experimental sequence and the devices in use.

bright enough to be detected. For that reason, it is crucial to attenuate light at wavelengths other than 780 nm using bandpass filters as shown in Figure 2.16.

Stray light such as from the dipole trap or even room light can also contribute to a transmission offset. An easy solution is to cover the fibers in black tape, to cover the fiber optics as good as possible and to enclose the photon counters in a box.

4.5.3 DETECTOR NONLINEARITY

Our single photon counters can operate with count rates up to 40 MHz. Approximately linear response is only available at low count rates. The reason is an intrinsic property of photo multipliers which leads to the information loss about any photon which arrives within a fixed time period, the dead time, after a successful detection event. In our Laser Components counter modules, the dead time is specified and measured to be $\tau_{\text{dead}} = 45$ ns. Our Excelitas counters have dead times of

$\tau_{\text{dead}} = 20$ ns. If the measured data shows a photon rate R , it can be corrected for the dead time with the formula

$$R_{\text{corrected}} = \frac{R}{1 - R\tau} \quad (4.19)$$

which is actually used in Chapter 6. It corrects the optical gain of the transistor to a slightly higher value. Note that high errors can occur if the correction is applied to data with only a few events. Therefore, it is advised to apply the correction after averaging and binning.

In this work, $R < 2$ MHz to stay in the approximately linear regime. For the Laser Components and Excelitas counters, the correction factors at $R = 2$ MHz are $\frac{1}{1-R\tau} = 1.10$ and 1.04 respectively.

Figure 4.8a shows how an EIT spectrum gets distorted at high count rates.

4.5.4 DOPPLER BROADENING

The thermal movement of atoms at finite temperature sets a minimum line width of any EIT spectrum or ion signal. The Doppler width in a counter-propagating probe/control setup is given by [140]

$$\Delta_{\text{FWHM}} = (f_c - f_p) \sqrt{\frac{8k_B T \log(2)}{m_{\text{Rb}} c^2}}. \quad (4.20)$$

The detected spectrum is a convolution of the natural line with a Gaussian of width Δ_{FWHM} . At $T = 10$ μK and for excitation frequencies $f_p = c/780$ nm and $f_c = c/480$ nm, the Doppler broadening is 58 kHz.

For a co-propagating probe/control setup, the optical frequencies in Equation 4.20 are not subtracted, but added, since both situations are subject to vector addition of the photon recoil (the \vec{k} vectors). In that case, for equal temperature, the broadening is 245 kHz. The different EIT spectra are easily measured but not shown here.

It is possible to eliminate the Doppler broadening even at nonzero temperature if a star-like geometry with three (or more) lasers with defined angles is set up. In that case, the photon recoil can cancel exactly [241].

Note that a broadened EIT peak may indicate thermal movement, but the measurement can be the cause. Probe photons transfer additional recoil energy onto the atoms heating up the sample with each absorption event. Therefore, it is crucial to keep the photon rate low and to check the time evolution of the spectrum.

4.5.5 A.C. STARK SHIFTS

From the evaluations in Section 2.8.3 and Figure 2.14, it is obvious that the dipole trap shifts the three EIT levels. The ground state transition is blue-shifted by

$$\Delta E_{\text{Stark}}^{\text{probe}} = (1943 \text{ MHz} + 3064 \text{ MHz}) \frac{P/[\text{W}]}{(w_0/[\mu\text{m}])^2} = 5007 \text{ MHz} \frac{P/[\text{W}]}{(w_0/[\mu\text{m}])^2} \quad (4.21)$$

for perfect π polarization. The upper transition is red-shifted by

$$\Delta E_{\text{Stark}}^{\text{control}} = (1646 \text{ MHz} - 3064 \text{ MHz}) \frac{P/[\text{W}]}{(w_0/[\mu\text{m}])^2} = -1418 \text{ MHz} \frac{P/[\text{W}]}{(w_0/[\mu\text{m}])^2}. \quad (4.22)$$

For off-resonant Rydberg excitation $\Delta_p \gg \Gamma_e$, it might be sufficient to adjust only one of the lasers. In that case, the necessary adjustment is a blue detuning of

$$\Delta E_{\text{Stark}}^{\text{offres}} = (5007 \text{ MHz} - 1418 \text{ MHz}) \frac{P/[\text{W}]}{(w_0/[\mu\text{m}])^2} = 3589 \text{ MHz} \frac{P/[\text{W}]}{(w_0/[\mu\text{m}])^2}. \quad (4.23)$$

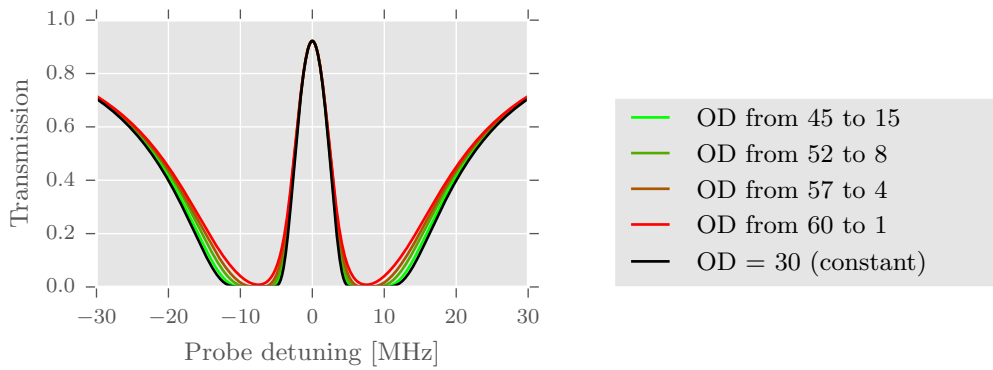
These values are valid in the laser focus. The atomic density extends also to the wings of the laser beam profile such that line broadening occurs [6].

In addition to these shifts, if imperfect polarization of the excitation lasers enables coupling to other excited states, the Zeeman state-dependent a.c. Stark shifts will mix up the energetic order of the excited states adding difficulty for the spectral interpretation.

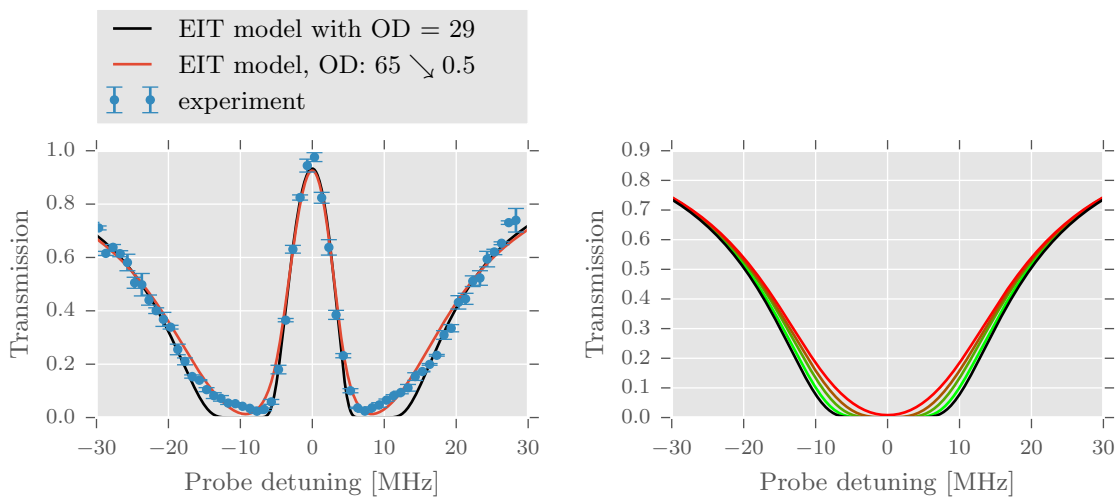
4.5.6 VARIATION OF OPTICAL DEPTH

There are numerous ways to distort a transmission spectrum. Asymmetric absorption lines due to lensing effects have been shown in Section 2.9 or dark counts can add a transmission offset. Here, a subtle distortion of an EIT spectrum, as shown in Figure 4.9 can give a hint about a severe problem. If EIT measurements are averaged over different atomic densities and resultant optical depths, only most extreme cases are detected. The change of the optical density within a measurement is a typical systematic error. Not only long-term drifts* are underlying reasons. It can also occur if multiple measurements are carried out in an experiment where the optical dipole trap recaptures atoms between the measurements. Due to heating, loss or even compression [242] during the recapture process, the optical depth can change between the measurements. If the the interrogation time of one of these

* as observed in other experiments than this



(a)



(b)

(c)

Figure 4.9: Influence of a variation of optical depth on the EIT spectra. If a spectrum is measured on a (radially) expanding atomic cloud, the optical depth decreases in time. Also, if atoms are recaptured and the spectrum is measured multiple times, a drop of optical depth can occur due to atom loss. To simulate this effect, a linear decrease of the optical depth is assumed, as indicated in the legend in (a) and compared to a constant optical depth of 30. It is remarkable that the black EIT spectrum in (a) and the absorption spectrum in (c) almost coincide with the green spectra despite the large variation of optical depth. Only if the variation is larger, the effect is resolved, also experimentally (b). As a result, caution is advised when interpreting the optical depth from an average of EIT or OD measurements.

measurements is too long, the free thermal expansion of the cloud causes an additional OD variation since none of the measurements in this thesis are done in-trap.

Figure 4.9a shows that the EIT model for a constant OD is barely different from the one obtained

by an average in the range $OD = 45 \dots 15$. The mathematical reason is that the EIT transmission spectrum (for all probe detunings Δ_p) fulfills the approximation

$$T(OD) \approx \frac{T(OD + \Delta) + T(OD - \Delta)}{2} \quad (4.24)$$

for $\Delta \lesssim OD/2$.

The data taken in Figure 4.9b was in fact taken with a strong variation of the optical depth due to insufficient cooling. If the EIT formula is averaged with a simplified linear variation of the optical depth $OD = 65 \dots 0.5$, the adapted EIT model yields a much better fit to our data.

4.5.7 INTERACTION EFFECTS

Due to the enormous properties of Rydberg atoms, it is not surprising that Rydberg lines exhibit rich features. Although there is theory on such systems [99, 100, 103], the many-body character, many levels and strong level mixing make it nearly impossible to obtain a full simulation.

One prominent example is that the Rydberg electron can even create an attractive potential for ground state atoms [243]. Therefore, the Rydberg state is red-shifted by the potential energy of the surrounding ground-state atoms. Interestingly, this shift is independent of the principal quantum number, because of the inverse scaling of the potential depth created by the Rydberg electron wave function and its size, so, the amount of ground state electrons it can cover at a constant density. The total shift of the Rydberg state is only given by the ground state density n , and reads

$$\Delta E = \frac{2\pi\hbar^2 a}{m_e} n. \quad (4.25)$$

where $a = -1\Gamma_e a_0$ is the triplet scattering length for the collision of an electron with a Rubidium atom [244]. The shift can be measured by ion detection [243]. In a long atomic cloud, this shift might not be very visible as a shift of the EIT line, but rather as damping. For a short cloud, the line shift would be more visible because the potential is only probed locally.

4.6 NONLINEAR OPTICS ON THE SINGLE PHOTON LEVEL

4.6.1 RYDBERG BLOCKADE

In this section, we combine the knowledge of interaction between Rydberg states from Chapter 3 with our experimental toolkit of EIT, which was explained in this chapter. Let us excite a Rydberg

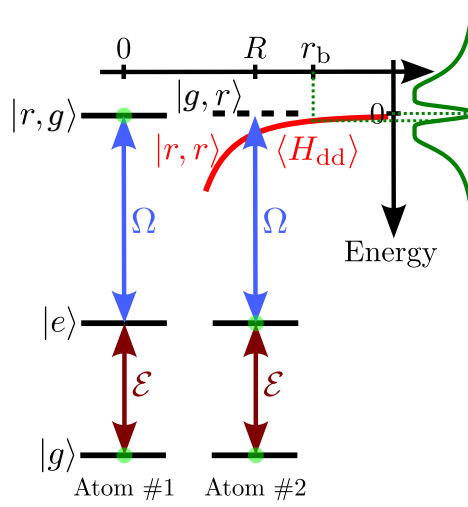


Figure 4.10: Rydberg blockade. The interaction between Rydberg states causes the right excitation to fail if the left atom is in the Rydberg state $|r\rangle$. A blockade radius can be defined as distance where the interaction shift equals the excitation linewidth.

atom in state $|r\rangle$ at position 0, as shown in Figure 4.10. The interaction between Rydberg atoms is strongly dependent on their distance. As a result, atoms in the vicinity experience modified eigenstates, as shown by the red line. The shift can scale as $\propto r^{-6}$ for van der Waals interaction or as $\propto r^{-3}$ for dipolar interaction, which is the case on strong Förster resonances.

Using the same lasers with same detunings as for the first excitation, it is impossible to excite the second atom at a small distance due to the interaction. What happens is that the upper transition is not in resonance any more due to the large detuning that the shift has caused. So, an effective coupled two-level system is remaining with states $|g\rangle$ and $|e\rangle$. Driving this transition with \mathcal{E} causes absorption and spontaneous emission, so, scattering of probe photons to the whole solid angle. Although in principle the interaction shift has infinite reach. Due to the finite excitation linewidth $\Delta\nu_{\text{EIT}}$, a considerable effect only occurs if the interaction shift is on the order of the linewidth. Therefore, the Rydberg blockade radius is defined as the distance where the interaction equals $h\Delta\nu_{\text{EIT}}$.

For a van der Waals interaction potential

$$V = \frac{C_6}{r^6} \quad (4.26)$$

and a linewidth

$$\Delta\nu_{\text{EIT}} = \frac{\Omega^2}{\Gamma_e \sqrt{\text{OD}}} \quad (4.27)$$

the blockade radius is thus given by

$$r_b = \sqrt[6]{\frac{\Gamma_e C_6 \sqrt{\text{OD}}}{\Omega^2}}. \quad (4.28)$$

Note that in the literature [88], values vary by the factor 2

$$r_b = \sqrt[6]{\frac{2C_6}{\gamma_{\text{EIT}}}} \text{ (not used here)} \quad (4.29)$$

with

$$\gamma_{\text{EIT}} = \frac{\Omega^2}{\Gamma_e}. \quad (4.30)$$

This is due to a different definition of Ω in the Hamiltonian, so, effectively the same.

Since the van der Waals potential can be derived in second order from the dipole-dipole potential, see Equation 3.20, the blockade radius can be rewritten

$$r_b = \sqrt[6]{\frac{\Gamma_e}{\Omega^2} \sum_i \frac{C_{3,i}^2}{\hbar \Delta_i}}. \quad (4.31)$$

with the coupling strength $C_{3,i}$ and the Förster defect Δ_i of pair state i .

On Förster resonance, the energies of the symmetric and antisymmetric states are

$$V = \pm \frac{C_3}{r^3}. \quad (4.32)$$

Our new insights [1] show that the potential as experienced by a polariton incident on a stored Rydberg impurity at position zero reads

$$V_{\text{ef}}(r) = \frac{C_3^2}{\Delta - \Delta_e - \Delta_c - i\gamma_p} \frac{1}{r^6} \quad (4.33)$$

and is always $\propto r^{-6}$, even close to a Förster resonance.

4.6.2 NONLINEAR TRANSMISSION

Due to the Rydberg blockade effect, there is a minimum separation between neighboring excitations. This also applies for Rydberg polaritons, which travel through the medium with Rydberg-EIT. Whenever photons, which enter into the cloud with reduced group velocity (Section 4.4), go below the blockade radius, one photon is lost due to scattering on the lower transition. This resembles a system of hard rods, which has been used to describe this system [245]. The blockade radius translates into the length of these rods, which we can describe in propagation time units τ . Approximately this time should show up as the time constant of anti-bunching, which can be made visible with by

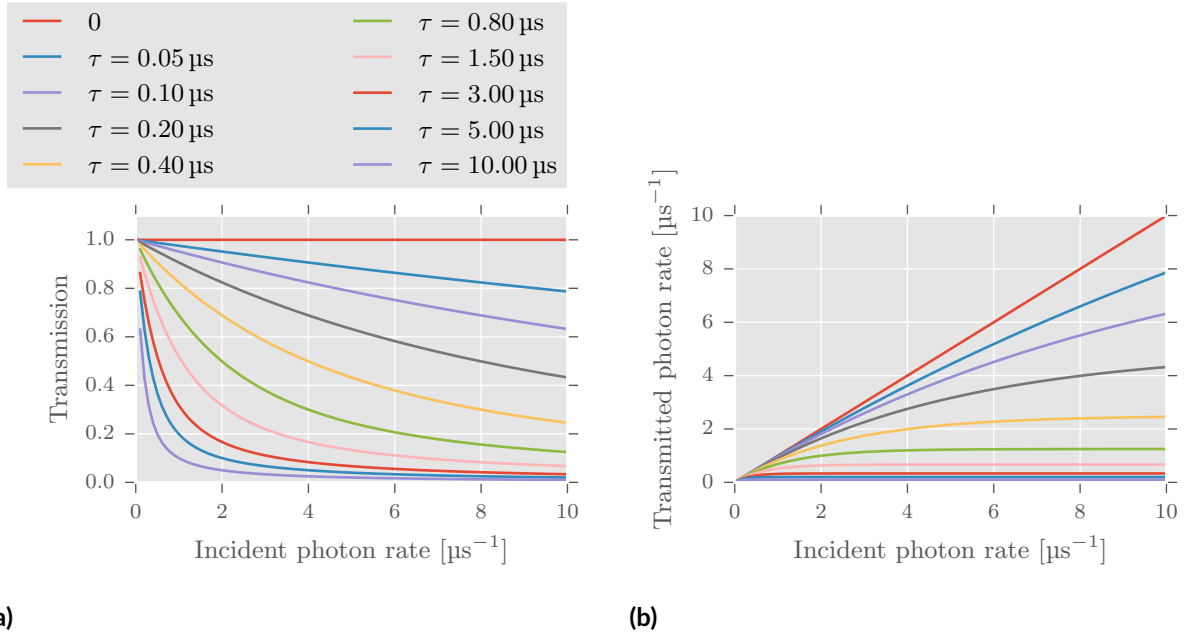


Figure 4.11: A hard rod model can be employed to simulate the nonlinear transmission of Rydberg-EIT. The rod length τ in time units is the propagation time it takes for a Rydberg polariton to travel the length of one blockade radius. Comparing the graphs to our data (later in text), we can estimate the anti-bunching time constant.

cross-correlations between HBT-counters [88]. This anti-bunching can be thought of as a photon turnstile [246] except that the photons are lost, not reordered. We use the hard rod model in this section to simulate the EIT transmission in Figure 4.11 in the typical parameter range of our experiments. However, in reality, Rydberg-EIT is more subtle than the system of hard rods [88].

We can compare the theory lines to our experimental data in Figure 4.12 to determine the photon separation.

As shown in Section 4.4, the group velocity is dependent on the control Rabi frequency. This results in a closer distance between the propagating Rydberg polaritons. Since Rydberg blockade inhibits close distances, the nonlinear response of the medium is changed, as can be seen in Figure 4.13.

4.7 RYDBERG INTERACTIONS AFFECT THE EIT SPECTRUM

If the probe rates are increased to the level where interactions take place, EIT can exhibit novel features. Although these features are very fascinating (to me), they require a more theoretical efforts, which unfortunately is not in the scope of this thesis.

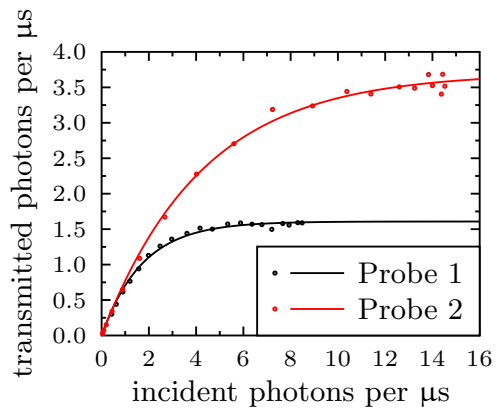


Figure 4.12: Strong interaction between Rydberg states mediates an optical nonlinearity. Separate measurements on our two probe beams reveal the interaction strength of the two different states which are addressed via Rydberg-EIT. According to Figure 4.11b, the photons in probe 1 ($|68S\rangle$) are separated by $\tau = 0.7 \mu\text{s}$ and by $\tau = 0.3 \mu\text{s}$ for probe 2 ($|66S\rangle$).

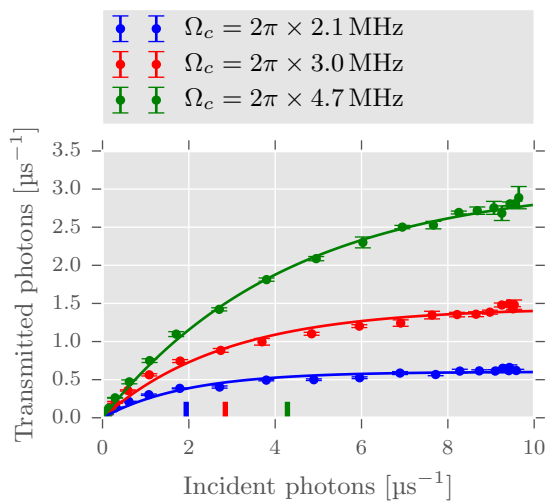


Figure 4.13: The control Rabi frequency affects the nonlinearity of the probe transmission due to the change in group velocity. The saturation photon rates are shown by the vertical lines.

Figure 4.14: The storage of Rydberg excitations causes a red-shifted, damped EIT peak. Detailed theoretical description was outside the scope of this thesis.

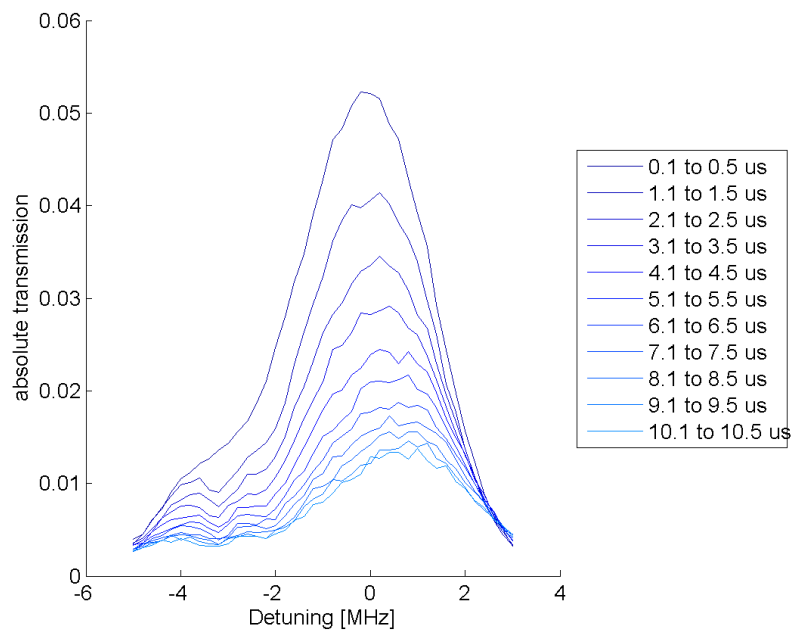
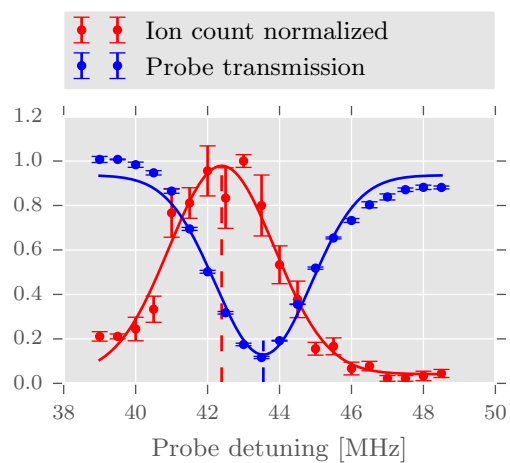


Figure 4.15: The observation of a large difference in the absorption line and the ion signal is due to interaction between Rydberg atoms. The formation of Rydberg aggregates could be an explanation.



Here, two examples shall be flashed: resonant EIT in Figure 4.14 and offresonant absorption in Figure 4.15. In both cases, there are unusual line shifts which are most likely due to Rydberg-Rydberg interaction.

In Figure 4.14, one EIT spectrum was measured at a high probe rate and evaluated at different time ranges after the start. Interestingly, there is a red shift with time and a strong damping, which is not in the textbook EIT description. Maybe this is due to *Rydberg pollution*, an effect also observed in Reference [88] (Supplemental Information).

The data of the offresonant absorption in Figure 4.15 cannot be modeled with reasonable parameters. The energy shift between the ion signal and the absorption line must be due to interacting Rydberg atoms. An explanation of the shift can be the formation of Rydberg aggregates [54–56].

5

Single photon transistor

THE FIRST MAJOR SCIENTIFIC RESULTS of our experiment are presented in this chapter, the first demonstration of a free-space single photon transistor [5]. Similar results were obtained in Reference [224]. We present a method that implements an effective interaction between two independent photon fields. In analogy to the electronic transistor, we call these fields *source* and *gate* fields or photons.

5.1 EXPERIMENTAL SCHEME

The first transistor experiments are carried out once per MOT loading cycle. As shown in Figure 5.1c, the light pulses of the transistor lasers occur right after the dipole trap light is turned off completely. That way, we can exclude (inhomogeneous) a.c. Stark shifts and broadenings which could deteriorate the performance. Although it is possible to recapture the atoms by turning the dipole trap on again and conducting several transistor measurements in one MOT cycle, we preferred to do only one measurement for the sake of simplicity and atom number stability. The atomic cloud in these measurements had a temperature of $40\ \mu\text{K}$. After further development, the temperature has been reduced such that atom recapture is easily realizable today. After all, our high MOT repetition rate of $1\ \text{s}^{-1}$ created enough statistics for the first transistor measurements.

The measurement is as follows. The transistor pulse sequence consists of the storage of a gate exci-

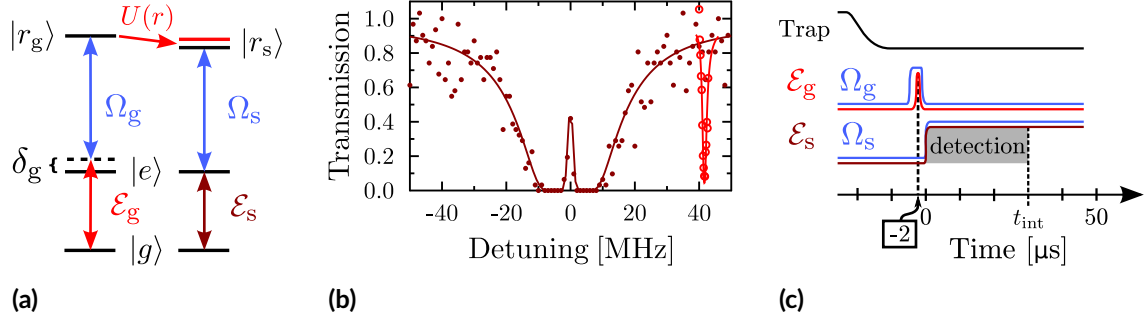


Figure 5.1: The relevant level scheme for the optical transistor is shown in (a). In the presence of the strong control light fields Ω_g and Ω_s the two weak probe fields \mathcal{E}_g and \mathcal{E}_s couple to strongly interacting Rydberg states $|r_g\rangle = |90S\rangle$ and $|r_s\rangle = |89S\rangle$ respectively. From the transmission spectra in (b), scanning the detuning of \mathcal{E}_g and \mathcal{E}_s , important parameters such as the optical depth, blockade radius and the storage efficiency of the source photons is extracted. Single gate photons are stored in the cloud with the pulse sequence in (c) affecting the transmission of many subsequent source photons within the interrogation time.

tation at time $t = -2\mu\text{s}$ followed by the detection of source photons during the interrogation time t_{int} . This measurement is repeated within 50 MOT cycles. In the first 50 cycles, we measure without gate photons by leaving the shutter for \mathcal{E}_g closed and in the next 50 cycles we send gate photons into the atomic cloud. This is done easily in our computer control GUI by creating two iterator variables:

- one special dummy variable called `iterator` which repeats the experiment 50 times and which, due to its name, signals that the time tagger GUI should save the data after the completion of this inner scan dimension.
- an iterator variable `refswitch` which is scanned from 0 to 1 in steps of 1. By making the gate shutter time during the transistor sequence a dynamic variable, it is possible to toggle the state of the shutter by multiplying the time the shutter is open with `refswitch`. Note that the shutter is closed before and after this time. Alternatively and equivalently, instead of multiplying this binary number, the shutter time itself could be scanned as an iterator variable with one step between zero and its *open* value.

We detect transmitted source and gate photons on both sides of the experiment. Although our HBT setup has the potential to analyze photon correlations, even time-resolved [2], this is not done here because of the low data rate at this stage of the experiment. Still, the HBT setup has the advantage that it minimizes the nonlinearity of the detectors (Section 4.5.3) because only half of the photon rate is detected on one device if two detectors are installed. Even though Figure 5.1c suggests a shorter

detection time, our detectors and the data acquisition are active for $200 \mu\text{s}$. The interrogation time t_{int} is a variable used for data analysis. A specific time range is selected for best results.

We define the following quantities, which are mean values averaged over the different experimental realizations, denoted by the bar:

- $\overline{N}_{\text{s,in}}$: number of source photons incident on the cloud,
- $\overline{N}_{\text{s,out}}$: number of source photons transmitted through the cloud,
- $\overline{N}_{\text{g,in}}$: number of incident gate photons,
- $\overline{N}_{\text{g,st}}$: number of gate photons stored as Rydberg excitations and
- $\overline{N}_{\text{g,out}}$: number of transmitted gate photons.

In analogy, the corresponding photon rates per microsecond are named $R_{\text{s,in}}$ and likewise. Section 2.9.2 describes how the number of photons is inferred from the HBT detector clicks. Note that the transmitted photon numbers only take light into account which propagates in the same fundamental spatial mode as initially. In particular, light which scatters at the atomic cloud is not detected.

5.1.1 GATE PHOTON STORAGE

The \mathcal{E}_{g} gate photon storage is realized by detuning the gate lasers with respect to the intermediate state $|e\rangle$ by 40 MHz, as shown in Figure 5.1a. That way, we achieve efficient single- or few-photon absorption and can excite a deterministic amount of Rydberg atoms depending on the cloud length and the blockade radius [2]. Here, we excite the $|90S_{1/2}\rangle$ Rydberg state. The blockade radius between our gate Rydberg excitations is $r_{\text{gg}} = 15 \mu\text{m}$ while our cloud has a $1/e$ -half-width of $40 \mu\text{m}$, so, only 3 Rydberg excitations can occur in an alignment of a quasi-1D chain.

The \mathcal{E}_{g} pulse is a Gaussian light pulse with a full width at half maximum (FWHM) of $t_{\text{g}} = 0.5 \mu\text{s}$. The width of this pulse is chosen large enough for the Fourier-broadening to be considerably smaller than the absorption linewidth. With the time-bandwidth product for Gaussian pulse shapes

$$\text{TBP} = 0.44 \text{ s Hz}, \quad (5.1)$$

the bandwidth of the pulse (Fourier broadening) yields

$$\Delta\nu_{\mathcal{E}_{\text{g}}} = \frac{\text{TBP}}{t_{\text{g}}} = 0.62 \text{ MHz}, \quad (5.2)$$

which is less than absorption line width measured quasi-continuous-wave (cw) in Figure 5.1b (red data): $\Delta\nu_{\text{gate}} = 2$ MHz. We limit the pulse duration because once a gate excitation is stored during the pulse, it can be re-emitted if $|e\rangle$ and $|r_g\rangle$ are still coupled by the control field Ω_g . Depending on the coherence of the stored spin-wave, the cooperative emission [247] can occur in the same mode and be detected similarly to storage and read-out experiments [1, 113, 198]. As a result, to maximize the storage efficiency, it is imperative to both limit the pulse duration and to immediately switch off the control light Ω_g after the pulse \mathcal{E}_g . In fact, by turning off the control light, we cut the Gaussian pulse in the end. We optimize the timing on the transistor gain and we can see the time of switching by an increase in transmission of the gate pulse tail. In principle, the Gaussian pulse shape is not ideal. For similar problems, Blackman pulses are used to minimize the Fourier broadening within a given time window [248, 249]. This could be tried in the future.

We determine the storage efficiency in the following way. The mean number of photons which could be stored as a Rydberg excitation or lost due to scattering at the intermediate state is given by the difference of incident and transmitted photons $\bar{N}_{g,\text{in}} - \bar{N}_{g,\text{out}}$. For $\Omega_g = 0$ (no blue light), we measure a finite gate absorption $A_{ge} = 0.15$ on the ground state transition caused by finite detuning. Our assumption is that this absorption is still present at $\Omega_g > 0$. Although established, this argument needs to be revised in the future with respect to the findings in Figure 4.3. Despite the uncertainty in A_{ge} , the mean number of stored gate photons reads

$$\bar{N}_{g,\text{st}} = (1 - A_{ge}) \cdot \bar{N}_{g,\text{in}} - \bar{N}_{g,\text{out}}. \quad (5.3)$$

5.1.2 SOURCE EIT

The source probe photons are on resonance to the lower transition and the source control field is resonant to the upper transition, as indicated in Figure 5.1a. The resonance condition is verified by measuring the spectrum, see Figure 5.1b. We measure it at low photon rates where blockade between source photons is statistically suppressed. The low photon rate is the reason for the limited data and the resultant data scattering. The control field Ω_s is chosen such that the source transmission is around $T_s = 0.5$. That way, we are not in the Autler-Townes regime, which would decrease the interaction strength with the gate excitation. We measure an EIT linewidth of $\Delta\nu_{\text{EIT}} = 2$ MHz. It would be even smaller at lower Ω_s , but it would come along with lower number of transmitted source photons which would decrease the optical gain. Also from a statistical point of view, intermediate values are advantageous since they lead to a higher visibility, which would be the switch contrast in this case.

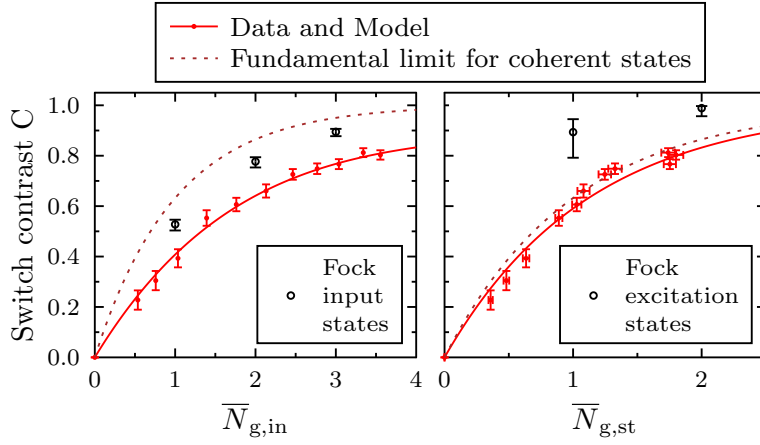


Figure 5.2: The switch contrast determines the ability to suppress the source transmission by a single gate photon. It is measured in the first $30 \mu\text{s}$ after the storage of the gate photon. The Poissonian distribution of the coherent gate photons sets a limit for the contrast. While incident gate photons cause a good contrast (left panel), stored excitations lead to an almost perfect switch (right panel).

5.2 SINGLE PHOTON SWITCH

We investigate how an incident or a stored gate photon affects the transmission of a source photon. Since in this first step, it is not important to us to influence a large amount of source photons, we set a rather low source photon rate of $R_{s,\text{in}} = 0.69(1) \mu\text{s}^{-1}$.

For the analysis, we include source photons detected in the first $t_{\text{int}} = 30 \mu\text{s}$ after the gate storage.

We define the contrast of the transistor as a measure for the visibility of the influence of gate photons on source photons

$$C = 1 - \left(\overline{N}_{s,\text{out}}^{\text{with gate}} / \overline{N}_{s,\text{out}}^{\text{no gate}} \right). \quad (5.4)$$

As will be seen, $\overline{N}_{s,\text{out}}^{\text{with gate}} < \overline{N}_{s,\text{out}}^{\text{no gate}}$ and thus $0 < C < 1$. If $C = 0$, gate photons do not have any effect on source photons, and if $C = 1$, gate photons have the maximum effect on the source photons: all source photons are scattered in the cloud and none are detected.

In Figure 5.2, the switch contrast is plotted for a range of incident gate photons. For $\overline{N}_{g,\text{in}} = 1.04(3)$, our switch yields $C_{\text{coh}} = 0.39(4)$. Note that the Poissonian statistics of our coherent laser source sets an upper limit to the contrast, as depicted by the dotted line. The limit arises from experimental realizations with zero gate photons, which occurs with probability

$$p(0) = e^{-\overline{N}_{g,\text{in}}}. \quad (5.5)$$

Therefore, the limit for coherent light is given by

$$C_{\text{coh}} = 1 - p(0) = 1 - e^{-\overline{N}_{g,\text{in}}}. \quad (5.6)$$

In our theoretical model, OD_{sp} depicts the optical depth which attenuates the source photons, caused by one incident gate photon. Assuming that only three gate excitations ($r_{\text{gg}} = 15 \mu\text{m}$) fit into the cloud ($\sigma_1 = 40 \mu\text{m}$), and that each of them attenuates the source transmission as $e^{-\text{OD}_{\text{sp}}}$, we derive the model for the switch contrast

$$C(\bar{N}_{\text{g,in}}) = 1 - \sum_{k=0}^{\infty} \frac{\bar{N}_{\text{g,in}}^k e^{-\bar{N}_{\text{g,in}}}}{k!} e^{-\min(k,3) \cdot \text{OD}_{\text{sp}}} . \quad (5.7)$$

Fitting Equation 5.7 to the data in Figure 5.2, we obtain $\text{OD}_{\text{sp}} = 0.75(5)$. The switch contrast for $N_{\text{g,in}}$ -Fock states is given by

$$C_{\text{sp}} = 1 - e^{(-\text{OD}_{\text{sp}} N_{\text{g,in}})} \in \{0.53, 0.78, 0.89\} \text{ for } N_{\text{g,in}} \in \{1, 2, 3\} \quad (5.8)$$

which is plotted as black data points.

As discussed in Section 5.1.1, we can calculate the number of Rydberg-stored gate excitations. So, we can plot the same contrast values versus this quantity and make a similar analysis as above

$$C(\bar{N}_{\text{g,st}}) = 1 - \sum_{k=0}^{\infty} \frac{\bar{N}_{\text{g,st}}^k e^{-\bar{N}_{\text{g,st}}}}{k!} e^{-\min(k,3) \cdot \text{OD}_{\text{st}}} . \quad (5.9)$$

We find that stored gate photons cause a high optical depth for source photons: $\text{OD}_{\text{st}} = 2.2(7)$. The contrasts for one and two gate excitation is $C_{\text{st}} = 0.89$ and 0.99 respectively.

5.3 FIRST DEMONSTRATION OF A FREE-SPACE SINGLE PHOTON TRANSISTOR

After proving a significant switch contrast, we can proceed investigating how many source photons can be attenuated by a single gate photon. Therefore, we increase the source photon rate systematically to study if the switch contrast is robust to an increased number of source photons. As expected from Section 4.6.2, the amount of transmitted source photon saturates due to their mutual Rydberg blockade, see red data in Figure 5.3 (a). Saturation at a lower value is observed if we open the gate shutter and send $\bar{N}_{\text{g,in}} = 0.75(3)$ into the atomic cloud prior to probing it with source photons. We plot the difference between these data points in Figure 5.3 (b) and observe that even though less than one gate photon was incident, more than 10 source photons have been attenuated, thus clearly demonstrating an optical transistor with gain. The amount of source photons attenuated by one gate photon, shall be called optical gain. This number is in first order independent of the number of gate

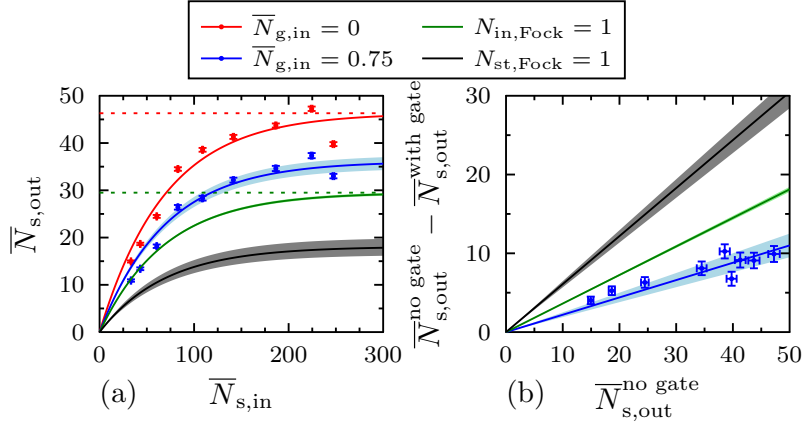


Figure 5.3: Demonstration of the optical transistor. (a) When increasing the number of incident source photons, the number of transmitted source photons (red) saturates due to Rydberg blockade. Even for less than one incident gate photon, there is a clear effect on many source photons (blue). (b) In fact, the amount of attenuated source photons depends linearly on the amount of transmitted source photons without gate which shows the robustness of our scheme. The optical gain of the transistor is given by the green line, which, in first order does not change with the amount of gate photons and therefore is more universal.

photons, if $\bar{N}_{g,in} \lesssim 1$ and thus saturation due to multiple gate photons is negligible. In our thorough analysis, we calculate the gain as number of attenuated source photons using an $N_{g,in} = 1$ Fock state. The result is plotted as a green line in Figure 5.3 (b). Therefore, we obtained an optical gain of 17 in this first data set. For $\bar{N}_{g,in} \lesssim 1$, the previous definition of optical gain can be approximated with a more convenient formula

$$\mathcal{G} = \left(\bar{N}_{s,out}^{no\ gate} - \bar{N}_{s,out}^{with\ gate} \right) / \bar{N}_{g,in} \quad (5.10)$$

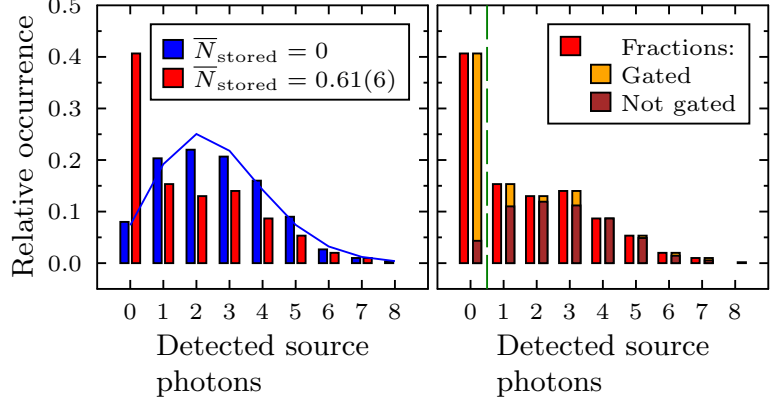
which does not require a statistical analysis.

5.4 HIGH FIDELITY SINGLE RYDBERG DETECTION

The optical gain can be interpreted as a high amplification factor. Like in the electronic transistor, many applications are possible. Here, we show that our scheme enables to predict the presence of a single Rydberg excitation with high detection fidelity. We use the gate laser to store a Rydberg excitation and judge by the number of detected source photons in a single shot and without destroying the Rydberg atom whether the excitation was present or not.

Our investigation starts with histograms of the detected source photons within $t_{int} = 32 \mu s$, as shown in Figure 5.4. Note that this differs from the amount of photons in the experiment by the factor $\eta = 0.31$. We take two histograms: with (red) and without (blue) gate photons using $\bar{N}_{stored} =$

Figure 5.4: Non-destructive single-shot detection of a single Rydberg excitation. The presence of a gate excitation can be measured by the number of detected source photons. To investigate the detection fidelity, we take histograms of source photons. With $\overline{N}_{\text{stored}} = 0.61(6)$ stored gate photons in average, the histogram is bimodal. The two modes can be distinguished knowing the storage efficiency and the reference histogram.



0.61(6) and $\overline{N}_{\text{stored}} = 0$ respectively and assigning the variables $h_{\text{gate}}(n)$ and $h_{\text{no gate}}(n)$. While the blue histogram is in excellent agreement with a Poissonian (blue line), the red histogram has a bimodal distribution with a very pronounced peak at zero. The reason for these two modes is again in the quantum statistics. At $\overline{N}_{\text{stored}} = 0.61(6)$, there is a $p(0) = 54\%$ chance to have experimental realizations with zero gate photons, according to Equation 5.5. Accordingly, the red histogram must be composed of the blue histogram, rescaled by $p(0)$, and depicted in brown

$$h_{\text{gate}}^{(0)}(n) = p(0)h_{\text{no gate}}(n) \quad (5.11)$$

and a remainder (gold) which corresponds to one or more gate photons

$$h_{\text{gate}}^{(\geq 1)}(n) = h_{\text{gate}}(n) - p(0)h_{\text{no gate}}(n). \quad (5.12)$$

Within the golden histogram, which makes up $\sum_{k=1}^{\infty} p(k) = 1 - p(0) = 46\%$ of the events, most of the times we store one excitation (73%) and sometimes two (22%).

To decide whether a gate excitation is present in the medium, we draw a (green, striped) discrimination line between zero and one (at $D = 0.5$) in the histogram. If one or more source photons are detected, it is likely that no gate photon was stored as a Rydberg excitation. If zero source photons are detected, we predict the presence of a Rydberg atom. The fidelity for each of the statements can be calculated by the distribution of the golden and brown histograms left and right of the discrimination

line.

$$\mathcal{F}_{\text{gate}} = \frac{\sum_{n=0}^D h_{\text{gate}}^{(\geq 1)}(n)}{\sum_{n=0}^{\infty} h_{\text{gate}}^{(\geq 1)}(n)} \quad (5.13)$$

$$\mathcal{F}_{\text{no gate}} = \frac{\sum_{n=D}^{\infty} h_{\text{gate}}^{(0)}(n)}{\sum_{n=0}^{\infty} h_{\text{gate}}^{(0)}(n)} \quad (5.14)$$

To break these detection fidelities down to one number we can estimate $\mathcal{F} \geq \min(\mathcal{F}_{\text{no gate}}, \mathcal{F}_{\text{gate}})$. Therefore, we specify the lower value as the detection fidelity, which is a conservative tactic.

An alternative approach would be to specify fidelities based on the exact number of detected source photons. For example, it is much more probable to predict the absence of a Rydberg atom if five source photons are detected as compared to one source photon.

Finally, in our data, we obtain a detection fidelity $\mathcal{F} = 76\%$. This value exceeds the detection efficiency of our counters including (fiber) optics by far. Note that this scheme has the advantage to be a non-destructive method as opposed to ion detection. However, non-destructive does not mean non-invasive. While the Rydberg state is probably unchanged, it is likely that the source photons imprint phase shifts on the gate Rydberg excitation and acts as quantum measurements, projective on subspaces as shown in Section 6.4 and in reference [113].

Precisely speaking, we showed that our scheme can distinguish between zero and *one or more* Rydberg excitations. But due to the high attenuation of stored gate excitations ($C_{\text{st}} = 0.89$), it is very likely to perform very similar with a deterministic photon source. After all, the two-component is rather small.

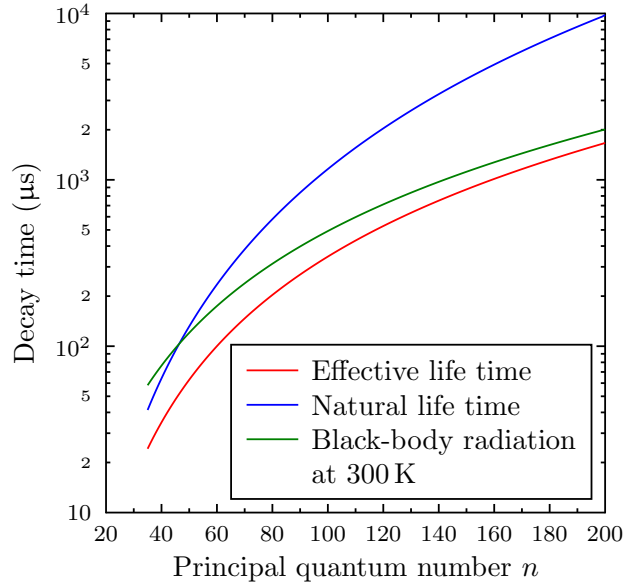
5.5 TUNING PARAMETERS FOR THE IMPROVEMENT OF THE OPTICAL TRANSISTOR

In this section, we analyze several system parameters which affect the performance of the optical transistor.

5.5.1 TUNING BY PRINCIPAL QUANTUM NUMBERS

The question, which principal quantum numbers are best for the optical transistor, is a highly non-trivial one. There are *sweet spots*, which can be determined using the strategy provided in Chapter 3, but there is also one systematic limit, which is monotonous in n : the maximum useful interrogation

Figure 5.5: Life time of Rydberg excitations. The effective life time is composed of two contributions: radiative decay to lower states causes a finite natural life time, and black-body radiation at room temperature introduces coupling to neighboring states. The life time is a limit to the optical transistor since source photons can only be scattered if the gate Rydberg excitation has not decayed. If, however, black-body radiation causes a small change of the gate principal quantum number, there can still be interaction. On the other hand, if the initial quantum numbers are optimized, in particular if a Förster resonance is addressed, any decay mechanism will cause a strong reduction of switch contrast and optical gain.



time, which, for low temperatures, is given by the decay time. For that reason, Figure 5.5 shows the life time which is calculated according to Reference [140].

While the life time is increasing with n , the thermal movement is increasing with available time, so one needs to assure that the gate excitation does not move out of the source beam. Also, the source transmission is decreased with n , so it is unclear where the optimum performance is.

In light of the findings in Reference [224], we have used the states $|71S, 69S\rangle$ and measure a significant increase in gain in Figure 5.6, which is certainly due to the higher amount of transmitted source photons, but also due to a state combination with a Förster resonance close-by.

5.5.2 THERMAL EFFECTS

Although we cool atoms down to the microkelvin range, the thermal movement of Rydberg atoms within the life time of the Rydberg state can lead to a decrease in optical gain. Assuming a temperature of $40 \mu\text{K}$, we would like to quantify the effect of thermal movement of gate excitation perpendicular to the source beam which leads to a loss of interaction.

Assuming the thermal energy $k_B T$ in the radial kinetic energy mv_r^2 , the mean time it takes a gate

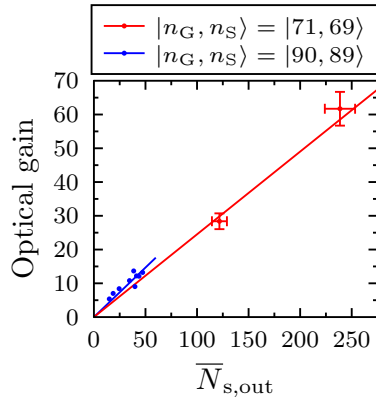


Figure 5.6: Optical gain with different principal quantum numbers. Lowering the principal quantum numbers can be advantageous because the number of transmitted source photons can be maximized. The maximum number of incident source photons is similar in the two data sets. A drawback with low n is decreased interaction. For special combinations, however, a near-Förster-resonance can increase the interaction between source and gate again.

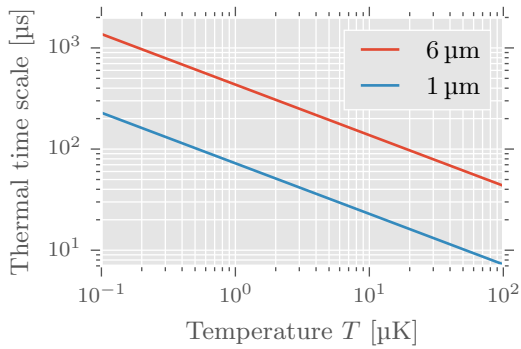


Figure 5.7: Thermal movement of the gate Rydberg excitation transversal to the source beam causes a decrease in optical gain. Here, the time scale for this effect is plotted versus the temperature of the atomic cloud for a beam waist of 6 μm (red). For comparison, the thermal time scale for a movement across the typical inter-particle distance of 1 μm is shown in blue.

excitation to move by one beam waist of $w_0 = 6 \mu\text{m}$ is given by

$$t_{\text{fly}} = \frac{w_0}{\sqrt{\frac{2k_{\text{B}}T}{m}}} = w_0 \sqrt{\frac{87u}{2k_{\text{B}}T}} = 69 \mu\text{s}. \quad (5.15)$$

This time is smaller than the Rydberg decay time for our states, as seen in Section 5.5.1. As a result, this effect dominates the time limitations. The reduction of the temperature to $3 \mu\text{K}$ later in this thesis will reduce this effect by enlarging the time scale to $t_{\text{fly}} = 250 \mu\text{s}$.

5.5.3 EXCITATION GEOMETRY, PROBE WAIST

The radial part of the Gaussian beam shape is given by

$$I(r) = I_0 e^{-2(r/w_0)^2} = I_0 e^{-0.5(r/\sigma_0)^2} \quad (5.16)$$

where w_0 is the beam waist and $\sigma_0 = w_0/\sqrt{2}$ is the corresponding standard deviation. Let $r = \sqrt{(x_s - x_g)^2 + (y_s - y_g)^2}$ be the radial distance between source and gate photons. The relative distance between source and gate photons is distributed as

$$P_{\text{rel}}(r) = \frac{r}{\sigma_0} e^{-0.5(r/\sigma_0)^2}. \quad (5.17)$$

A direct consequence from this equation is observed in Reference [88]. For $w \gtrsim r_{\text{b}}$, the rate of transmitted photons of a single EIT experiment scales as $R \propto (w/r_{\text{b}})^2$.

In Figure 5.8, the attenuated transmission of source photons due to a deterministic single gate Rydberg excitation is shown. We use Beer's Law to calculate the attenuation within the blockade radius. The simulation is a Monte-Carlo simulation taking into account the parameters of our measurements in Reference [5]. We sample the atomic density distribution and the beam profile at $\text{OD} = 25$. The graph can be used to plan the probe waists and the blockade radius (via principal quantum number combinations). Ideal performance of the transistor takes place for configurations in the black area in Figure 5.8. The situation of Section 5.2 is indicated by the white asterisk. The simulation agrees well with our measured data. Our measured attenuation of $\text{OD}_{\text{st}} = 2.2$ is also approximately predicted by the value on the asterisk. The white lines correspond to $\text{OD}_{\text{st}} = 2.2$, the upper $\text{OD}_{\text{st}} = 2.9$ and lower $\text{OD}_{\text{st}} = 1.6$ bounds from the measurement respectively. So, the middle line shows parameters resulting in the same transistor performance as in our measurements.

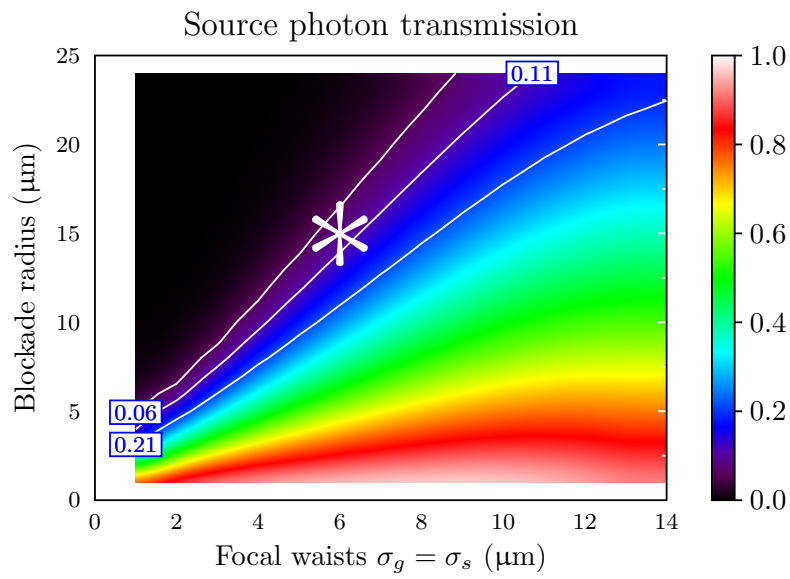


Figure 5.8: A Monte-Carlo simulation is done to predict the switch contrast of the optical transistor. We plot the relative source transmission after attenuation due to a gate Rydberg blockade. The data is an average of many realizations taking the geometry of the atomic cloud and the source and gate beams into account. The asterisk shows the experimental parameters. The middle line shows possible parameters for the measured relative transmission of the transistor. The other lines represent the uncertainties of the value. Since the asterisk is almost on the central line, the simulation agrees very well with our data.

6

Enhancement of single-photon nonlinearities by Förster Resonances

Interaction between Rydberg atoms can be strong if the Förster defect is small and the radial coupling strengths is large, as seen in Chapter 3. We saw in Chapter 5 that for the demonstration of a single photon transistor with gain $\mathcal{G} = 17$, it is sufficient to be in the van der Waals regime.[†] The optical gain was limited due to the high principal quantum number of the source Rydberg state which limits the amount of transmitted photons. However, with lower principal quantum numbers, the interaction between source and gate Rydberg states is decreased typically, unless the states are carefully tuned to a Förster resonance. We showed already in Section 5.5.1 that due to the increased amount of transmitted source photons at low n , and in the vicinity of Förster resonances, the optical gain can be increased.

The question is how the transistor performance can be further increased by precisely tuning the states to a strong resonance. Since the detection efficiency of single Rydberg excitations is still considerably far away from 100 % and the optical gain has not reached our psychologically important threshold of 100, we would like to achieve a significant quantitative advance with this approach, too, besides the qualitative difference. To that point, it was not clear whether Rydberg excitation hopping would cause any surprising effects on the Förster resonance, so, a measurement will give an answer to that question [1].

[†]Despite being Swabian, we shall not be thrifty here.

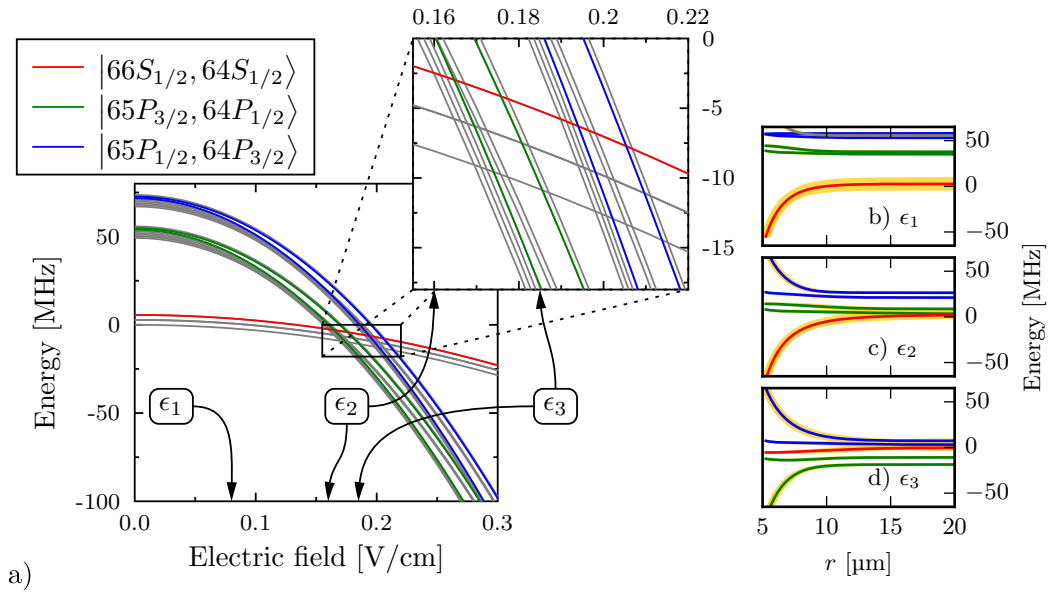


Figure 6.1: The panels in a) show the Stark shift of Zeeman pair states for a constant magnetic field of 1 G parallel to the electric field. No interaction between atoms is considered here, which resembles $r = \infty$. Our state of interest $m_1 = m_2 = 1/2$ (red) mixes at $\theta = 0$ to states marked in green and blue. In the panels b), c) and d) the interaction of two Rydberg atoms is calculated by diagonalizing the dipole-dipole interaction Hamiltonian matrix at different electric fields. For high precision, we include 14×10^3 pair states into our computation basis. At large r , the lines correspond to the states in a) of the same color. We encode the overlap $|\langle 66S_{1/2}, 64S_{1/2} | \Psi_i \rangle|^2$ between each of the lines Ψ_i and the pure initial state in the opacity of the yellow stripe surrounding the lines to visualize the state mixing.

6.1 THEORETICAL ANALYSIS OF THE POTENTIALS AND STATE MIXING

The choice of our state combination, i.e., the principal quantum numbers for the source and gate Rydberg states, is based on the findings in Section 3.5. The measurements of reference [224] show that there are Förster resonances with a small Förster defect for the state combination $n_s = n_g - 2$, at $n_g \approx 70$. Our calculation confirms that these resonances are strong and that this combination, depicted in Figure 3.7a, have a positive Förster defect for $n_g < 70$. Actually, there are two different state combinations with a small energy difference due to fine structure: $|(n_g - 1)P_{1/2}, (n_g - 2)P_{3/2}\rangle$ and $|(n_g - 1)P_{3/2}, (n_g - 2)P_{1/2}\rangle$. They are also shown in Figure 3.4, depicted as yellow triangles pointing left and right respectively. For $n_g \leq 51$, a different resonance is available with a positive defect. It is the P state combination with $J'_1 = J'_2 = \frac{1}{2}$ which we will work with later in this chapter. In Figure 3.4, this series of resonances is depicted as small yellow triangles pointing down. For $n_g > 70$, there is yet another resonance with $\Delta > 0$: the P state combination with $J'_1 = J'_2 = \frac{3}{2}$. It can be

tuned to resonance over a wide range of principal quantum numbers, even up to $n_g = 110$, with the best radial coupling strength, see the big yellow triangles pointing up in Figure 3.4 and the electric fields in Table 3.1.

For low n_g , all these resonances have a positive Förster defect, so in principle, all can be tuned to resonance. Since the defects become quite large, electric field tuning becomes problematic, as discussed in Section 3.5.3.

In addition to the fine structure, there is also the Zeeman structure which we must take into account at our magnetic field $B = 1$ G defining the quantization axis along \vec{e}_y in our laboratory frame, so along the excitation axis.*

The Zeeman splitting causes anisotropic resonances, which can be addressed with the electric field, as shown in Figure 3.3. Here, we concentrate on PP' Zeeman states which are coupled to our prepared SS' state with $m_1 = m_2 = \frac{1}{2}$ in a head to tail configuration ($\theta = 0$). These states are depicted in blue and green in Figure 6.1. Strong coupling between these states and our prepared state causes a state mixture. To quantify the mixing, we plot thick yellow lines around the potential curves in Figure 6.1(b,c,d) with the opacity denoting the SS' part of the mixture (the projection).

The situation in Figure 6.1a is the simplest case. There is a van der Waals coupling between the SS' state and many different PP' states. The visible states, depicted in green and blue have the highest contribution due to the large coupling strength and the relatively low energy offset.

In Figure 6.1b, there is a Förster resonance with one of the green states. In comparison with panel (a), it is visible that the red potential from panel (a) is steeper, in particular comparing large r . Although strong mixing is observed, there is still a large SS' contribution in the red state for low distances, as can be seen by the opacity of the yellow band. For small distances, however, there is also a significant contribution of SS' in the blue potential.

There is a very interesting situation in panel (d). The red potential is almost constant due to its location between the other states. From $r = \infty$ to $r = 5 \mu\text{m}$, almost the whole SS' part is lost in the wave function and found in two other states bending up and down respectively. With the commonly used way to get the Rydberg blockade radius, one would get a value of around zero. But since the red state is not coupled to $|e\rangle$ any more for low r , EIT breaks down. Our theory curves in this chapter, calculated by Przemek Bienias, take these effects into account. Also, the theory includes coupling to the grey potential lines which occurs in a 3D geometry. Still, the experimental output, the optical gain of the transistor, is of great importance in this peculiar situation and helps understanding Förster resonances.

*In Chapter 3, the quantization axis is z , in accordance with literature.

6.2 OPTICAL DETECTION OF ELECTRICALLY TUNED FÖRSTER RESONANCES

The measurements in this chapter require some experimental efforts in advance. First of all, a lot of data needs to be acquired if the transistor gain shall be measured versus the electric field, with fine resolution and reasonable statistics. As a result, the data rate and the stability need to be optimized. Second, we need to make sure that changing the electric field does not affect both the gate storage and the source EIT.

6.2.1 MEASUREMENT SEQUENCE

To meet the increased requirement on the data rate, we take multiple (23) experiments in one MOT loading cycle. This is made possible by forced evaporative cooling in our crossed optical dipole trap.* Ramping down the optical dipole trap, we perform our experiments with 2×10^4 atoms at 3 μK . Each experiment lasts 200 μs . The time is needed to scatter many source photons until the gate excitation has decayed. The time for the gate storage pulse is very short. Ramping Ω_c to store the gate photon is done in less than 1 μs . After the experiment, the Rydberg atoms are ionized with a maximum field of $\epsilon_x = 175 \text{ Vcm}^{-1}$ and the crossed optical dipole trap is turned on again to recapture ground state atoms. We keep the trap on for (100to200) μs for best performance. Our number of pulses $n_p = 23$ is chosen such that atom loss is still negligible, even after multiple *atom release* and *atom recapture* sequences. With slightly different initial conditions, we achieve OD between 10 and 30 in this chapter.

The field ionization is done to assure that all Rydberg excitations are removed. With field ionization, it is possible to have short sequences with an even higher n_p without affecting the following realizations. If the Rydberg atoms are not removed, they could accumulate, leading for example to high source attenuation (not exactly “gain”) in the last pulses of the transistor.

The 23 experimental realizations are repeated in 20 MOT cycles. Afterwards, our time tagger (Section 2.10.4) saves the data on our lab network drive. In these realizations, the gate photons were blocked using the shutter. The next file consists of the same sequence but with gate photons. Then, in principle, one data point can be generated. However, we require more statistics. Since we need to change parameters such as the electric field or the source photon rate, we scan these in the next scan dimension in a triangular scan. That way, we exclude jumps in the detunings, which can cause a failure of the laser frequency stabilization (Section 2.5). Now, the whole sequence is repeated. With the repetition variable being the outermost scan dimension, systematic drifts in the experiment are evenly distributed over the parameter range.

* As of 2016, even 1000 experiments can be done within one MOT cycle. Although the pulse lengths are slightly shorter, this is mainly achieved utilizing Raman sideband cooling.

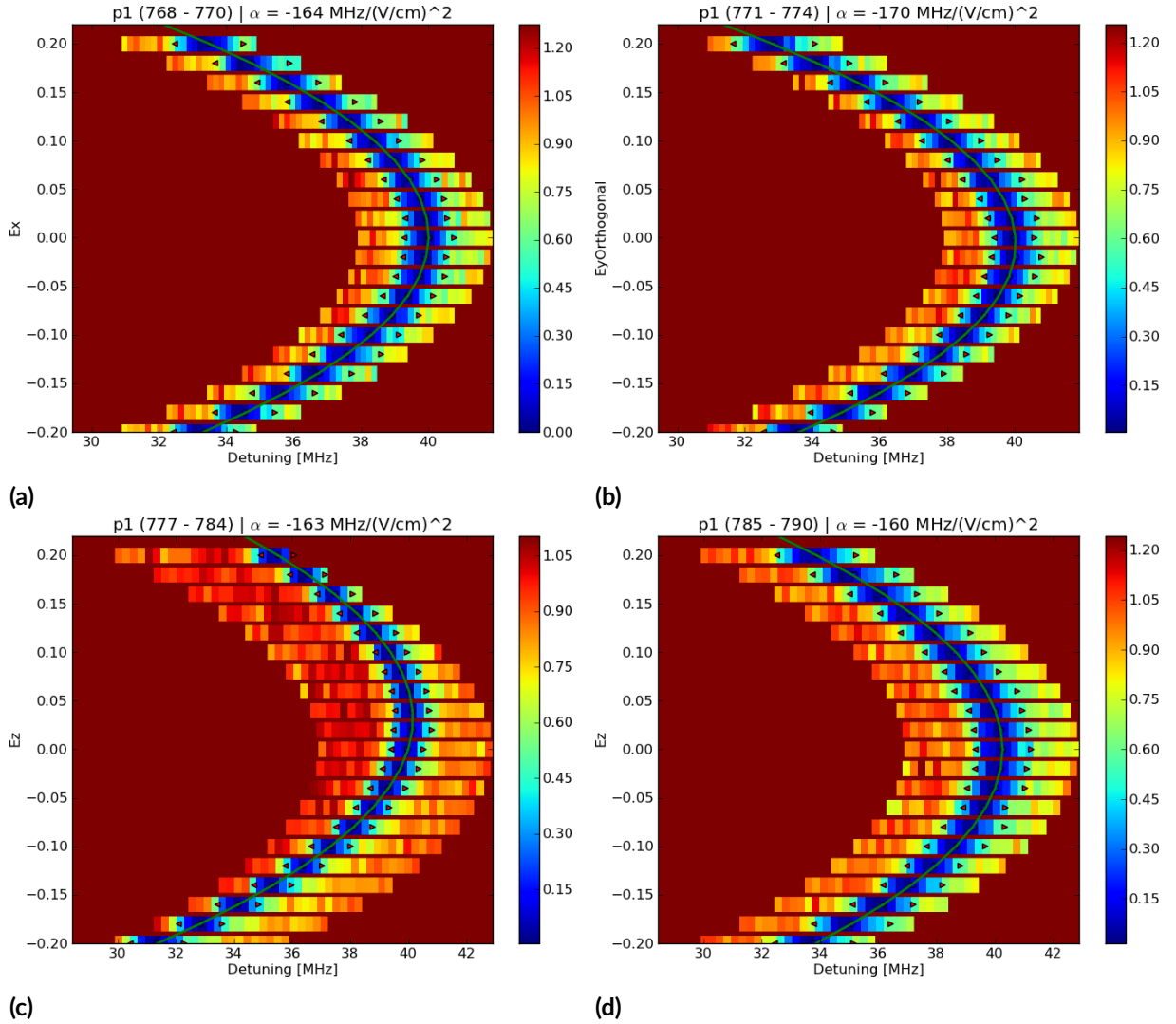


Figure 6.2: Electric field cancellation with Stark maps. We take 2D scans of the probe detuning and the electric field around the two-photon absorption line keeping the control detuning fixed at typically $\Delta_c = 40$ MHz. From a parabolic fit of the resonant detunings, we obtain the offset field which needs to be corrected for. Due to orthogonality, see Section 2.3, the field cancellation in one axis does not affect the field offset in another axis, so we do not need to repeat everything. Here, consecutive field cancellation is done in the (a) x , (b) y , (c) z directions. In z direction, a larger field was detected. So, the field measurement was repeated to verify cancellation.

6.2.2 ELECTRIC FIELD CANCELLATION AND DYNAMIC DETUNINGS

FIELD CANCELLATION

Our requirement is to control the absolute electric field. The field which we apply on our electrodes in the vacuum chamber is additional to any stray electric field arising from the lab equipment or from

surface charges. Only if we measure the stray electric field, we know what needs to be compensated. The measurement and cancellation procedure is shown in Figure 6.2. We detect the transmission spectrum of a probe laser with the control light detuned to typically $\Delta_c = 40$ MHz, c.f. the level scheme of the gate lasers. As shown in the previous chapters, a spectral line of the two-photon absorption is detected. Due to the nature of the Stark shift, the energy of the Rydberg state is lowered for our low angular momentum states, so the electrostatic polarizability α is negative. This means that for Rydberg S states, the absorption line is shifted towards *red* or smaller detunings. The trick is to maximize the resonant detuning by applying an additional electric field. The field with maximum resonant detuning is the compensation field for stray fields. In Figure 6.2c, there was a visible stray electric field. By fitting a parabola to the resonant detunings

$$\Delta_p = \Delta_{p,0} + \frac{\alpha}{2}(\epsilon_z - \epsilon_{z,0})^2 \quad (6.1)$$

one can find the offset field via the fit parameter $\epsilon_{z,0}$. This gives a better result than finding the value with a *maximum* algorithm and without a parabola. If the field is compensated, the polarizability can be measured with a good precision, better than 1%. To do so, a larger field range needs to be scanned. Note that in the plot titles, the values correspond to half the polarizability. In this example, we studied the $66S_{1/2}$ state, for which we calculate a theoretical polarizability of $\alpha_{66S} = 2 \times -174 \text{ MHz}/(\text{V}/\text{cm})^2$. Our measured values are in a good agreement.

We can do those standard measurement routines quickly. One scan takes less than one minute with good statistics. One reason for the fast acquisition is that the scan range of the detuning is set dynamically as a function of the total electric field $\epsilon = \sqrt{\epsilon_x^2 + \epsilon_y^2 + \epsilon_z^2}$ with offsets to both directions. Another reason is that we do not measure one data point in one MOT loading cycle, but a whole detuning scan is done within the recapture pulses of the optical dipole trap.

DYNAMIC DETUNINGS FOR TRANSISTOR MEASUREMENTS

In our transistor measurements, we want to measure the optical gain versus the electric field. As can be seen in Figure 6.2, if we scan the electric field, we need to adapt one of the laser detunings. We could adapt the probe laser detunings to remain resonant on the two-photon transition. For the gate storage, this would be a possibility. The source EIT, on the other hand, would completely change its character and eventually turn into an offresonant absorption due to the Stark shift. For that reason, we adapt the detunings of the control lasers and keep the detuning of the probe transition constant. For example, to adjust the source control detuning on the $64S$ state with $\alpha_{64S} = 2 \times -140.5 \text{ MHz}/(\text{V}/\text{cm})^2$, we set

$$\text{dControl2} = -140.5 * \text{EyOrthogonal} ** 2$$

in our computer control system.

In analogy, the storage of gate photons with an excited state detuning of $\Delta_e = 40$ MHz at electric fields EyOrthogonal is realized by setting the gate control detuning to

$$\text{dControl1} = -174 * \text{EyOrthogonal} ** 2 + 40$$

In practice, our dynamic detunings differ slightly from the theoretical values and we use the full polynomial of $\mathcal{O}(2)$ in EyOrthogonal . We fit the polynomial to scans similar to Figure 6.2, but scanning the control detuning at three different electric fields with a constant probe detuning. This yields for example

$$\text{dControl2} = 150.875 * \text{EyOrthogonal} ** 2 + 0.175 * \text{EyOrthogonal} + 0.59$$

which accounts for an offset due to absolute frequency calibration of the lower transition (technical problem) but also bending of the Stark lines, which is an intrinsic property.

In the end, our main figures of merit are a constant EIT level for the source photons and a constant storage efficiency of the gate photons. These are optimized using the full polynomial.

DETECTION OF RYDBERG PAIR STATES AND BOOSTING THE OPTICAL NONLINEARITY

Having fulfilled the experimental requirement, we can proceed and measure the optical gain of our single photon transistor as a function of the applied electric field $\epsilon = \epsilon_y$, as seen in Figure 6.3. The measurement is started directly after the field cancellation. After the measurement, the field cancellation procedure is repeated to quantify drifts in the electric field. However, evaluating the transistor data without gate photons (every other data file, see Section 6.2.1), we also verify that the source transmission is constant over time and independent of ϵ . In Figure 6.3a, which took two days of measurements, the electric field calibration after data taking yielded a shift of only $\epsilon_{y,0} = 0.009 \text{ V cm}^{-1}$. Our electric field scale is based on this second electric field zero calibration. The difference between the calibration before and after the measurement is on the same order as the resolution of 0.005 V cm^{-1} . Also, the uncertainty in the energy defects affects the crossing points on the same order of magnitude. We take our field calibration after the data to set the electric field axis in Figure 6.3a, which gives slightly better results.

We measure pronounced resonances in the optical gain coinciding with the electric fields of the pair state crossings. As a consequence, we can confirm that Förster resonances can be employed to boost

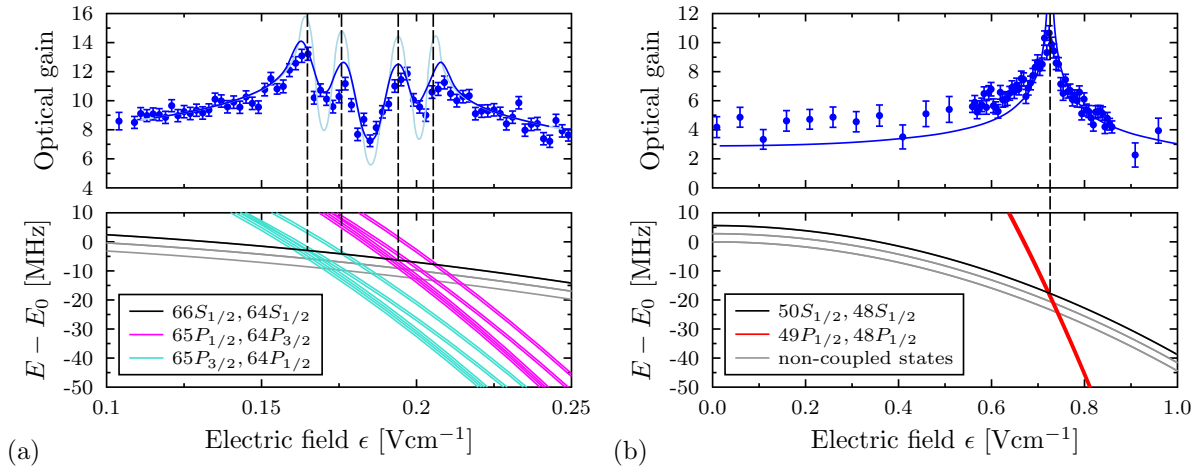


Figure 6.3: Measurement of the optical gain of the single-photon transistor at two different initial states, (a) $r_g = 66S, r_s = 64S$, and (b) $r_g = 50S, r_s = 48S$. The lower panels show the Stark shift of Zeeman pair states for a constant magnetic field of 1 G parallel to the electric field. We measure resonances in the optical gain of the transistor which coincide with the electric fields of the state crossings, the Förster resonances. Between the resonances, the optical gain can even be reduced. The blue curve is based on theory of a polariton incident on a stored gate excitation without free parameters.

the optical nonlinearity of our medium. While the optical gain is increased on the Förster resonances, it is minimized between resonances, most prominently between the central resonances, as elaborated on in Section 6.1.

One limit for the optical gain is the stability of our electric field. The theory established by Przemek Bienias and Hans-Peter Büchler takes into account a field stability of $\Delta\epsilon = \pm 2 \text{ mV cm}^{-1}$. In Figure 6.3a, the theory curve is shown in light blue. For $\Delta\epsilon = \pm 4.5 \text{ mV cm}^{-1}$, which is the electric field drift within the measurement, we obtain the blue curve, which is in very good agreement to our data.

A much simpler situation occurs for the state combination $50S, 48S$, as shown in Figure 6.3b. Due to $J'_1 = J'_2$, the permutation is the identical PP' pair state. Since $J'_1 = J'_2 = \frac{1}{2}$, there are only two different possible magnetic quantum numbers per atom: $\pm \frac{1}{2} = \uparrow$ or \downarrow . So, there are only four Zeeman pair states: $\uparrow\uparrow, \uparrow\downarrow, \downarrow\uparrow, \downarrow\downarrow$. In a head-to-tail configuration, $\theta = 0$, there is only coupling of the form

$$|50S_{1/2} \uparrow, 48S_{1/2} \uparrow\rangle \longleftrightarrow |49P_{1/2} \uparrow, 48P_{1/2} \uparrow\rangle. \quad (6.2)$$

However, we take our three-dimensional geometry due to the finite beam waist into account in our theory and include the other PP' states, which contribute for $\theta > 0$. We only include pair states shown in Figure 6.3. The next Förster resonance of similar strength for $|50S_{1/2}, 48S_{1/2}\rangle$ is in combi-

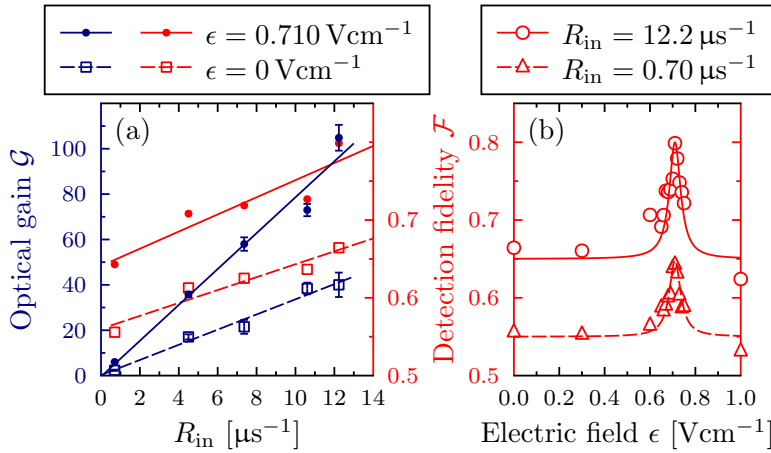


Figure 6.4: Gain and single Rydberg detection enhanced by an electric field exploiting a Förster resonance. The optical gain and the single Rydberg detection fidelity are studied at different source photon rates and at different electric fields. While the optical gain is still increasing with more source photon and a gain of 200 is possible, we restrict the range to prevent source excitation storage. Both the fidelity and the gain show a substantial increase on the Förster resonance.

nation with $|49P_{3/2}, 48P_{1/2}\rangle$ at $\Delta = 840 \text{ MHz}$.

6.3 THE DIPOLE-ENHANCED SINGLE PHOTON TRANSISTOR ON A FÖRSTER RESONANCE

We would like to increase the optical gain of the transistor. To do so, we increase the source rate systematically and measure the optical gain of the transistor at the $|50S_{1/2}, 48S_{1/2}\rangle$ at $\epsilon = 0.710 \text{ V cm}^{-1}$ and compare it to zero field. Shown in Figure 6.4, there is a clear increase in optical gain \mathcal{G} on resonance. At source photon rates of $R_{\text{in}} = 12 \mu\text{s}^{-1}$, the optical gain exceeds $\mathcal{G} = 100$. The linear dependence of \mathcal{G} on R_{in} shows that our optical transistor scheme is robust. After scattering a lot of source photons, the gain does not change.

We performed also a measurement at even higher rates $R_{\text{in}} = 35 \mu\text{s}^{-1}$ and got an optical gain of $\mathcal{G} = 200$. Although, from our measurement procedure, there is no doubt that over 200 source photons have been scattered by storing one gate excitation, there is a point which should be noted. In this regime of high source photon rates, the probability of *Rydberg pollution* sets in, an effect also seen in Reference [88] (Supplemental Information). This effect is independent of the gate photon. It causes a storage of source Rydberg excitations which might or might not dephase or decay to other nearby states. The effect is made visible by tracking the source transmission versus time. For low rates $R_{\text{in}} \lesssim 12 \mu\text{s}^{-1}$, the transmission is almost constant, it decreases by less than 10% due to storage and subsequent scattering with these excitations.

Aside from the optical gain, we also evaluate the single Rydberg excitation detection fidelity \mathcal{F} from the exact same data. For each data point, we perform the procedure described in Section 5.4.

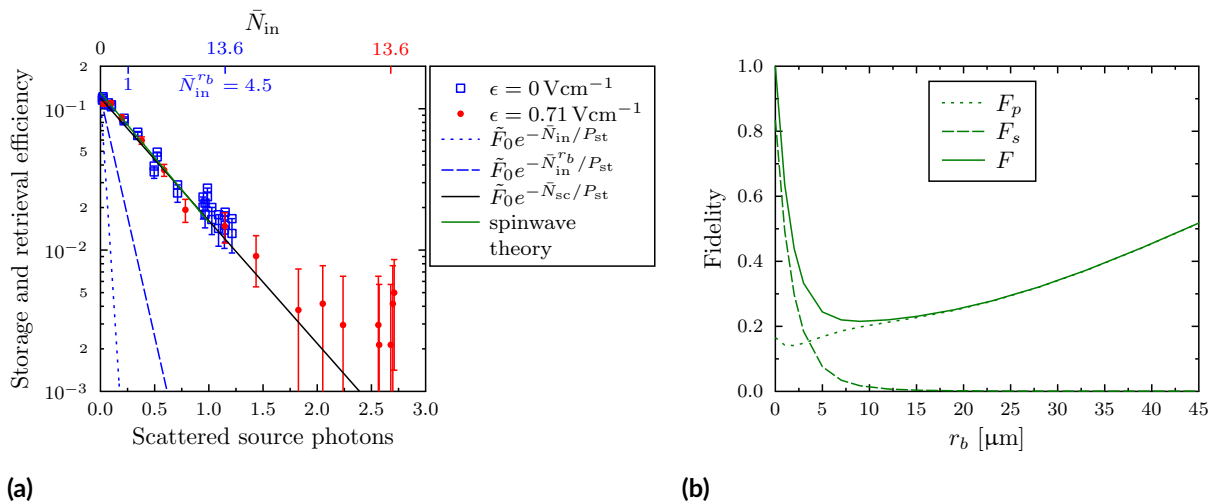


Figure 6.5: (a) With the sequence in Figure 6.6a, we scatter source photons at the gate excitation and try to read out the gate photon afterwards. Although a fair fraction of gate photons can be retrieved without source photons, we see an exponential decrease. The black line is an estimate for our coherent light where the readout is inhibited by one or more scattered source photons. The fact that both data on and off Förster resonance (blue squares and red dots) fall on that line, suggests that this mechanism is present. A similar curve is also obtained if a more sophisticated theory is employed (b). This theory predicts the readout fidelity in a 1D system. We scale it to our 3D geometry, see the green line in (a).

The highest fidelity is obtained on resonance and with the maximum source photon rate. We achieve $\mathcal{F} = 0.8$, which is an improvement compared to Chapter 5. This value is limited by the probe waists $w_0 = 6.2 \mu\text{m}$ of our source and gate lasers.

6.4 TOWARDS PHOTONIC PHASE GATES: READOUT OF THE GATE EXCITATION AND SUSCEPTIBILITY TO SOURCE PHOTON SCATTERING

We would like to retrieve the gate photon after the transistor sequence with gate and source Rydberg states $50S$ and $48S$ respectively. This is possible if the stored gate excitation has not dephased before retrieval. Retrieval is done by shining in the gate control light. Similar to slowing down the gate polariton group velocity to zero during the storage process by reducing the control Rabi frequency, we increase the Rabi frequency again to continue the propagation. Since the gate excitation is a collective state comprising many atoms in the excitation volume and a symmetric superposition of Rydberg excitation states, the coherence of the excitation and thus the directional read-out is quite fragile. Several mechanisms lead to decoherence and therefore to a reduced read-out rate over storage time. Any spatial dependence influences the relative phases. Most prominently, the thermal movement of atoms

causes decoherence. This effect can be minimized by cooling the atoms close to BEC temperatures. Phase imprints can also occur due to electric field gradients. Due to the high polarizability of Rydberg states, this causes inhomogeneous phase shifts. Similarly, the control laser beam itself causes such shifts if it is as small as the gate beam. In that case, phase lag already occurs in the storage process for Rydberg states on the wings of the excitation volume.

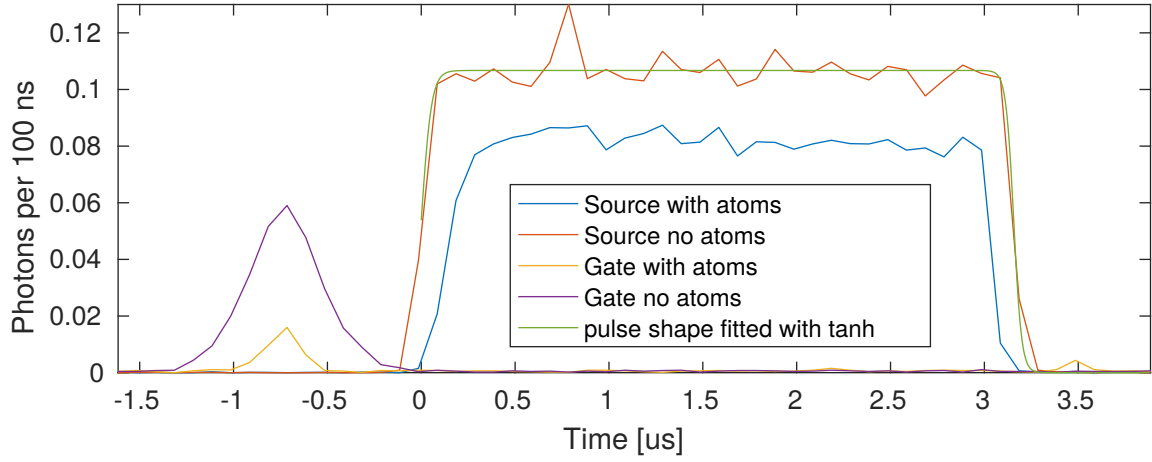
For these reasons, we reduce the interrogation time of source photon scattering to $T = 3.2 \mu\text{s}$, so we perform gate photon read-out $4.2 \mu\text{s}$ after the storage process, see Figure 6.6a. Our data is shown in Figure 6.5a. From a mean number of $\bar{N}_g = 0.8$ incident gate photons, we are able to store and retrieve a considerable fraction: $\tilde{F}_0 = 13\%$. However, if we switch on the source photons, we see an approximately exponential decay in the read-out efficiency with the source rate. The measurement is carried out on the Förster resonance (red dots) and at zero field (blue squares). In both cases, the scan range of incident source photons \bar{N}_{in} is between zero and 13.6. Interestingly, the data collapses on one line in our semi-logarithmic plot, if we plot the data versus the number of scattered source photons.

The number of source photons is controlled by changing the pulse amplitude. Our source photon pulse can best be modeled by

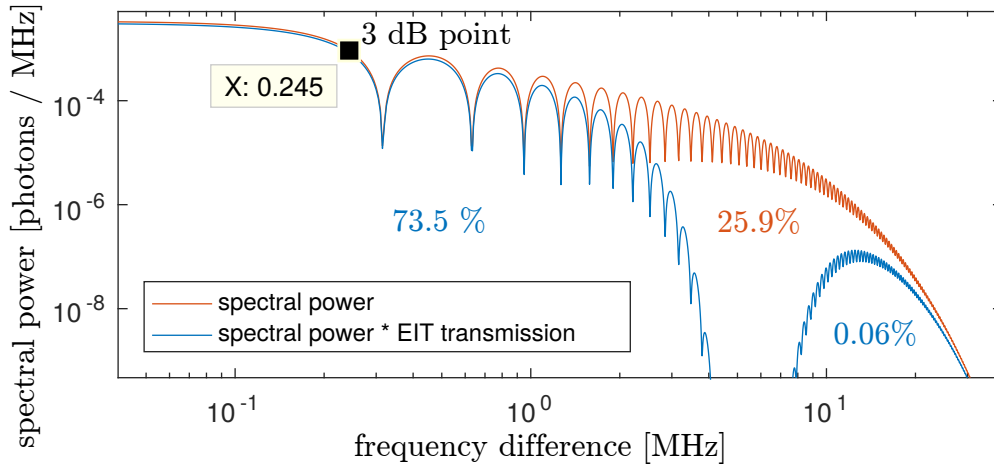
$$R_{\text{in}}(t) = R_{\text{in}}^{\text{max}} \frac{\tanh\left(\frac{t}{t_{\text{rise}}}\right) - \tanh\left(\frac{t-T}{t_{\text{fall}}}\right)}{2} \quad (6.3)$$

as shown in Figure 6.6a. To investigate the frequency components of the source pulse, we make a Fourier transformation in Figure 6.6b (orange curve). We calculate the 3 dB attenuation point to be at $0.245 \text{ MHz} \ll \Delta\nu_{\text{source}} = 3 \text{ MHz}$, so a large fraction would fit into the EIT transparency window. We can quantify this by multiplying the spectrum with our EIT model (blue curve). The largest fraction fits into the EIT window (73.5%), there is absorption due to dephasing (25.9%), and a very small part (0.06%) can be transmitted through high Fourier components. This evaluation is only applicable for small source rates where Rydberg blockade is statistically suppressed. In that case, it is in good agreement with the measured transmission in Figure 6.6a.

We come back to Figure 6.5 to analyze the reasons for the decay in coherence. To do that, we plot several lines in Figure 6.5a which correspond to different scenarios that inhibit gate photon readout. One scenario is that already one incident source photon inhibits the gate photon readout. Due to the Poissonian distribution of gate and source photons, the scenario would cause a readout efficiency of $\tilde{F}_0 e^{-\frac{\bar{N}_{\text{in}}}{P_{\text{st}}}}$, depicted by short blue dashes. It is important to account for the storage efficiency [250], which we measure to be $P_{\text{st}} = 0.5$. Clearly, our data show a much higher readout efficiency, so we exclude this scenario. Similarly, we exclude the scenario where one source photon which is incident in the gate-source blockade sphere destroys the coherence completely, see long dashes in Figure 6.5a.



(a)



(b)

Figure 6.6: (a) Pulse shapes as detected with our single photon counters after averaging over multiple experiments. From the purple pulse (no atoms present), we infer the number of incident gate photons. If we prepare an atomic cloud, the gate pulse can be stored as a Rydberg excitation. Only a small part is transmitted (yellow). The read out gate photons are detected around $3.5 \mu\text{s}$. The read-out efficiency depends on the amount of scattered source photons. The pulse shape of incident source photons (orange) is modeled with Equation 6.3. This is used in (b) to calculate the Fourier components of the pulse (orange). If we multiply this with our EIT transmission, we can derive the fractions which are transmitted through the EIT window (73.5%), absorbed (25.9%) and transmitted with high detunings (0.06%).

In our third scenario we assume that the coherence is destroyed by one scattered source photon (black line). The fact that both data sets, on and off Förster resonance, fall on that line, suggests

that this is actually happening. However, it is not clear, because from the incident source photons, only around one tenth is scattered. It is probable that transmitted source photons also imprint phase shifts on the stored spin-wave, which would decrease the expected read-out efficiency. The extreme assumption that one scattered source photon would inhibit the readout completely, might be similarly unlikely.

To quantify these probabilities, we can make use of existing theory [113] from our collaborators in Nottingham, Weibin Li and Igor Lesanovsky. They are able to simulate the impact of an incident source photon on the many-body wave function of the gate excitation. This can be modeled in one dimension for different interaction potentials and corresponding blockade radii, as shown in Figure 6.5b. The impact is quantified as the quantum mechanical *fidelity*, between the initial and final state [251]

$$F = \left[\text{Tr} \left| \sqrt{\hat{\rho}_i} \sqrt{\hat{\rho}_f} \right| \right]^2 = F_p + F_s \quad (6.4)$$

which is composed of a fidelity where source photons have propagated through the medium, F_p , and a fidelity corresponding to scattering, F_s . These fidelities should in first order give a good estimate about our readout efficiency. Note that this theory does not cover the mode overlap of the outgoing photon field with the mode defined by our optical fibers. In particular, the distance between the atoms and our fiber collimator is not in the theory.

Still, we can try and map the 1D theory to our 3D case to get an idea of the contributions. Our blockade is anisotropic. It is well described by an ellipsoid with semi-axes $r_{b\perp}$ and $r_{b\parallel}$. For $|50S, 48S\rangle$, $r_{b\perp} = 3.87 \mu\text{m}$ and $r_{b\parallel} = 3.23 \mu\text{m}$ according to Equation 4.31 with the C_3 coefficients as calculated in Section 3.5.2. The ellipse equation reads

$$\frac{r^2}{r_{b\perp}^2} + \frac{z^2}{r_{b\parallel}^2} = 1. \quad (6.5)$$

The distance that source photons travel through the blockade ellipsoid is therefore

$$r_b^{\text{eff}} = 2z = 2r_{b\parallel} \Re \left(\sqrt{1 - \frac{r^2}{r_{b\perp}^2}} \right). \quad (6.6)$$

We model our 3D system with many 1D systems parallel to our optical axis with an offset r and with an effective blockade radius as calculated by Equation 6.6. To find the fidelity for our system, we calculate the fidelities for each of these 1D systems by determining the values from Figure 6.5b. The fidelities are weighted by the probability for such a 1D system. The probability is based on the probe beam profile. As a result, we obtain the mean fidelity for a single incident source photon Fock state.

We account for our coherent light statistics and yield the green line in Figure 6.5a, which fits very well to our data.

Our interpretation of these results are such that in this kind of geometry where the blockade radius is much smaller than the excitation volume, it is not likely to sustain the atomic coherence of the gate spin wave. That is why our data fits the estimate curve which allows read-out only for the zero component of the source photon distribution. In a short and dense cloud compared to the blockade radius, we estimate a better chance to read out the gate photons after scattering source photons, as suggested by theory [113].

7

Conclusion and Thoughts

7.1 CONCLUSION

A VERSATILE QUANTUM OPTICS EXPERIMENT WAS BUILT. This experiment is capable of cooling Rubidium atoms to the $1\mu\text{K}$ range. We can trap atoms in a crossed optical dipole trap with a small crossing angle. That way, a cigar-shaped atomic cloud is created. The cloud is transferred to a stretched state using optical pumping. We can detect the size from two sides with absorption imaging, and can monitor atoms with a fluorescence camera. On the *cigar axis*, we can perform Rydberg-EIT with two independent systems (four lasers). We can detect single probe photons on both sides with two HBT setups. Rydberg atoms can be ionized and the ions can be detected on our MCP. Very precise control of electric fields is possible with drifts of less than 5 mV cm^{-1} per day. Fully-automated control of the experimental devices is achieved by computer interfaces. Still, an experimental physicist needs to think about the results.

WE HAVE WITNESSED STRONG OPTICAL NONLINEARITIES IN RYDBERG-EIT. The Rydberg blockade effect mediates an effective interaction for probe photons which leads to saturation at levels of a few photons per μs .

A SINGLE PHOTON SWITCH HAS BEEN DEMONSTRATED. The switch contrast quantifies the ability

to attenuate the transmission of the source EIT by the gate photons. At a mean number of incident gate photons of I , we yield a switch contrast of $C_{\text{coh}} = 0.39(4)$.

SINGLE PHOTON TRANSISTOR. The optical gain \mathcal{G} of the transistor is the amount of source photons which are attenuated by a single incident gate photon. The optical gain is linearly dependent on the rate of source photons. At higher source rates where saturation takes place, we *pollute* our medium with source Rydberg excitations. In the approximately undestructive (and linear) range, we achieve values $\mathcal{G} > 200$.

SINGLE RYDBERG DETECTION. Our optical transistor can be used to detect single Rydberg atoms without removing them with a detection fidelity of 80 % in a single shot. This fidelity can be obtained by analyzing the bimodal distribution of source photons with the modes depending on the presence of a stored gate Rydberg atom.

ELECTRICALLY TUNED FÖRSTER RESONANCES are used to tune the interaction strength of our single photon transistor. That way, we can perform experiments at lower principal quantum numbers which allows higher optical gain. Förster resonances are more than a tool to increase the interaction strength. For example, one can make use of anisotropic resonances due to the Zeeman splitting. We showed that the potential for Rydberg polaritons incident on a Rydberg gate impurity is a r^{-6} potential, and not r^{-3} . With our electric field control, we can identify the fine structure and Zeeman components. This constitutes a new kind of pair state spectroscopy method.

GATE PHOTON READ-OUT AND ATOMIC COHERENCE. We investigated the atomic coherence of the stored Rydberg gate excitation. Although we could read out a considerable fraction of stored photons, this was mainly due to the realizations where no source photons were present. New experiments should be carried out with a short cloud and a large blockade radius.

7.2 THOUGHTS

SPATIALLY RESOLVE RYDBERG EXCITATION WITH TIME-OF-FLIGHT ION DETECTION. The one-dimensional alignment of Rydberg excitations in our cigar-shaped atomic cloud enable the ability to localize Rydberg excitations via the arrival time of Rb^+ ions on the detector. One could do postselection of different arrival times and therefore a postselection of gate excitation positions. That way, the

optical gain of the transistor could be measured for gate excitations stored only in the center of the cloud.

TUNE SELF-NONLINEARITY WITH E-FIELD. It would be very interesting to go to a high-lying Rydberg SS state and to tune it with electric fields. According to our plot in Figure 3.9, the interaction should be reduced with higher fields because the main contribution are due to PP' states with a small negative Förster defect. This would result in reduced nonlinearity of single-state Rydberg-EIT.

OPTICAL TRANSISTOR WITH RYDBERG DRESSED GROUND STATES. One could try to implement Rydberg dressing proposals. It would be interesting to see the effect on the gain and the life time. Maybe the gate photon read-out could be more robust to source photon scattering.

IF THE EXPERIMENT WAS TO BE REBUILT, I WOULD...

- change the geometry of the crossed dipole trap to make space for larger probe optics, at least 1 inch optics. That way, a smaller probe focus can be achieved. The probe beam would not clip on the border and a better beam profile could be obtained. In light of our recent efforts to make the cloud as short as possible to be shorter than one blockade sphere, it is not necessary any more to have such a shallow angle between the dipole trap beams.
- use a different mode of operation in the single photon counters. So far, the counters were programmed such that their output is the number of counts in certain bins. However, there is a mode called dump, which can output actual time tags. In many experiments, we wanted to have a very good time resolution, so we decreased the bin time. As a result, the vast majority of bins stayed empty. Even though the Python matrices are constructed such that only small memory is allocated for the entries, `uint8`, the large dimensionality in four counters were limiting the experiment and created unnecessarily large files despite compression. If actual time tags are recorded, the choice of binning can be decided after the experiment, since optimal bin times depend on the amount of data, the required resolution and statistical significance.

A

Rydberg energy calculation

The energies of a Rydberg state with principal quantum number n can be calculated with the Rydberg formula

$$E = \frac{-\mathcal{R}^*}{n^2} = \frac{-\mathcal{R}^*}{(n - \delta_0 - \delta_2/(n - \delta_0)^2)^2} . \quad (\text{A.1})$$

Since there are many different measurements[citations!] for the quantum defects δ_0, δ_2 and for the Rydberg constant \mathcal{R}^* , here are the numbers for the Rydberg states used in this work.

For ^{87}Rb , the Rydberg constant has been measured [252]:

$$\mathcal{R}^* = h \times 3289.821\,194\,66(2) \text{ THz} . \quad (\text{A.2})$$

The quantum defect depends on the angular momentum quantum number L of the Rydberg state [252]:

$$\text{for } nS_{1/2}: \quad \delta_0 = 3.1311807(8), \quad \delta_2 = 0.1787(2) \quad (\text{A.3})$$

$$\text{for } nD_{3/2}: \quad \delta_0 = 1.3480948(11), \quad \delta_2 = -0.6054(4) \quad (\text{A.4})$$

$$\text{for } nD_{5/2}: \quad \delta_0 = 1.3464622(11), \quad \delta_2 = -0.5940(4) . \quad (\text{A.5})$$

For P states, we use data from [253]

$$\begin{aligned}
 \mathcal{R}^* &= h \times R_{\text{Rb}} \times c \\
 &= h \times 109\,736.605 \text{ cm}^{-1} \times 2.997\,924\,58 \times 10^{10} \text{ cm/s} \\
 &= h \times 3289.820\,654\,552\,509 \text{ THz}
 \end{aligned}
 \tag{A.6}$$

$$\text{for } nP_{1/2}: \quad \delta_0 = 2.6548849(10), \quad \delta_2 = 0.2900(6)
 \tag{A.7}$$

$$\text{for } nP_{3/2}: \quad \delta_0 = 2.6416737(10), \quad \delta_2 = 0.2950(7) .
 \tag{A.8}$$

For F states, values are taken from [196]. For higher angular momenta and $n \geq 8$, the energies approach the hydrogen spectrum, so we can approximate $\delta_0 = \delta_2 = 0$ and

$$\mathcal{R}^* = h \times 3289.821\,194\,66(2) \text{ THz}.
 \tag{A.9}$$

A look-up table is provided together with the electrostatic polarizabilities in Table B.I.

B

Electrostatic polarizabilities

Here is a reference for electrostatic polarizabilities α . With $E_{\text{Stark}} = -\frac{\alpha}{2}\epsilon^2$, the energy shift due to the d.c. Stark effect at a given field ϵ can quickly be evaluated. This formula is only valid for small fields, before state crossings with the hydrogenic manifolds.

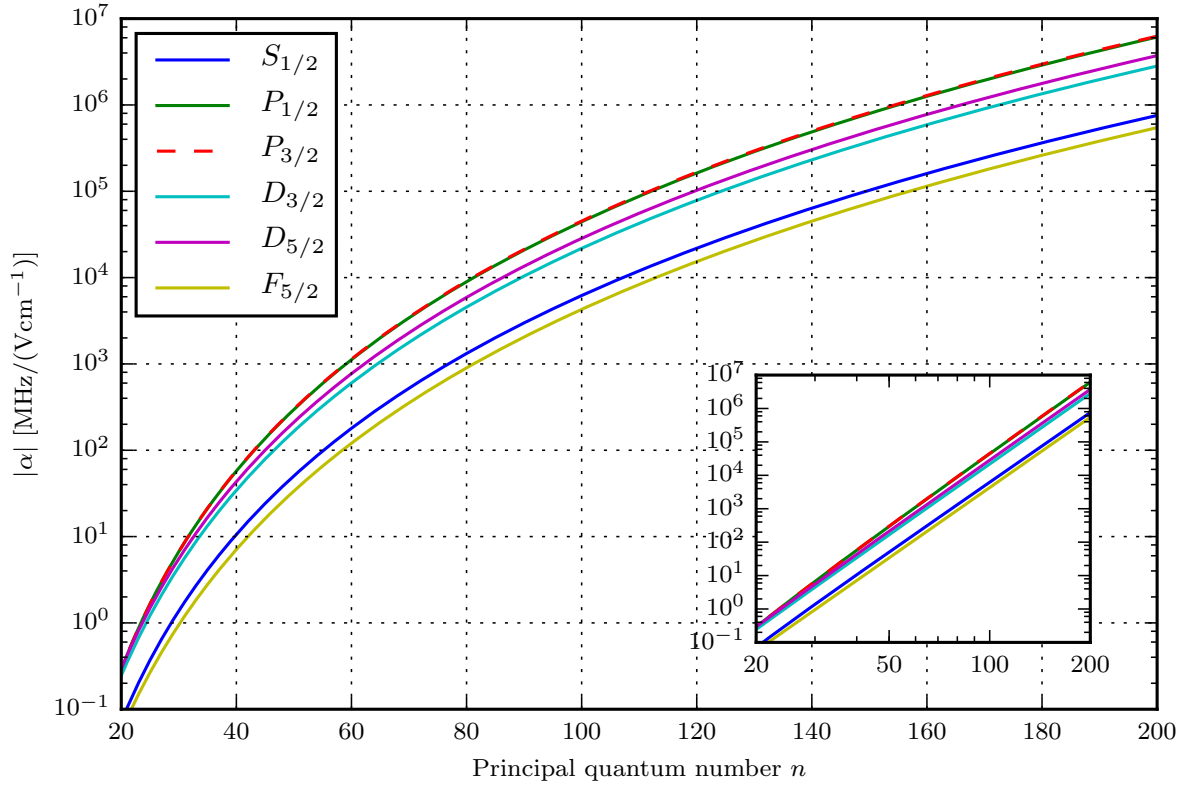


Figure B.1: Electrostatic polarizabilities. These values determine the d.c. Stark shift. The difference in the Stark shift is used to tune the relative energy of pair states, in particular to degeneracy, which is where strong Förster resonances can occur. In the inset, the same data is plotted with two logarithmic axes. Comparing values of one order of magnitude in n , we can easily see the power scaling $\alpha \propto n^7$. For similar scalings, see Reference [140].

n	E_S [GHz]	α_S [MHz cm/V]	$E_{P_{1/2}}$	$\alpha_{P_{1/2}}$	$E_{P_{3/2}}$	$\alpha_{P_{3/2}}$	$E_{D_{3/2}}$	$\alpha_{D_{3/2}}$	$E_{D_{5/2}}$	$\alpha_{D_{5/2}}$
10	-69805.863	-0.0002722	-61066.343	-0.0008112	-60847.195	-0.0007784	-43865.451	-0.001469	-43850.522	-0.001628
11	-53170.679	-0.0006271	-47284.884	-0.001953	-47135.887	-0.001884	-35266.437	-0.003029	-35255.426	-0.003404
12	-41847.818	-0.001305	-37693.024	-0.004257	-37586.898	-0.004123	-28965.614	-0.005824	-28957.296	-0.006622
13	-33791.184	-0.002521	-30751.929	-0.008548	-30673.983	-0.008308	-24212.859	-0.01057	-24206.431	-0.01214
14	-27856.622	-0.004567	-25565.820	-0.0161	-25505.861	-0.01572	-20540.018	-0.01827	-20534.954	-0.02119
15	-23358.777	-0.007862	-21589.373	-0.02875	-21543.504	-0.02811	-17643.272	-0.03032	-17639.214	-0.03545
16	-19868.621	-0.01295	-18473.650	-0.04908	-18436.455	-0.04817	-15318.524	-0.04857	-15315.224	-0.05724
17	-17106.120	-0.02053	-15986.851	-0.08063	-15956.872	-0.0793	-13424.581	-0.07538	-13421.862	-0.08958
18	-14882.180	-0.03133	-13969.548	-0.1286	-13944.365	-0.1269	-11861.253	-0.1142	-11858.987	-0.1364
19	-13065.376	-0.0465	-12311.695	-0.199	-12291.310	-0.1962	-10555.858	-0.1698	-10553.950	-0.2028
20	-11562.061	-0.07026	-10936.192	-0.293	-10919.570	-0.2903	-9454.637	-0.2458	-9453.016	-0.295
21	-10304.046	-0.1035	-9776.246	-0.4304	-9762.195	-0.4271	-8517.138	-0.3493	-8515.749	-0.4211
22	-9240.723	-0.1459	-8791.528	-0.6196	-8779.543	-0.6158	-7712.450	-0.488	-7711.251	-0.5906
23	-8333.894	-0.2022	-7948.439	-0.8759	-7938.134	-0.8717	-7016.625	-0.6713	-7015.583	-0.8154
24	-7554.289	-0.2759	-7221.063	-1.218	-7212.139	-1.214	-6410.879	-0.9106	-6409.968	-1.11
25	-6879.177	-0.3713	-6589.153	-1.668	-6581.374	-1.665	-5880.311	-1.219	-5879.509	-1.491
26	-6290.683	-0.4933	-6036.705	-2.255	-6029.883	-2.252	-5412.977	-1.614	-5412.269	-1.979
27	-5774.599	-0.6478	-5550.933	-3.009	-5544.917	-3.008	-4999.216	-2.112	-4998.586	-2.598
28	-5319.515	-0.8415	-5121.523	-3.969	-5116.191	-3.972	-4631.141	-2.737	-4630.579	-3.376
29	-4916.183	-1.082	-4740.081	-5.181	-4735.333	-5.19	-4302.266	-3.515	-4301.763	-4.344
30	-4557.043	-1.38	-4399.720	-6.697	-4395.474	-6.714	-4007.218	-4.473	-4006.765	-5.543
31	-4235.867	-1.743	-4094.745	-8.578	-4090.932	-8.606	-3741.510	-5.648	-3741.101	-7.013
32	-3947.487	-2.185	-3820.415	-10.89	-3816.979	-10.94	-3501.379	-7.077	-3501.009	-8.806
33	-3687.585	-2.719	-3572.758	-13.73	-3569.651	-13.79	-3283.643	-8.805	-3283.307	-10.98
34	-3452.531	-3.361	-3348.426	-17.17	-3345.606	-17.26	-3085.604	-10.88	-3085.297	-13.59
35	-3239.255	-4.126	-3144.577	-21.32	-3142.011	-21.45	-2904.953	-13.37	-2904.673	-16.72
36	-3045.148	-5.036	-2958.793	-26.31	-2956.451	-26.48	-2739.715	-16.32	-2739.459	-20.45
37	-2867.980	-6.111	-2789.000	-32.26	-2786.856	-32.49	-2588.184	-19.82	-2587.949	-24.87
38	-2705.836	-7.375	-2633.414	-39.34	-2631.447	-39.64	-2448.886	-23.94	-2448.669	-30.09
39	-2557.063	-8.854	-2490.493	-47.7	-2488.684	-48.09	-2320.537	-28.77	-2320.337	-36.21
40	-2420.232	-10.58	-2358.900	-57.54	-2357.232	-58.04	-2202.021	-34.41	-2201.835	-43.38
41	-2294.096	-12.58	-2237.467	-69.07	-2235.926	-69.71	-2092.357	-40.98	-2092.185	-51.72
42	-2177.571	-14.9	-2125.175	-82.53	-2123.749	-83.32	-1990.686	-48.59	-1990.526	-61.41
43	-2069.703	-17.58	-2021.129	-98.18	-2019.807	-99.16	-1896.249	-57.38	-1896.101	-72.6
44	-1969.656	-20.65	-1924.542	-116.3	-1923.313	-117.5	-1808.376	-67.5	-1808.238	-85.51

n	E_S [GHz]	α_S [MHz cm/V]	$E_{P_{1/2}}$	$\alpha_{P_{1/2}}$	$E_{P_{3/2}}$	$\alpha_{P_{3/2}}$	$E_{D_{3/2}}$	$\alpha_{D_{3/2}}$	$E_{D_{5/2}}$	$\alpha_{D_{5/2}}$
45	-1876.692	-24.17	-1834.716	-137.2	-1833.572	-138.7	-1726.472	-79.11	-1726.343	-100.3
46	-1790.157	-28.18	-1751.036	-161.3	-1749.969	-163.1	-1650.009	-92.4	-1649.889	-117.3
47	-1709.473	-32.75	-1672.952	-188.8	-1671.956	-191	-1578.516	-107.5	-1578.403	-136.7
48	-1634.123	-37.94	-1599.978	-220.4	-1599.046	-223	-1511.570	-124.8	-1511.465	-158.7
49	-1563.647	-43.82	-1531.676	-256.3	-1530.803	-259.4	-1448.795	-144.3	-1448.696	-183.7
50	-1497.634	-50.45	-1467.656	-297.1	-1466.837	-300.9	-1389.850	-166.4	-1389.757	-212.1
51	-1435.715	-57.92	-1407.568	-343.4	-1406.799	-347.8	-1334.431	-191.4	-1334.344	-244.1
52	-1377.558	-66.32	-1351.095	-395.8	-1350.372	-401	-1282.262	-219.5	-1282.179	-280.1
53	-1322.865	-75.73	-1297.955	-454.8	-1297.274	-460.9	-1233.093	-251	-1233.015	-320.7
54	-1271.365	-86.26	-1247.889	-521.2	-1247.247	-528.4	-1186.699	-286.4	-1186.625	-366.1
55	-1222.815	-98.02	-1200.664	-595.8	-1200.059	-604.1	-1142.875	-325.9	-1142.805	-417
56	-1176.994	-111.1	-1156.071	-679.3	-1155.499	-689	-1101.434	-370	-1101.368	-473.8
57	-1133.701	-125.7	-1113.917	-772.6	-1113.376	-783.8	-1062.207	-419.2	-1062.145	-537.1
58	-1092.753	-141.8	-1074.027	-876.8	-1073.514	-889.7	-1025.039	-473.8	-1024.980	-607.5
59	-1053.984	-159.7	-1036.242	-992.7	-1035.756	-1008	-989.788	-534.4	-989.732	-685.7
60	-1017.243	-179.5	-1000.416	-1122	-999.955	-1139	-956.325	-601.6	-956.272	-772.3
61	-982.390	-201.4	-966.417	-1265	-965.979	-1284	-924.530	-675.8	-924.480	-868.2
62	-949.298	-225.5	-934.122	-1423	-933.706	-1445	-894.295	-757.8	-894.247	-974.1
63	-917.850	-252	-903.419	-1598	-903.023	-1623	-865.520	-848.2	-865.474	-1091
64	-887.939	-281.1	-874.205	-1791	-873.829	-1819	-838.111	-947.6	-838.067	-1219
65	-859.467	-313	-846.386	-2003	-846.027	-2036	-811.984	-1057	-811.942	-1361
66	-832.343	-348	-819.874	-2237	-819.532	-2274	-787.060	-1177	-787.020	-1516
67	-806.483	-386.3	-794.588	-2494	-794.262	-2536	-763.266	-1308	-763.228	-1686
68	-781.809	-428.2	-770.454	-2776	-770.143	-2823	-740.535	-1452	-740.498	-1872
69	-758.251	-473.8	-747.404	-3085	-747.106	-3137	-718.804	-1609	-718.769	-2076
70	-735.742	-523.5	-725.372	-3423	-725.088	-3481	-698.016	-1780	-697.983	-2298
71	-714.220	-577.7	-704.301	-3792	-704.028	-3857	-678.117	-1967	-678.085	-2540
72	-693.629	-636.5	-684.134	-4195	-683.874	-4268	-659.057	-2170	-659.027	-2804
73	-673.916	-700.4	-664.822	-4633	-664.572	-4715	-640.789	-2391	-640.760	-3091
74	-655.032	-769.7	-646.315	-5111	-646.076	-5201	-623.271	-2632	-623.243	-3403
75	-636.930	-844.7	-628.571	-5630	-628.342	-5730	-606.461	-2892	-606.434	-3741
76	-619.568	-926	-611.548	-6193	-611.328	-6304	-590.322	-3174	-590.297	-4108
77	-602.907	-1014	-595.207	-6804	-594.995	-6927	-574.819	-3480	-574.795	-4505
78	-586.909	-1109	-579.512	-7466	-579.309	-7603	-559.919	-3810	-559.895	-4935
79	-571.539	-1211	-564.430	-8183	-564.235	-8333	-545.591	-4167	-545.568	-5399

n	E_S [GHz]	α_S [MHz cm/V]	$E_{P_{1/2}}$	$\alpha_{P_{1/2}}$	$E_{P_{3/2}}$	$\alpha_{P_{3/2}}$	$E_{D_{3/2}}$	$\alpha_{D_{3/2}}$	$E_{D_{5/2}}$	$\alpha_{D_{5/2}}$
80	-556.765	-1321	-549.929	-8958	-549.742	-9123	-531.805	-4552	-531.783	-5901
81	-542.557	-1440	-535.980	-9794	-535.800	-9977	-518.536	-4968	-518.515	-6442
82	-528.886	-1568	-522.555	-1.07e+04	-522.381	-1.09e+04	-505.757	-5415	-505.737	-7024
83	-515.725	-1705	-509.629	-1.167e+04	-509.461	-1.189e+04	-493.445	-5897	-493.425	-7651
84	-503.049	-1833	-497.176	-1.272e+04	-497.014	-1.296e+04	-481.577	-6414	-481.558	-8326
85	-490.835	-2011	-485.173	-1.385e+04	-485.018	-1.411e+04	-470.132	-6971	-470.114	-9051
86	-479.060	-2181	-473.601	-1.506e+04	-473.451	-1.535e+04	-459.090	-7568	-459.072	-9829
87	-467.704	-2363	-462.437	-1.636e+04	-462.292	-1.668e+04	-448.433	-8208	-448.416	-1.066e+04
88	-456.748	-2557	-451.664	-1.776e+04	-451.524	-1.81e+04	-438.142	-8894	-438.126	-1.156e+04
89	-446.171	-2765	-441.263	-1.926e+04	-441.128	-1.963e+04	-428.202	-9629	-428.186	-1.252e+04
90	-435.958	-2988	-431.216	-2.086e+04	-431.086	-2.127e+04	-418.596	-1.042e+04	-418.581	-1.354e+04
91	-426.092	-3226	-421.510	-2.258e+04	-421.384	-2.303e+04	-409.310	-1.126e+04	-409.295	-1.464e+04
92	-416.556	-3479	-412.127	-2.442e+04	-412.005	-2.491e+04	-400.330	-1.215e+04	-400.315	-1.581e+04
93	-407.338	-3750	-403.034	-2.639e+04	-402.936	-2.692e+04	-391.641	-1.311e+04	-391.627	-1.707e+04
94	-398.421	-4038	-394.277	-2.849e+04	-394.163	-2.906e+04	-383.233	-1.414e+04	-383.220	-1.84e+04
95	-389.795	-4345	-385.784	-3.073e+04	-385.674	-3.135e+04	-375.093	-1.523e+04	-375.079	-1.983e+04
96	-381.446	-4672	-377.563	-3.312e+04	-377.456	-3.379e+04	-367.209	-1.639e+04	-367.196	-2.135e+04
97	-373.362	-5019	-369.601	-3.567e+04	-369.498	-3.64e+04	-359.571	-1.765e+04	-359.559	-2.297e+04
98	-365.532	-5389	-361.889	-3.839e+04	-361.789	-3.917e+04	-352.169	-1.894e+04	-352.157	-2.469e+04
99	-357.946	-5781	-354.416	-4.128e+04	-354.319	-4.213e+04	-344.993	-2.034e+04	-344.981	-2.652e+04
100	-350.594	-6198	-347.172	-4.436e+04	-347.077	-4.527e+04	-338.034	-2.183e+04	-338.023	-2.846e+04
101	-343.466	-6641	-340.147	-4.769e+04	-340.056	-4.861e+04	-331.284	-2.341e+04	-331.273	-3.053e+04
102	-336.553	-7109	-333.334	-5.11e+04	-333.245	-5.216e+04	-324.734	-2.509e+04	-324.723	-3.272e+04
103	-329.847	-7607	-326.723	-5.479e+04	-326.637	-5.593e+04	-318.376	-2.686e+04	-318.366	-3.505e+04
104	-323.339	-8132	-320.307	-5.871e+04	-320.224	-5.994e+04	-312.204	-2.875e+04	-312.194	-3.752e+04
105	-317.022	-8690	-314.079	-6.286e+04	-313.997	-6.418e+04	-306.209	-3.075e+04	-306.199	-4.014e+04
106	-310.889	-9280	-308.030	-6.727e+04	-307.951	-6.868e+04	-300.385	-3.286e+04	-300.375	-4.291e+04
107	-304.931	-9903	-302.154	-7.193e+04	-302.077	-7.345e+04	-294.725	-3.51e+04	-294.716	-4.584e+04
108	-299.144	-1.056e+04	-296.445	-7.687e+04	-296.370	-7.85e+04	-289.224	-3.747e+04	-289.215	-4.894e+04
109	-293.519	-1.126e+04	-290.896	-8.21e+04	-290.823	-8.384e+04	-283.876	-3.998e+04	-283.867	-5.223e+04
110	-288.052	-1.199e+04	-285.501	-8.763e+04	-285.431	-8.95e+04	-278.674	-4.262e+04	-278.666	-5.57e+04
111	-282.736	-1.277e+04	-280.255	-9.347e+04	-280.187	-9.547e+04	-273.615	-4.542e+04	-273.607	-5.936e+04
112	-277.565	-1.359e+04	-275.153	-9.965e+04	-275.086	-1.018e+05	-268.692	-4.837e+04	-268.684	-6.323e+04
113	-272.536	-1.445e+04	-270.188	-1.062e+05	-270.123	-1.085e+05	-263.900	-5.148e+04	-263.892	-6.731e+04
114	-267.642	-1.536e+04	-265.357	-1.131e+05	-265.294	-1.155e+05	-259.236	-5.477e+04	-259.228	-7.162e+04

n	E_S [GHz]	α_S [MHz cm/V]	$E_{P_{1/2}}$	$\alpha_{P_{1/2}}$	$E_{P_{3/2}}$	$\alpha_{P_{3/2}}$	$E_{D_{3/2}}$	$\alpha_{D_{3/2}}$	$E_{D_{5/2}}$	$\alpha_{D_{5/2}}$
115	-262.878	-1.632e+04	-260.694	-1.203e+05	-260.592	-1.229e+05	-254.694	-5.823e+04	-254.687	-7.616e+04
116	-258.241	-1.733e+04	-256.075	-1.28e+05	-256.015	-1.308e+05	-250.270	-6.188e+04	-250.263	-8.095e+04
117	-253.725	-1.839e+04	-251.615	-1.361e+05	-251.557	-1.39e+05	-245.961	-6.572e+04	-245.954	-8.599e+04
118	-249.326	-1.95e+04	-247.271	-1.446e+05	-247.215	-1.477e+05	-241.762	-6.976e+04	-241.755	-9.13e+04
119	-245.041	-2.068e+04	-243.039	-1.535e+05	-242.984	-1.569e+05	-237.670	-7.402e+04	-237.663	-9.688e+04
120	-240.866	-2.191e+04	-238.914	-1.63e+05	-238.861	-1.665e+05	-233.681	-7.85e+04	-233.674	-1.028e+05
121	-236.796	-2.321e+04	-234.894	-1.729e+05	-234.841	-1.767e+05	-229.791	-8.32e+04	-229.785	-1.089e+05
122	-232.829	-2.457e+04	-230.974	-1.833e+05	-230.923	-1.874e+05	-225.997	-8.815e+04	-225.991	-1.154e+05
123	-228.960	-2.6e+04	-227.151	-1.943e+05	-227.102	-1.986e+05	-222.297	-9.335e+04	-222.291	-1.223e+05
124	-225.187	-2.75e+04	-223.423	-2.058e+05	-223.374	-2.104e+05	-218.687	-9.88e+04	-218.681	-1.294e+05
125	-221.507	-2.907e+04	-219.786	-2.179e+05	-219.738	-2.228e+05	-215.164	-1.045e+05	-215.159	-1.37e+05
126	-217.916	-3.072e+04	-216.236	-2.307e+05	-216.190	-2.358e+05	-211.726	-1.105e+05	-211.720	-1.448e+05
127	-214.412	-3.245e+04	-212.772	-2.44e+05	-212.727	-2.495e+05	-208.369	-1.168e+05	-208.364	-1.531e+05
128	-210.991	-3.426e+04	-209.391	-2.58e+05	-209.347	-2.638e+05	-205.092	-1.235e+05	-205.087	-1.618e+05
129	-207.652	-3.616e+04	-206.089	-2.727e+05	-206.046	-2.788e+05	-201.891	-1.304e+05	-201.886	-1.709e+05
130	-204.391	-3.815e+04	-202.865	-2.881e+05	-202.823	-2.946e+05	-198.765	-1.376e+05	-198.760	-1.805e+05
131	-201.207	-4.023e+04	-199.716	-3.043e+05	-199.675	-3.111e+05	-195.711	-1.452e+05	-195.706	-1.905e+05
132	-198.096	-4.24e+04	-196.640	-3.212e+05	-196.600	-3.284e+05	-192.726	-1.532e+05	-192.721	-2.009e+05
133	-195.057	-4.468e+04	-193.635	-3.389e+05	-193.595	-3.465e+05	-189.809	-1.615e+05	-189.805	-2.119e+05
134	-192.088	-4.706e+04	-190.697	-3.574e+05	-190.659	-3.655e+05	-186.958	-1.703e+05	-186.954	-2.233e+05
135	-189.186	-4.955e+04	-187.826	-3.768e+05	-187.789	-3.854e+05	-184.171	-1.794e+05	-184.167	-2.355e+05
136	-186.349	-5.215e+04	-185.020	-3.971e+05	-184.983	-4.062e+05	-181.446	-1.889e+05	-181.441	-2.479e+05
137	-183.575	-5.486e+04	-182.276	-4.183e+05	-182.240	-4.279e+05	-178.781	-1.989e+05	-178.776	-2.61e+05
138	-180.863	-5.77e+04	-179.592	-4.403e+05	-179.557	-4.506e+05	-176.174	-2.093e+05	-176.169	-2.747e+05
139	-178.210	-6.066e+04	-176.967	-4.637e+05	-176.933	-4.744e+05	-173.623	-2.201e+05	-173.619	-2.89e+05
140	-175.616	-6.375e+04	-174.400	-4.88e+05	-174.366	-4.992e+05	-171.128	-2.315e+05	-171.124	-3.039e+05
141	-173.077	-6.697e+04	-171.888	-5.133e+05	-171.855	-5.251e+05	-168.686	-2.433e+05	-168.682	-3.195e+05
142	-170.594	-7.034e+04	-169.429	-5.397e+05	-169.397	-5.522e+05	-166.296	-2.557e+05	-166.292	-3.358e+05
143	-168.163	-7.384e+04	-167.024	-5.673e+05	-166.992	-5.804e+05	-163.956	-2.686e+05	-163.952	-3.528e+05
144	-165.784	-7.749e+04	-164.669	-5.961e+05	-164.638	-6.099e+05	-161.665	-2.821e+05	-161.662	-3.705e+05
145	-163.455	-8.13e+04	-162.363	-6.261e+05	-162.333	-6.406e+05	-159.422	-2.961e+05	-159.419	-3.89e+05
146	-161.175	-8.526e+04	-160.106	-6.574e+05	-160.076	-6.727e+05	-157.226	-3.107e+05	-157.222	-4.082e+05
147	-158.942	-8.94e+04	-157.895	-6.901e+05	-157.866	-7.061e+05	-155.074	-3.26e+05	-155.071	-4.283e+05
148	-156.755	-9.37e+04	-155.730	-7.241e+05	-155.701	-7.41e+05	-152.967	-3.418e+05	-152.963	-4.492e+05
149	-154.613	-9.817e+04	-153.609	-7.596e+05	-153.581	-7.773e+05	-150.902	-3.584e+05	-150.898	-4.71e+05

n	E_S [GHz]	α_S [MHz cm/V]	$E_{P_{3/2}}$	$\alpha_{P_{3/2}}$	$E_{P_{3/2}}$	$\alpha_{P_{3/2}}$	$E_{D_{3/2}}$	$\alpha_{D_{3/2}}$	$E_{D_{3/2}}$	$\alpha_{D_{3/2}}$
150	-152.515	-1.028e+05	-151.531	-7.965e+05	-151.504	-8.151e+05	-148.878	-3.756e+05	-148.875	-4.937e+05
151	-150.459	-1.077e+05	-149.495	-8.335e+05	-149.468	-8.545e+05	-146.895	-3.935e+05	-146.892	-5.173e+05
152	-148.445	-1.127e+05	-147.499	-8.751e+05	-147.473	-8.956e+05	-144.952	-4.121e+05	-144.948	-5.418e+05
153	-146.470	-1.18e+05	-145.544	-9.167e+05	-145.518	-9.382e+05	-143.046	-4.315e+05	-143.043	-5.674e+05
154	-144.535	-1.234e+05	-143.627	-9.601e+05	-143.602	-9.827e+05	-141.178	-4.517e+05	-141.175	-5.94e+05
155	-142.638	-1.291e+05	-141.747	-1.005e+06	-141.723	-1.029e+06	-139.347	-4.727e+05	-139.344	-6.216e+05
156	-140.778	-1.35e+05	-139.905	-1.052e+06	-139.881	-1.077e+06	-137.550	-4.945e+05	-137.547	-6.503e+05
157	-138.954	-1.411e+05	-138.098	-1.101e+06	-138.074	-1.127e+06	-135.789	-5.171e+05	-135.786	-6.802e+05
158	-137.165	-1.474e+05	-136.325	-1.152e+06	-136.302	-1.179e+06	-134.060	-5.407e+05	-134.058	-7.113e+05
159	-135.411	-1.54e+05	-134.587	-1.204e+06	-134.564	-1.233e+06	-132.365	-5.651e+05	-132.362	-7.435e+05
160	-133.690	-1.609e+05	-132.882	-1.259e+06	-132.860	-1.289e+06	-130.702	-5.905e+05	-130.699	-7.77e+05
161	-132.002	-1.68e+05	-131.209	-1.316e+06	-131.187	-1.347e+06	-129.070	-6.169e+05	-129.067	-8.118e+05
162	-130.345	-1.753e+05	-129.567	-1.375e+06	-129.546	-1.408e+06	-127.468	-6.443e+05	-127.465	-8.479e+05
163	-128.720	-1.83e+05	-127.936	-1.436e+06	-127.915	-1.471e+06	-125.896	-6.727e+05	-125.893	-8.854e+05
164	-127.124	-1.909e+05	-126.375	-1.5e+06	-126.354	-1.536e+06	-124.352	-7.022e+05	-124.350	-9.242e+05
165	-125.558	-1.991e+05	-124.823	-1.566e+06	-124.802	-1.604e+06	-122.837	-7.327e+05	-122.835	-9.646e+05
166	-124.021	-2.076e+05	-123.299	-1.635e+06	-123.279	-1.674e+06	-121.350	-7.645e+05	-121.347	-1.006e+06
167	-122.512	-2.165e+05	-121.803	-1.706e+06	-121.784	-1.747e+06	-119.889	-7.973e+05	-119.887	-1.05e+06
168	-121.031	-2.256e+05	-120.334	-1.78e+06	-120.315	-1.822e+06	-118.455	-8.314e+05	-118.452	-1.095e+06
169	-119.576	-2.351e+05	-118.892	-1.856e+06	-118.873	-1.901e+06	-117.046	-8.667e+05	-117.043	-1.141e+06
170	-118.147	-2.449e+05	-117.475	-1.935e+06	-117.457	-1.982e+06	-115.662	-9.034e+05	-115.659	-1.19e+06
171	-116.743	-2.551e+05	-116.084	-2.017e+06	-116.065	-2.066e+06	-114.302	-9.413e+05	-114.300	-1.24e+06
172	-115.365	-2.656e+05	-114.717	-2.103e+06	-114.699	-2.153e+06	-112.967	-9.805e+05	-112.964	-1.292e+06
173	-114.011	-2.765e+05	-113.374	-2.191e+06	-113.356	-2.243e+06	-111.654	-1.021e+06	-111.652	-1.345e+06
174	-112.680	-2.878e+05	-112.054	-2.282e+06	-112.037	-2.337e+06	-110.365	-1.063e+06	-110.362	-1.401e+06
175	-111.373	-2.994e+05	-110.758	-2.377e+06	-110.741	-2.434e+06	-109.097	-1.107e+06	-109.095	-1.458e+06
176	-110.088	-3.115e+05	-109.484	-2.474e+06	-109.467	-2.534e+06	-107.851	-1.152e+06	-107.849	-1.518e+06
177	-108.825	-3.24e+05	-108.231	-2.576e+06	-108.215	-2.638e+06	-106.627	-1.199e+06	-106.625	-1.58e+06
178	-107.584	-3.369e+05	-107.000	-2.681e+06	-106.984	-2.746e+06	-105.423	-1.247e+06	-105.421	-1.643e+06
179	-106.364	-3.503e+05	-105.790	-2.789e+06	-105.774	-2.857e+06	-104.240	-1.297e+06	-104.238	-1.709e+06
180	-105.165	-3.641e+05	-104.601	-2.901e+06	-104.585	-2.972e+06	-103.076	-1.349e+06	-103.074	-1.778e+06
181	-103.985	-3.783e+05	-103.431	-3.017e+06	-103.415	-3.091e+06	-101.932	-1.402e+06	-101.930	-1.848e+06
182	-102.826	-3.931e+05	-102.281	-3.137e+06	-102.266	-3.214e+06	-100.806	-1.457e+06	-100.804	-1.921e+06
183	-101.686	-4.083e+05	-101.149	-3.262e+06	-101.135	-3.341e+06	-99.699	-1.514e+06	-99.698	-1.996e+06
184	-100.565	-4.24e+05	-100.037	-3.39e+06	-100.022	-3.473e+06	-98.611	-1.573e+06	-98.609	-2.074e+06

n	E_S [GHz]	α_S [MHz cm/V]	$E_{P_{1/2}}$	$\alpha_{P_{1/2}}$	$E_{P_{3/2}}$	$\alpha_{P_{3/2}}$	$E_{D_{3/2}}$	$\alpha_{D_{3/2}}$	$E_{D_{5/2}}$	$\alpha_{D_{5/2}}$
185	-99.462	-4.403e+05	-98.943	-3.523e+06	-98.928	-3.609e+06	-97.540	-1.634e+06	-97.538	-2.155e+06
186	-98.377	-4.571e+05	-97.866	-3.66e+06	-97.852	-3.749e+06	-96.486	-1.697e+06	-96.484	-2.238e+06
187	-97.310	-4.744e+05	-96.807	-3.801e+06	-96.794	-3.894e+06	-95.449	-1.762e+06	-95.448	-2.324e+06
188	-96.260	-4.923e+05	-95.766	-3.947e+06	-95.752	-4.044e+06	-94.429	-1.829e+06	-94.428	-2.412e+06
189	-95.227	-5.107e+05	-94.741	-4.098e+06	-94.727	-4.199e+06	-93.426	-1.899e+06	-93.424	-2.504e+06
190	-94.210	-5.298e+05	-93.732	-4.254e+06	-93.719	-4.359e+06	-92.438	-1.97e+06	-92.436	-2.599e+06
191	-93.210	-5.494e+05	-92.739	-4.415e+06	-92.726	-4.524e+06	-91.466	-2.044e+06	-91.464	-2.696e+06
192	-92.226	-5.697e+05	-91.762	-4.582e+06	-91.749	-4.694e+06	-90.509	-2.12e+06	-90.507	-2.797e+06
193	-91.257	-5.906e+05	-90.801	-4.753e+06	-90.788	-4.87e+06	-89.567	-2.199e+06	-89.565	-2.901e+06
194	-90.303	-6.122e+05	-89.854	-4.93e+06	-89.842	-5.052e+06	-88.639	-2.28e+06	-88.638	-3.008e+06
195	-89.364	-6.344e+05	-88.922	-5.113e+06	-88.910	-5.239e+06	-87.726	-2.364e+06	-87.725	-3.119e+06
196	-88.440	-6.573e+05	-88.005	-5.301e+06	-87.993	-5.432e+06	-86.827	-2.45e+06	-86.826	-3.233e+06
197	-87.530	-6.81e+05	-87.101	-5.496e+06	-87.090	-5.631e+06	-85.942	-2.539e+06	-85.940	-3.35e+06
198	-86.634	-7.053e+05	-86.212	-5.696e+06	-86.200	-5.837e+06	-85.070	-2.631e+06	-85.068	-3.472e+06
199	-85.751	-7.304e+05	-85.336	-5.903e+06	-85.324	-6.049e+06	-84.211	-2.723e+06	-84.210	-3.597e+06
200	-84.883	-7.563e+05	-84.473	-6.116e+06	-84.462	-6.267e+06	-83.366	-2.823e+06	-83.364	-3.723e+06

Table B.1: Ionization energies and electrostatic polarizabilities of Rydberg S , P , and D states are listed here for convenience. Stark maps yield these values in case the electric field is compensated in all directions.

Acronyms

- AOM acousto-optical modulator. 26–33, 37, 38, 57, 60, 151, 154, *Glossary*: acousto-optical modulator
- API application programming interface. 55, 60, 151, *Glossary*: application programming interface
- BEC Bose-Einstein condensate. 7, 8, 133, 151, *Glossary*: Bose-Einstein condensate
- C-NOT controlled NOT. 9, 151, *Glossary*: controlled NOT
- CF conflat. 16, 151, *Glossary*: conflat
- CSV comma-separated values. 58
- cw continuous-wave. 112
- DAVLL dichroic atomic vapour laser lock. 25, 151, *Glossary*: dichroic atomic vapour laser lock
- DDI dipole-dipole interaction. 151, *Glossary*: dipole-dipole interaction
- DDS direct digital synthesizer. 28, 151, *Glossary*: direct digital synthesizer
- EIT electromagnetically induced transparency. iii, 10, 24, 25, 50, 83, 87, 90, 94–96, 98–101, 103–105, 107, 112, 125, 126, 128, 129, 133, 134, 137–139
- EOM electro-optical modulator. 26, 151, 153, *Glossary*: electro-optical modulator
- FPGA field-programmable gate array. 55, 57, 151, *Glossary*: field-programmable gate array
- FWHM full width at half maximum. 111
- GUI graphical user interface. 53, 55, 57, 58, 63, 110, 151, *Glossary*: graphical user interface
- HBT Hanbury Brown and Twiss. 45, 46, 96, 104, 110, 111, 137, 151, *Glossary*: Hanbury Brown and Twiss

LIAD light-induced atomic desorption. 16, 152, *Glossary*: light-induced atomic desorption

LSB least significant bit. 60

MCP multi channel plate. 18–20, 58–60, 92, 137, 152, *Glossary*: multi channel plate

MOT magneto-optical trap. 7, 15, 33, 36, 53, 109, 110, 126, 128, 152, *Glossary*: magneto-optical trap

PBS polarizing beam splitter. 38, 43, 44, 152, *Glossary*: polarizing beam splitter

PCB printed circuit board. 29

PID proportional–integral–derivative controller. 27, 32, 33, 37, 152, *Glossary*: proportional–integral–derivative controller

UV ultraviolet. 154

Glossary

- acousto-optical modulator Similar to the EOM, an optical element which can be used to modulate the amplitude or frequency of a laser beam. In this work, we use it to quickly modulate the amplitude of the light which is diffracted in the ± 1 st order and frequency shifted by RF in a crystal. 27, 151
- application programming interface Especially for high-level programming languages, functions or definitions to serve a particular purpose or communicate with a special device are packed into an API. That way, common problems do not need to be solved again each time they appear. 55, 151
- austenitic An austenitic material is iron or an alloy (e.g. with manganese and nickel) in a face-centered cubic crystallographic configuration which is paramagnetic. This type of steel is desirable if controlled magnetic fields have to be applied and switched. 19
- Bose-Einstein condensate A state of matter which occurs at temperatures very close to zero. Its characteristic is that the atomic sample in the BEC is described by a macroscopic wave function instead of independent particle wave functions. This is due to the increase of the de Broglie wavelength with decreasing temperature. 7, 151
- conflat Standard for vacuum flanges, where knife-edge flanges cut into a copper gasket for sealing. 16, 151
- controlled NOT A quantum gate operating on two qubits. The state of the first qubit determines whether or not the state of the second qubit shall be negated (NOT). 9, 151
- dichroic atomic vapour laser lock A technique which produces a dispersive error signal from Doppler-broadened absorption lines in magnetic fields. 25, 151
- dipole-dipole interaction The electric DDI is the fundamental interaction mechanism for transitions between electronic states, the d.c. and a.c. Stark Effect and the interaction potential between Rydberg atoms. 151

direct digital synthesizer A frequency synthesizer based on a system clock and digital electronics. Compared to analog frequency synthesizers with a phase-locked loop, better phase noise is achieved. Typically, the frequencies are more precise as compared to voltage-controlled oscillators. 28, 151

electro-optical modulator Similar to the AOM, an optical element which can be used to modulate the phase of a light beam. In this work, it is used to add frequency sidebands on the laser light spectrum. 26, 151

field-programmable gate array A chip containing a logic which can be programmed. For some applications, FPGAs can outperform microcontrollers in terms of speed due to the parallel design. 55, 151

graphical user interface Computer program which allows graphical user interaction as opposed to text based programs. 53, 151

Hanbury Brown and Twiss The setup used by Robert Hanbury Brown and Richard Q. Twiss employs two photon detectors to investigate the statistics of an incident light beam. By splitting the beam into two arms of similar intensity, it is possible to measure two-photon correlations in a time domain which is even smaller than the dead time of a single detector. 45, 151

light-induced atomic desorption With this technique, the vapour pressure in a vacuum chamber can be increased very quickly. Strong ultraviolet (UV) light is directed on vacuum glass interfaces (viewports, glass cell) to adsorb the (Rubidium) atoms in the interior of the vacuum chamber. 16, 152

magneto-optical trap The standard laser-cooling technique applicable for dilute gases of atoms, ions and even molecules. 7, 152

multi channel plate Also known as microchannel plate. An ion detector based on the amplification of an ion by electron multiplication in narrow tubes with a strong electric field. 19, 152

polarizing beam splitter An optical element which splits incident light into two linearly polarized components S and P . While there are also PBS plates, only PBS cubes are built into our experiment. 38, 152

proportional–integral–derivative controller A controller used to stabilize a measured value to a set value. From the difference between these values, an error signal is produced, from which feedback can be generated to a device which influences the measured value. The feedback can depend on the error signal in a proportional, integrative or derivative way. 27, 152

References

- [1] H. Gorniaczyk, C. Tresp, P. Bienias, A. Paris-Mandoki, W. Li, I. Mirgorodskiy, H. P. Büchler, I. Lesanovsky, and S. Hofferberth. “Enhancement of Rydberg-mediated single-photon nonlinearities by electrically tuned Förster resonances”. In: *Nat Commun* 7.12480 (Aug. 2016).
- [2] C. Tresp, C. Zimmer, I. Mirgorodskiy, H. Gorniaczyk, A. Paris-Mandoki, and S. Hofferberth. “Single-Photon Absorber Based on Strongly Interacting Rydberg Atoms”. In: *Physical Review Letters* 117.22 (Nov. 2016). Editors’ suggestion. ISSN: 1079-7114. DOI: 10.1103/physrevlett.117.223001.
- [3] Asaf Paris-Mandoki, Hannes Gorniaczyk, Christoph Tresp, Ivan Mirgorodskiy, and Sebastian Hofferberth. “Tailoring Rydberg interactions via Förster resonances: state combinations, hopping and angular dependence”. In: *Journal of Physics B: Atomic, Molecular and Optical Physics* 49.16 (July 2016), page 164001. ISSN: 1361-6455. DOI: 10.1088/0953-4075/49/16/164001.
- [4] C. Tresp, P. Bienias, S. Weber, H. Gorniaczyk, I. Mirgorodskiy, H. P. Büchler, and S. Hofferberth. “Dipolar Dephasing of Rydberg *D*-State Polaritons”. In: *Phys. Rev. Lett.* 115 (8 Aug. 2015), page 083602. DOI: 10.1103/PhysRevLett.115.083602.
- [5] H. Gorniaczyk, C. Tresp, J. Schmidt, H. Fedder, and S. Hofferberth. “Single-Photon Transistor Mediated by Interstate Rydberg Interactions”.

- In: *Phys. Rev. Lett.* 113 (5 July 2014). Editors' suggestion, APS Physics Viewpoint, page 053601. DOI: 10.1103/PhysRevLett.113.053601.
- [6] Hannes Gorniaczyk. "A crossed optical dipole trap". Master's thesis. Universität Stuttgart, Dec. 2011.
- [7] Markus Falkenau, Valentin V. Volchkov, Jahn Rührig, Hannes Gorniaczyk, and Axel Griesmaier. "Evaporation-limited loading of an atomic trap". In: *Phys. Rev. A* 85 (2 Feb. 2012), page 023412. DOI: 10.1103/PhysRevA.85.023412.
- [8] A. Einstein. "Zur Quantentheorie der Strahlung". In: *Physikalische Zeitschrift* 18 (1917).
- [9] R. H. Dicke. "Coherence in Spontaneous Radiation Processes". In: *Phys. Rev.* 93 (1 Jan. 1954), pages 99–110. DOI: 10.1103/PhysRev.93.99.
- [10] A. L. Schawlow and C. H. Townes. "Infrared and Optical Masers". In: *Physical Review* 112.6 (Dec. 1958), pages 1940–1949. ISSN: 0031-899X. DOI: 10.1103/physrev.112.1940.
- [11] Claude N. Cohen-Tannoudji. "Nobel Lecture: Manipulating atoms with photons". In: *Rev. Mod. Phys.* 70.3 (July 1998), pages 707–719. ISSN: 1539-0756. DOI: 10.1103/revmodphys.70.707.
- [12] Stig Stenholm. "The semiclassical theory of laser cooling". In: *Rev. Mod. Phys.* 58 (3 July 1986), pages 699–739. DOI: 10.1103/RevModPhys.58.699.
- [13] William D. Phillips. "Nobel Lecture: Laser cooling and trapping of neutral atoms". In: *Rev. Mod. Phys.* 70.3 (July 1998), pages 721–741. ISSN: 1539-0756. DOI: 10.1103/revmodphys.70.721.
- [14] Steven Chu. "Nobel Lecture: The manipulation of neutral particles". In: *Rev. Mod. Phys.* 70.3 (July 1998), pages 685–706. ISSN: 1539-0756. DOI: 10.1103/revmodphys.70.685.

- [15] M. H. Anderson, J. R. Ensher, M. R. Matthews, C. E. Wieman, and E. A. Cornell. “Observation of Bose-Einstein Condensation in a Dilute Atomic Vapor”. In: *Science* 269.5221 (July 1995), pages 198–201. DOI: 10.1126/science.269.5221.198.
- [16] C. C. Bradley, C. A. Sackett, J. J. Tollett, and R. G. Hulet. “Evidence of Bose-Einstein Condensation in an Atomic Gas with Attractive Interactions”. In: *Phys. Rev. Lett.* 75 (9 Aug. 1995), pages 1687–1690. DOI: 10.1103/PhysRevLett.75.1687.
- [17] K. B. Davis, M. -O. Mewes, M. R. Andrews, N. J. van Druten, D. S. Durfee, D. M. Kurn, and W. Ketterle. “Bose-Einstein Condensation in a Gas of Sodium Atoms”. In: *Physical Review Letters* 75.22 (Nov. 1995), pages 3969–3973. ISSN: 1079-7114. DOI: 10.1103/physrevlett.75.3969.
- [18] Franco Dalfovo, Stefano Giorgini, Lev P. Pitaevskii, and Sandro Stringari. “Theory of Bose-Einstein condensation in trapped gases”. In: *Rev. Mod. Phys.* 71.3 (Apr. 1999), pages 463–512. ISSN: 1539-0756. DOI: 10.1103/revmodphys.71.463.
- [19] John Weiner, Vanderlei S. Bagnato, Sergio Zilio, and Paul S. Julienne. “Experiments and theory in cold and ultracold collisions”. In: *Rev. Mod. Phys.* 71 (1 Jan. 1999), pages 1–85. DOI: 10.1103/RevModPhys.71.1.
- [20] J. Stuhler, A. Griesmaier, T. Koch, M. Fattori, T. Pfau, S. Giovanazzi, P. Pedri, and L. Santos. “Observation of Dipole-Dipole Interaction in a Degenerate Quantum Gas”. In: *Phys. Rev. Lett.* 95 (15 Oct. 2005), page 150406. DOI: 10.1103/PhysRevLett.95.150406.
- [21] T Lahaye, C Menotti, L Santos, M Lewenstein, and T Pfau. “The physics of dipolar bosonic quantum gases”. In: *Reports on Progress in Physics* 72.12 (2009), page 126401.

- [22] Holger Kadau, Matthias Schmitt, Matthias Wenzel, Clarissa Wink, Thomas Maier, Igor Ferrier-Barbut, and Tilman Pfau. “Observing the Rosensweig instability of a quantum ferrofluid”. In: *Nature* 530.7589 (Feb. 2016), pages 194–197. ISSN: 1476-4687. DOI: 10.1038/nature16485.
- [23] S. L. Cornish, N. R. Claussen, J. L. Roberts, E. A. Cornell, and C. E. Wieman. “Stable 85 Rb Bose-Einstein Condensates with Widely Tunable Interactions”. In: *Physical Review Letters* 85.9 (Aug. 2000), pages 1795–1798. ISSN: 1079-7114. DOI: 10.1103/physrevlett.85.1795.
- [24] Thorsten Köhler, Krzysztof Góral, and Paul S. Julienne. “Production of cold molecules via magnetically tunable Feshbach resonances”. In: *Rev. Mod. Phys.* 78.4 (Dec. 2006), pages 1311–1361. ISSN: 1539-0756. DOI: 10.1103/revmodphys.78.1311.
- [25] Thierry Lahaye, Tobias Koch, Bernd Fröhlich, Marco Fattori, Jonas Metz, Axel Griesmaier, Stefano Giovanazzi, and Tilman Pfau. “Strong dipolar effects in a quantum ferrofluid”. In: *Nature* 448 (2007), pages 672–675. DOI: doi:10.1038/nature06036.
- [26] T. Koch, T. Lahaye, J. Metz, B. Fröhlich, A. Griesmaier, and T. Pfau. “Stabilization of a purely dipolar quantum gas against collapse”. In: *Nat Phys* 4.3 (Mar. 2008), pages 218–222. ISSN: 1745-2473.
- [27] R. Grimm, M. Weidemuller, and Y.B. Ovchinnikov. “Optical dipole traps for neutral atoms”. In: *Adv. in Atomic, Molec., and Opt. Phys.* ADVANCES IN ATOMIC MOLECULAR AND OPTICAL PHYSICS 42 (2000), pages 95–170. DOI: doi:10.1016/S1049-250X(08)60186-X.
- [28] J. Dalibard and C. Cohen-Tannoudji. “Dressed-atom approach to atomic motion in laser light: the dipole force revisited”. In: *J. Opt. Soc. Am. B* 2.11 (Nov. 1985), page 1707. ISSN: 1520-8540. DOI: 10.1364/josab.2.001707.

- [29] Takahiro Kuga, Yoshio Torii, Noritsugu Shiokawa, Takuya Hirano, Yukiko Shimizu, and Hiroyuki Sasada. “Novel Optical Trap of Atoms with a Doughnut Beam”. In: *Physical Review Letters* 78.25 (June 1997), pages 4713–4716. ISSN: 1079-7114. DOI: 10.1103/physrevlett.78.4713.
- [30] Nir Davidson, Heun Jin Lee, Charles S. Adams, Mark Kasevich, and Steven Chu. “Long Atomic Coherence Times in an Optical Dipole Trap”. In: *Physical Review Letters* 74.8 (Feb. 1995), pages 1311–1314. ISSN: 1079-7114. DOI: 10.1103/physrevlett.74.1311.
- [31] S Kulin, S Aubin, S Christe, B Peker, S L Rolston, and L A Orozco. “A single hollow-beam optical trap for cold atoms”. In: *Journal of Optics B: Quantum and Semiclassical Optics* 3.6 (Oct. 2001), pages 353–357. ISSN: 1741-3575. DOI: 10.1088/1464-4266/3/6/301.
- [32] D. Jaksch, C. Bruder, J. I. Cirac, C. W. Gardiner, and P. Zoller. “Cold Bosonic Atoms in Optical Lattices”. In: *Phys. Rev. Lett.* 81 (15 Oct. 1998), pages 3108–3111. DOI: 10.1103/PhysRevLett.81.3108.
- [33] M. Greiner, O. Mandel, T. Esslinger, T. W. Hänsch, and I. Bloch. “Quantum phase transition from a superfluid to a Mott insulator in a gas of ultracold atoms”. In: *Nature* 415 (2002), pages 39–44. DOI: doi:10.1038/415039a.
- [34] Alexey V. Gorshkov, Liang Jiang, Markus Greiner, Peter Zoller, and Mikhail D. Lukin. “Coherent Quantum Optical Control with Subwavelength Resolution”. In: *Phys. Rev. Lett.* 100 (9 Mar. 2008), page 093005. DOI: 10.1103/PhysRevLett.100.093005.
- [35] Maxwell F. Parsons, Florian Huber, Anton Mazurenko, Christie S. Chiu, Widagdo Setiawan, Katherine Wooley-Brown, Sebastian Blatt, and Markus Greiner. “Site-Resolved Imaging of Fermionic ${}^6\text{Li}$ in an Optical

- Lattice”. In: *Phys. Rev. Lett.* 114 (21 May 2015), page 213002. DOI: 10.1103/PhysRevLett.114.213002.
- [36] Oliver Morsch and Markus Oberthaler. “Dynamics of Bose-Einstein condensates in optical lattices”. In: *Rev. Mod. Phys.* 78.1 (Feb. 2006), pages 179–215. ISSN: 1539-0756. DOI: 10.1103/revmodphys.78.179.
- [37] Immanuel Bloch, Jean Dalibard, and Wilhelm Zwerger. “Many-body physics with ultracold gases”. In: *Rev. Mod. Phys.* 80.3 (July 2008), pages 885–964. ISSN: 1539-0756. DOI: 10.1103/revmodphys.80.885.
- [38] Jonathan Simon, Waseem S. Bakr, Ruichao Ma, M. Eric Tai, Philipp M. Preiss, and Markus Greiner. “Quantum simulation of antiferromagnetic spin chains in an optical lattice”. In: *Nature* 472.7343 (Apr. 2011), pages 307–312. ISSN: 0028-0836.
- [39] J. I. Cirac and P. Zoller. “Quantum Computations with Cold Trapped Ions”. In: *Phys. Rev. Lett.* 74 (20 May 1995), pages 4091–4094. DOI: 10.1103/PhysRevLett.74.4091.
- [40] A. Friedenauer, H. Schmitz, J. T. Glueckert, D. Porras, and T. Schaetz. “Simulating a quantum magnet with trapped ions”. In: *Nature Physics* 4.10 (July 2008), pages 757–761. ISSN: 1745-2481. DOI: 10.1038/nphys1032.
- [41] Joseph W. Britton, Brian C. Sawyer, Adam C. Keith, C.-C. Joseph Wang, James K. Freericks, Hermann Uys, Michael J. Biercuk, and John J. Bollinger. “Engineered two-dimensional Ising interactions in a trapped-ion quantum simulator with hundreds of spins”. In: *Nature* 484.7395 (Apr. 2012), pages 489–492. ISSN: 1476-4687. DOI: 10.1038/nature10981.
- [42] B. P. Lanyon, C. Hempel, D. Nigg, M. Müller, R. Gerritsma, F. Zähringer, P. Schindler, J. T. Barreiro, M. Rambach, G. Kirchmair, M. Hennrich, P. Zoller, R. Blatt, and C. F. Roos. “Universal Digital

- Quantum Simulation with Trapped Ions”. In: *Science* 334.6052 (Sept. 2011), pages 57–61. ISSN: 1095-9203. DOI: 10.1126/science.1208001.
- [43] R. Gerritsma, G. Kirchmair, F. Zaehring, E. Solano, R. Blatt, and C. F. Roos. “Quantum simulation of the Dirac equation”. In: *Nature* 463 (2010), pages 68–71. DOI: doi:10.1038/nature08688.
- [44] S. Debnath, N. M. Linke, C. Figgatt, K. A. Landsman, K. Wright, and C. Monroe. “Demonstration of a small programmable quantum computer with atomic qubits”. In: *Nature* 536.7614 (Aug. 2016), pages 63–66. ISSN: 0028-0836.
- [45] C. J. Ballance, T. P. Harty, N. M. Linke, M. A. Sepiol, and D. M. Lucas. “High-Fidelity Quantum Logic Gates Using Trapped-Ion Hyperfine Qubits”. In: *Phys. Rev. Lett.* 117 (6 Aug. 2016), page 060504. DOI: 10.1103/PhysRevLett.117.060504.
- [46] D. Jaksch, J. I. Cirac, P. Zoller, S. L. Rolston, R. Côté, and M. D. Lukin. “Fast Quantum Gates for Neutral Atoms”. In: *Phys. Rev. Lett.* 85 (10 Sept. 2000), pages 2208–2211. DOI: 10.1103/PhysRevLett.85.2208.
- [47] Gavin K. Brennen, Carlton M. Caves, Poul S. Jessen, and Ivan H. Deutsch. “Quantum Logic Gates in Optical Lattices”. In: *Physical Review Letters* 82.5 (Feb. 1999), pages 1060–1063. ISSN: 1079-7114. DOI: 10.1103/physrevlett.82.1060.
- [48] Hendrik Weimer, Markus Mueller, Igor Lesanovsky, Peter Zoller, and Hans Peter Büchler. “A Rydberg quantum simulator”. In: *Nature Phys.* 6 (2010), pages 382–388. DOI: doi:10.1038/nphys1614.
- [49] Rolf Heidemann, Ulrich Raitzsch, Vera Bendkowsky, Björn Butscher, Robert Löw, Luis Santos, and Tilman Pfau. “Evidence for Coherent Collective Rydberg Excitation in the Strong Blockade Regime”. In: *Phys.*

- Rev. Lett.* 99 (2007), page 163601. DOI: 10.1103/PhysRevLett.99.163601.
- [50] M. D. Lukin, M. Fleischhauer, R. Cote, L. M. Duan, D. Jaksch, J. I. Cirac, and P. Zoller. “Dipole Blockade and Quantum Information Processing in Mesoscopic Atomic Ensembles”. In: *Phys. Rev. Lett.* 87 (2001), page 037901. DOI: 10.1103/PhysRevLett.87.037901.
- [51] T. Vogt, M. Viteau, J. Zhao, A. Chotia, D. Comparat, and P. Pillet. “Dipole Blockade at Förster Resonances in High Resolution Laser Excitation of Rydberg States of Cesium Atoms”. In: *Phys. Rev. Lett.* 97 (2006), page 083003. DOI: 10.1103/PhysRevLett.97.083003.
- [52] P. Schauss, M. Cheneau, M. Endres, T. Fukuhara, S. Hild, A. Omran, T. Pohl, C. Gross, S. Kuhr, and I. Bloch. “Observation of spatially ordered structures in a two-dimensional Rydberg gas”. In: *Nature* 491 (2012), page 87. DOI: doi:10.1038/nature11596.
- [53] C. Ates, T. Pohl, T. Pattard, and J. M. Rost. “Antiblockade in Rydberg Excitation of an Ultracold Lattice Gas”. In: *Physical Review Letters* 98.2 (Jan. 2007). ISSN: 1079-7114. DOI: 10.1103/physrevlett.98.023002.
- [54] A. Urvoy, F. Ripka, I. Lesanovsky, D. Booth, J. P. Shaffer, T. Pfau, and R. Löw. “Strongly Correlated Growth of Rydberg Aggregates in a Vapor Cell”. In: *Phys. Rev. Lett.* 114 (20 May 2015), page 203002. DOI: 10.1103/PhysRevLett.114.203002.
- [55] N. Malossi, M. M. Valado, S. Scotto, P. Huillery, P. Pillet, D. Ciampini, E. Arimondo, and O. Morsch. “Full Counting Statistics and Phase Diagram of a Dissipative Rydberg Gas”. In: *Phys. Rev. Lett.* 113 (2 July 2014), page 023006. DOI: 10.1103/PhysRevLett.113.023006.

- [56] H. Schempp, G. Günter, M. Robert-de-Saint-Vincent, C. S. Hofmann, D. Breyel, A. Komnik, D. W. Schönleber, M. Gärttner, J. Evers, S. Whitlock, and M. Weidemüller. “Full Counting Statistics of Laser Excited Rydberg Aggregates in a One-Dimensional Geometry”. In: *Phys. Rev. Lett.* 112 (1 Jan. 2014), page 013002. DOI: 10.1103/PhysRevLett.112.013002.
- [57] L. Isenhower, E. Urban, X. L. Zhang, A. T. Gill, T. Henage, T. A. Johnson, T. G. Walker, and M. Saffman. “Demonstration of a Neutral Atom Controlled-NOT Quantum Gate”. In: *Phys. Rev. Lett.* 104.1 (Jan. 2010), page 010503. DOI: 10.1103/PhysRevLett.104.010503.
- [58] C. Monroe, D. M. Meekhof, B. E. King, W. M. Itano, and D. J. Wineland. “Demonstration of a Fundamental Quantum Logic Gate”. In: *Phys. Rev. Lett.* 75 (25 Dec. 1995), pages 4714–4717. DOI: 10.1103/PhysRevLett.75.4714.
- [59] M. Saffman, T. G. Walker, and K. Mølmer. “Quantum information with Rydberg atoms”. In: *Rev. Mod. Phys.* 82 (2010), page 2313. DOI: 10.1103/RevModPhys.82.2313.
- [60] Henning Labuhn, Daniel Barredo, Sylvain Ravets, Sylvain de Léséleuc, Tommaso Macrì, Thierry Lahaye, and Antoine Browaeys. “Tunable two-dimensional arrays of single Rydberg atoms for realizing quantum Ising models”. In: *Nature* (June 2016). ISSN: 1476-4687. DOI: 10.1038/nature18274.
- [61] S. E. Anderson, K. C. Younge, and G. Raithel. “Trapping Rydberg Atoms in an Optical Lattice”. In: *Physical Review Letters* 107.26 (Dec. 2011). ISSN: 1079-7114. DOI: 10.1103/physrevlett.107.263001.
- [62] Brian J. Lester, Niclas Luick, Adam M. Kaufman, Collin M. Reynolds, and Cindy A. Regal. “Rapid Production of Uniformly Filled Arrays of Neutral

- Atoms”. In: *Physical Review Letters* 115.7 (Aug. 2015). ISSN: 1079-7114. DOI: 10.1103/physrevlett.115.073003.
- [63] Y H Fung and M F Andersen. “Efficient collisional blockade loading of a single atom into a tight microtrap”. In: *New J. Phys.* 17.7 (July 2015), page 073011. ISSN: 1367-2630. DOI: 10.1088/1367-2630/17/7/073011.
- [64] M. Saffman and K. Mølmer. “Scaling the neutral-atom Rydberg gate quantum computer by collective encoding in holmium atoms”. In: *Phys. Rev. A* 78 (1 July 2008), page 012336. DOI: 10.1103/PhysRevA.78.012336.
- [65] J. Honer, H. Weimer, T. Pfau, and H. P. Büchler. “Collective Many-Body Interaction in Rydberg Dressed Atoms”. In: *Phys. Rev. Lett.* 105 (2010), page 160404. DOI: 10.1103/PhysRevLett.105.160404.
- [66] J. B. Balewski, A. T. Krupp, A. Gaj, S. Hofferberth, R. Loew, and T. Pfau. “Rydberg dressing: understanding of collective many-body effects and implications for experiments”. In: *New Journal of Physics* 16 (2014), page 063012. DOI: doi :10.1088/1367-2630/16/6/063012.
- [67] S Helmrich, A Arias, N Pehoviak, and S Whitlock. “Two-body interactions and decay of three-level Rydberg-dressed atoms”. In: *Journal of Physics B: Atomic, Molecular and Optical Physics* 49.3 (2016), 03LT02.
- [68] C. Gaul, B. J. DeSalvo, J. A. Aman, F. B. Dunning, T. C. Killian, and T. Pohl. “Resonant Rydberg Dressing of Alkaline-Earth Atoms via Electromagnetically Induced Transparency”. In: *Physical Review Letters* 116.24 (June 2016). ISSN: 1079-7114. DOI: 10.1103/physrevlett.116.243001.
- [69] T. F. Gallagher, K. A. Safinya, F. Gounand, J. F. Delpéch, W. Sandner, and R. Kachru. “Resonant Rydberg-atom – Rydberg-atom collisions”. In: *Phys. Rev. A* 25 (4 Apr. 1982), pages 1905–1917. DOI: 10.1103/PhysRevA.25.1905.

- [70] W. R. Anderson, J. R. Veale, and T. F. Gallagher. “Resonant Dipole-Dipole Energy Transfer in a Nearly Frozen Rydberg Gas”. In: *Phys. Rev. Lett.* 80.2 (Jan. 1998), pages 249–252. DOI: 10.1103/PhysRevLett.80.249.
- [71] K. Afrousheh, P. Bohlouli-Zanjani, D. Vagale, A. Mugford, M. Fedorov, and J. D. D. Martin. “Spectroscopic Observation of Resonant Electric Dipole-Dipole Interactions between Cold Rydberg Atoms”. In: *Phys. Rev. Lett.* 93 (23 Nov. 2004), page 233001. DOI: 10.1103/PhysRevLett.93.233001.
- [72] G. Guenter, H. Schempp, M. Robert-de-Saint-Vincent, V. Gavryusev, S. Helmrich, C. S. Hofmann, S. Whitlock, and M. Weidemuller. “Observing the Dynamics of Dipole-Mediated Energy Transport by Interaction-Enhanced Imaging”. In: *Science* 342 (2013), pages 954–956. DOI: 10.1126/science.1244843.
- [73] Sylvain Ravets, Henning Labuhn, Daniel Barredo, Lucas Beguin, Thierry Lahaye, and Antoine Browaeys. “Coherent dipole-dipole coupling between two single Rydberg atoms at an electrically-tuned Förster resonance”. In: *Nature Physics* 10 (2014), pages 914–917. DOI: doi:10.1038/nphys3119.
- [74] I. I. Ryabtsev, D. B. Tretyakov, I. I. Beterov, and V. M. Entin. “Observation of the Stark-Tuned Förster Resonance between Two Rydberg Atoms”. In: *Phys. Rev. Lett.* 104 (2010), page 073003. DOI: 10.1103/PhysRevLett.104.073003.
- [75] J. Nipper, J. B. Balewski, A. T. Krupp, B. Butscher, R. Löw, and T. Pfau. “Highly Resolved Measurements of Stark-Tuned Förster Resonances between Rydberg Atoms”. In: *Phys. Rev. Lett.* 108 (11 Mar. 2012), page 113001. DOI: 10.1103/PhysRevLett.108.113001.

- [76] P. Bohlouli-Zanjani, J. A. Petrus, and J. D. D. Martin. “Enhancement of Rydberg Atom Interactions Using ac Stark Shifts”. In: *Phys. Rev. Lett.* 98.20 (May 2007), page 203005. DOI: 10.1103/PhysRevLett.98.203005.
- [77] J S Cabral, J M Kondo, L F Gonçalves, V A Nascimento, L G Marcassa, D Booth, J Tallant, A Schwettmann, K R Overstreet, J Sedlacek, and J P Shaffer. “Effects of electric fields on ultracold Rydberg atom interactions”. In: *Journal of Physics B: Atomic, Molecular and Optical Physics* 44.18 (2011), page 184007.
- [78] A. Osterwalder and F. Merkt. “Using High Rydberg States as Electric Field Sensors”. In: *Physical Review Letters* 82.9 (Mar. 1999), pages 1831–1834. ISSN: 1079-7114. DOI: 10.1103/physrevlett.82.1831.
- [79] R. P. Abel, C. Carr, U. Krohn, and C. S. Adams. “Electrometry near a dielectric surface using Rydberg electromagnetically induced transparency”. In: *Physical Review A* 84.2 (Aug. 2011). ISSN: 1094-1622. DOI: 10.1103/physreva.84.023408.
- [80] V. Bendkowsky, B. Butscher, J. Nipper, J. P. Shaffer, R. Löw, and T. Pfau. “Observation of ultralong-range Rydberg molecules”. In: *Nature* 458 (2009), pages 1005–1008. DOI: 10.1038/nature07945.
- [81] V. Bendkowsky, B. Butscher, J. Nipper, J. B. Balewski, J. P. Shaffer, R. Löw, T. Pfau, W. Li, J. Stanojevic, T. Pohl, and J. M. Rost. “Rydberg Trimers and Excited Dimers Bound by Internal Quantum Reflection”. In: *Phys. Rev. Lett.* 105.16 (Oct. 2010), page 163201. DOI: 10.1103/PhysRevLett.105.163201.
- [82] T. C. Killian. “Ultracold Neutral Plasmas”. In: *Science* 316.5825 (May 2007), pages 705–708. ISSN: 1095-9203. DOI: 10.1126/science.1130556.

- [83] J. A. Armstrong, N. Bloembergen, J. Ducuing, and P. S. Pershan. “Interactions between Light Waves in a Nonlinear Dielectric”. In: *Phys. Rev.* 127 (6 Sept. 1962), pages 1918–1939. DOI: 10.1103/PhysRev.127.1918.
- [84] K.-J. Boller, A. Imamoglu, and S. E. Harris. “Observation of electromagnetically induced transparency”. In: *Physical Review Letters* 66.20 (May 1991), pages 2593–2596. ISSN: 0031-9007. DOI: 10.1103/physrevlett.66.2593.
- [85] S.E. Harris. “Electromagnetically Induced Transparency”. In: *Phys. Today* 50 (1997), pages 36–42.
- [86] A. K. Mohapatra, T. R. Jackson, and C. S. Adams. “Coherent Optical Detection of Highly Excited Rydberg States Using Electromagnetically Induced Transparency”. In: *Phys. Rev. Lett.* 98 (2007), page 113003. DOI: 10.1103/PhysRevLett.98.113003.
- [87] J. D. Pritchard, D. Maxwell, A. Gauguier, K. J. Weatherill, M. P. A. Jones, and C. S. Adams. “Cooperative Atom-Light Interaction in a Blocked Rydberg Ensemble”. In: *Phys. Rev. Lett.* 105 (2010), page 193603. DOI: 10.1103/PhysRevLett.105.193603.
- [88] T. Peyronel, O. Firstenberg, Q. Liang, S. Hofferberth, A.V. Gorshkov, T. Pohl, M.D. Lukin, and V. Vuletic. “Quantum nonlinear optics with single photons enabled by strongly interacting atoms”. In: *Nature* 488 (2012), pages 57–60. DOI: 10.1038/nature11361.
- [89] S. Zhang, F. Robicheaux, and M. Saffman. “Magic-wavelength optical traps for Rydberg atoms”. In: *Phys. Rev. A* 84 (4 Oct. 2011), page 043408. DOI: 10.1103/PhysRevA.84.043408.
- [90] L. Li, Y. O. Dudin, and A. Kuzmich. “Entanglement between light and an optical atomic excitation”. In: *Nature* 498 (2013), pages 466–469. DOI: 10.1038/nature12227.

- [91] Y. O. Dudin and A. Kuzmich. “Strongly Interacting Rydberg Excitations of a Cold Atomic Gas”. In: *Science* 336 (2012), pages 887–889. DOI: 10.1126/science.1217901.
- [92] C. S. Hofmann, G. Günter, H. Schempp, M. Robert-de-Saint-Vincent, M. Gärttner, J. Evers, S. Whitlock, and M. Weidemüller. “Sub-Poissonian Statistics of Rydberg-Interacting Dark-State Polaritons”. In: *Phys. Rev. Lett.* 110 (20 May 2013), page 203601. DOI: 10.1103/PhysRevLett.110.203601.
- [93] O. Firstenberg, T. Peyronel, Q. Liang, A. V. Gorshkov, M. D. Lukin, and V. Vuletic. “Attractive photons in a quantum nonlinear medium”. In: *Nature* 502 (2013), pages 71–75. DOI: doi:10.1038/nature12512.
- [94] Jens Honer, R. Löw, Hendrik Weimer, Tilman Pfau, and Hans Peter Büchler. “Artificial Atoms Can Do More Than Atoms: Deterministic Single Photon Subtraction from Arbitrary Light Fields”. In: *Phys. Rev. Lett.* 107 (9 Aug. 2011), page 093601. DOI: 10.1103/PhysRevLett.107.093601.
- [95] Christoph Tresp. “To be published”. PhD thesis. Universität Stuttgart, 2016.
- [96] B. Olmos, W. Li, S. Hofferberth, and I. Lesanovsky. “Amplifying single impurities immersed in a gas of ultracold atoms”. In: *Phys. Rev. A* 84 (4 Oct. 2011), page 041607. DOI: 10.1103/PhysRevA.84.041607.
- [97] G. Günter, M. Robert-de-Saint-Vincent, H. Schempp, C. S. Hofmann, S. Whitlock, and M. Weidemüller. “Interaction Enhanced Imaging of Individual Rydberg Atoms in Dense Gases”. In: *Phys. Rev. Lett.* 108 (1 Jan. 2012), page 013002. DOI: 10.1103/PhysRevLett.108.013002.

- [98] Vladislav Gavryusev, Miguel Ferreira-Cao, Armin Kekić, Gerhard Zürn, and Adrien Signoles. “Interaction Enhanced Imaging of Rydberg P states”. In: *The European Physical Journal Special Topics* 225.15-16 (Dec. 2016), pages 2863–2889. ISSN: 1951-6401. DOI: 10.1140/epjst/e2015-50339-8.
- [99] David Petrosyan, Johannes Otterbach, and Michael Fleischhauer. “Electromagnetically Induced Transparency with Rydberg Atoms”. In: *Phys. Rev. Lett.* 107 (21 Nov. 2011), page 213601. DOI: 10.1103/PhysRevLett.107.213601.
- [100] A. V. Gorshkov, J. Otterbach, M. Fleischhauer, T. Pohl, and M. D. Lukin. “Photon-Photon Interactions via Rydberg Blockade”. In: *Phys. Rev. Lett.* 107 (2011). arXiv:1103.3700v1, page 133602. DOI: 10.1103/PhysRevLett.107.133602.
- [101] P. Bienias, S. Choi, O. Firstenberg, M. F. Maghrebi, M. Gullans, M. D. Lukin, A. V. Gorshkov, and H. P. Büchler. “Scattering resonances and bound states for strongly interacting Rydberg polaritons”. In: *Phys. Rev. A* 90 (5 Nov. 2014), page 053804. DOI: 10.1103/PhysRevA.90.053804.
- [102] Liu Yang, Bing He, Jin-Hui Wu, Zhaoyang Zhang, and Min Xiao. “Interacting photon pulses in a Rydberg medium”. In: *Optica* 3.10 (Oct. 2016), pages 1095–1103. DOI: 10.1364/OPTICA.3.001095.
- [103] M. J. Gullans, J. D. Thompson, Y. Wang, Q.-Y. Liang, V. Vuletić, M. D. Lukin, and A. V. Gorshkov. “Effective Field Theory for Rydberg Polaritons”. In: *Physical Review Letters* 117.11 (Sept. 2016). ISSN: 1079-7114. DOI: 10.1103/physrevlett.117.113601.
- [104] M. Bajcsy, S. Hofferberth, V. Balic, T. Peyronel, M. Hafezi, A. S. Zibrov, V. Vuletic, and M. D. Lukin. “Efficient All-Optical Switching Using Slow

- Light within a Hollow Fiber”. In: *Phys. Rev. Lett.* 102 (2009), page 203902. DOI: 10.1103/PhysRevLett.102.203902.
- [105] J. Hwang, M. Pototschnig, R. Lettow, G. Zumofen, A. Renn, S. Goetzinger, and V. Sandoghdar. “A single-molecule optical transistor”. In: *Nature* 460 (2009), pages 76–80. DOI: doi:10.1038/nature08134.
- [106] Serge Haroche. “Nobel Lecture: Controlling photons in a box and exploring the quantum to classical boundary”. In: *Rev. Mod. Phys.* 85.3 (July 2013), 1083–1102. ISSN: 1539-0756. DOI: 10.1103/revmodphys.85.1083.
- [107] W. Chen, K. M. Beck, R. Bucker, M. Gullans, M. D. Lukin, H. Tanji-Suzuki, and V. Vuletic. “All-Optical Switch and Transistor Gated by One Stored Photon”. In: *Science* 341.6147 (July 2013), pages 768–770. ISSN: 1095-9203. DOI: 10.1126/science.1238169.
- [108] Darrick E. Chang, Anders S. Sorensen, Eugene A. Demler, and Mikhail D. Lukin. “A single-photon transistor using nanoscale surface plasmons”. In: *Nature Phys.* 3 (2007), pages 807–812. DOI: doi:10.1038/nphys708.
- [109] Marco T. Manzoni, Florentin Reiter, Jacob M. Taylor, and Anders S. Sørensen. “Single-photon transistor based on superconducting systems”. In: *Physical Review B* 89.18 (May 2014). ISSN: 1550-235X. DOI: 10.1103/physrevb.89.180502.
- [110] Oleksandr Kyriienko and Anders S. Sørensen. “Continuous-Wave Single-Photon Transistor Based on a Superconducting Circuit”. In: *Physical Review Letters* 117.14 (Sept. 2016). ISSN: 1079-7114. DOI: 10.1103/physrevlett.117.140503.

- [111] Jeffrey H. Shapiro. “Single-photon Kerr nonlinearities do not help quantum computation”. In: *Phys. Rev. A* 73 (6 June 2006), page 062305. DOI: 10.1103/PhysRevA.73.062305.
- [112] Daniel Tiarks, Steffen Schmidt, Gerhard Rempe, and Stephan Dürr. “Optical π phase shift created with a single-photon pulse”. In: *Science Advances* 2.4 (2016). DOI: 10.1126/sciadv.1600036. eprint: <http://advances.sciencemag.org/content/2/4/e1600036.full.pdf>.
- [113] Weibin Li and Igor Lesanovsky. “Coherence in a cold-atom photon switch”. In: *Phys. Rev. A* 92 (4 Oct. 2015), page 043828. DOI: 10.1103/PhysRevA.92.043828.
- [114] William Happer. “Optical Pumping”. In: *Rev. Mod. Phys.* 44 (2 Apr. 1972), pages 169–249. DOI: 10.1103/RevModPhys.44.169.
- [115] J. P. Gordon, H. J. Zeiger, and C. H. Townes. “Molecular Microwave Oscillator and New Hyperfine Structure in the Microwave Spectrum of NH_3 ”. In: *Phys. Rev.* 95 (1 July 1954), pages 282–284. DOI: 10.1103/PhysRev.95.282.
- [116] T. H. Maiman. “Stimulated Optical Radiation in Ruby”. In: *Nature* 187 (Aug. 1960), pages 493–494. DOI: 10.1038/187493a0.
- [117] R. N. Hall, G. E. Fenner, J. D. Kingsley, T. J. Soltys, and R. O. Carlson. “Coherent Light Emission From GaAs Junctions”. In: *Phys. Rev. Lett.* 9 (9 Nov. 1962), pages 366–368. DOI: 10.1103/PhysRevLett.9.366.
- [118] J. H. Gurian, P. Cheinet, P. Huillery, A. Fioretti, J. Zhao, P. L. Gould, D. Comparat, and P. Pillet. “Observation of a Resonant Four-Body Interaction in Cold Cesium Rydberg Atoms”. In: *Phys. Rev. Lett.* 108 (2 Jan. 2012), page 023005. DOI: 10.1103/PhysRevLett.108.023005.

- [119] T. L. Gustavson, A. P. Chikkatur, A. E. Leanhardt, A. Görlitz, S. Gupta, D. E. Pritchard, and W. Ketterle. “Transport of Bose-Einstein Condensates with Optical Tweezers”. In: *Phys. Rev. Lett.* 88 (2 Dec. 2001), page 020401. DOI: 10.1103/PhysRevLett.88.020401.
- [120] Julian Léonard, Moonjoo Lee, Andrea Morales, Thomas M Karg, Tilman Esslinger, and Tobias Donner. “Optical transport and manipulation of an ultracold atomic cloud using focus-tunable lenses”. In: *New Journal of Physics* 16.9 (Sept. 2014), page 093028. ISSN: 1367-2630. DOI: 10.1088/1367-2630/16/9/093028.
- [121] Markus Greiner, Immanuel Bloch, Theodor W. Hänsch, and Tilman Esslinger. “Magnetic transport of trapped cold atoms over a large distance”. In: *Phys. Rev. A* 63 (3 Feb. 2001), page 031401. DOI: 10.1103/PhysRevA.63.031401.
- [122] H. J. Lewandowski, D. M. Harber, D. L. Whitaker, and E. A. Cornell. “Simplified System for Creating a Bose-Einstein Condensate”. In: *J. Low Temp. Phys.* 132 (2003), page 309.
- [123] William D. Phillips and Harold Metcalf. “Laser Deceleration of an Atomic Beam”. In: *Phys. Rev. Lett.* 48 (9 Mar. 1982), pages 596–599. DOI: 10.1103/PhysRevLett.48.596.
- [124] K Dieckmann, RJC Spreeuw, M Weidemüller, and JTM Walraven. “Two-dimensional magneto-optical trap as a source of slow atoms”. In: *Physical Review A* 58.5 (1998), page 3891.
- [125] Markus Falkenau, Valentin V. Volchkov, Jahn Rührig, Axel Griesmaier, and Tilman Pfau. “Continuous Loading of a Conservative Potential Trap from an Atomic Beam”. In: *Phys. Rev. Lett.* 106 (16 Apr. 2011), page 163002. DOI: 10.1103/PhysRevLett.106.163002.

- [126] Will Gunton, Mariusz Semczuk, and Kirk W. Madison. “Realization of BEC-BCS-crossover physics in a compact oven-loaded magneto-optic-trap apparatus”. In: *Phys. Rev. A* 88 (2 Aug. 2013), page 023624. DOI: 10.1103/PhysRevA.88.023624.
- [127] C. Klempt, T. van Zoest, T. Henninger, O. Topic, E. Rasel, W. Ertmer, and J. Arlt. “Ultraviolet light-induced atom desorption for large rubidium and potassium magneto-optical traps”. In: *Phys. Rev. A* 73 (1 Jan. 2006), page 013410. DOI: 10.1103/PhysRevA.73.013410.
- [128] Lara Torralbo-Campo, Graham D. Bruce, Giuseppe Smirne, and Donatella Cassettari. “Light-induced atomic desorption in a compact system for ultracold atoms”. In: *Scientific Reports* 5 (Oct. 2015), page 14729. ISSN: 2045-2322. DOI: 10.1038/srep14729.
- [129] Cheng Chin, Rudolf Grimm, Paul Julienne, and Eite Tiesinga. “Feshbach resonances in ultracold gases”. In: *Rev. Mod. Phys.* 82 (2 Apr. 2010), pages 1225–1286. DOI: 10.1103/RevModPhys.82.1225.
- [130] H. M. J. M. Boesten, C. C. Tsai, J. R. Gardner, D. J. Heinzen, and B. J. Verhaar. “Observation of a shape resonance in the collision of two cold Rb 87 atoms”. In: *Physical Review A* 55.1 (Jan. 1997), 636–640. ISSN: 1094-1622. DOI: 10.1103/physreva.55.636.
- [131] Immanuel Bloch, Markus Greiner, Olaf Mandel, Theodor W. Hänsch, and Tilman Esslinger. “Sympathetic cooling of 85 Rb and 87 Rb”. In: *Physical Review A* 64.2 (July 2001). ISSN: 1094-1622. DOI: 10.1103/physreva.64.021402.
- [132] L. J. Kieffer and Gordon H. Dunn. “Electron Impact Ionization Cross-Section Data for Atoms, Atomic Ions, and Diatomic Molecules: I. Experimental Data”. In: *Reviews of Modern Physics* 38.1 (Jan. 1966), pages 1–35. DOI: 10.1103/revmodphys.38.1.

- [133] Yong-Ki Kim, Jacek Migdalek, Wojciech Siegel, and Jacek Bieroń. “Electron-impact ionization cross section of rubidium”. In: *Physical Review A* 57.1 (Jan. 1998), pages 246–254. ISSN: 1094-1622. DOI: 10.1103/physreva.57.246.
- [134] Y.-K. Kim, K.K. Irikura, M.E. Rudd, M.A. Ali, P.M. Stone, J. Chang, J.S. Coursey, R.A. Dragoset, A.R. Kishore, K.J. Olsen, A.M. Sansonetti, G.G. Wiersma, D.S. Zucker, and M.A. Zucker. *NIST electron-impact ionization cross section database*. Feb. 2016. URL: <http://www.nist.gov/pml/data/ionization/>.
- [135] *UHV-24/UHV-24p Ionization Gauge*. Rev. E. Agilent Technologies. July 2004.
- [136] T. Arpornthip, C. A. Sackett, and K. J. Hughes. “Vacuum-pressure measurement using a magneto-optical trap”. In: *Phys. Rev. A* 85 (3 Mar. 2012), page 033420. DOI: 10.1103/PhysRevA.85.033420.
- [137] Rowan W. G. Moore, Lucie A. Lee, Elizabeth A. Findlay, Lara Torralbo-Campo, Graham D. Bruce, and Donatella Cassettari. “Measurement of vacuum pressure with a magneto-optical trap: A pressure-rise method”. In: *Review of Scientific Instruments* 86.9 (Sept. 2015), page 093108. ISSN: 1089-7623. DOI: 10.1063/1.4928154.
- [138] Johannes Schmidt. “Generation of non-classical light using ultra-cold Rydberg ensembles”. Master’s thesis. Universität Stuttgart, Oct. 2014.
- [139] Thomas Dieterle. “Characterization Of A Single Ion Detector In A Rydberg Experiment”. Bachelor’s Thesis. Universität Stuttgart, Oct. 2015.
- [140] Robert Loew, Hendrik Weimer, Johannes Nipper, Jonathan B Balewski, Bjoern Butscher, Hans Peter Buechler, and Tilman Pfau. “An experimental and theoretical guide to strongly interacting Rydberg gases”. In: *Journal of Physics B: Atomic, Molecular and Optical Physics* 45.11 (2012), page 113001.

- [141] Jan R. Rubbmark, Michael M. Kash, Michael G. Littman, and Daniel Kleppner. “Dynamical effects at avoided level crossings: A study of the Landau-Zener effect using Rydberg atoms”. In: *Physical Review A* 23.6 (June 1981), pages 3107–3117. ISSN: 0556-2791. DOI: 10.1103/physreva.23.3107.
- [142] Christoph Tresp. “A Setup for Highly Precise Excitation and Detection of Rydberg Atoms”. Master’s thesis. Universität Stuttgart, Oct. 2012.
- [143] J. Guena, M. Abgrall, D. Rovera, P. Laurent, B. Chupin, M. Lours, G. Santarelli, P. Rosenbusch, M. E. Tobar, and Ruoxin Li. “Progress in atomic fountains at LNE-SYRTE”. In: *IEEE Trans. Ultrason., Ferroelect., Freq. Contr.* 59.3 (Mar. 2012), pages 391–409. ISSN: 0885-3010. DOI: 10.1109/tuffc.2012.2208.
- [144] D. A. Steck. *Rubidium 87 D Line Data*. 2001.
- [145] Christoph Braun. “Implementation of a Raman Sideband Cooling for 87Rb”. Bachelor’s Thesis. Universität Stuttgart, Oct. 2015.
- [146] Wolfgang Ketterle, Kendall B. Davis, Michael A. Joffe, Alex Martin, and David E. Pritchard. “High densities of cold atoms in a dark spontaneous-force optical trap”. In: *Physical Review Letters* 70.15 (Apr. 1993), pages 2253–2256. ISSN: 0031-9007. DOI: 10.1103/physrevlett.70.2253.
- [147] J. Deiglmayr, M. Reetz-Lamour, T. Amthor, S. Westermann, A.L. de Oliveira, and M. Weidemüller. “Coherent excitation of Rydberg atoms in an ultracold gas”. In: *Optics Communications* 264.2 (Aug. 2006), pages 293–298. ISSN: 0030-4018. DOI: 10.1016/j.optcom.2006.02.058.
- [148] M. S. O’Sullivan and B. P. Stoicheff. “Scalar polarizabilities and avoided crossings of high Rydberg states in Rb”. In: *Phys. Rev. A* 31 (4 Apr. 1985), pages 2718–2720. DOI: 10.1103/PhysRevA.31.2718.

- [149] B. Cheron, H. Gilles, J. Hamel, O. Moreau, and H. Sorel. “Laser frequency stabilization using Zeeman effect”. In: *Journal de Physique III* 4.2 (Feb. 1994), pages 401–406. ISSN: 1286-4897. DOI: 10.1051/jp3:1994136.
- [150] Kristan L. Corwin, Zheng-Tian Lu, Carter F. Hand, Ryan J. Epstein, and Carl E. Wieman. “Frequency-Stabilized Diode Laser with the Zeeman Shift in an Atomic Vapor”. In: *Appl. Opt.* 37.15 (May 1998), pages 3295–3298. DOI: 10.1364/AO.37.003295.
- [151] T. Petelski, M. Fattori, G. Lamporesi, J. Stuhler, and G.M. Tino. “Doppler-free spectroscopy using magnetically induced dichroism of atomic vapor: a new scheme for laser frequency locking”. In: *Eur. Phys. J. D* 22 (2003), pages 279–283. DOI: DOI:10.1140/epjd/e2002-00238-4.
- [152] R. W. P. Drever, J. L. Hall, F. V. Kowalski, J. Hough, G. M. Ford, A. J. Munley, and H. Ward. “Laser phase and frequency stabilization using an optical resonator”. In: *Applied Physics B: Lasers and Optics* 31 (2 1983). 10.1007/BF00702605, pages 97–105. ISSN: 0946-2171.
- [153] U. Schünemann, H. Engler, R. Grimm, M. Weidemüller, and M. Zielonkowski. “Simple scheme for tunable frequency offset locking of two lasers”. In: *Review of Scientific Instruments* 70.1 (1999), page 242. ISSN: 0034-6748. DOI: 10.1063/1.1149573.
- [154] Michael Schlagmueller. “A single Rydberg Atom interacting with a Dense and Ultracold Gas”. PhD thesis. Universität Stuttgart, 2016.
- [155] *DET10 A(/M) Si Biased Detector User Guide*. Rev. E. Thorlabs, Inc. Mar. 2015.
- [156] C.J. Foot. *Atomic Physics*. Oxford Master Series in Physics. OUP Oxford, 2004. ISBN: 9780191037078.
- [157] H. J. Metcalf and P. van der Straten. *Laser Cooling and Trapping*. Springer, 2001.

- [158] C.S. Adams and E. Riis. “Laser cooling and trapping of neutral atoms”. In: *Progress in Quantum Electronics* 21.1 (Jan. 1997), pages 1–79. ISSN: 0079-6727. DOI: 10.1016/S0079-6727(96)00006-7.
- [159] E. L. Raab, M. Prentiss, Alex Cable, Steven Chu, and D. E. Pritchard. “Trapping of Neutral Sodium Atoms with Radiation Pressure”. In: *Phys. Rev. Lett.* 59 (23 Dec. 1987), pages 2631–2634. DOI: 10.1103/PhysRevLett.59.2631.
- [160] W. Ketterle, D. S. Durfee, and D. M. Stamper-Kurn. “Making, probing and understanding Bose-Einstein condensates”. In: *eprint arXiv:cond-mat/9904034* (Apr. 1999). eprint: cond-mat/9904034.
- [161] S. J. M. Kuppens, K. L. Corwin, K. W. Miller, T. E. Chupp, and C. E. Wieman. “Loading an optical dipole trap”. In: *Phys. Rev. A* 62 (2000), page 013406. DOI: <http://dx.doi.org/10.1103/PhysRevA.62.013406>.
- [162] J. D. Miller, R. A. Cline, and D. J. Heinzen. “Far-off-resonance optical trapping of atoms”. In: *Physical Review A* 47.6 (June 1993), R4567–R4570. ISSN: 1094-1622. DOI: 10.1103/physreva.47.r4567.
- [163] T. Lauber, J. Küber, O. Wille, and G. Birkl. “Optimized Bose-Einstein-condensate production in a dipole trap based on a 1070-nm multifrequency laser: Influence of enhanced two-body loss on the evaporation process”. In: *Phys. Rev. A* 84 (4 Oct. 2011), page 043641. DOI: 10.1103/PhysRevA.84.043641.
- [164] Weilun Hung, Panpan Huang, Feng-Chuan Wu, M. Bruvelis, Hau-Yl Xiao, A. Ekers, and Ite A. Yu. “Storage time of cold Rb atoms in an optical dipole trap formed by a multimode fiber laser”. In: *J. Opt. Soc. Am. B* 32.5 (Apr. 2015), B32. ISSN: 1520-8540. DOI: 10.1364/josab.32.000b32.

- [165] Marcel Mudrich, Stephan Kraft, Jörg Lange, Allard Mosk, Matthias Weidemüller, and Eite Tiesinga. “Hyperfine-changing collisions in an optically trapped gas of ultracold cesium and lithium”. In: *Physical Review A* 70.6 (Dec. 2004). ISSN: 1094-1622. DOI: 10.1103/physreva.70.062712.
- [166] E. Snitzer, H. Po, F. Hakimi, R. Tumminelli, and B. C. McCollum. “Erbium fiber laser amplifier at 1.55 μm with pump at 1.49 μm and Yb sensitized Er oscillator”. In: *Optical Fiber Communication*. Optical Society of America, 1988, PD2. DOI: 10.1364/OFC.1988.PD2.
- [167] K Henderson, C Ryu, C MacCormick, and M G Boshier. “Experimental demonstration of painting arbitrary and dynamic potentials for Bose–Einstein condensates”. In: *New J. Phys.* 11.4 (Apr. 2009), page 043030. ISSN: 1367-2630. DOI: 10.1088/1367-2630/11/4/043030.
- [168] Silvia Bergamini, Benoît Darquié, Matthew Jones, Lionel Jacubowicz, Antoine Browaeys, and Philippe Grangier. “Holographic generation of microtrap arrays for single atoms by use of a programmable phase modulator”. In: *J. Opt. Soc. Am. B* 21.11 (Nov. 2004), page 1889. ISSN: 1520-8540. DOI: 10.1364/josab.21.001889.
- [169] Christof Weitenberg, Manuel Endres, Jacob F. Sherson, Marc Cheneau, Peter Schauß, Takeshi Fukuhara, Immanuel Bloch, and Stefan Kuhr. “Single-spin addressing in an atomic Mott insulator”. In: *Nature* 471.7338 (Mar. 2011), pages 319–324. ISSN: 1476-4687. DOI: 10.1038/nature09827.
- [170] C. Ryu, M. Andersen, P. Cladé, Vasant Natarajan, K. Helmerson, and W. Phillips. “Observation of Persistent Flow of a Bose-Einstein Condensate in a Toroidal Trap”. In: *Physical Review Letters* 99.26 (Dec. 2007). ISSN: 1079-7114. DOI: 10.1103/physrevlett.99.260401.

- [171] D. Jacob, E. Mimoun, L. De Sarlo, M. Weitz, J. Dalibard, and F. Gerbier. “Production of sodium Bose-Einstein condensates in an optical dimple trap”. In: *New Journal of Physics* 13 (2011), page 065022.
- [172] T. A. Savard, K. M. O’Hara, and J. E. Thomas. “Laser-noise-induced heating in far-off resonance optical traps”. In: *Physical Review A* 56.2 (Aug. 1997), R1095–R1098. ISSN: 1094-1622. DOI: 10.1103/physreva.56.r1095.
- [173] M. S. Safronova, Carl J. Williams, and Charles W. Clark. “Optimizing the fast Rydberg quantum gate”. In: *Physical Review A* 67.4 (Apr. 2003). ISSN: 1094-1622. DOI: 10.1103/physreva.67.040303.
- [174] R Mukherjee, J Millen, R Nath, M P A Jones, and T Pohl. “Many-body physics with alkaline-earth Rydberg lattices”. In: *Journal of Physics B: Atomic, Molecular and Optical Physics* 44.18 (2011), page 184010.
- [175] E. A. Goldschmidt, D. G. Norris, S. B. Koller, R. Wyllie, R. C. Brown, J. V. Porto, U. I. Safronova, and M. S. Safronova. “Magic wavelengths for the $5s - 18s$ transition in rubidium”. In: *Physical Review A* 91.3 (Mar. 2015). ISSN: 1094-1622. DOI: 10.1103/physreva.91.032518.
- [176] S. K. Dutta, J. R. Guest, D. Feldbaum, A. Walz-Flannigan, and G. Raithel. “Ponderomotive Optical Lattice for Rydberg Atoms”. In: *Phys. Rev. Lett.* 85 (26 Dec. 2000), pages 5551–5554. DOI: 10.1103/PhysRevLett.85.5551.
- [177] R. Hanbury Brown and R. Q. Twiss. “Correlation between Photons in two Coherent Beams of Light”. In: *Nature* 177.4497 (Jan. 1956), pages 27–29. ISSN: 0028-0836. DOI: 10.1038/177027a0.
- [178] Markus Koch, Christian Sames, Maximilian Balbach, Haytham Chibani, Alexander Kubanek, Karim Murr, Tatjana Wilk, and Gerhard Rempe. “Three-Photon Correlations in a Strongly Driven Atom-Cavity System”. In: *Phys. Rev. Lett.* 107 (2 July 2011), page 023601. DOI: 10.1103/PhysRevLett.107.023601.

- [179] E. Hecht. *Optics*. Addison-Wesley, 2002. ISBN: 9780805385663.
- [180] H.A. Lorentz. *The Theory of Electrons and Its Applications to the Phenomena of Light and Radiant Heat*. Leipzig : B.G. Teubner ; New York : G.E. Stechert, 1916.
- [181] Olivier Morice, Yvan Castin, and Jean Dalibard. “Refractive index of a dilute Bose gas”. In: *Phys. Rev. A* 51 (5 May 1995), pages 3896–3901. DOI: 10.1103/PhysRevA.51.3896.
- [182] P. C. Bons, R. de Haas, D. de Jong, A. Groot, and P. van der Straten. “Quantum Enhancement of the Index of Refraction in a Bose-Einstein Condensate”. In: *Physical Review Letters* 116.17 (Apr. 2016). ISSN: 1079-7114. DOI: 10.1103/physrevlett.116.173602.
- [183] C. Cohen-Tannoudji, J. Dupont-Roc, and G. Grynberg. *Atom-Photon Interactions: Basic Processes and Applications*. A Wiley-Interscience publication. Wiley, 1998. ISBN: 9780471293361.
- [184] R. Loudon. *The Quantum Theory of Light*. OUP Oxford, 2000. ISBN: 9780191589782.
- [185] Jingshan Han, Thibault Vogt, Manukumara Manjappa, Ruixiang Guo, Martin Kiffner, and Wenhui Li. “Lensing effect of electromagnetically induced transparency involving a Rydberg state”. In: *Physical Review A* 92.6 (Dec. 2015). ISSN: 1094-1622. DOI: 10.1103/physreva.92.063824.
- [186] Claude Cohen-Tannoudji and Alfred Kastler. “I Optical Pumping”. In: edited by E. Wolf. Volume 5. *Progress in Optics*. Elsevier, 1966, pages 1–81. DOI: [http://dx.doi.org/10.1016/S0079-6638\(08\)70450-5](http://dx.doi.org/10.1016/S0079-6638(08)70450-5).
- [187] Christian Zimmer. “Single-Photon Gates Mediated by Single-Blockade-Sized Rydberg Medium”. Master’s thesis. Universität Stuttgart, May 2016.

- [188] Stephan Jennewein. “Building an Apparatus for Cold Rubidium Rydberg Atoms”. Master’s thesis. Universität Stuttgart, 2012.
- [189] Felix Engel. “Entwicklung eines FPGA basierten Pulsgenerators mit Nanosekunden-Auflösung für schnelle Rydberg-Experimente”. Bachelor thesis. Universität Stuttgart, 2013.
- [190] Fabian Böttcher. “Detection of Few-Photon Pulses for a Rydberg Quantum Optics Experiment”. Master’s thesis. Universität Stuttgart, Aug. 2013.
- [191] S. Hofferberth, I. Lesanovsky, B. Fischer, J. Verdu, and J. Schmiedmayer. “Radiofrequency-dressed-state potentials for neutral atoms”. In: *Nature Phys.* 2 (2006), pages 710–716. DOI: 10.1038/nphys420.
- [192] Charles C. Agosta, Isaac F. Silvera, H. T. C. Stoof, and B. J. Verhaar. “Trapping of neutral atoms with resonant microwave radiation”. In: *Phys. Rev. Lett.* 62 (20 May 1989), pages 2361–2364. DOI: 10.1103/PhysRevLett.62.2361.
- [193] R. J. C. Spreeuw, C. Gerz, Lori S. Goldner, W. D. Phillips, S. L. Rolston, C. I. Westbrook, M. W. Reynolds, and Isaac F. Silvera. “Demonstration of neutral atom trapping with microwaves”. In: *Physical Review Letters* 72.20 (May 1994), pages 3162–3165. ISSN: 0031-9007. DOI: 10.1103/physrevlett.72.3162.
- [194] Y. Colombe, E. Knyazchyan, O. Morizot, B. Mercier, V. Lorent, and H. Perrin. “Ultracold atoms confined in rf-induced two-dimensional trapping potentials”. In: *EPL (Europhysics Letters)* 67.4 (2004), page 593.
- [195] Vladimir Djokic, Georg Enzian, Frank Vewinger, and Martin Weitz. “Resonance retrieval of stored coherence in an rf-optical double-resonance experiment”. In: *Physical Review A* 92.6 (Dec. 2015). ISSN: 1094-1622. DOI: 10.1103/physreva.92.063802.

- [196] Jianing Han, Yasir Jamil, D. V. L. Norum, Paul J. Tanner, and T. F. Gallagher. “Rb nf quantum defects from millimeter-wave spectroscopy of cold ^{85}Rb Rydberg atoms”. In: *Phys. Rev. A* 74 (5 Nov. 2006), page 054502. DOI: 10.1103/PhysRevA.74.054502.
- [197] H. Saßmannshausen, F. Merkt, and J. Deiglmayr. “High-resolution spectroscopy of Rydberg states in an ultracold cesium gas”. In: *Phys. Rev. A* 87 (3 Mar. 2013), page 032519. DOI: 10.1103/PhysRevA.87.032519.
- [198] D. Maxwell, D. J. Szwer, D. Paredes-Barato, H. Busche, J. D. Pritchard, A. Gauguet, K. J. Weatherill, M. P. A. Jones, and C. S. Adams. “Storage and Control of Optical Photons Using Rydberg Polaritons”. In: *Phys. Rev. Lett.* 110 (10 Mar. 2013), page 103001. DOI: 10.1103/PhysRevLett.110.103001.
- [199] C Veit, G Epple, H Kübler, T G Euser, P St J Russell, and R Löw. “RF-dressed Rydberg atoms in hollow-core fibres”. In: *Journal of Physics B: Atomic, Molecular and Optical Physics* 49.13 (June 2016), page 134005. ISSN: 1361-6455. DOI: 10.1088/0953-4075/49/13/134005.
- [200] J. A. Sedlacek, A. Schwettmann, H. Kübler, and J. P. Shaffer. “Atom-Based Vector Microwave Electrometry Using Rubidium Rydberg Atoms in a Vapor Cell”. In: *Physical Review Letters* 111.6 (Aug. 2013). ISSN: 1079-7114. DOI: 10.1103/physrevlett.111.063001.
- [201] K. R. Overstreet, A. Schwettmann, J. Tallant, D. Booth, and J. P. Shaffer. “Observation of electric-field-induced Cs Rydberg atom macrodimers”. In: *Nature Physics* 5 (2009), pages 581–585. DOI: doi:10.1038/nphys1307.
- [202] Randall G. Hulet and Daniel Kleppner. “Rydberg Atoms in Circular States”. In: *Phys. Rev. Lett.* 51 (16 Oct. 1983), pages 1430–1433. DOI: 10.1103/PhysRevLett.51.1430.

- [203] W A Molander, C R Stroud Jr, and J A Yeazell. “Excitation of high angular momentum Rydberg states”. In: *Journal of Physics B: Atomic and Molecular Physics* 19.12 (1986), page L461.
- [204] Adrien Facon, Eva-Katharina Dietsche, Dorian Grosso, Serge Haroche, Jean-Michel Raimond, Michel Brune, and Sébastien Gleyzes. “A sensitive electrometer based on a Rydberg atom in a Schrödinger-cat state”. In: *Nature* 535.7611 (July 2016), pages 262–265. ISSN: 0028-0836.
- [205] D. Maxwell, D. J. Szwer, D. Paredes-Barato, H. Busche, J. D. Pritchard, A. Gauguet, M. P. A. Jones, and C. S. Adams. “Microwave control of the interaction between two optical photons”. In: *Phys. Rev. A* 89 (4 Apr. 2014), page 043827. DOI: 10.1103/PhysRevA.89.043827.
- [206] Robert J. Le Roy. “Long-Range Potential Coefficients From RKR Turning Points: C6 and C8 for B(3ΠO_u⁺)-State Cl₂, Br₂, and I₂”. In: *Canadian Journal of Physics* 52.3 (1974), pages 246–256. DOI: 10.1139/p74-035.
eprint:
<http://www.nrcresearchpress.com/doi/pdf/10.1139/p74-035>.
- [207] Kilian Singer, Jovica Stanojevic, Matthias Weidemüller, and Robin Côté. “Long-range interactions between alkali Rydberg atom pairs correlated to the n s– n s, n p– n p and n d– n d asymptotes”. In: *Journal of Physics B: Atomic, Molecular and Optical Physics* 38.2 (Jan. 2005), S295–S307. ISSN: 1361-6455. DOI: 10.1088/0953-4075/38/2/021.
- [208] Hans A. Bethe and Edwin E. Salpeter. “The hydrogen atom without external fields”. In: *Quantum Mechanics of One- and Two-Electron Atoms*. Boston, MA: Springer US, 1977, pages 4–118. ISBN: 978-1-4613-4104-8. DOI: 10.1007/978-1-4613-4104-8_2.

- [209] Johannes Deiglmayr. “Long-range interactions between Rydberg atoms”. In: *Physica Scripta* 91.10 (Sept. 2016), page 104007. ISSN: 1402-4896. DOI: 10.1088/0031-8949/91/10/104007.
- [210] M R Flannery, D Vrinceanu, and V N Ostrovsky. “Long-range interaction between polar Rydberg atoms”. In: *Journal of Physics B: Atomic, Molecular and Optical Physics* 38.2 (Jan. 2005), S279. ISSN: 1361-6455. DOI: 10.1088/0953-4075/38/2/020.
- [211] Arne Schwettmann, Jeff Crawford, K. Richard Overstreet, and James P. Shaffer. “Cold Cs Rydberg-gas interactions”. In: *Phys. Rev. A* 74 (2 Aug. 2006), page 020701. DOI: 10.1103/PhysRevA.74.020701.
- [212] Johannes Deiglmayr, Heiner Saßmannshausen, Pierre Pillet, and Frédéric Merkt. “Observation of Dipole-Quadrupole Interaction in an Ultracold Gas of Rydberg Atoms”. In: *Phys. Rev. Lett.* 113 (19 Nov. 2014), page 193001. DOI: 10.1103/PhysRevLett.113.193001.
- [213] I. Mourachko, D. Comparat, F. de Tomasi, A. Fioretti, P. Nosbaum, V. M. Akulin, and P. Pillet. “Many-Body Effects in a Frozen Rydberg Gas”. In: *Phys. Rev. Lett.* 80.2 (Jan. 1998), pages 253–256. DOI: 10.1103/PhysRevLett.80.253.
- [214] A. Walz-Flannigan, J. R. Guest, J.-H. Choi, and G. Raithel. “Cold-Rydberg-gas dynamics”. In: *Phys. Rev. A* 69 (6 June 2004), page 063405. DOI: 10.1103/PhysRevA.69.063405.
- [215] Wenhui Li, Michael W. Noel, Michael P. Robinson, Paul J. Tanner, Thomas F. Gallagher, Daniel Comparat, Bruno Laburthe Tolra, Nicolas Vanhaecke, Thibault Vogt, Nassim Zahzam, Pierre Pillet, and Duncan A. Tate. “Evolution dynamics of a dense frozen Rydberg gas to plasma”. In: *Physical Review A* 70.4 (Oct. 2004). ISSN: 1094-1622. DOI: 10.1103/physreva.70.042713.

- [216] A. Reinhard, T. Cubel Liebisch, K. C. Younge, P. R. Berman, and G. Raithel. “Rydberg-Rydberg Collisions: Resonant Enhancement of State Mixing and Penning Ionization”. In: *Physical Review Letters* 100.12 (Mar. 2008). ISSN: 1079-7114. DOI: 10.1103/physrevlett.100.123007.
- [217] A. Reinhard, T. Cubel Liebisch, B. Knuffman, and G. Raithel. “Level shifts of rubidium Rydberg states due to binary interactions”. In: *Phys. Rev. A* 75.3 (Mar. 2007), page 032712. DOI: 10.1103/PhysRevA.75.032712.
- [218] T. G. Walker and M. Saffman. “Consequences of Zeeman degeneracy for the van der Waals blockade between Rydberg atoms”. In: *Phys. Rev. A* 77 (2008), page 032723. DOI: 10.1103/PhysRevA.77.032723.
- [219] Hashem Zoubi. “Van der Waals interactions among alkali Rydberg atoms with excitonic states”. In: *Journal of Physics B: Atomic, Molecular and Optical Physics* 48.18 (Aug. 2015), page 185002. ISSN: 1361-6455. DOI: 10.1088/0953-4075/48/18/185002.
- [220] D. Barredo, S. Ravets, H. Labuhn, L. Béguin, A. Vernier, F. Nogrette, T. Lahaye, and A. Browaeys. “Demonstration of a Strong Rydberg Blockade in Three-Atom Systems with Anisotropic Interactions”. In: *Phys. Rev. Lett.* 112 (18 May 2014), page 183002. DOI: 10.1103/PhysRevLett.112.183002.
- [221] Constantine E. Theodosiou. “Lifetimes of alkali-metal atom Rydberg states”. In: *Phys. Rev. A* 30 (6 Dec. 1984), pages 2881–2909. DOI: 10.1103/PhysRevA.30.2881.
- [222] M. Marinescu, H. R. Sadeghpour, and A. Dalgarno. “Dispersion coefficients for alkali-metal dimers”. In: *Phys. Rev. A* 49 (2 Feb. 1994), pages 982–988. DOI: 10.1103/PhysRevA.49.982.

- [223] I. I. Beterov and M. Saffman. “Rydberg blockade, Förster resonances, and quantum state measurements with different atomic species”. In: *Physical Review A* 92.4 (Oct. 2015). ISSN: 1094-1622. DOI: 10.1103/physreva.92.042710.
- [224] Daniel Tiarks, Simon Baur, Katharina Schneider, Stephan Dürr, and Gerhard Rempe. “Single-Photon Transistor Using a Förster Resonance”. In: *Phys. Rev. Lett.* 113 (5 July 2014), page 053602. DOI: 10.1103/PhysRevLett.113.053602.
- [225] Jonathan Pritchard. “Cooperative Optical Non-linearity in a blockaded Rydberg ensemble”. PhD thesis. Durham University, 2011.
- [226] M. Fleischhauer, A. Imamoglu, and J.P. Marangos. “Electromagnetically induced transparency: Optics in coherent media”. In: *Rev. Mod. Phys.* 77 (2005), page 633. DOI: 10.1103/RevModPhys.77.633.
- [227] P.D. Nation and J.R. Johansson. *Lindblad Master Equation Solver*. Accessed on Aug 03, 2016. 2015. URL: <http://qutip.org/docs/3.1.0/guide/dynamics/dynamics-master.html> (visited on 12/08/2015).
- [228] V Gavryusev, A Signoles, M Ferreira-Cao, G Zürn, C S Hofmann, G Günter, H Schempp, M Robert-de-Saint-Vincent, S Whitlock, and M Weidemüller. “Density matrix reconstruction of three-level atoms via Rydberg electromagnetically induced transparency”. In: *Journal of Physics B: Atomic, Molecular and Optical Physics* 49.16 (2016), page 164002.
- [229] U Volz and H Schmoranzler. “Precision lifetime measurements on alkali atoms and on helium by beam–gas–laser spectroscopy”. In: *Physica Scripta* 1996.T65 (1996), page 48.

- [230] C. D. Herold, V. D. Vaidya, X. Li, S. L. Rolston, J. V. Porto, and M. S. Safronova. “Precision Measurement of Transition Matrix Elements via Light Shift Cancellation”. In: *Physical Review Letters* 109.24 (Dec. 2012). ISSN: 1079-7114. DOI: 10.1103/physrevlett.109.243003.
- [231] M J Piotrowicz, C MacCormick, A Kowalczyk, S Bergamini, I I Beterov, and E A Yakshina. “Measurement of the electric dipole moments for transitions to rubidium Rydberg states via Autler–Townes splitting”. In: *New J. Phys.* 13.9 (Sept. 2011), page 093012. ISSN: 1367-2630. DOI: 10.1088/1367-2630/13/9/093012.
- [232] S. E. Harris, J. E. Field, and A. Kasapi. “Dispersive properties of electromagnetically induced transparency”. In: *Physical Review A* 46.1 (July 1992), R29–R32. ISSN: 1094-1622. DOI: 10.1103/physreva.46.r29.
- [233] Min Xiao, Yong-qing Li, Shao-zheng Jin, and Julio Gea-Banacloche. “Measurement of Dispersive Properties of Electromagnetically Induced Transparency in Rubidium Atoms”. In: *Physical Review Letters* 74.5 (Jan. 1995), pages 666–669. ISSN: 1079-7114. DOI: 10.1103/physrevlett.74.666.
- [234] L.V. Hau, S.E. Harris, Z. Dutton, and C.H. Behroozi. “Light speed reduction to 17 metres per second in an ultracold atomic gas”. In: *Nature* 397.6720 (1999), pages 594–598.
- [235] Yuri Rostovtsev, Olga Kocharovskaya, George R. Welch, and Marlan O. Scully. “Slow, Ultraslow, Stored, and Frozen Light”. In: *Optics & Photonics News* 13.6 (June 2002), page 44. ISSN: 1541-3721. DOI: 10.1364/opn.13.6.000044.
- [236] M. D. Lukin and A. Imamoglu. “Controlling photons using electromagnetically induced transparency”. In: *Nature* 413 (2001), page 273. DOI: 10.1038/35095000.

- [237] JohnC Howell and RyanM Camacho. “Slow Light in Atomic Vapors”. In: *Optical Science and Engineering*. CRC Press, Dec. 2008. DOI: 10.1201/9781420061529.pt1.
- [238] M. J. McDonnell, D. N. Stacey, and A. M. Steane. “Laser linewidth effects in quantum state discrimination by electromagnetically induced transparency”. In: *Physical Review A* 70.5 (Nov. 2004). ISSN: 1094-1622. DOI: 10.1103/physreva.70.053802.
- [239] S. M. Iftiqar. “Electromagnetically induced transparency at high optical power”. In: *ArXiv e-prints* (Nov. 2007). arXiv: 0711.2662 [physics.atom-ph].
- [240] S Sevinçli, C Ates, T Pohl, H Schempp, C S Hofmann, G Günter, T Amthor, M Weidemüller, J D Pritchard, D Maxwell, A Gauguet, K J Weatherill, M P A Jones, and C S Adams. “Quantum interference in interacting three-level Rydberg gases: coherent population trapping and electromagnetically induced transparency”. In: *Journal of Physics B: Atomic, Molecular and Optical Physics* 44.18 (Sept. 2011), page 184018. ISSN: 1361-6455. DOI: 10.1088/0953-4075/44/18/184018.
- [241] I. I. Ryabtsev, I. I. Beterov, D. B. Tretyakov, V. M. Entin, and E. A. Yakshina. “Doppler- and recoil-free laser excitation of Rydberg states via three-photon transitions”. In: *Physical Review A* 84.5 (Nov. 2011). ISSN: 1094-1622. DOI: 10.1103/physreva.84.053409.
- [242] Hubert Ammann and Nelson Christensen. “Delta Kick Cooling: A New Method for Cooling Atoms”. In: *Physical Review Letters* 78.11 (Mar. 1997), pages 2088–2091. ISSN: 1079-7114. DOI: 10.1103/physrevlett.78.2088.
- [243] J. Balewski, A. Krupp, A. Gaj, D. Peter, H.P. Buchler, R. Low, S. Hofferberth, and T. Pfau. “Coupling a single electron to a Bose-Einstein

- condensate”. In: *Nature* 502 (2013), pages 664–667. DOI: doi:10.1038/nature12592.
- [244] C Bahrim, U Thumm, and I I Fabrikant. “ $^3S^e$ and $^1S^e$ scattering lengths for $e^- + \text{Rb}$, Cs and Fr collisions”. In: *Journal of Physics B: Atomic, Molecular and Optical Physics* 34.6 (2001), page L195.
- [245] S. Ji, C. Ates, J. P. Garrahan, and I. Lesanovsky. “Equilibration of quantum hard rods in one dimension”. In: *J. Stat. Mech.* 2013 (2013), P2005. DOI: doi:10.1088/1742-5468/2013/02/P02005.
- [246] P. Michler, A. Kiraz, C. Becher, W. V. Schoenfeld, P. M. Petroff, Lidong Zhang, E. Hu, and A. Imamoglu. “A Quantum Dot Single-Photon Turnstile Device”. In: *Science* 290 (2000), pages 2282–2285. DOI: 10.1126/science.290.5500.2282.
- [247] Line Hjortshøj Pedersen and Klaus Mølmer. “Few qubit atom-light interfaces with collective encoding”. In: *Physical Review A* 79.1 (Jan. 2009). ISSN: 1094-1622. DOI: 10.1103/physreva.79.012320.
- [248] Mark Kasevich and Steven Chu. “Laser cooling below a photon recoil with three-level atoms”. In: *Physical Review Letters* 69.12 (Sept. 1992), pages 1741–1744. ISSN: 0031-9007. DOI: 10.1103/physrevlett.69.1741.
- [249] F.J. Harris. “On the use of windows for harmonic analysis with the discrete Fourier transform”. In: *Proc. IEEE* 66.1 (1978), pages 51–83. ISSN: 0018-9219. DOI: 10.1109/proc.1978.10837.
- [250] C R Murray, A V Gorshkov, and T Pohl. “Many-body decoherence dynamics and optimized operation of a single-photon switch”. In: *New Journal of Physics* 18.9 (Sept. 2016), page 092001. ISSN: 1367-2630. DOI: 10.1088/1367-2630/18/9/092001.

- [251] A. Uhlmann. “The “transition probability” in the state space of a $*$ -algebra”. In: *Reports on Mathematical Physics* 9.2 (1976), pages 273–279. ISSN: 0034-4877. DOI: 10.1016/0034-4877(76)90060-4.
- [252] Markus Mack, Florian Karlewski, Helge Hattermann, Simone Höckh, Florian Jessen, Daniel Cano, and József Fortágh. “Measurement of absolute transition frequencies of ^{87}Rb to nS and nD Rydberg states by means of electromagnetically induced transparency”. In: *Phys. Rev. A* 83 (5 May 2011), page 052515. DOI: 10.1103/PhysRevA.83.052515.
- [253] Wenhui Li, I. Mourachko, M. W. Noel, and T. F. Gallagher. “Millimeter-wave spectroscopy of cold Rb Rydberg atoms in a magneto-optical trap: Quantum defects of the ns , np , and nd series”. In: *Phys. Rev. A* 67 (5 May 2003), page 052502. DOI: 10.1103/PhysRevA.67.052502.

OPTICAL TRANSISTOR FLIPS ON WITH ONE PHOTON.
A computer based entirely on optical components could perform some tasks much faster than existing computers, which rely on electronic components whose speed is limited by heat generation. However, a fundamental limitation to making the components for an all-optical processor is that photons do not interact: unlike electrons that interact strongly and therefore can easily be used to manipulate other electrons, interactions between photons are generally too weak for one or several photons to be able to block or redirect others. However, recent experiments have shown that highly excited atomic states could mediate the necessary coupling between photons. Experimentalists have used these states to make a single-photon source, a single-photon phase shifter, and now, as reported by two independent research groups in *Physical Review Letters*, a single-photon transistor. Gerhard Rempe and his colleagues at the Max Planck Institute of Quantum Optics and Sebastian Hofferberth and his colleagues at University of Stuttgart, both in Germany, have succeeded in making the first single-photon transistors with high gain—a measure of efficiency—which is a key step [...] to build more complex optical circuits. [...]

Charles Adams, APS Physics Viewpoint
DOI: 10.1103/Physics.7.80